



POZNAŃ UNIVERSITY OF TECHNOLOGY

DOCTORAL THESIS

Direct approach noise analysis of a transonic axial compressor blade

Author:

MSc. Eng. Jędrzej MOSIEŻNY

Supervisor:

Prof. DSc. Eng. Michał CIAŁKOWSKI

*A thesis submitted in fulfilment of the requirements
for the degree of Doctor of Philosophy. Engineer.*

in the

Faculty of Work Machines and Transportation
Chair of Thermal Engineering

October 23, 2018

Declaration of Authorship

I, MSc. Eng. Jędrzej MOSIEŻNY, declare that this thesis titled, 'Direct approach noise analysis of a transonic axial compressor blade' and the work presented in it are my own. I confirm that:

- This work was done wholly or mainly while in candidature for a research degree at this University.
- Where any part of this thesis has previously been submitted for a degree or any other qualification at this University or any other institution, this has been clearly stated.
- Where I have consulted the published work of others, this is always clearly attributed.
- Where I have quoted from the work of others, the source is always given. With the exception of such quotations, this thesis is entirely my own work.
- I have acknowledged all main sources of help.
- Where the thesis is based on work done by myself jointly with others, I have made clear exactly what was done by others and what I have contributed myself.

Signed:

Date:

Abstract

This thesis proposes a method of assessing flow generated noise in transonic flows by direct formulation.

First a steady state Reynolds Averaged Navier-Stokes analysis of NASA R67 transonic axial compressor is performed as a validation study of the mesh and numerical setup. The result of the steady state analysis is then used as an initialization for transient DDES analysis performed on high quality, 11 million cells hexagonal mesh. The transient analysis covers 0.05s of physical flow time, which corresponds to about 800 revolutions of the rotor. Both steady state and transient simulations are performed on PL-Grid HPC infrastructure.

Transient results are analyzed with an in-house build program. The program uses information about static pressure, transient particle velocity and vorticity from each timestep. This data is then postprocessed into sound pressure levels, sound frequency and effective sound power level.

Information on generation of sound phenomena occurring in the blade passage are gathered from direct formulation and may be used as a validation case for FW-H or other computational aeroacoustic analogies dealing with flows in transonic regimes in rotating machinery.

Acknowledgements

In this place I would like to thank the Chair of Thermal Engineering of Poznań University of Technology, with special recognition to MSc. Eng. Bartosz Ziegler and PhD Eng. Przemysław Grzymisławski for thorough scientific and personal support during this project.

Thanks to PhD Martyna Urbanek – Trzeciak for thorough training in Python data analysis and support during preparation of Python post processing and visualization scripts.

Thanks to MSc. Eng. Natalia Lewandowska for thorough review, proof reading and providing quality of this work.

A big recognition goes to the owners and maintainers of the PLGRID - Polish HPC infrastructure, especially team in HPC Cyfronet center in AGH University of Science and Technology in Kraków. Being able to use the state of the art HPC clusters for analyses made this project possible.

Thank you to the Python and L^AT_EX community worldwide for tips & tricks, that helped software development and typesetting of this document. All code and typesetting developed for this project is Open Source and publicly available on the project GitHub repository.

Contents

Declaration of Authorship	iii
Abstract	v
Acknowledgements	vii
Contents	ix
List of Figures	xi
List of Tables	xv
Abbreviations	xvii
Symbols	xix
Indices	xxi
1 Introduction	1
1.1 Introduction and motivation	1
1.2 Growth of air traffic movements in early 20th century	2
1.3 Some excerpts from airworthiness regulations	7
1.4 Aircraft propulsion noise generation	13
2 Current research on Computational Aeroacoustics	17
2.1 Classification of CAA methods	17
2.2 Lighthill-Curle theory of aerodynamic sound	18
2.3 FW-H Analogy	20
2.4 Limitations to acoustic analogies	23
3 Approach and direct formulation of noise analysis	25
3.1 Direct formulation of noise analysis	25
3.2 CFD analysis requirements	27
3.3 Mesh sizing requirements	36
3.4 Timestep requirements	39
3.5 Limiting factors of the direct approach	40
4 Test case	41
4.1 NASA Rotor 67 transonic axial compressor	41
4.2 3D geometry preparation	42

4.3	Meshing approach	43
5	CFD Analysis	49
5.1	Case preprocessing	49
5.2	Flowfield initialization & RANS	50
5.3	DDES analysis	52
5.4	Validation of the results	54
6	Results of flow field noise analysis	57
6.1	Transition from flow-field to sound signal data	57
6.2	Sound levels results	57
6.3	Frequency analysis results	61
7	Conclusions & Further work	67
7.1	Results discussion	67
7.2	Improvements to the method	68
7.3	Further work	69
7.4	Closing remarks	70
A	RMS values plots	73
B	FFT plots	101
C	CFD validation	131
D	Code for direct formulation of noise analysis	143
E	Folder Structure	145
F	Code for RMS computation	147
G	Code for discrete Fourier analysis	149
H	Blade design surface coordinates	151
	Bibliography	165

List of Figures

1.1	Number of aircraft registered in the EU (EUROSTAT)	3
1.2	Growth rate of number of aircraft registered in the EU	3
1.3	Total number of passengers in the EU (EUROSTAT)	4
1.4	Growth rate. Total number of passengers in the EU	4
1.5	Number of airports (EUROSTAT)	5
1.6	Growth rate. Number of airports (self study)	5
1.7	Average annual growth (scenario C: Regulated Growth) [2]	7
1.8	Total traffic in 2035 [2]	7
1.9	CDA approach (solid line) vs. Standard approach (dash line)	11
1.10	Heathrow noise contours. 83% western & 17% eastern traffic [18]	12
1.11	Sources of noise of a turbofan engine [28]	14
1.12	Impact of aircraft noise sources at take-off and landing [28]	14
1.13	Engine nacelle chevron on a GEnx engine	15
1.14	Exemplary analysis on a chevron engine outlet [16]	15
3.1	Resolving eddies in different kinds of CFD analyses	28
3.2	Scenario 1. Wavelength smaller than cell edge length	37
3.3	Scenario 2. Wavelength equal to cell edge length	38
3.4	Scenario 3. Wavelength equal four minimum edge lengths	38
3.5	Scenario 4. Wavelength larger than four minimum edge lengths	38
4.1	Geometry of NASA R67	41
4.2	Final single passage geometry. Some features hidden for clarity	44
4.3	Vectors Used to Compute Orthogonal Quality for a Cell	45
4.4	Vectors Used to Compute Orthogonal Quality for a Cell	45
4.5	Mesh topology with conforming periodic boundaries	46
4.6	Mesh h-topology	46
4.7	Mesh quality histogram	48
4.8	Completed Mesh	48
5.1	Flowchart of the PISO algorithm	52
5.2	Constant pitch (left) and constant chord (right) lines [27]	54
5.3	Inlet pressure validation	55
5.4	Outlet pressure validation	55
6.1	Tip gap streamlines. Velocity in [m/s]	59
6.2	SPL to flowfield turbulence values correlation. Internal surfaces.	61
6.3	SPL to flowfield turbulence values correlation. Blade surfaces.	61
6.4	Exemplary FFT heatmap of magnitude. Random data.	62

6.5 AWF to flowfield turbulence values correlation. Internal surfaces	65
6.6 AWF to flowfield turbulence values correlation. Blade surfaces	65
A.1 Blade surface RMS Sound pressure [Pa]	73
A.2 Blade surface RMS SPLdB [dB]	74
A.3 RMS Sound pressure at int-01 mark	75
A.4 RMS Sound pressure decibel level at int-01 mark	75
A.5 RMS Sound intensity at int-01 mark	76
A.6 RMS Sound intensity decibel level at int-01 mark	76
A.7 RMS Sound pressure at int-02 mark	77
A.8 RMS Sound pressure decibel level at int-02 mark	77
A.9 RMS Sound intensity at int-02 mark	78
A.10 RMS Sound intensity decibel level at int-02 mark	78
A.11 RMS Sound pressure at int-03 mark	79
A.12 RMS Sound pressure decibel level at int-03 mark	79
A.13 RMS Sound intensity at int-03 mark	80
A.14 RMS Sound intensity decibel level at int-03 mark	80
A.15 RMS Sound pressure at int-04 mark	81
A.16 RMS Sound pressure decibel level at int-04 mark	81
A.17 RMS Sound intensity at int-04 mark	82
A.18 RMS Sound intensity decibel level at int-04 mark	82
A.19 RMS Sound pressure at int-05 mark	83
A.20 RMS Sound pressure decibel level at int-05 mark	83
A.21 RMS Sound intensity at int-05 mark	84
A.22 RMS Sound intensity decibel level at int-05 mark	84
A.23 RMS Sound pressure at int-06 mark	85
A.24 RMS Sound pressure decibel level at int-06 mark	85
A.25 RMS Sound intensity at int-06 mark	86
A.26 RMS Sound intensity decibel level at int-06 mark	86
A.27 RMS Sound pressure at int-07 mark	87
A.28 RMS Sound pressure decibel level at int-07 mark	87
A.29 RMS Sound intensity at int-07 mark	88
A.30 RMS Sound intensity decibel level at int-07 mark	88
A.31 RMS Sound pressure at int-08 mark	89
A.32 RMS Sound pressure decibel level at int-08 mark	89
A.33 RMS Sound intensity at int-08 mark	90
A.34 RMS Sound intensity decibel level at int-08 mark	90
A.35 RMS Sound pressure at int-09 mark	91
A.36 RMS Sound pressure decibel level at int-09 mark	91
A.37 RMS Sound intensity at int-09 mark	92
A.38 RMS Sound intensity decibel level at int-09 mark	92
A.39 RMS Sound pressure at int-10 mark	93
A.40 RMS Sound pressure decibel level at int-10 mark	93
A.41 RMS Sound intensity at int-10 mark	94
A.42 RMS Sound intensity decibel level at int-10 mark	94
A.43 RMS Sound pressure at int-11 mark	95
A.44 RMS Sound pressure decibel level at int-11 mark	95

A.45 RMS Sound intensity at int-11 mark	96
A.46 RMS Sound intensity decibel level at int-11 mark	96
A.47 RMS Sound pressure at int-12 mark	97
A.48 RMS Sound pressure decibel level at int-12 mark	97
A.49 RMS Sound intensity at int-12 mark	98
A.50 RMS Sound intensity decibel level at int-12 mark	98
A.51 RMS Sound pressure at int-tip mark	99
A.52 RMS Sound pressure decibel level at int-tip mark	99
A.53 RMS Sound intensity at int-tip mark	100
A.54 RMS Sound intensity decibel level at int-tip mark	100
B.1 Blade surface amplitude weighted average frequency [dB]	101
B.2 Blade surface frequency of peak amplitude[Hz]	102
B.3 Blade surface peak amplitude [dB]	103
B.4 Spectrum plot at int-01 mark	104
B.5 Amplitude weighted average frequency at int-01 mark	104
B.6 Peak amplitude frequency int-01 mark	105
B.7 Peak magnitude at int-01 mark	105
B.8 Spectrum plot at int-02 mark	106
B.9 Amplitude weighted average frequency at int-02 mark	106
B.10 Peak amplitude frequency int-02 mark	107
B.11 Peak magnitude at int-02 mark	107
B.12 Spectrum plot at int-03 mark	108
B.13 Amplitude weighted average frequency at int-03 mark	108
B.14 Peak amplitude frequency int-03 mark	109
B.15 Peak magnitude at int-03 mark	109
B.16 Spectrum plot at int-04 mark	110
B.17 Amplitude weighted average frequency at int-04 mark	110
B.18 Peak amplitude frequency int-04 mark	111
B.19 Peak magnitude at int-04 mark	111
B.20 Spectrum plot at int-05 mark	112
B.21 Amplitude weighted average frequency at int-05 mark	112
B.22 Peak amplitude frequency int-05 mark	113
B.23 Peak magnitude at int-05 mark	113
B.24 Spectrum plot at int-06 mark	114
B.25 Amplitude weighted average frequency at int-06 mark	114
B.26 Peak amplitude frequency int-06 mark	115
B.27 Peak magnitude at int-06 mark	115
B.28 Spectrum plot at int-07 mark	116
B.29 Amplitude weighted average frequency at int-07 mark	116
B.30 Peak amplitude frequency int-07 mark	117
B.31 Peak magnitude at int-07 mark	117
B.32 Spectrum plot at int-08 mark	118
B.33 Amplitude weighted average frequency at int-08 mark	118
B.34 Peak amplitude frequency int-08 mark	119
B.35 Peak magnitude at int-08 mark	119
B.36 Spectrum plot at int-09 mark	120

B.37 Amplitude weighted average frequency at int-09 mark	120
B.38 Peak amplitude frequency int-09 mark	121
B.39 Peak magnitude at int-09 mark	121
B.40 Spectrum plot at int-10 mark	122
B.41 Amplitude weighted average frequency at int-10 mark	122
B.42 Peak amplitude frequency int-10 mark	123
B.43 Peak magnitude at int-10 mark	123
B.44 Spectrum plot at int-11 mark	124
B.45 Amplitude weighted average frequency at int-11 mark	124
B.46 Peak amplitude frequency int-11 mark	125
B.47 Peak magnitude at int-11 mark	125
B.48 Spectrum plot at int-12 mark	126
B.49 Amplitude weighted average frequency at int-12 mark	126
B.50 Peak amplitude frequency int-12 mark	127
B.51 Peak magnitude at int-12 mark	127
B.52 Spectrum plot at int-tip mark	128
B.53 Amplitude weighted average frequency at int-tip mark	128
B.54 Peak amplitude frequency int-tip mark	129
B.55 Peak magnitude at int-tip mark	129
C.1 Relative Mach number at S10P20 streamline	131
C.2 Relative velocity angle at S10P20 streamline	131
C.3 Relative Mach number at S10P50 streamline	132
C.4 Relative velocity angle at S10P50 streamline	132
C.5 Relative Mach number at S10P80 streamline	133
C.6 Relative velocity angle at S10P80 streamline	133
C.7 Relative Mach number at S50P20 streamline	134
C.8 Relative velocity angle at S50P20 streamline	134
C.9 Relative Mach number at S50P50 streamline	135
C.10 Relative velocity angle at S50P50 streamline	135
C.11 Relative Mach number at S50P80 streamline	136
C.12 Relative velocity angle at S50P80 streamline	136
C.13 Relative Mach number at S90P20 streamline	137
C.14 Relative velocity angle at S90P20 streamline	137
C.15 Relative Mach number at S90P50 streamline	138
C.16 Relative velocity angle at S90P50 streamline	138
C.17 Relative Mach number at S90P80 streamline	139
C.18 Relative velocity angle at S90P80 streamline	139
C.19 RANS Mach number contour plot at int-04 mark	140
C.20 DDES Mach number contour plot at int-04 mark	140
C.21 RANS Mach number contour plot at int-09 mark	141
C.22 DDES Mach number contour plot at int-09 mark	141
C.23 RANS Mach number contour plot at int-12 mark	142
C.24 DDES Mach number contour plot at int-12 mark	142

List of Tables

1.1	Noise measurement points per ICAO Annex 16 [1]	10
1.2	Maximum noise levels per ICAO Annex 16 [1]	10
1.3	Noise Quota Count classification in Heathrow [18]	12
1.4	Examples of QC aircraft classification [18]	13
4.1	Basic R67 parameters	42
4.2	Test case boundary conditions	47
4.3	Location of compressor desing surfaces	47
5.1	Standard air properties	49
5.2	Test case boundary conditions	50
H.1	int-00 coordinates	151
H.2	int-01 coordinates	152
H.3	int-02 coordinates	153
H.4	int-03 coordinates	154
H.5	int-04 coordinates	155
H.6	int-05 coordinates	156
H.7	int-06 coordinates	157
H.8	int-07 coordinates	158
H.9	int-08 coordinates	159
H.10	int-09 coordinates	160
H.11	int-10 coordinates	161
H.12	int-11 coordinates	162
H.13	int-12 coordinates	163
H.14	int-tip coordinates	164

Abbreviations

APU	Auxillary Power Unit
BPF	Blade Passing Frequency
CAA	Computational Aero Acoustics
CAEP	Commitee on Aircraft Engine Emissions
CDA	Continuous Descent Approach
CFD	Computational Fluid Dynamics
CS	Coordinate System
DDES	Delayed Detached Eddy Simulation
DES	Detached Eddy Simulation
DFT	Discrete Fourier Transform
DNS	Direct Numerical Situation
EPNdB	Effective Perceived Noise dB
FMG	Full Multi Grid
FVM	Finite Volume Method
FWH	Ffowcks Williams Hawkins
HPC	Hight Power Computing
HVAC	Heating Ventilation Air Conditioning
ICAO	International Civil Aviation Organization
IFR	Instrumental Flight Rrules
ILU	Incomplete Lower Upper
LDA	Laser Doppler Anemometry
LES	Large Eddy Simulation
MCA	Multiple Circular Approach
MTOW	Maximum Take Off Weight
N-S	Navier Stokes
PISO	Pressure Implicit with Splitting of Operators
RANS	Reynolds Averaged Nnavier Stokes
RMS	Root Mean Square
S-A	Spallart Allmaras
SAS	Scale Adaptive Simulation
SBES	Stress Blended Eddy Simulation
SDES	Shielded Detached Eddy Simulation
SGS	Sub Grid Scale
SPLdB	Sound Pressure Level dB
SILDdB	Sound Intensity Level dB
SRS	Scale Resolving Simulation
SST	Shear Stress Transport

Symbols

A_i	Vector normal to cell wall at wall center	-
Amp	Amplitude	-
C_p	Specific heat at constant pressure	J/(kg · K)
Co	Courant number	-
G	Filter function	-
M	Moll weight	kg/kmol
Ma	Mach number	-
N	Total number of samples	-
$H(f)$	Heaviside function	-
P_i	Dipole acoustical strength	Pa
P_{ij}	Compression stress tensor	-
$Q(x, t)$	Mass introduced to system	kg
R	Gas constant	J/(kg · K)
Re	Reynolds number	-
S	Discontinuity surface	-
S_{ij}	Rate of Strain Tensor	-
T	Temperature	K
T_{ij}	Lighthill stress tensor	-
U	Velocity vector	-
V	Integration volume	-
X	DFT complex coefficient	-
a	Speed of sound	m/s
d	Mesh wall spacing	m
e	Euler number	-
f	Frequency	Hz
f_i	Vector connecting cell centroid and cell wall center	-
j	Imaginary number	-
k	k-th frequency bin	-
k	Turbulence kinetic energy	J/kg
n	Normal vector, n-th sample, blade count, cell count	-
p	Pressure	Pa
$q(t)$	Mass introduction rate	kg/s
r	Radiation vector	m
Δs	Mesh first layer thickness	m
t	Time	s
u, v, w	Velocity component	m/s
x, y, z	Distance over coordinate, location coordinate	m

Δ	Mesh wall spacing (Spalart-Allmaras)	m
Σ	Surface of discontinuity	-
Ω	Mean rate of rotation	-
δ	Mesh wall spacing (Spalart-Allmaras)	m
$\delta_{ij}, \delta(f)$	Dirac delta	-
η	Kolmogorov limit	-
θ	Phase shift	rad
κ	Specific Heat Ratio	-
λ	Wavelength	m
λ	Heat conductivity coefficient	W/(m · K)
ϕ	Conservation variable	-
ϕ'	Variable offset from average	-
$\bar{\phi}$	Filtered variable (LES derivation)	-
$\bar{\phi}$	Averaged variable (direct approach)	-
$\tilde{\phi}$	Density weighted filtering operator (LES derivation)	-
μ	Dynamic viscosity	Pa · s
μ_t	Turbulent viscosity	Pa · s
ν	Kinematic viscosity	m^2/s
$\tilde{\nu}$	Modified turbulent kinematic viscosity	m^2/s
ρ	Density	kg/m ³
σ_{ij}	Molecular viscosity stress tensor	-
τ	Retarded time	s
τ_{ij}	Subgrid scale tensor	s
ω	Angular frequency	rads ⁻¹
ω	Turbulence specific dissipation rate	1/s

Indices

0	initial, ambient conditions	-
<i>fric</i>	denotes friction component	-
<i>i, j, k</i>	summation indices	-
<i>k</i>	k-th sample, frequency bin	-
<i>n</i>	normal direction	-
<i>r</i>	radiation direction	-
<i>particle</i>	denotes particle specific value	-
<i>ref</i>	denotes reference value	-
<i>sound</i>	denotes sound value	-
<i>wall</i>	denotes near wall component	-
<i>wm</i>	wall modeled	-
<i>wr</i>	wall resolved	-
<i>x, y, z</i>	denotes direction of variable	m

To my wife. For limitless patience. . .

Chapter 1

Introduction

1.1 Introduction and motivation

Pollution by sound conducted by aircraft becomes one of the major concerns while introducing new aircraft to the market. Airframe noise and engine noise are considered as disturbing to population inhabiting the areas near the aerodrome, especially during take-off and landing operations. The concerns regarding the influence of the aircraft noise on the surrounding environment lead to development of international regulations defining the limits of the Effective Perceived Noise Levels for aircraft of certain type or family, maximum take off weight and engine count, as well as methods for measuring the aircraft noise. Although relatively easy to conclude, measuring aircraft noise as described in the regulations in consideration is achievable only when the aircraft is capable of flying, which, obviously, is at the final end of the process of introducing the aircraft to the market.

In order to asses the noise of the aircraft a set of engineering methods allowing predicting the noise of the aircraft is conceived. Such methods include, but are not limited to, vibroacoustics describing the effect of vibrating elements of devices on generation of sound, and aeroacoustics describing the effect of airflow and flow with solid boundary interaction on generation of sound.

Aeroacoustics as such is a relatively new branch of physics combining the classical approach to propagation of sound with mathematical formulation of fluid flow known from fluid mechanics. It is said that modern approach to aeroacoustics originated with the works of Lighthill [19] [20] in mid 1950s. Combining the mathematical formulation of equations governing the fluid flow with equations describing wave propagation, sound power and sound intensity allowed to asses the sound levels of turbulent flow.

Along with improvements of the computational methods in fields of computational fluid dynamics, general numerical methods and availability of computational resources,

Computational Aero Acoustics (described further in this work as computational aeroacoustics) was developed as an engineering tool for assessing sound generated by fluid flow without the necessity of manufacturing the device and performing expensive experiments.

This thesis opens with a high level overview of commercial air traffic situation based on data provided by EUROSTAT. The development and changes in the IFR movements in the European Union airspace are presented along with the forecast prepared by EUROSTAT and EUROCONTROL. This is followed by a high level analysis of current requirements regarding the noise emissions of a non-military aircraft. Following is a brief study of components of an aircraft responsible for generating sound pollution during various stages of flight. It is established that one of the main sources of noise generated by the aircraft is the fan and first stage of the low pressure compressor and therefore this component shall be investigated further.

The main focus of this thesis is generation of sound by a single blade of a low pressure compressor. It is assumed, that identifying sources of noise in the compressor flow will provide an insight for designing an efficient compressor blade with reduced noise emission and, therefore, allow for designing a quieter jet engine which directly translates to a less noisy aircraft. A NASA R67 1st stage compressor blade is the test subject for the thesis. The given compressor was chosen as the operating parameters range is similar to a modern day first stage fan of a twin spool, large bypass turbofan engine and large quantities of experimental and validation data. A comparison between different aeroacoustic methods is provided and a modification to a direct noise analysis method is suggested. The blade for the compressor is than analyzed using the proposed method and results are visualized and presented. The work is concluded and suggestions for designing a compressor blade with reduced generation of noise are formulated, along with suggestions for further work within researching the generation of compressor noise.

1.2 Growth of air traffic movements in early 20th century

Statistical records on commercial air movement between countries in Europe since year 2000 is available from EUROSTAT. Information regarding number of passengers, flights, registered aircraft and number of airports in the 1st decade of 20th century is extracted to describe the increase in the movement of commercial aircraft. Furthermore, a brief analysis of the long term forecasts (up to year 2035) provide some predictions on the future air traffic. Both statistics of the past movements and long term forecasts show an increase in the commercial air traffic above Europe. Combining the increase of number of flight operations from existing airports with rapid urban sprawl leads to increasing noise pollution in the urban areas.

1.2.1 Years 2000 – 2010

First number to be shown is the total number of aircraft in the EU (fig. 1.1). Trends for passenger aircraft and total number of aircraft show a slow increase of these numbers. Chain growth ratio of number of aircraft (fig. 1.2) shows a rapid increase in year 2006 and stabilization afterwards. At this point situation on European skies is rather comforting. But comparing these numbers with figure 1.3 may change the perspective.

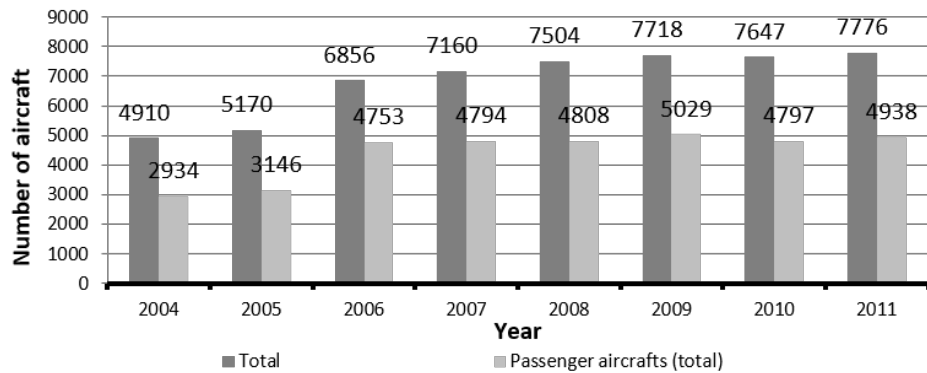


FIGURE 1.1: Number of aircraft registered in the EU (EUROSTAT)

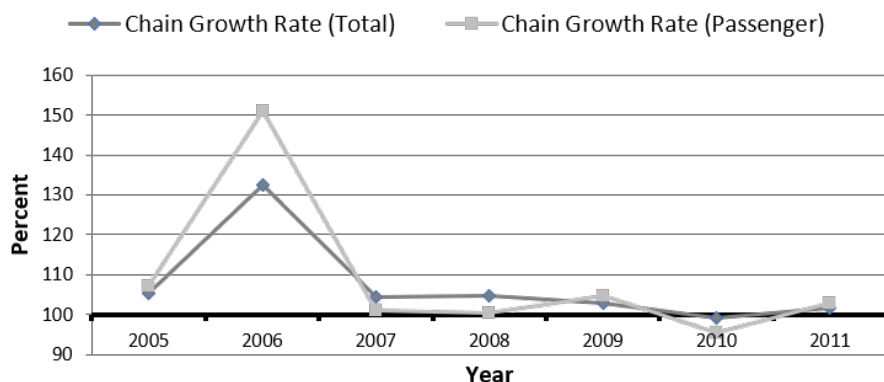


FIGURE 1.2: Growth rate of number of aircraft registered in the EU

As by figure 1.3, number of passengers is increasing, at average 50 to 70 million passengers every year. The growth rates (fig. 1.4) show large annual fluctuation of passenger count. Slowdown in year 2008 and decrease of passenger number in year 2009 are the aftermath of Financial Crisis of 2007-08. The situation recovers in years 2010-11. With roughly the same number of passenger airplanes (2007-11) this leads to rapid increase of passenger flights.

Existing fleet is supposed to deliver people and freight 24 hours a day, with very short overhaul periods, even shorter times to refuel and reload. Grounded aircraft generates loss instead of profit. Increasing number of flights generates yet another problem. All

airplanes need an airfield with proper infrastructure to perform flight operations, basic maintenance, serve passengers and so on.

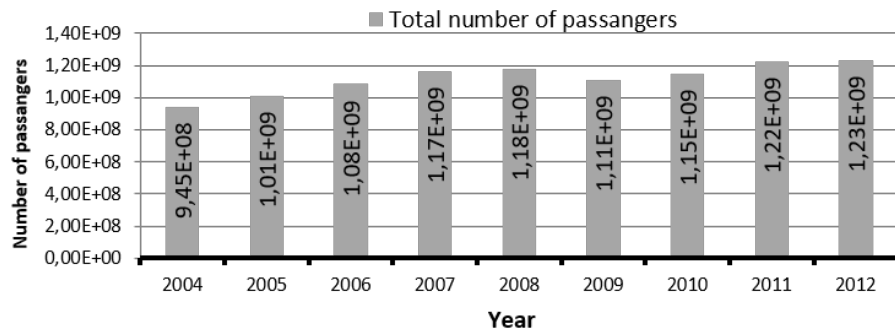


FIGURE 1.3: Total number of passengers in the EU (EUROSTAT)

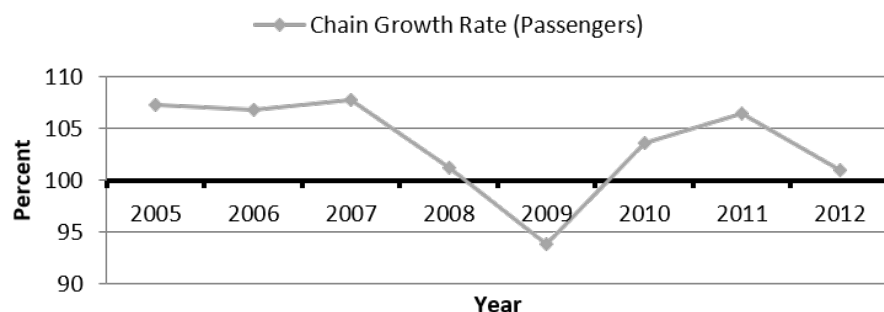


FIGURE 1.4: Growth rate. Total number of passengers in the EU

Surprisingly, the number of main airports is not following the trend set up by number of passengers. As seen on figure 1.5 number of main airports (serving more than 150 000 passengers a year) remains roughly the same, with very slight increase in research period. Change in number of main airports (fig. 1.6) is caused by varying number of passengers, rather than closing and opening airports. Decrease of number of airports in year 2009 is the aftermath of the economy crisis. Total number of airports varies among the years. This number includes small and medium airports such as club airfields and regional airports. Total number of airports (including registered regional and club airports) was under more influence of crisis and changed more rapidly.

1.2.2 Years 2010 – 2035

Trends presented in previous section may not give the full perspective. Years 2001–2012 show a significant increase in air traffic in Europe. Expansion of the EU in year 2004, Financial Crisis of 2007-2008, Arab Spring trampling through the Middle East and Northern Africa all have their reflection in air movements on the continent. These factors make the predictions harder than simple extrapolation of data.

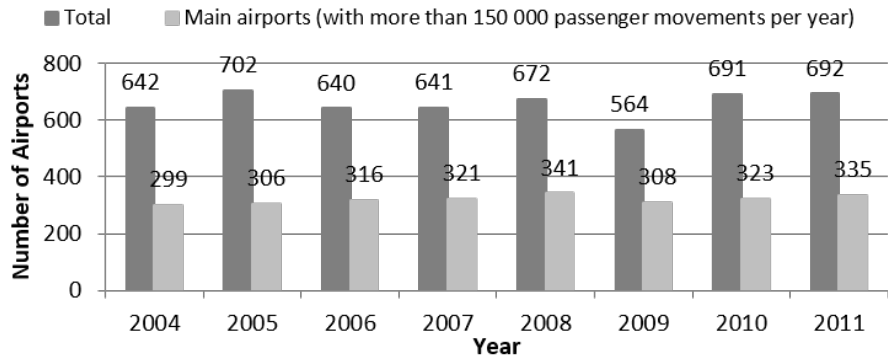


FIGURE 1.5: Number of airports (EUROSTAT)

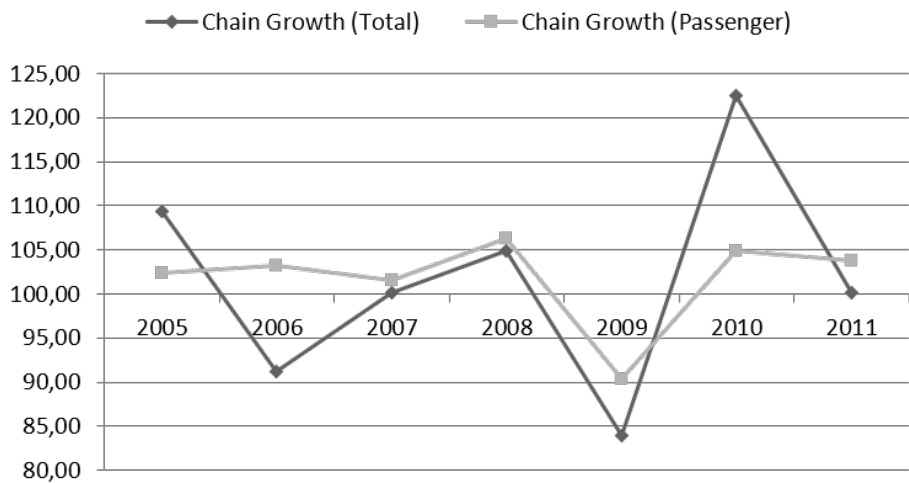


FIGURE 1.6: Growth rate. Number of airports (self study)

In order to show how air traffic will change, EUROCONTROL prepares medium and long term forecast for IFR movements. These forecasts are used mainly for planning purposes for airlines.

Long term forecast, published in June 2013 covers IFR flight movements for years 2013-2035. Because of the range, the forecast is more robust and is divided into four scenarios [3]

Scenario A: Global Growth (Technological Growth): Strong economic growth in an increasingly globalized World, with technology used successfully to mitigate the effects of sustainability challenges such as the environment or resources availability.

Scenario B: Not covered in [3].

Scenario C: Regulated Growth: Moderate economic growth, with regulation reconciling the environmental, social and economic demands to address the growing

global sustainability concerns. This scenario has been constructed as the most likely of the four, most closely following the trends.

Scenario C': Happy Localism: this scenario is introduced to investigate an alternative path for the future. With European economies being more and more fragile, increasing pressure on costs, stricter environmental constraints, air travel in Europe would adapt to new global environment but taking an inwards perspective. There would be less globalization, more trade inside EU (e.g. Turkey joining Europe is important in this scenario). Also, slow growth of leisure travel to outside Europe, however certainly more inside EU. More point-to-point traffic within Europe. It does not mean that Europe does not grow or does not adapt to new technologies and innovation but its main focus is local. Although this scenario is mostly based on scenario C (as its name indicates), it also inherits some aspects of other scenarios like higher fuel prices or low business aviation traffic of scenario D.

Scenario D: Fragmenting World: A World of increasing tensions between regions, with more security threats, higher fuel prices, reduced trade and transport integration and knock-on effects of weaker economies.

Scenario C: Regulated growth is considered to be the most likely at point of publishing the report. This forecast predicts 14.4 million flights in Europe 2035, which is 1.5 times more than in 2012. That creates an average growth of 1.8% per year. Forecast predicts that in 2025 traffic growth will decelerate due to predicted economic slowdown and reaching the capacity of airports.

As in medium term forecast, growth is not uniform across Europe. Due to lower starting point in calculations, more growth is expected in Eastern countries.

This however is not the full view on the situation. While growth will be faster in the East (figure 1.7), it is still mainly the big western countries that will need to deal with the greatest increase in the number of flights (figure 1.8).

Presented forecasts show, that air traffic in Europe will grow significantly in the next few years. With no actions taken, two paths are available. On one hand, running such traffic on existing fleet with airports (reaching maximum capacity) located near city centers will create an environment filled with constant aircraft noise. On a preventive side, noise emission regulations are being tightened nearly every year. And the only way to conform strict regulations is to use state of the art engines and airplanes, because in this case, silence is golden.

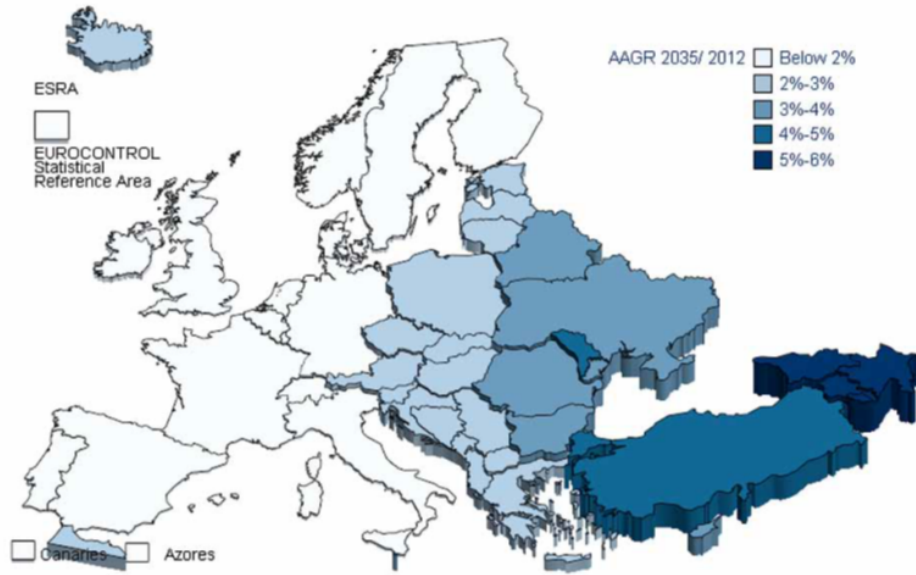


FIGURE 1.7: Average annual growth (scenario C: Regulated Growth) [2]

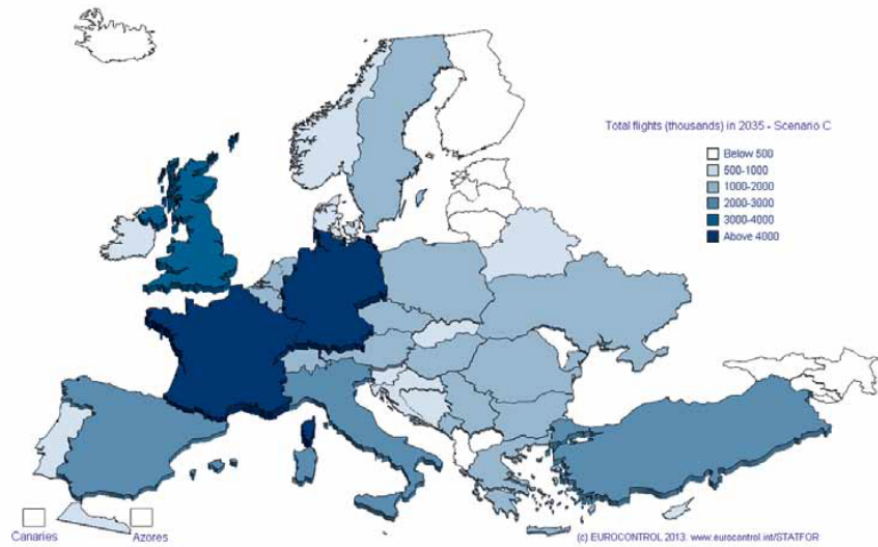


FIGURE 1.8: Total traffic in 2035 [2]

1.3 Some excerpts from airworthiness regulations

Any aircraft intended to carry people, both crew and passengers must fulfill rigorous airworthiness requirements including maximum stresses on the airframe, safety and ecological impact induced while the aircraft is in use. Initially, the requirements were created by the country of origin of aircraft manufacturer, but since aerial operations become international and intercontinental, the airworthiness regulations evolved. Current airworthiness requirements are developed, introduced and maintained by international

organizations such as ICAO. Excerpts from some top level requirements regarding generation of noise by aircraft at different stages of flight are presented in further sections.

1.3.1 CAEP regulations

ICAO's current environmental activities are largely undertaken through the Committee on Aviation Environmental Protection (CAEP), which was established by the Council in 1983, superseding the Committee on Aircraft Noise (CAN) and the Committee on Aircraft Engine Emissions (CAEE).

The current structure of the Committee includes three working groups and four support groups. The working groups deal with the technical and operational aspects of noise reduction and mitigation, with the aircraft noise and emissions issues linked to airports and operations and with the technical and operational aspects of aircraft emissions. One support group provides information on the economic costs and environmental benefits of the noise and emissions options considered by CAEP, one addresses models and databases issues, one deals specifically with the ICAO Carbon Calculator and the last one is aimed at scientific understanding of aviation environmental impacts.

About once a year, CAEP meets as a Steering Group to review and provide guidance on the progress of the activities of the working groups. So far, CAEP has held eight formal meetings: in 1986 (CAEP/1), 1991 (CAEP/2), 1995 (CAEP/3), 1998 (CAEP/4,) 2001 (CAEP/5), 2004 (CAEP/6), 2007 (CAEP/7) and 2010 (CAEP/8). Each formal CAEP meeting produces a report with specific recommendations for the consideration of the ICAO Council.

The Council acts on recommendations from CAEP in the light of any comments received from the Air Navigation Commission and, if there are economic aspects, from the Air Transport Committee. In the case of recommendations to introduce or amend Standards and Recommended Practices, there are established procedures for consulting States, after which the final decision rests with the Council.

1.3.2 ICAO Annex 16

Historically the oldest and presumably the most important regulations are stated in ICAO Annex 16 – Environmental Protection, Volume 1. First issue of this document was released in year 1981. At time of writing this article the latest issue is 6th, released in year 2011. Document contains standards (not strict requirements), Recommended Practices and Guide of the noise certification of aircraft that are operated in international air navigation, in accordance with the classification set out in the individual chapters: Each

chapter describes different noise measurement points (Table 1.1) and noise levels for specific aircraft types:

- a) Annex 16 Chapter 2 describes requirements for subsonic, jet engine propelled air-craft certified before 6th November 1977. With exceptions;
- b) Annex 16 Chapter 3 describes requirements for:
 - Subsonic, jet engine propelled aircraft certified between 6th November 1977 and 1st January 2006,
 - Propeller driven aircraft (MTOW over 8618 kg) certified between 1st January 1985 and 1st January 2006;
- c) Annex 16 Chapter 4 describes requirements for:
 - Subsonic, jet engine propelled aircraft certified after 1st January 2006;
 - Propeller driven aircraft (MTOW over 8618 kg) certified after 1st January 2006.

Separate Chapters contain information on light aircraft (Annex 16 Chapter 7) and helicopters (Annex 16 Chapters 8 & 11) and will not be discussed.

Table 1.1 and 1.2 contain a brief summarize of maximum noise levels and their measurement points. Noise levels and measurement points are not rigid. Maximum noise levels are logarithmic dependent from Maximum Take-Off Weight (MTOW) of certified aircraft. Highest noise levels are for heavier aircraft, with MTOW above 385 000 kg. Annex 16 fully describes weather requirements, flight procedures and equipment setup for proper measurements. Noise levels are presented in EPNdB (Effective Perceived Noise dB). This unit is not measurable in a direct manner. EPNdB calculations are based on measurements of noise level (measurements of acoustical pressure), spectrum of noise level and corrected with sustainability factors and noise damping of air (also dependent on weather). Methods on how to establish a measurement point, calculate correction factors from weather, wind, inaccurate measurement point are described in Annex or in its Addenda. Data presented below is an excerpt from chapters 2, 3 and 4 from 6th edition of ICAO Annex 16 (Table 1.1).

Maximum noise levels taken from Annex 16 are below 108 EPNdB. In comparison: Heavy traffic generates around 85dB, pneumatic road drill - circa 100dB, live rock concert generates circa 110-115dB noise. Exposition to noise level higher than 110dB for over 15 minutes may result in hearing damage. Short term (less than 10 minutes) exposure to 120 results in hearing damage, 130 dB is considered as a threshold of pain, 150dB causes eardrum rapture, while 194dB is considered as theoretical limit for sound barrier at 1 atmosphere of pressure.

TABLE 1.1: Noise measurement points per ICAO Annex 16 [1]

Chapter	Noise measurement point		
	Name	Distance	Point
2	Sideway	650m	On line parallel to runway where measured noise is max
	Fly-by	6.5km	On extent of runway axis measured from start of take-off
	Approach	2000m	From runway threshold below approach path
3, 4	Sideway (jet)	450m	On line parallel to runway where measured noise is max
	Sideway (prop)	650m	Below take-off path for take-off power climb
	Fly-by	6.5km	On extent of runway axis measured from start of take-off
	Approach	2000m	From runway threshold below approach path

TABLE 1.2: Maximum noise levels per ICAO Annex 16 [1]

Chapter	Point	Engine count	Maximum EPNdB
2	Sideway	N/A	108-102
	Fly-by	N/A	108-93
	Approach	N/A	108-102
3, 4	Sideway	N/A 1 or 2	103-94 101-89
	Fly-by	3	104-89
		4	106-89
	Approach	N/A	105-98

Noise levels appear to be high. But such levels occur only in the nearest vicinity of the airport. Concerning that nearly any main airport in Europe is surrounded by a large perimeter, nearest housing areas are subjected to noise levels that are safe, but may be considered as annoying. Also, many airports create their own noise requirements and do not allow air traffic operations of aircraft not conforming to such.

1.3.3 Local regulations

One of the airports with most strict noise requirements is London Heathrow. It is the third busiest airport in the world, serving more than 70 million passengers in 2012 and handling more international passengers than any other airport in the world.

In order to prevent nearby housing areas from noise effects, particularly at night, Heathrow airport introduced their own regulations for incoming and departing traffic. Air traffic Control at Heathrow Approach Control guides traffic incoming from four major routes into one approach stream. When possible, Controllers advise the use of Continuous Descent Approach (CDA). CDA allows for a smooth, constant-angle descent to landing (Fig. 1.9). A continuous descent approach starts ideally from the top of descent, i.e. at cruise altitude, and allows the aircraft flying its individual optimal vertical profile down to runway threshold.

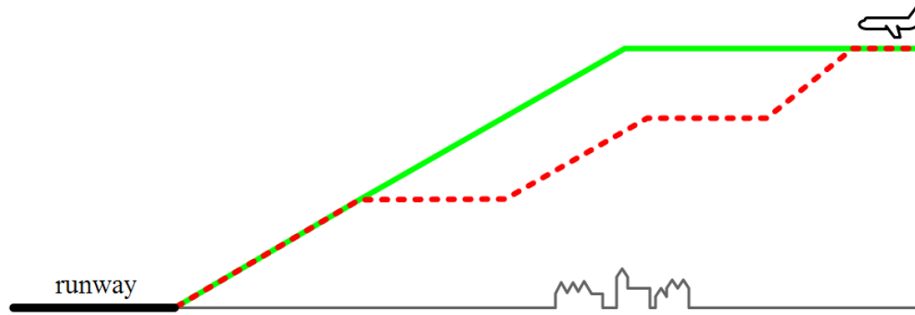


FIGURE 1.9: CDA approach (solid line) vs. Standard approach (dash line)

Night-time flights at Heathrow are subject to restrictions. Between 23:00 and 07:00, the noisiest aircraft (rated QC/8 and QC/16) cannot be scheduled for operation. In addition, during the night quota period (23:30–06:00) there are four limits:

- A limit on the number of flights allowed;
- A quota count system which limits the total amount of noise permitted, but allows operators to choose to operate fewer noisy aircraft or a greater number of quieter planes;
- QC/4 aircraft cannot be scheduled for operation;
- A voluntary agreement with the airlines that no early morning arrivals will be scheduled to land before 04:30.

A trial of "noise relief zones" ran from December 2012 to March 2013, which concentrated approach flight paths into defined areas compared with the existing paths which were spread out. The zones used alternated weekly, meaning residents in the "no-fly" areas received respite from aircraft noise for set periods. However, it was concluded that some residents in other areas experienced a significant disbenefit as a result of the trial and that it should therefore not be taken forward in its current form.

The Quota Count (QC) system was introduced on Heathrow in 1993. Each aircraft is classified and awarded a grade, called a Quota Count, based on how much noise it generates. Quieter aircraft are given a smaller grade. Aircraft are classified separately for landing and take-off. Take-off quota count values are based on the average of the certificated flyover and sideline noise levels at maximum take-off weight, with 1.75 EPNdB added for ICAO Annex 16 Chapter 2 aircraft. Landing quota count values are based on the certificated approach noise level at maximum landing weight minus 9.0 EPNdB.

Noise classification for aircraft is described in Table 1.3. Examples of aircraft classified in the QC system are presented in Table 1.4.

TABLE 1.3: Noise Quota Count classification in Heathrow [18]

Noise Classification	Quota Count
Below 84 EPNdB	Exempt
84-86.9 EPNdB	0.25
87-89.9 EPNdB	0.5
90-92.9 EPNdB	1
93-95.9 EPNdB	2
96-98.9 EPNdB	4
99-101.9 EPNdB	8
Greater than 101.9 EPNdB	16

Noise levels required by Heathrow Airport are far stricter than those stated in ICAO Annex 16. Such restrictions result in relatively noise friendly environment around Heathrow. ERCD report 1101 – Noise Exposure Contours for Heathrow Airport [18], prepared by Environmental Research and Consultancy Department of British Civil Aviation Authority shows the effect of Heathrow Airport traffic on nearby locations. Report prepared in year 2010, presents number and location of households affected by specific noise levels generated by Heathrow air traffic (Fig. 1.10).

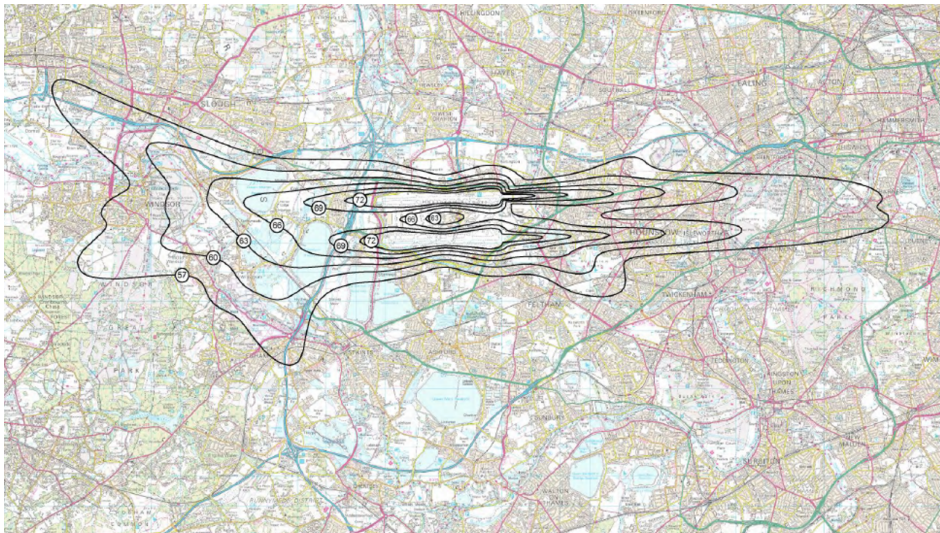


FIGURE 1.10: Heathrow noise contours. 83% western & 17% eastern traffic [18]

Noise contours (Fig. 1.10) show that 83dB of perceived noise level contains the terminal area, 72dB – in the nearest vicinity of the runway and 66dB outside the aerodrome premises. 60dB noise is comparable to normal office space or restaurant rustle. 70dB is the sound level of moderate traffic and may be annoying to some people.

This concludes that Heathrow airport restricts the movements of really loud airships to prevent its neighbors from aircraft noise. Presumably, Heathrow restrictions will lower the acceptable noise levels even more, due to increasing air traffic and urban sprawl around the airport.

TABLE 1.4: Examples of QC aircraft classification [18]

Aircraft type	QA Departure	QC Arrival
Airbus A320 family	0.5-1	0.25-0.5
Airbus A380	2	0.5
Boeing 737 Classic	0.25-0.5	1
Boeing 747-400	4	2
Boeing 747-8	2	1
Boeing 757-200	0.5	0.25
Boeing 767-300	1 - 2	1
Boeing 777-200ER	2	1
Embraer 145	0.25	0.25

1.4 Aircraft propulsion noise generation

Requirements described above are obviously relevant to an aircraft as a whole entity. In order to engineer a flying machine capable of fulfilling the stated requirements, one must identify the sources of noise within the aircraft in question.

Let's consider a "generic" airliner-kind of aircraft. Main sources of noise of such are the engines, aerodynamic surfaces and fuselage inducing turbulence and aerodynamically generated sound, APU as well as various internal aggregates (fuel and oil pumps, HVAC systems, electrical motors).

Research provided by Traub [28] gives an insight towards the components of noise generated by the aircraft during takeoff and landing, that is during two flight stages where the sound induced by aircraft is the most audible by the population on the ground. During the take-off phase, with engines set to maximum thrust generation, the fan noise and jet noise are the dominant components of the overall sound generation. During approach and landing phase, where engines are set to idle thrust, the dominant components are the engine fan and the airframe. The airframe noise is generated mostly by the extended high lift system generating flow of significant turbulence and vorticity 1.11.

The engine noise generation is distributed over its main components 1.11. A rather obvious conclusion arises. The more accessible the component is from the outside, the higher noise levels of the component are registered. Following that statement, for a large bypass turbofan engine, the impact of fan and exhaust jet is the most significant during the take-off and landing phase.

At this stage of study it can be assumed, that noise generation by the jet engine consists of three phenomena: noise generated by interaction of rotating machinery, combustion and combustion instability noise, and noise of mixing in shear layer in the exhaust jet. Detailed studies on sound generation by turbomachinery are found in set of articles in proceedings [17]. Details on combustion noise are presented in book [23].

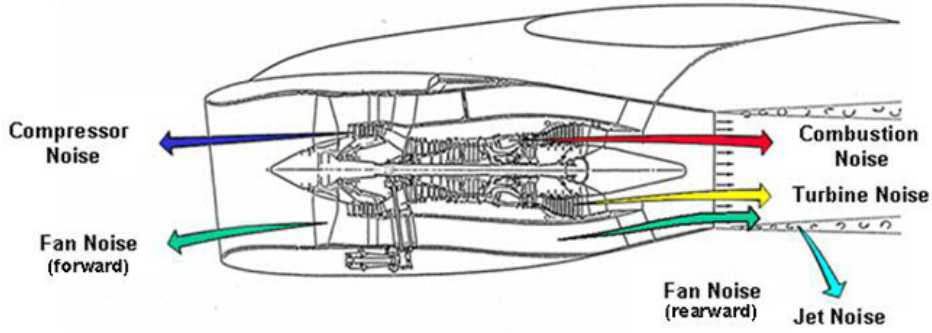


FIGURE 1.11: Sources of noise of a turbofan engine [28]

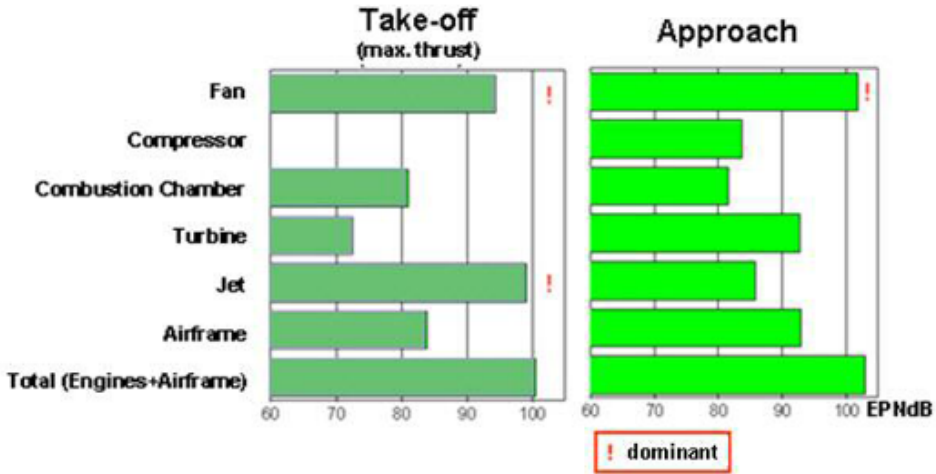


FIGURE 1.12: Impact of aircraft noise sources at take-off and landing [28]

Reducing the noise of a jet engine is a daring engineering task. Yet, the easiest element to handle with regard to noise emission is to reduce the sound emission of exhaust jet by introducing the additional turbulence degrading the mixing in the shear layer of the air stream behind the engine. This is achieved by introducing a minor modification to an engine nacelle and outlet nozzle that enforces rapid dissipation of the shear layer between the ambient air and the engine exhaust jet (fig. 1.13).

Implementation of a chevron enforces fluid motion, so that with minor (below 0.5%) decrease of thrust, achieving a decrease in EPNdB of a jet stream by 2.5 decibels, as performed on a scale tests performed by NASA (fig. 1.14) [16]. Such devices are becoming more popular in modern (or retrofitted) airliners in order to conform the strict requirements.

Reduction of noise generated by a fan requires deeper modifications to the engine construction. Both passive and active modifications to the fan rotor blades require extensive testing and certification on nearly all stages of the design process.



FIGURE 1.13: Engine nacelle chevron on a GEnx engine

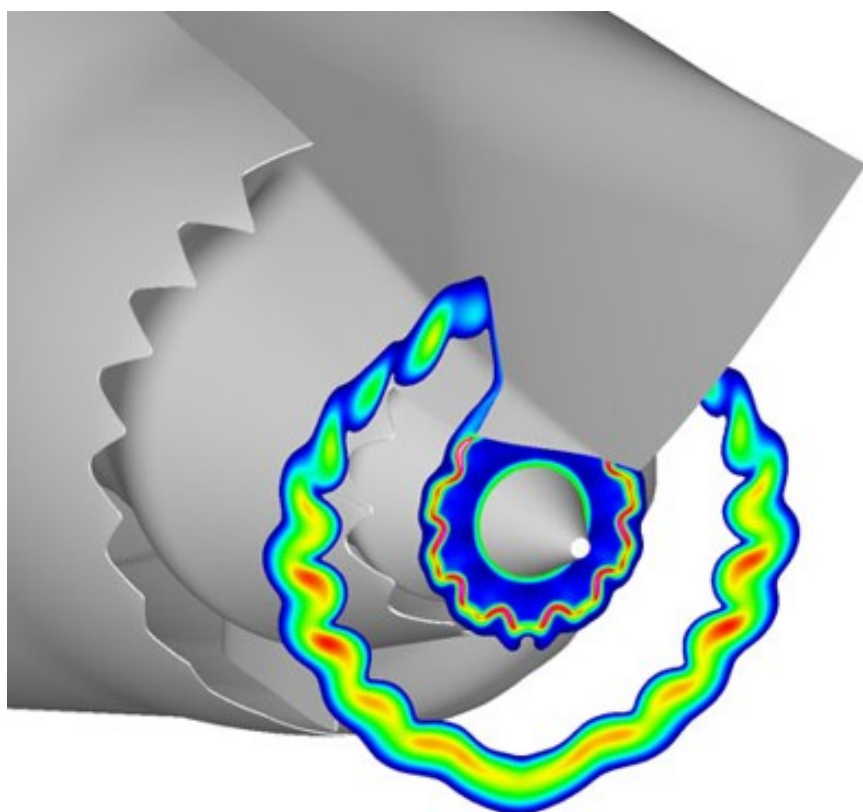


FIGURE 1.14: Exemplary analysis on a chevron engine outlet [16]

Chapter 2

Current research on Computational Aeroacoustics

2.1 Classification of CAA methods

Computational aeroacoustics is a branch of aeroacoustics that aims to analyze the generation of noise by turbulent flows by means of numerical methods. A following classification of available methods is currently in use.

1. Hybrid Approach.
 - (a) Integral Method
 - i. Lighthill's Analogy
 - ii. Kirchoff Integral
 - iii. FW-H
 - (b) Linearized Euler Equations
 - (c) Pseudo Spectral
 - (d) EIF
 - (e) APE
2. Direct approach.

The direct approach is the core of this thesis and will be described in detail in chapter 3. A brief introduction to Lightill's analogy with Curle's modification is provided below. Ffowcs Williams Hawkings analogy as an extension to the theory is also provided.

2.2 Lighthill-Curle theory of aerodynamic sound

A mathematically formulated linkage between description of fluid flow and sound generation phenomena was proposed and solved by M. J. Lighthill. His work [19] focused on sound generation as a byproduct of airflow as distinct from sound generated by vibration of solids.

Consider a system with fluctuating flow occupying a very large volume of fluid, at which the non fluctuating part is at rest. Three mechanism of introducing kinetic energy to the system and transforming it to "acoustic energy" are following:

- I By forcing a mass of the fluid in a fixed region to fluctuate, as in the loudspeaker diaphragm
- II By forcing the momentum in fixed space to fluctuate or by forcing the rates of flux through a given control surface to vary, as in vibrating part of a machine (or after striking a tuning-fork)
- III By forcing the rates of flux through a given control surface to vary, without the vibrating motion of solid boundaries, as in noise generated turbulence in flow.

Efficiency of transformation the kinetic energy do sound decreases down the list. First two phenomena are well established in current knowledge and were described in many sources. The research on sound generated aerodynamically starts (probably) with aforementioned work [20].

Lighthill proposes, that Reynolds momentum equation (derived in chapter 3) already expresses that the momentum changes at exactly the same rate as if the medium was at rest under the combined action of real stresses and fluctuating Reynolds stresses. Uniform acoustic medium at rest experiences stresses only from variation of density proportional to the speed of sound squared. A Lighthill stress tensor is therefore introduced to describe the fluctuations of the fluid medium subject to acoustic stresses:

$$T_{ij} = \rho v_i v_j + P_{ij} - a_0^2 \rho \delta_{ij} \quad (2.1)$$

Term P_{ij} is the compression tensor defined as:

$$P_{ij} = (p - p_0) \delta_{ij} - \sigma_{ij} \quad (2.2)$$

where σ_{ij} is the stress tensor due to molecular viscosity defined by:

$$\sigma_{ij} \equiv \left[\mu \left(\frac{\partial \bar{u}_i}{\partial x_j} + \frac{\partial \bar{u}_j}{\partial x_i} \right) \right] - \frac{2}{3} \mu \frac{\partial \bar{u}_l}{\partial x_l} \delta_{ij} \quad (2.3)$$

Propagation of sound in fluid medium without external forces is presented by following governing equations:

$$\frac{\partial \rho}{\partial t} + \frac{\partial}{\partial x_i} (\rho v_i) = 0 \quad (2.4)$$

$$\frac{\partial}{\partial t} (\rho v_i) + a_0^2 \frac{\partial \rho}{\partial x_i} = 0 \quad (2.5)$$

$$\frac{\partial^2 \rho}{\partial t^2} - a_0^2 \nabla^2 \rho = 0 \quad (2.6)$$

The equation 2.4 is the continuity equation for a compressible fluid, equation 2.5 is an approximate equation of momentum and equation 2.6 is established by eliminating the ρv_i term from the previous equations.

By implementing the T_{ij} tensor to the equations 2.4 thru 2.6, the following form is obtained:

$$\frac{\partial \rho}{\partial t} + \frac{\partial}{\partial x_i} (\rho v_i) = 0 \quad (2.7)$$

$$\frac{\partial}{\partial t} (\rho v_i) + a_0^2 \frac{\partial \rho}{\partial x_i} = - \frac{\partial T_{ij}}{\partial x_j} \quad (2.8)$$

$$\frac{\partial^2 \rho}{\partial t^2} - a_0^2 \nabla^2 \rho = \frac{\partial^2 T_{ij}}{\partial x_i \partial x_j} \quad (2.9)$$

Therefore a term describing the fluctuations related to acoustic phenomena is now linked to the flow governing equations. It is now assumed, that resolving fluid flow along with the appropriate stress, strain and deformation terms can be now used to asses the sound phenomena in the flow field.

Should the receiver of the acoustical signal be outside the computational domain, further investigation must be concluded. Consider an unbounded flow field with a fluctuating point source, so that mass $Q(x, t)$ is introduced to the system at point x and time t , with total rate of introduction of $q(t)$. The density field is than given by the equation:

$$\rho - \rho_0 = \frac{1}{4\pi a_0^2} \frac{q' \left(\frac{t-r}{a_0} \right)}{r} \quad (2.10)$$

where r is the distance from source and $q'(t)$ is the time derivative of $q(t)$ and is defined as instantaneous source strength. For distributed source the equation 2.10 takes form:

$$\rho - \rho_0 = \frac{1}{4\pi a_0^2} \int \frac{\partial}{\partial t} Q \left(y, t - \frac{|x-y|}{a_0} \right) \frac{dy}{|x-y|} \quad (2.11)$$

The equation 2.11 is then solved to a form:

$$\rho - \rho_0 = \frac{1}{4\pi a_0^2} \frac{\partial^2}{\partial x_i \partial x_j} \int T_{ij} \left(y, t - \frac{|x-y|}{a_0} \right) \frac{dy}{|x-y|} \quad (2.12)$$

The equation 2.12 considers an unbounded flow field with point or volumetric source of fluctuations considered as quadrupole sources of acoustic fluctuations. This concept was evolved by Curle [13] to include the effect of solid boundaries on their reflection and diffraction. The modification of the original equation 2.12 is:

$$\begin{aligned} \rho - \rho_0 &= \frac{1}{4\pi a_0^2} \frac{\partial^2}{\partial x_i \partial x_j} \int_V T_{ij} \left(y, t - \frac{r}{a_0} \right) \frac{dy}{r} \\ &\quad - \frac{1}{4\pi a_0^2} \frac{\partial}{\partial x_i} \int_S P_i \left(y, t - \frac{r}{a_0} \right) \frac{dS(y)}{r} \end{aligned} \quad (2.13)$$

where:

$$P_i = -l_j P_{ij} \quad (2.14)$$

where: $l_i = (l_1, l_2, l_3) = n$ is the direction cosines of the outward normal from the fluid, and the sound generated in a medium at rest by a distribution of dipoles of strength P_i per unit area and therefore P_i is the force per unit area exerted on the fluid by the solid boundaries in the x_i direction.

2.3 FW-H Analogy

Further development of analogies developed in references [19], [20] and [13] is presented in work [33]. The extension to the theory includes the effect of arbitrary convective motion of fluid. More over, the FW-H analogy switches from Lighthill's unbounded fluid to a bounded volume. Thus it is possible to compute the flow phenomena within the acoustic near field (which in this case would be a CFD domain) and compute the sound propagation outwards to the acoustic far field (outside the CFD domain) using wave propagation equations.

FW-H analogy derives it's governing equation from a volume of fluid V enclosed by a surface Σ , divided into regions 1 and 2 with surface of the discontinuity S moving into region 2 with velocity v . By formulating the rate of change of mass within volume V and deriving a generalized continuity and momentum equations, an equation governing the generation and propagation of sound is obtained.

$$\left(\frac{\partial^2}{\partial t^2} - a^2 \frac{\partial^2}{\partial x_i^2} \right) (\overline{\rho - \rho_0}) = \frac{\partial^2 \overline{T_{ij}}}{\partial x_i \partial x_j} - \frac{\partial}{\partial x_i} \left(P_{ij} \delta(f) \frac{\partial f}{\partial x_j} \right) + \frac{\partial}{\partial t} \left(\rho_0 v_i \delta(f) \frac{\partial f}{\partial x_i} \right) \quad (2.15)$$

where: $(\overline{\rho - \rho_0})$ is the generalized density perturbation - the amplitude of sound and $\overline{T_{ij}}$ is equal to T_{ij} (eq. 2.1) outside any surfaces and equal 0 when within them. Equation $f = 0$ defines the division surface surface S , such that $f < 0$ is in the region 1 and $f > 0$ in region 2 (Heavyside function). The $\delta(f)$ is the Dirac delta function.

The equation 2.15 shows that sound can be regarded as generated by three source distributions: in volume - the quadrupole distribution of strength T_{ij} , on surface - the distribution of dipoles of strength density $P_{ij}n_j$ and monopole distributions from the displacement of volume by the moving surface.

Equation 2.15 can be rewritten to a different form:

$$\begin{aligned} \frac{1}{a_0^2} \frac{\partial^2 (p')}{\partial t^2} - \nabla^2 (p') &= \frac{\partial^2}{\partial x_i \partial x_j} \{ T_{ij} H(f) \} \\ &- \frac{\partial}{\partial x_i} \{ [P_{ij} n_j + \rho u_i (u_n - v_n)] \delta(f) \} \\ &+ \frac{\partial}{\partial t} \{ [\rho_0 v_n + \rho (u_n - v_n)] \delta(f) \} \end{aligned} \quad (2.16)$$

where:

$p' = p - p_0$ — sound pressure fluctuation

u_i — fluid velocity in the x_i direction

u_n — fluid velocity component normal to the surface $f = 0$

v_i — surface velocity in the x_i direction

v_n — surface velocity component normal to the surface

$H(f)$ — Heaviside function

$\delta(f)$ — Dirac delta function

The rewritten equation 2.16 represents an inhomogeneous wave equation can be integrated under specific assumptions and the solutions consists of surface (monopole and dipole sources) and volume integrals (quadrupole sources). Software package used

for further computations omits the effect of volume integral, therefore the result is of following form:

$$p'(x, t) = p'_T(x, t) + p'_L(x, t) \quad (2.17)$$

with further development of the solution:

$$\begin{aligned} 4\pi p'_T(x, t) &= \int_{f=0} \left[\frac{\rho_0 (\dot{U}_n + U_{\dot{n}})}{r (1 - M_r)^2} \right] dS \\ &+ \int_{f=0} \left[\frac{\rho_0 U_n \{ r \dot{M}_r + a_0 (M_r - M^2) \}}{r^2 (1 - M_r)^3} \right] dS \end{aligned} \quad (2.18)$$

$$\begin{aligned} 4\pi p'_L(x, t) &= \frac{1}{a_0} \int_{f=0} \left[\frac{\dot{L}_r}{r (1 - M_r)^2} \right] dS \\ &+ \int_{f=0} \left[\frac{L_r - L_M}{r^2 (1 - M_r)^2} \right] dS \\ &+ \frac{1}{a_0} \int_{f=0} \left[\frac{L_r \{ r \dot{M}_r + a_0 (M_r - M^2) \}}{r^2 (1 - M_r)^3} \right] dS \end{aligned} \quad (2.19)$$

where:

$$U_i = v_i + \frac{\rho}{\rho_0} (u_i - v_i) \quad (2.20)$$

$$L_i = P_{ij} n_j + \rho v_i (u_i - v_i) \quad (2.21)$$

When the integration surface coincides with an impenetrable wall, the two terms equation 2.17, $p'_T(x, t)$ and $p'_L(x, t)$ are often referred to as thickness and loading terms, respectively, in light of their physical meanings. The square brackets in equations 2.18 and 2.19 denote that the kernels of the integrals are computed at the corresponding retarded times, τ , defined as in equation 2.22, given the receiver time, t , and the distance to the receiver, r .

$$\tau = t - \frac{r}{a_0} \quad (2.22)$$

The various subscripted quantities appearing in equations 2.18 and 2.19 are the inner products of a vector and a unit vector implied by the subscript. For instance, $L_r = \vec{L} \cdot \vec{r} = L_i r_i$ and $U_n = \vec{U} \cdot \vec{n} = U_i n_i$, where \vec{r} and \vec{n} denote the unit vectors in the radiation and wall-normal directions, respectively. The Mach number vector M_i in equations 2.18 and 2.19 relates to the motion of the integration surface: $M_i = \frac{v_i}{a_0}$. The L_i quantity is a scalar product $L_i M_i$. The dot over a variable denotes source-time differentiation of that variable [4] [33] [9].

FW-H analogy is therefore the general form of Lighthill's acoustic analogy for aerodynamically generated noise, including volume sources of quadrupole kind, such as turbulence in free stream, and dipole and monopole sources of the moving solid body surface within the flow. Solution of the governing equation 2.15 given in equations 2.17, 2.19 & 2.18 omits the sources as weak.

2.4 Limitations to acoustic analogies

Hybrid methods, including the presented Ffowcs Williams – Hawking analogy provide a computationally efficient task for engineering problems such as airframe noise, noise of jet injection to ambient medium at rest (that is jet engine noise problem), effect of wake generated by automobile mirror on noise in the vehicle cabin. The solution to the FW-H governing equation presented in equations 2.18 and 2.19 may reach instability when the Mach number in the sound radiation direction M_r approaches 1, that is: when the freestream flow velocity approaches sonic conditions. Using the hybrid approach with acoustic analogies may be challenging and poses a risk of obtaining "non-physical" results for case considered in this thesis, that is blade of axial compressor in stationary reference frame.

For phenomena characteristic to axial compressor flow, that is strong shockwaves, shockwave with boundary layer interaction, high separation of flow enforced by shock waves, and high adverse pressure gradient may cause mathematical and numerical instabilities to the solution. Considering the pressure change within the computational domain, or, from the governing equation's standpoint, the volume enclosed by a surface, poses some difficulty to choosing free-stream values of density and pressure.

Further attempts towards gaining insight of the sound generation phenomena shall be performed by attempting to use a direct formulation method.

Chapter 3

Approach and direct formulation of noise analysis

3.1 Direct formulation of noise analysis

The intention behind this study is to perform a flow field noise analysis in CFD without implementation of acoustical analogies to the CFD code itself. Moreover, very limited information on direct formulation of noise analysis was found during the research, with even fewer research on acoustical nearfield of transonic axial compressors or axial fans of twin spool jet engines.

The process for the direct formulation noise analysis is following:

1. Obtain raw flowfield data of static pressure, velocity magnitude from CFD analysis,
2. Perform averaging over time of pressure and velocity magnitude for each point or cell in the flowfield (equation 3.1),
3. Obtain offset from mean static pressure and velocity magnitude for every timestep for every point/cell in the saved flow field (equation 3.2).

$$\bar{p} = \frac{1}{n} \sum_{n=1}^N p_k \quad \text{and} \quad \bar{u} = \frac{1}{n} \sum_{n=1}^N u_k \quad (3.1)$$

$$p_{k \text{ sound}} = p_k - \bar{p} \quad \text{and} \quad u_{k \text{ particle}} = u_k - \bar{u} \quad (3.2)$$

Sound pressure signal and flow velocity offset is obtained for every node or cell centroid throughout the simulation flowtime. This dataset can be now post processed. Dataset obtained in described manner now contains sound pressure in the flowfield in

every mesh node or cell centroid throughout the computational time. The dataset is now post processed to obtain quantity information of the acoustic nearfield.

Sound intensity for cells/nodes in fluid volume is calculated using formula 3.3.

$$I_k = p_{k \text{ sound}} \cdot u_{k \text{ particle}} \quad (3.3)$$

RMS sound pressure level and intensity level can be obtained from the respective data with use of the formula 3.4.

$$p_{rms} = \sqrt{\frac{\sum_{n=1}^N p_{k \text{ sound}}^2}{N}} \quad I_{rms} = \sqrt{\frac{\sum_{n=1}^N u_{k \text{ particle}}^2}{N}} \quad (3.4)$$

Sound pressure decibel level (SPLdB) for time specific $p_{k \text{ sound}}$ values and RMS values p_{rms} is computed using formula 3.5 with standard reference pressure $p_{ref} = 20\mu Pa$, whereas for sound intensity with formula 3.6 and with reference intensity $I_{ref} = 1pW/m^2$.

$$SPLdB = 20 \cdot \log_{10} \left(\frac{|p_{k \text{ sound}}|}{p_{ref}} \right) \quad (3.5)$$

$$SILdB = 10 \cdot \log_{10} \left(\frac{|I_k|}{I_{ref}} \right) \quad (3.6)$$

The signal obtained by direct approach is stored in discrete samples. Using a continuous Fourier Transform would require approximation of the sampled signal to a continuous function, which for large datasets is unjustified. In order to obtain ordinary sinuses of the acoustic signal a Discrete Fourier Transform is performed (eq. 3.7).

$$X_k = \sum_{n=0}^{N-1} x_n \cdot e^{-\frac{j2\pi kn}{N}} \quad (3.7)$$

Let's assume that:

$$b_n = \frac{2\pi kn}{N} \quad (3.8)$$

Therefore, the equation 3.7 can be written as:

$$X_k = x_0 e^{-jb_0} + x_1 e^{-jb_1} + x_2 e^{-jb_2} + \dots + x_{N-1} e^{-jb_{N-1}} \quad (3.9)$$

Using Euler's identity the exponent is decomposed (eq. 3.10) to a complex sum:

$$e^{jx} = \cos(x) + j \cdot \sin(x) \quad (3.10)$$

Therefore the equation 3.7 can be written as:

$$X_k = x_0[\cos(-b_0) + j \sin(-b_0)] + \dots + x_{N-1}[\cos(-b_{N-1}) + j \sin(-b_{N-1})] \quad (3.11)$$

Rearranging the equation 3.11 and summing up the real and imaginary components will return a complex vector X_k for "k-th" frequency bin.

$$X_k = A_k + jB_k \quad (3.12)$$

The frequency resolution of the DFT depends on the sampling frequency and number of samples, and is calculated by formula 3.13.

$$f_{bin} = \frac{f_s}{N} \quad (3.13)$$

Fourier coefficients are then used to compute the amplitude (eq. 3.14) and phase shift (eq. 3.15) for the "k-th" frequency bin ordinary sinus.

$$\text{Amp}_k = 2 \cdot \sqrt{A_k^2 + B_k^2} \cdot \frac{1}{N} \quad (3.14)$$

$$\theta_k = \arctan \frac{B_k}{A_k} \quad (3.15)$$

3.2 CFD analysis requirements

References [19], [20], [33] and [13] provide a theoretical insight on generating sound in fluid flow due to shear mixing of flows or by implementing a solid boundary in the flow. General remark is: any source of turbulence that result in pressure fluctuation will result in generating sound. Therefore the main requirement for CFD analysis used in direct approach noise analysis is the capability of resolving turbulent flow and corresponding fluctuations of pressure.

Let's consider the effect of injection of energy to the fluid resulting in creation of eddies (Fig. 3.1). Once the energy is injected to the fluid, a large scale eddy is formed and due to the fluid viscosity the eddy dissipates along with the dissipation of energy up to the point where the particle movement is considered as heat.

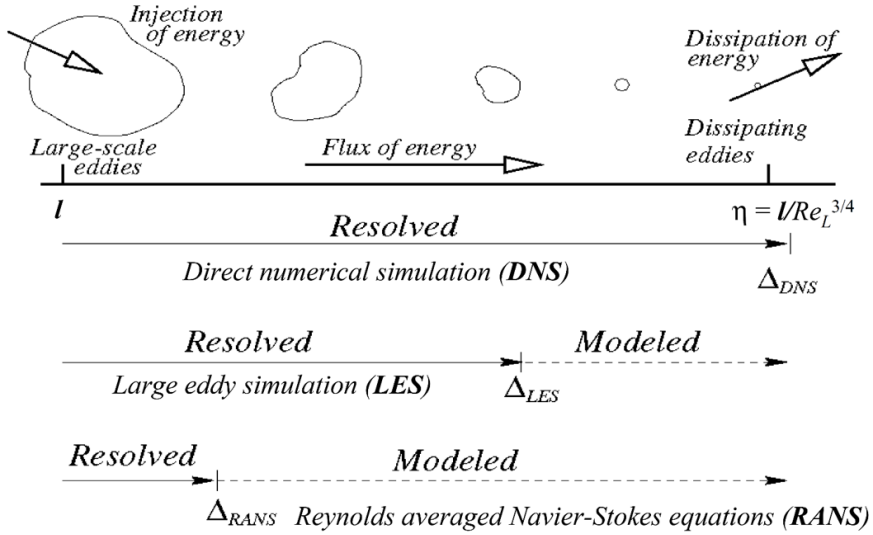


FIGURE 3.1: Resolving eddies in different kinds of CFD analyses

3.2.1 Governing equations

Computational fluid dynamics is based upon two equations governing the motion and deformation of the fluid: the continuity (3.16) and momentum (3.17) equations.

$$\frac{\partial \rho}{\partial t} + \nabla(\rho U) = 0 \quad (3.16)$$

$$\frac{dU}{dt} = -\frac{1}{\rho} \nabla p + \nu \nabla^2 U \quad (3.17)$$

In order to solve the governing equations in a computational grid, using a software system that is incapable of solving partial differential equations, a set of special treatments must be conducted to the equations. Problems regarding the formulation, discretization, preconditioning and solving the equations can be found in many literature sources [6], [30], [4].

3.2.2 Direct Numerical Simulation

Considering the direct formulation of noise, the Direct Numerical Simulation is seemingly the best tool of choice. The DNS formulation of flow solves directly the discrete form of Navier-Stokes Equation with direct resolving of turbulent flows. Size limit of the resolved eddies is the Kolmogorov limit (eq. 3.18). In order to properly resolve the DNS simulation up to this scale, the mesh sizing must be at least as small as the expected Kolmogorov limit at given Reynolds number.

$$\eta \approx \frac{l}{Re^{3/4}} \quad (3.18)$$

Reference [10] provides information on calculating the mesh grid node count for DNS calculations (eq. 3.19) for flat plate airfoil of aspect ratio L_z/L_x . The computational box for this case is of size $L_x \times \delta \times L_z$ in streamwise, normal to plate and spanwise direction respectively, where δ is the boundary layer thickness.

$$N_{DNS} = 0.000153 \frac{L_z}{L_x} Re_{L_x}^{37/14} \left[1 - \left(\frac{Re_{x_0}}{Re_{L_x}} \right)^{23/14} \right] \quad (3.19)$$

Point x_0 is the location where formulas 3.20 and 3.21 are valid for Reynolds number range ($10^6 \leq Re_x \leq 10^9$).

$$\delta = x \cdot 0.16 Re_x^{(-1/7)} \quad (3.20)$$

$$c_f = 0.027 Re_x^{(-1/7)} \quad (3.21)$$

For aspect ratio $L_z/L_x = 4$ and $Re_{x_0} = 5 \cdot 10^5$ the node count for streamwise $Re = 10^6$ is roughly $2.99 \cdot 10^{12}$ nodes and for $Re = 10^7$ is roughly $1.92 \cdot 10^{15}$ nodes.

Such node and cell counts are impossible to solve within practical walltime, therefore usage of DNS for sound analysis is limited to small (10^3) Reynolds numbers.

3.2.3 Large Eddy Simulation

Large eddy simulation (LES) is a mathematical model for modeling turbulent flows used in computational fluid dynamics. It was initially proposed in 1963 by Joseph Smagorinsky to simulate atmospheric air currents [24].

The principal idea behind LES is to reduce the computational cost by ignoring the smallest length scales, which are the most computationally expensive to resolve, via low-pass filtering of the Navier–Stokes equations. Such a low-pass filtering, which can be viewed as a time- and spatial-averaging, effectively removes small-scale information from the numerical solution. This information is not irrelevant, however, and its effect on the flow field must be modeled, a task which is an active area of research for problems in which small-scales can play an important role, such as acoustics [31].

The governing equations employed for LES are obtained by filtering the time dependent Navier-Stokes equations in either Fourier (wave-number) space or configuration (physical) space. The filtering process effectively filters out the eddies whose scales are

smaller than the filter width or grid spacing used in the computations. The resulting equations therefore governs the dynamics of large eddies [4].

A filtered variable is defined by:

$$\bar{\phi}(x) = \int_D \phi(x') G(x, x') dx' \quad (3.22)$$

where D is the fluid domain, and G is the filter function that determines the scale of the resolved eddies. The finite volume discretization itself implicitly provides the filtering operation:

$$\bar{\phi}(x) = \frac{1}{V} \int_{\nu} \phi(x') dx', \quad x' \in \nu \quad (3.23)$$

where V is the volume of a computational cell. The filter function, $G(x, x')$ implied here is then:

$$G(x, x') = \begin{cases} \frac{1}{V}, & \text{if } x' \in \nu \\ 0, & \text{otherwise} \end{cases} \quad (3.24)$$

For compressible flows, it is convenient to introduce the density-weighted (or Favre) filtering operator:

$$\tilde{\phi} = \frac{\overline{\rho\phi}}{\overline{\phi}} \quad (3.25)$$

Filtering the continuity 3.16 and momentum 3.17 equations following form is obtained:

$$\frac{\partial \rho}{\partial t} + \frac{\partial}{\partial x_i} (\rho \bar{u}_i) = 0 \quad (3.26)$$

$$\frac{\partial}{\partial t} \rho \bar{u}_i + \frac{\partial}{\partial x_j} (\rho \bar{u}_i \bar{u}_j) = \frac{\partial}{\partial x_j} (\sigma_{ij}) - \frac{\partial \bar{p}}{\partial x_i} - \frac{\partial \tau_{ij}}{\partial x_j} \quad (3.27)$$

where σ_{ij} is the stress tensor due to molecular viscosity defined by:

$$\sigma_{ij} \equiv \left[\mu \left(\frac{\partial \bar{u}_i}{\partial x_j} + \frac{\partial \bar{u}_j}{\partial x_i} \right) \right] - \frac{2}{3} \mu \frac{\partial \bar{u}_l}{\partial x_l} \delta_{ij} \quad (3.28)$$

and τ_{ij} is the subgrid-scale stress defined by:

$$\tau_{ij} \equiv \rho \bar{u}_i \bar{u}_j - \rho \bar{u}_i \bar{u}_j \quad (3.29)$$

The Favre Filtered Navier-Stokes equation takes the same form as equation 3.27. The compressible form of the subgrid stress tensor is defined as:

$$\tau_{ij} = \bar{\rho} u_i \tilde{u}_j - \bar{\rho} \tilde{u}_i \tilde{u}_j \quad (3.30)$$

The subgrid-scale stresses resulting from the filtering operation are unknown, and require modeling. The subgrid-scale turbulence models employ the Boussinesq hypothesis [15] in the RANS models, computing subgrid-scale turbulent stresses from:

$$\tau_{ij} - \frac{1}{3} \tau_{kk} \delta_{ij} = -2\mu_t \overline{S_{ij}} \quad (3.31)$$

where μ_t is the subgrid-scale turbulent viscosity. The isotropic part of the subgrid-scale stresses τ_{kk} is not modeled, but added to the filtered static pressure term. S_{ij} is the rate-of-strain tensor for the resolved scale defined by:

$$\overline{S_{ij}} \equiv \frac{1}{2} \left(\frac{\partial \bar{u}_i}{\partial x_j} + \frac{\partial \bar{u}_j}{\partial x_i} \right) \quad (3.32)$$

Equation 3.30 is split into its isotropic and deviatoric parts:

$$\tau_{ij} - \frac{1}{3} \tau_{kk} \delta_{ij} = -2\mu_t \left(S_{ij} - \frac{1}{3} S_{kk} \delta_{ij} \right) \quad (3.33)$$

Using LES approach is viable for resolving directly formulated noise, yet the computational cost of such calculations is still relatively large due to mesh sizing requirements. As stated by [10] the required node count for the analysis can be described by formulas 3.34 and 3.35 for modeled and resolved boundary layers respectively.

$$N_{wm} = 54.7 \frac{L_z}{L_x} n_x n_y n_z Re_{L_x}^{2/7} \left[\left(\frac{Re_{L_x}}{Re_{x_0}} \right)^{(5/7)} - 1 \right] \quad (3.34)$$

$$N_{wr} = 0.021 \frac{n_y}{\Delta x_w^+ \Delta z_w^+} \frac{L_z}{L_x} Re_{L_x}^{13/7} \left[1 - \left(\frac{Re_{L_x}}{Re_{x_0}} \right)^{(6/7)} \right] \quad (3.35)$$

The computational box for this case is of size $L_x \times \delta \times L_z$ in streamwise, normal to plate and spanwise direction respectively, where δ is the boundary layer thickness.

For $L_z/L_x = 4$ and $Re_{x_0} = 5 \cdot 10^5$ the node count for streamwise $Re = 10^6$ and $Re = 10^7$ is computed. The $n_x n_y n_z$ product is the number of grid points to resolve the cubic computational volume δ^3 exterior to the viscous wall region. Suggested value of $n_x n_y n_z = 2500$, where $n_x = 10$ $n_y = 25$ $n_z = 10$ was used for the computation of node

count with equation 3.34. Suggested $\Delta x_w^+ \approx 100$, $\Delta z_w^+ \approx 20$ and $n_y \approx 10$ was used for computation of node count with equation 3.35.

Node count for $Re = 10^6$ is roughly $1.82 \cdot 10^7$ nodes for modelled and $2.61 \cdot 10^7$ nodes for resolved wall flow. For $Re = 10^7$ the figures are $4.10 \cdot 10^8$ and $3.88 \cdot 10^9$ nodes respectively [10].

It must be noted that provided cell count is solely for a flow box of boundary layer width. Respective mesh sizing should be propagated towards volume of the computational domain thus enlarging the mesh even further.

LES analyses are commonly used in research and engineering and the method used is feasible for the direct noise formulation. The computational expense of the LES analysis is high, although manageable. It must be noted, that at time of performing this study the resources to carry out the analysis of that kind were unavailable to the author. Second limiting factor for LES is the amount of data generated during the process. As the direct approach requires storing at least every second time step for further processing, terabytes of data are predicted.

3.2.4 Reynolds Averaged Navier Stokes

The most computationally efficient method for resolving turbulent flows is using Reynolds Averaged Navier Stokes equation.

Consider a conservation variable ϕ of fluid described by spatial and temporal variables. The quantity may be decomposed to a sum of time averaged value in given spatial coordinates and time dependent fluctuations (eq. 3.36).

$$\phi(x, y, z, t) = \overline{\phi(x, y, z, t)} + \phi'(x, y, z, t) \quad (3.36)$$

Consider at first the continuity equation 3.16. By applying Reynolds decomposition to velocity vector we obtain:

$$\frac{\partial \rho}{\partial t} + \frac{\partial \overline{\rho u_i}}{\partial x_i} + \frac{\partial \rho u'_i}{\partial x_i} = 0 \quad (3.37)$$

By averaging the both sides of the equation 3.37 and applying averaging rules to its components we obtain:

$$\frac{\partial \rho}{\partial t} + \frac{\partial \overline{\rho u_i}}{\partial x_i} + \frac{\partial \overline{\rho u'_i}}{\partial x_i} = 0 \quad (3.38)$$

Because the average of an average is equal average, and the average of the fluctuation component is equal 0 we obtain equation 3.39, the Reynolds averaged continuity equation.

$$\frac{\partial \rho}{\partial t} + \frac{\partial \rho u_i}{\partial x_i} = 0 \quad (3.39)$$

By taking the momentum equation 3.17, switching to the index notation and applying the Reynolds decomposition we obtain the equation 3.40

$$\underbrace{\frac{\partial (\bar{u}_i + u'_i)}{\partial t}}_1 + \underbrace{(\bar{u}_j + u'_j) \frac{\partial (\bar{u}_i + u'_i)}{\partial x_j}}_2 = - \underbrace{\frac{1}{\rho} \frac{\partial (\bar{p} + p')}{\partial x_i}}_3 + \nu \underbrace{\frac{\partial^2 (\bar{u}_i + u'_i)}{\partial x_j^2}}_4 \quad (3.40)$$

Components 1, 3 and 4 of the above equation are treated in the same manner as the continuity equation and thus we obtain:

$$\underbrace{\frac{\partial \bar{u}_i}{\partial t}}_1 \quad \underbrace{\frac{1}{\rho} \frac{\partial \bar{p}}{\partial x_i}}_3 \quad \underbrace{\nu \frac{\partial^2 \bar{u}_i}{\partial x_j^2}}_4 \quad (3.41)$$

The decomposition of component 2 from the equation 3.40 requires multiplication of the components within the braces and performing Reynolds averaging on each of the products:

$$\underbrace{\left((\bar{u}_j + u'_j) \cdot \frac{\partial (\bar{u}_i + u'_i)}{\partial x_j} \right)}_2 = \underbrace{\left(\bar{u}_j \frac{\partial \bar{u}_i}{\partial x_j} \right)}_{M \cdot M \neq 0} + \underbrace{\left(\bar{u}_j \frac{\partial u'_i}{\partial x_j} \right)}_{M \cdot F = 0} + \underbrace{\left(u'_j \frac{\partial \bar{u}_i}{\partial x_j} \right)}_{F \cdot M = 0} + \underbrace{\left(u'_j \frac{\partial u'_i}{\partial x_j} \right)}_{F \cdot F \neq 0} \quad (3.42)$$

The $F \cdot F \neq 0$ product can be further simplified by equation:

$$\frac{\partial u'_j u'_i}{\partial x_j} = \underbrace{u'_i \frac{\partial u'_j}{\partial x_j}}_{= 0} + \underbrace{u'_j \frac{\partial u'_i}{\partial x_j}}_{F \cdot F \neq 0} \quad (3.43)$$

By inserting the components 1 through 4 from equations 3.41 and 3.42 modified by equation 3.43 to the equation 3.40 we obtain the Reynolds averaged momentum equation:

$$\frac{d\bar{U}}{dt} = - \frac{1}{\rho} \frac{\partial \bar{p}}{\partial x_i} + \frac{\partial}{\partial x_j} \left[\nu \frac{\partial \bar{u}_j}{\partial x_j} - \bar{u}'_i \bar{u}'_j \right] \quad (3.44)$$

By representing the viscous terms as a stress tensor (eq. 3.45) we obtain the momentum equation with turbulent stress (eq 3.46)

$$\nu \frac{\partial^2 \bar{u}_i}{\partial x_j^2} = \frac{1}{\rho} \frac{\partial}{\partial x_j} \tau_{ij} \quad (3.45)$$

$$\frac{d\bar{U}}{dt} = -\frac{1}{\rho} \nabla \bar{p} + \frac{1}{\rho} \frac{\partial}{\partial x_j} \left[\tau_{ij} - \rho \bar{u}'_i \bar{u}'_j \right] \quad (3.46)$$

The $\rho \bar{u}'_i \bar{u}'_j$ term can be further transformed to Reynolds stress tensor linked to shear stress.

The remaining fluctuating component is then modeled rather than resolved, by one of many turbulence model based on Boussinesque theory.

3.2.5 Hybrid RANS/LES Methods

At first, the concepts of Reynolds Averaging and Spatial Filtering seem incompatible, as they result in different additional terms in the momentum equations (Reynolds Stresses and sub-grid stresses). This would preclude hybrid models like Scale-Adaptive Simulation (SAS), Detached Eddy Simulation (DES), Shielded DES (SDES), or Stress-Blended Eddy Simulation (SBES), which are based on one set of momentum equations throughout the RANS and LES portions of the domain. However, it is important to note that once a turbulence model is introduced into the momentum equations, they no longer carry any information concerning their derivation (averaging). Case in point is that the most popular models, both in RANS and LES, are eddy viscosity models that are used to substitute either the Reynolds- or the sub-grid stress tensor. After the introduction of an eddy viscosity (turbulent viscosity), both the RANS and LES momentum equations are formally identical. The difference lies exclusively in the size of the eddy-viscosity provided by the underlying turbulence model. This allows the formulation of turbulence models that can switch from RANS to LES mode, by lowering the eddy viscosity in the LES zone appropriately, without any formal change to the momentum equations [4].

For further calculations, Delayed Detached Eddy Simulation with $k - \omega SST$ model was chosen. In the DES approach, the unsteady RANS models are employed in the boundary layer, while the LES treatment is applied to the separated regions. The LES region is normally associated with the core turbulent region where large unsteady turbulence scales play a dominant role. In this region, the DES models recover LES-like subgrid models. In the near-wall region, the respective RANS models are recovered [4].

Formulation of DES is the development of the Spalart-Allmaras turbulence model for RANS formulation [26], therefore the theoretical formulations are derived from the S-A model.

The S-A model uses modified turbulent viscosity $\tilde{\nu}$ in place of the turbulent kinematic viscosity.

$$\frac{\partial}{\partial t} (\rho \tilde{\nu}) + \frac{\partial}{\partial x_i} (\rho \tilde{\nu} u_i) = G_\nu + \frac{1}{\sigma_{\tilde{\nu}}} \left[\frac{\partial}{\partial t} \left\{ (\mu + \rho \tilde{\nu}) \frac{\partial \tilde{\nu}}{\partial x_j} \right\} + C_{b2} \rho \left(\frac{\partial \tilde{\nu}}{\partial x_j} \right)^2 \right] - Y_\nu + S_{\tilde{\nu}} \quad (3.47)$$

Turbulence production G_ν and destruction Y_ν terms are modeled as:

$$G_\nu = C_{b1} \rho \tilde{S} \tilde{\nu} \quad (3.48)$$

$$Y_\nu = C_{wq} \rho f_w \left(\frac{\tilde{\nu}}{d} \right)^2 \quad (3.49)$$

where d is the length scale calculated as the distance to the closest wall and \tilde{S} being the measure of deformation tensor:

$$\tilde{S} \equiv S + \frac{\tilde{\nu}}{\kappa^2 d^2} f_{v2} \quad (3.50)$$

where C_{b1} and κ are model constants and S is the scalar measure of deformation tensor:

$$S \equiv |\Omega_{ij}| + C_{prod} \min(0, |S_{ij}| - |\Omega_{ij}|) \quad (3.51)$$

where:

$$C_{prod} = 2.0, \quad |\Omega_{ij}| \equiv \sqrt{2\Omega_{ij}\Omega_{ij}}, \quad |S_{ij}| \equiv \sqrt{2S_{ij}S_{ij}} \quad (3.52)$$

with the mean strain rate defined as:

$$S_{ij} = \frac{1}{2} \left(\frac{\partial u_j}{\partial x_i} + \frac{\partial u_i}{\partial x_j} \right) \quad (3.53)$$

The equation 3.49 shows that $\tilde{\nu}$ is proportional to the local deformation rate and wall distance: $\tilde{\nu} \propto S d^2$. Smagorinsky model for "Sub-Grid-Scale" (SGS) scales the turbulent viscosity with local deformation and grid spacing: $\tilde{\nu} \propto S \Delta^2$.

By replacing the d in the S-A destruction term (eq. 3.49) with \tilde{d} :

$$\tilde{d} \equiv \min(d, C_{DES} \Delta) \quad (3.54)$$

a single model is obtained, acting as RANS with S-A turbulence modeling in regions where $d \ll \Delta$ and with LES behavior where $d \gg \Delta$. Grid spacing Δ is defined as the

largest dimension of the computational cell $\Delta \equiv \max(\Delta x, \Delta y, \Delta z)$. In case of an ambiguous grid definition, where $\Delta < \delta$ the DES limiter can activate the LES mode inside the boundary layer, where the grid is not fine enough to sustain resolved turbulence. Therefore, a new formulation [25] of DES is available to preserve the RANS mode throughout the boundary layer. This is known as the delayed option or DDES for delayed DES [4].

DES and DDES methods can be used with other RANS turbulence models. Further analyses presented in this thesis use a $k - \omega$ SST model. For hybrid model the dissipation of turbulent kinetic energy is modified:

$$Y_k = \rho \beta^* k \omega F_{DES} \quad (3.55)$$

where β^* is the model constant, and:

$$F_{DES} = \max \left(\frac{L_t}{C_{DES} \Delta_{max}} (1 - F_{SST}), 1 \right) \quad (3.56)$$

where C_{DES} is a calibration constant used in the DES model and has a value of 0.61, with $F_{SST} = 0, F_1, F_2$ where F_1 and F_2 are the blending functions of the Baseline and $k - \omega$ SST model. The turbulent length scale is the parameter that defines this RANS model:

$$F_{DES} = \max \left(\frac{L_t}{C_{DES} \Delta_{max}}, 1 \right) \quad (3.57)$$

The F_{DDES} blending function is given by equation 3.57 with model constants $C_{d1} = 20$, $C_{d2} = 3$ and r_d as defined by eq. 3.59:

$$F_{DDES} = \tanh \left[(C_{d1} r_d)^{C_{d2}} \right] \quad (3.58)$$

$$r_d = \frac{\nu_t + \nu}{\kappa^2 y^2 \sqrt{0.5 (S^2 + \Omega^2)}} \quad (3.59)$$

3.3 Mesh sizing requirements

Let's assume a sinusoidal pressure fluctuation $y(t)$ (eq. 3.60) of ordinary frequency of f and amplitude A , moving through ambient medium for more than 5 cycles at speed of sound (eq. 3.61). The mathematical and numerical methods for solving flow field described in section above are capable of computing such pressure fluctuation in a computational mesh of relevant resolution.

$$y(t) = A \sin(2\pi f t + \phi) \quad (3.60)$$

$$a = \sqrt{\kappa R T} \quad (3.61)$$

Cell size and time step size are limited by the wave length, and therefore frequency of the discussed pressure fluctuation. The wavelength is calculated by formula 3.62.

$$\lambda = \frac{v}{f} \quad (3.62)$$

Considered fluctuation travels through the finite volumes (that is: CFD mesh cells) in the stationary CFD mesh. Pressure value is measured at the cell centroid for each timestep. At this stage, it is assumed that timestep is of relevant resolution for the analysis, the mesh is isotropic in x , y and z directions and that the propagation has only one directional component. Four possibilities are considered.

Scenario 1: wavelength is smaller than the edge length of the cell in the direction of propagation. In this condition, the pressure fluctuation performs a number of cycles within one cell (Fig. 3.2). Due to the numerical approach, such fluctuation will be filtered out.

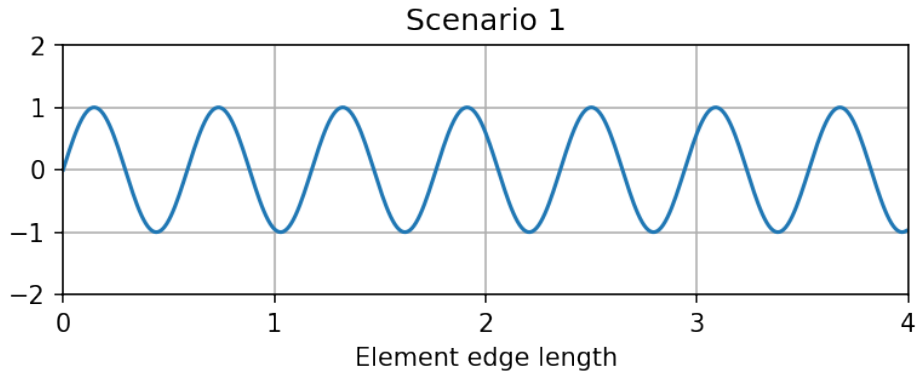


FIGURE 3.2: Scenario 1. Wavelength smaller than cell edge length

Scenario 2: wavelength and cell edge length in the direction of propagation are equal. In this condition, the pressure fluctuation performs one cycle within one cell in the direction of the fluctuation propagation (Fig. 3.3). Such pressure change will be also filtered out by the numerical scheme.

Scenario 3: wavelength is equal to 4 cell edge lengths. This is the minimum cell size condition for proposed approach. In this condition, the pressure fluctuation performs one cycle within four cells in the direction of the fluctuation propagation (Fig. 3.4). FVM

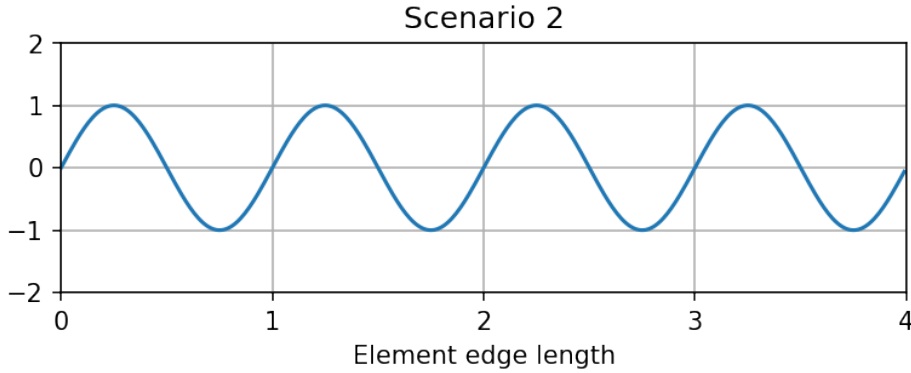


FIGURE 3.3: Scenario 2. Wavelength equal to cell edge length

method is now capable of computing the pressure fluctuations resulting from sound wave propagation.

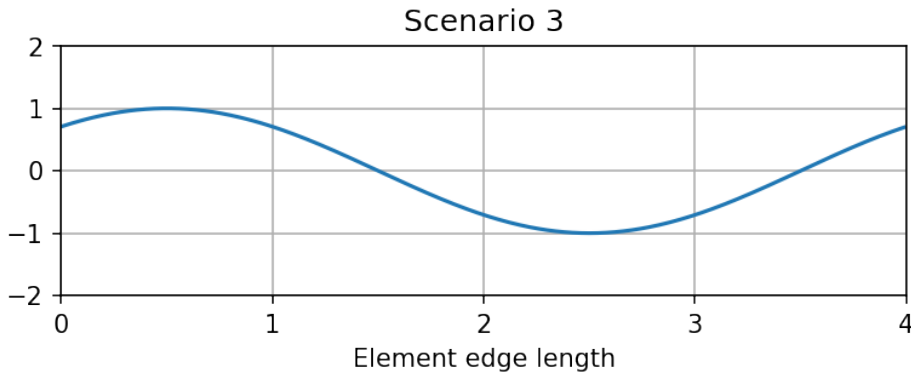


FIGURE 3.4: Scenario 3. Wavelength equal four minimum edge lengths

Scenario 4: wavelength is larger than 4 cell edge lengths. In this condition, the pressure fluctuation performs one cycle within multiple cells in the direction of the fluctuation propagation (Fig. 3.5). FVM method computes pressure from the sound wave propagation across multiple cells.

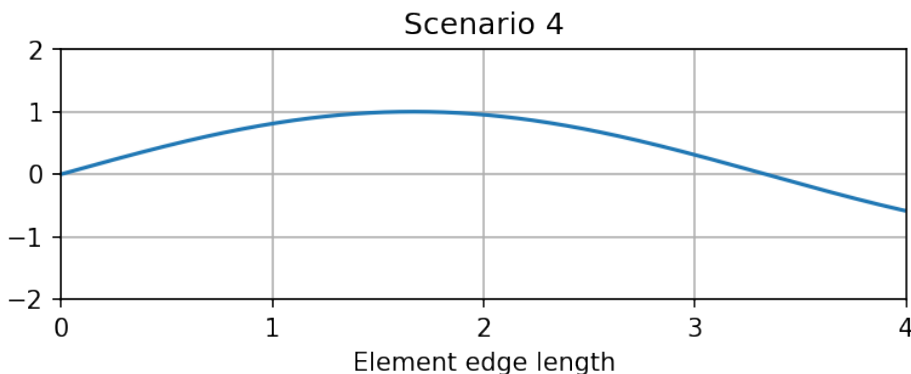


FIGURE 3.5: Scenario 4. Wavelength larger than four minimum edge lengths

Based on these possibilities, the edge sizing of the finite volume cell should be at least four times smaller than the shortest wavelength expected in the flowfield.

3.4 Timestep requirements

There are two limiting factors for timestep requirements. The high frequency signal is limited by the timestep size, whereas the low frequencies are limited to the total number of timesteps and physical flow time calculated. The timestep size is calculated first.

Once mesh cell sizing is established, time at which the fluctuation passes the cell is established by simple formula 3.63. Distance r is the cell edge sizing, obtained as in section 3.3 and the relation between cell size and wavelength is presented in equation 3.65.

$$a = \frac{r}{t} \quad (3.63)$$

where

$$t = \frac{1}{f} \quad (3.64)$$

$$r = \frac{\lambda}{4} \quad (3.65)$$

By rearranging the equation 3.63 to solve for t and substituting λ by 3.62 we obtain:

$$t = \frac{r}{a} = \frac{\lambda}{4a} = \frac{a}{f} \cdot \frac{1}{4a} = \frac{1}{4f} \quad (3.66)$$

Time step t must comply with the requirements of the FFT analysis occurring further in the process as it becomes the minimum sampling time for the sound pressure signal. Therefore it must be compared with the requirements stated by Shannon-Nyquist-Whitaker theorem: *If a function $x(t)$ contains no frequencies higher than B hertz, it is completely determined by giving its ordinates at a series of points spaced $1/(2B)$ seconds apart.*

Equation 3.66 shows that time step for the analysis is dependent from the expected value of high frequency fluctuations.

In order to capture frequencies on the low end of the spectrum, the analysis must be performed long enough to capture at least a single, with optimum 5 or more fluctuations of the desired low frequency. Assuming lower end of the audible frequency spectrum,

the 20Hz frequency, the simulation time must resemble at least 0.05s of flowtime with optimum 0.25s of flowtime at given timestep.

3.5 Limiting factors of the direct approach

Described direct formulation noise analysis is solely a post processing approach relying on data generated on CFD analysis. In order to obtain reasonable results down the process, the analysis itself must be capable of delivering pressure fluctuations that can be considered as acoustic in source.

It is advised to use a turbulence model that is capable of resolving small scale turbulence on a mesh that will allow such resolution. Utilizing LES formulation or at least hybrid RANS/LES turbulence model such as DDES. Using an averaging formulation such as RANS will cut off all of the fluctuations and is not suitable for this approach.

The range of frequencies captured by this method depends on the mesh sizing and timestep sizing. Therefore, if the range of expected frequencies is known or at least estimated, the mesh sizing and timestep size can be adjusted for the given case. For analysis within audible range, 4000 timesteps are required for one 20Hz period. Considering the mesh sizing requirements, the mesh cell count will rise up to tens of millions for a single passage axial compressor blade. This makes the case files and storing data for each timestep relatively challenging and requires securing adequate storage beforehand.

A major limiting factor is the implementation of the direct noise formulation post-processing. For this thesis, the method was implemented in Python v.3.5 high level programming language. Python programming language is written in C/C++ and provides a vast array of additional libraries for handling files, tabular data and performing mathematical operations. The code is presented in appendices to this dissertation. Although easy to implement, python code is known to be inefficient and slow while managing large amounts of data. Tools and algorithms used in implementing the averaging, obtaining sound pressure and particle velocity as well as DFT are built in tools from specific libraries. As convenient for the implementation, the post-processing code requires some amount of operational memory and disk space for generating the results.

The programming language used for the post-processing of data must be capable of generating 2D and 3D plots for visualization purposes. Ideally the processed and visualized data should resemble the mesh from which the initial data was gathered.

Chapter 4

Test case

4.1 NASA Rotor 67 transonic axial compressor

The direct approach noise analysis is conducted on a NASA Rotor 67 (R67) transonic axial compressor. Originating as a first stage of two stage fan for evaluation of design procedures, validation of experimental facilities as well as meshing and CFD tools. The test case was used in a multitude of studies for turbomachinery aerodynamics, geometry optimisation, noise analyses and structural analyses. Full design procedure can be found in references [12] and [29]. The CFD analysis and direct approach noise analysis is performed on a single passage of a first stage rotor of the compressor. The setup for the calculations (apart from the single passage constraint) is relevant to a case described in study [27], which was the main source for geometry and flowfield data.

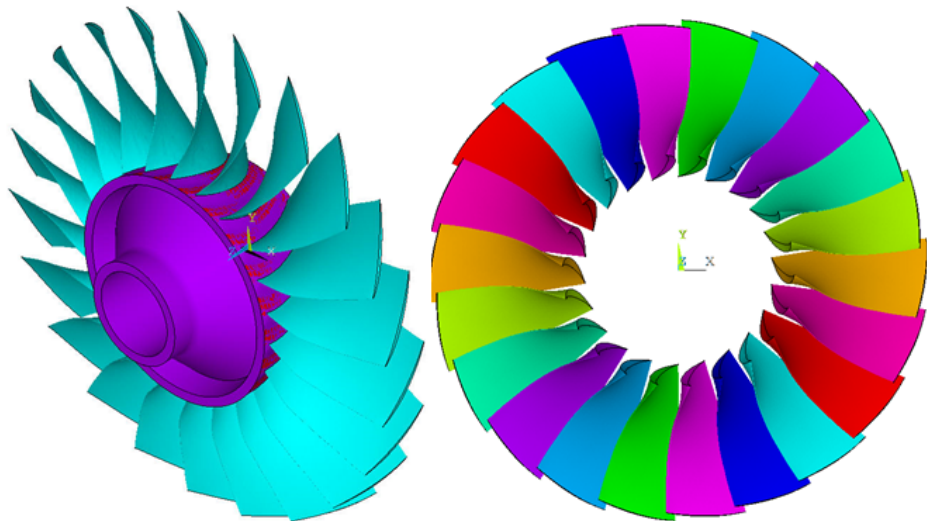


FIGURE 4.1: Geometry of NASA R67

Basic parameters of the given rotor are, design pressure ratio of 1.63 at massflow of 33.25 kg/sec. The design rotational speed is 16 043 rpm, which yields a tip speed of 429 m/s and an inlet tip relative Mach number of 1.38. The rotor has 22 blades and an aspect ratio of 1.56 (based on average span/root axial chord). The inlet and exit tip diameters are 514 and 485 mm, respectively, and the inlet and exit hub/tip radius ratios are 0.375 and 0.478, respectively. A fillet radius of 1.78 mm is used at the airfoil-hub juncture. The square root of the mean square of the airfoil surface finish is 0.8 μm or better, the airfoil surface tolerance is ± 0.04 mm, and the running tip clearance is approximately 1.0 mm [27]. Surface roughness and some of the geometrical features are omitted during the preparation of the geometry and CFD mesh for reasons described in sections 4.2 and 4.3. General geometry of NASA R67 is presented on fig 4.1. Basic parameters of the test subject are presented in table 4.1

TABLE 4.1: Basic R67 parameters

Parameter	Value	Unit
Π	1.63	-
\dot{m}	33.25	kg/s
ω	16043	rpm
v_t	429	m/s
Mat	1.38	-
blade count	22	-

4.2 3D geometry preparation

References [12] and [29] provide the blade geometry for both stages of the compressor as a Multiple-Circular-Arc definition. In the MCA approach the design blade elements lie on conical surfaces which approximate the actual stream flow surfaces. More specifically, the mean camber line and the suction and pressure surface lines of a blade element are lines with a constant rate of angle change with path distance on a specified conical surface [11]. Although relatively comfortable for design purposes, such approach requires transforming the MCA blade to Cartesian or cylindrical coordinates. Reference [11] provides an extended definition of MCA blade description as well as Fortran code for generating blade cross-section and computing geometric properties of the blade.

Source [27] provides a list of coordinates for 14 profiles of the 1st stage rotor blade suction and pressure surface, as well as coordinates for hub and casing path in the meridional plane. These coordinates were used to create the geometry of the single passage of the subject blade. Cartesian coordinates are also available in Appendix H and project Github repository [21].

The coordinate system is a standard right-hand Cartesian CS. Rotation axis is set to Z-axis with flow in positive Z direction. The compressor rotation is set as in right-hand rule, the compressor rotates in clockwise direction when viewing the blade leading edge. Z = 0 coordinate is defined by point number 1 on 1st blade design surface.

Hub and casing flow paths were created by importing formatted point data as a b-spline curve, followed by extrusion the curve to surface by rotating it by $\pm 60^\circ$. Suction and pressure surface of the blade were created by importing the Cartesian coordinates if the design airfoils and creating a lofted surface along the imported splines. Leading and trailing edge radii were created in a similar manner, with use of edge radius and edge tangency points given in original study [27]. Tip gap of the blade was created by offsetting the casing surface by 1.016 mm in the normal direction towards the rotation axis and creating a section line between blade surfaces and the offset surface.

Due to the estimated mesh cell count, only one blade passage is created, therefore a set of periodic surfaces must be defined. ICEM software is capable of creating a midline as an average of coordinates of two given lines. A midline was created for every design profile and was manually extended beyond the blade leading and trailing edge. Midlines were lofted to create a midsurface which was later on copied with rotation by $\pm 0.5 \cdot \frac{360^\circ}{22}$ to create two identical periodic surfaces.

Aforementioned midlines were also rotated along Z-axis to create control surfaces for mesh stabilization and data acquisition down the process.

Reference [27] provides coordinates of hub and casing for the full experiment, however only a rotating part of the experimental rotor setup is be used. Two surfaces normal to Z direction at coordinates Z = -13.74 mm and Z = 93.65 mm are placed as inlet and outlet boundary conditions. Geometry was finished by necessary extrusions, trimming and other finishing operations to ensure high quality surface for meshing.

Physical experiment test compressor has a 1.78 mm fillet at airfoil-hub juncture. This feature was omitted as it would unnecessarily complicate the meshing process and increase the cell count.

Such approach allowed for creating a geometry for single blade passage with centered blade of 1st stage rotor of the test compressor (Fig 4.2).

4.3 Meshing approach

Following requirements are posed to the mesh for the discussed case:

- Possibly low number of elements fulfilling the mesh sizing requirements stated in chapter 3.1,

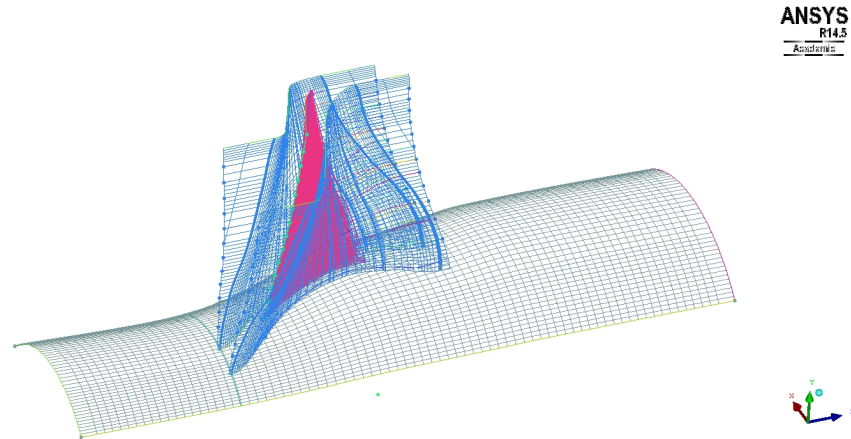


FIGURE 4.2: Final single passage geometry. Some features hidden for clarity

- Mesh should be a fully structural mesh including the tip gap,
- The periodic boundary mesh must be identical/conforming for both boundaries,
- The mesh must have high quality metrics in terms of cell orthogonality and skew.

The orthogonal quality (or orthogonality) of the mesh is calculated as in equation 4.1. The orthogonality value ranges from -1 to 1, where 1 denotes the best orthogonality, 0 – a zero volume cell and -1 – a cell with reversed normal direction or negative volume.

$$\text{Orthogonality} = \frac{\vec{A}_i \cdot \vec{f}_i}{|\vec{A}_i| \cdot |\vec{f}_i|} \quad (4.1)$$

Schematic representation of vectors used for calculation of orthogonality are presented in figure 4.3.

For a hexahedral element, skewness is defined as the normalized worst angle between each of the 6 face normals and the vector defined by the centroid of the hexahedron and the center of the face.

One of the initial mesh concepts was an unstructured mesh with triangular surface mesh extruded to prism boundary layer and mostly isotropic tetrahedra in the volume. This approach was quickly rejected for bad quality elements near the airfoil/hub junction and tip gap, as well as element count in range of 4.5 million cells for sizing relevant for RANS analysis. This approach was quickly dropped.

A non-trivial topology with fully conforming periodic boundaries was introduced (fig 4.5). The topology creates a high quality mesh, yet it is impossible to apply a structural tip gap due to non-conforming element count on the pressure and suction side of the mesh. A RANS sufficient mesh without tip gap area (blade was extended to the casing surface) was created. The cell count for this mesh is below 0.5 million cells with better

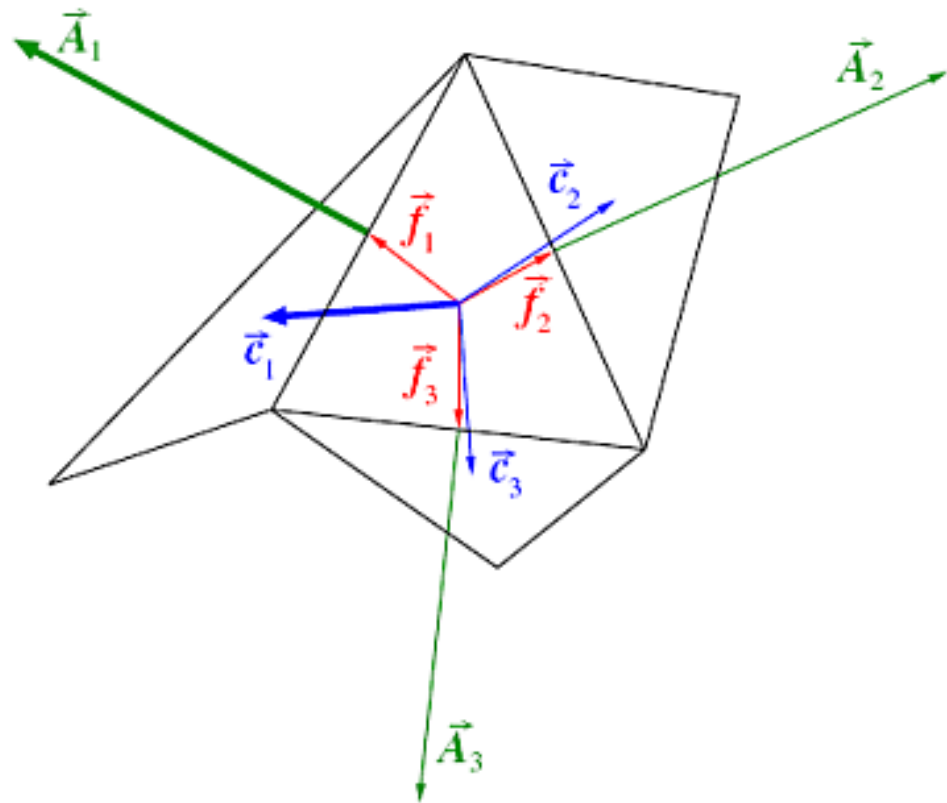


FIGURE 4.3: Vectors Used to Compute Orthogonal Quality for a Cell

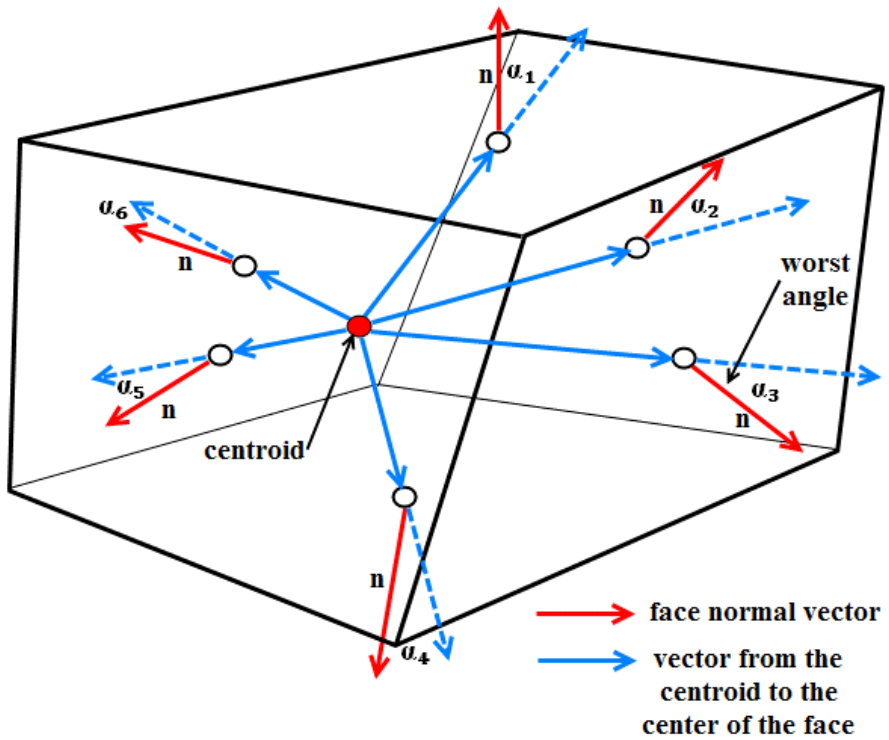


FIGURE 4.4: Vectors Used to Compute Orthogonal Quality for a Cell

skewness and orthogonal quality. This mesh was utilized for initial numerical setup and data acquisition testing.

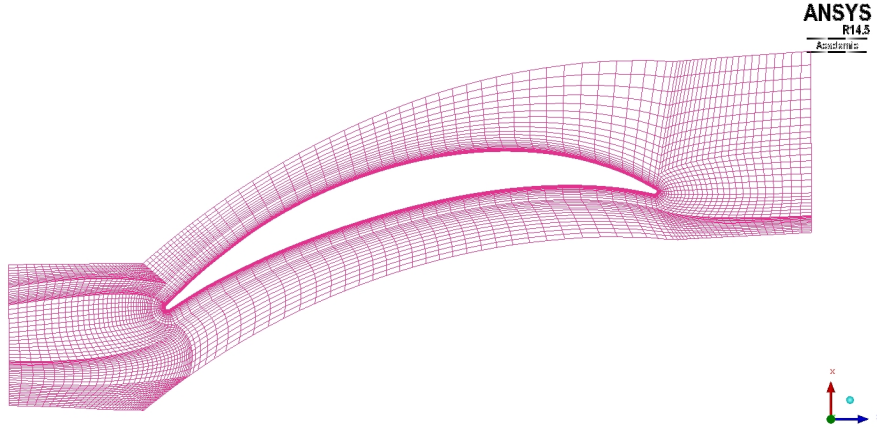


FIGURE 4.5: Mesh topology with conforming periodic boundaries

Final topology was a standard h-grid topology for generic airfoils (fig. 4.6). Although it is impossible to create a conforming periodic interface with such mesh topology, a fully structural tip gap was implemented. Omitting the blade-hub juncture fillet simplified the mesh. Such topology eradicates the necessity of placing 5-way topology points.

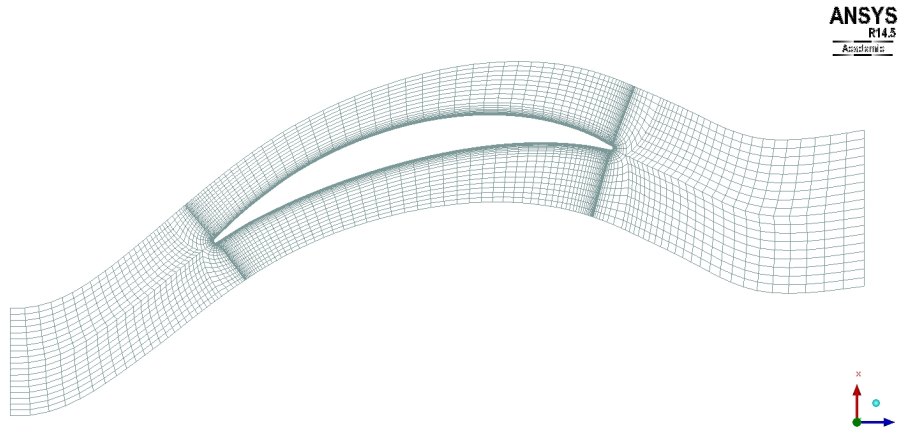


FIGURE 4.6: Mesh h-topology

As there were no information about the frequency of the pressure fluctuations at time of creating the mesh, the analysis will focus on the audible range of sound frequencies from 20Hz to 20 000Hz. The wavelengths for given frequencies are calculated by formula 3.62 and divided by four to obtain the required cell sizing. The velocity of sound obtained by equation 3.61 with reference temperature $T = 300K$. The results are presented in table 4.2.

Maximum element edge length is limited to 3 mm, with 5 mm at inlet and outlet boundary conditions. The mesh cell sizing requirements are described in chapter 3. Blade

TABLE 4.2: Test case boundary conditions

Frequency [Hz]	Wave length [m]	Cell size [m]
20	17.390	4.347
20 000	0.01739	0.004347

boundary layer is produced by creating an o-grid around blade surface mesh. Hub and casing boundary layers are created by changing the sizing on the blocks adjacent to respective surface mesh. Sizing of the first element is estimated with y^+ parameter as described in equation: 4.2. First element thickness in on the blade surfaces ranges from is $2\mu m$ on tip airfoil and $10\mu m$ on hub airfoil. This corresponds to $y^+ \approx 2$ calculated by streamline velocity values given in experimental study [27].

$$\Delta s = \frac{y^+ \mu}{U_{fric} \rho} \quad (4.2)$$

where:

$$U_{fric} = \sqrt{\frac{\tau_{wall}}{\rho}} \quad (4.3)$$

where:

$$\tau_{wall} = \frac{C_f \rho U_\infty^2}{2} \quad (4.4)$$

where:

$$C_f = \frac{0.026}{Re_x^{1/7}} \quad (4.5)$$

Internal volume of the mesh was stabilized by attaching the mesh blocks to the internal design surfaces, which represent the design streamline surfaces of the experimental rotor. This ensures that mesh layers are mostly coincident with the primary flow streamlines. The internal surface mesh is also used for data acquisition purposes. The markers are named hub, int-01 thru int-12 and int-tip corresponding to following locations of the design surfaces. The span percentage is calculated from the hub.

TABLE 4.3: Location of compressor desing surfaces

Boundary marker	Location
hub	0% span
int-01 - int-12	7.7% - 92.3% every 7.7% span
int-tip	100% span

Figure 4.7 provides overview of mesh quality defined above. The quality of created mesh is sufficient for both RANS and DDES analyses (chapter 5). Final mesh reached c.a. 11.5 million cell count. Final mesh is presented in figure 4.8

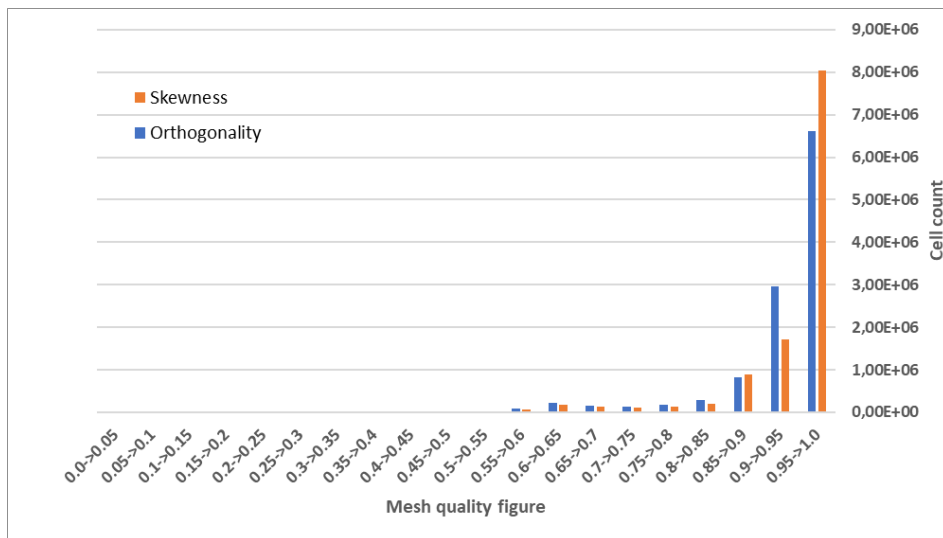


FIGURE 4.7: Mesh quality histogram

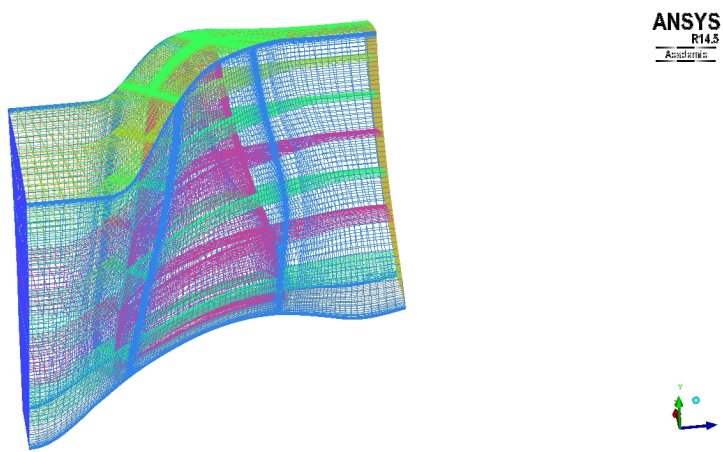


FIGURE 4.8: Completed Mesh

Chapter 5

CFD Analysis

5.1 Case preprocessing

CFD analyses for generating raw pressure field data are performed in ANSYS Fluent 17.2 software on Prometheus HPC cluster located in Kraków. Access for this infrastructure was granted by PLGrid infrastructure. Calculations were run on 5 nodes of 24CPU cores and 128GB RAM each [5], which resulted in decomposition to 120 cores, resulting in allocating around 110 thousand cells to a single CPU core.

The analysis is set to "peak efficiency" conditions of the experimental test case. Apart from the turbulence modeling approach, the set up is consistent throughout the CFD cases.

Material used in the analysis resembles standard air modeled as ideal gas as in equation with following properties described in table 5.1

TABLE 5.1: Standard air properties

C_p	1006.43	J/(kg · K)
λ	0.0242	W/(m · K)
μ	$1.7894 \cdot 10^{-5}$	kg/(m · s)
M	28.966	kg/kmol

$$pV = nRT \quad (5.1)$$

Analysis operating pressure is set to 0 Pascal, which is a standard practice in compressible flow CFD. Internal mesh zone is set as "frozen rotor" reference frame. Although no mesh motion is implied, the effect of Coriolis accelerations and centrifugal acceleration will be taken into account by adding respective acceleration components to momentum equations as described in chapter 3. The rotational velocity is set to 1680 rad/s.

Following boundary conditions were applied. The setup is typical for compressible flow CFD cases performed in the authors institute.

TABLE 5.2: Test case boundary conditions

Boundary marker	Boundary type			
Inlet	Pressure Inlet	101350	Pa	
Outlet	Pressure Outlet	102000	Pa	
Hub	Moving wall	1680	rad/s	
Blade	Moving wall	1680	rad/s	
Casing	Stationary wall			
Internal profiles	Internal			
Periodic boundaries	Interface			

5.2 Flowfield initialization & RANS

RANS analysis is not suitable for generating acoustic nearfield data as the method averages the fluctuations over time (chapter 3). Yet, this approach is used to solve the initial flowfield at a relatively low computational effort. Furthermore the RANS analysis provides initial validation results of the model setup and solver settings.

The solver is set up to steady-state, density based, coupled-implicit solver with $k - \omega$ SST turbulence model. Such setup is a go-to setup for nearly all compressible aerodynamics CFD done in the author's institute.

The density-based solver in ANSYS Fluent solves the governing equations of continuity, momentum, and (where appropriate) energy and species transport simultaneously as a set, or vector, of equations. Governing equations for additional scalars will be solved sequentially (that is, segregated from one another and from the coupled set). Two algorithms are available for solving the coupled set of equations, the coupled-explicit formulation and the coupled-implicit formulation [4].

The system of governing equations for a single-component fluid, written to describe the mean flow properties, is cast in integral Cartesian form for an arbitrary control volume V with differential surface area dA as follows:

$$\frac{\partial}{\partial t} \int_V W dV + \oint_V [F - G] \cdot dA = \int_V H dV \quad (5.2)$$

where:

$$W = \begin{bmatrix} \rho \\ \rho u \\ \rho v \\ \rho w \\ \rho E \end{bmatrix} \quad F = \begin{bmatrix} \rho v \\ \rho uv + pi \\ \rho vv + pj \\ \rho ww + pk \\ \rho vE + pv \end{bmatrix} \quad G = \begin{bmatrix} 0 \\ \tau_{xi} \\ \tau_{yi} \\ \tau_{zi} \\ \tau_{ij}v_j + q \end{bmatrix} \quad (5.3)$$

and where the vector H is the body forces and energy source vector.

The ρ, v, E, p are respectively the density, velocity, total energy per unit mass and pressure of the fluid. τ is the viscous stress tensor and q is the heat flux.

Total energy E and total enthalpy H are related by the formulas:

$$E = H - \frac{p}{\rho} \quad (5.4)$$

$$H = h + \frac{|v|^2}{2} \quad (5.5)$$

Equation 5.2 is preconditioned, convective fluxes are splitted with Roe Flux-Difference Scheme and the preconditioned equation is discretized with Euler Implicit discretization and combined with Newton type linearization of fluxes. Obtained equation system is solved by the Incomplete Lower Upper (ILU) factorization in conjunction with the Algebraic-Multi-Grid. Details on the solver theory used in this study are available in source [4]

Flowfield is initialized at first with constant values populated from the "inlet" boundary condition patch. Next a Full-Multi-Grid initialization is performed to generate coarsened flowfield. The analysis is then processed by first, second and third order discretization schemes for all of the conservation values, up to a given residual value. It must be noted, that for second and third order scheme analyses, convergence criteria may not be reached. Should this case occur, the analysis is stopped once the residual plots reach a plateau and the resulting flowfield is considered acceptable. Once the third order scheme analysis is completed, data is acquired from inlet and outlet boundary conditions, and the constant pitch vs. span streamlines.

The analysis is set to a moderately strict residual convergence criteria of 10^{-6} , however is monitored during runtime. Once the convergence plot reaches plateau and the internal surfaces flow field is not changing throughout iterations the analysis is stopped and switched to a higher discretization scheme or finalized and saved.

5.3 DDES analysis

Once the RANS analysis is converged to a satisfactory level the setup is changed to a transient, pressure-based, PISO scheme solver with DDES turbulence model and $k - \omega SST$ RANS formulation for shielded regions and subgrid scale. Rationale for the DDES analysis is provided in chapter 3. Pressure based solver is required by the DDES implementation in the used software. Utilization of the pressure based solvers for compressible flows is known to be unstable during the calculations, especially for the adverse pressure gradient cases. However, once the initial flow field resembles the final flowfield, the pressure based calculations are rather stable even at high velocity adverse pressure gradients.

Pressure based solver solves the discretized continuity equation with obtaining the velocity field from the momentum equations. The pressure field is obtained by solving and manipulating the continuity and momentum equations within a pressure velocity coupling scheme.

Transformed and discretized equations are solved by a linear solver and the intermittent solutions are coupled using a pressure velocity coupling algorithm. For this specific case PISO scheme is chosen for the computation. The algorithm is suitable for calculating problems with larger (in comparison to density-based acoustical timescale) pseudo-timestep and with decreased computational expense. Figure 5.1 presents the flow of the PISO algorithm.

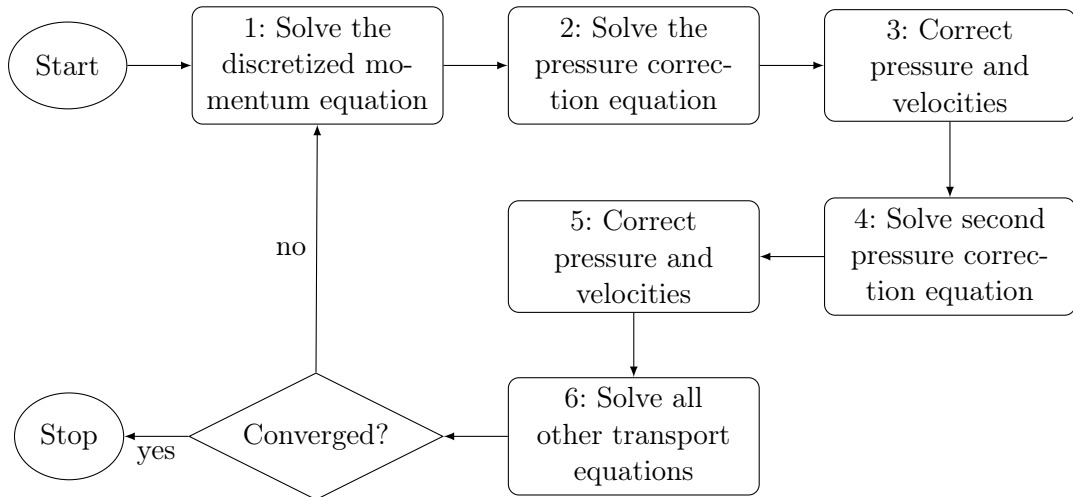


FIGURE 5.1: Flowchart of the PISO algorithm

As the flowfield resulting from the RANS analysis is averaged over time and has no distinguishable features of a turbulent flow, the DDES analysis is divided into two runs. The first run is set to create a flowfield with random flow features. This is also used for testing the convergence and data acquisition process.

Although not required by the "frozen-rotor" configuration, the timestepping is based on the rotor Blade-Pass-Frequency number. The BPF parameter is obtained by formula 5.6

$$BPF = \frac{n \cdot t}{60} \quad (5.6)$$

where t is the number of blades and n is the rotational speed in rpm.

For NASA R67 the base Blade Passing Frequency is equal to 5882.36Hz . By multiplying the BPF by four a frequency of 23529.44Hz is obtained. The frequency is above the human audible range and will be used to compute the timestep. As stated in chapter 3, in order to capture a given frequency, the timestep must be at least 4 times smaller than the period of the oscillations (equation 3.66). By this approach the maximum timestep of the DDES calculation is $1.06 \cdot 10^{-5}\text{s}$. The timestep is compared with the requirements of the Courant-Friedrichs-Levy condition defined by equation 5.7

$$Co = \frac{u \cdot \Delta t}{\Delta x} \quad (5.7)$$

Considering that $u_{max} = 426.72\text{m/s}$ and $\Delta x = 0.25 \cdot \lambda = 0.003695\text{m}$ for desired frequency of 23529.44Hz and timestep of $1.06 \cdot 10^{-5}\text{s}$ the Courant number obtained is equal to 1.22. By rearranging the equation to solve for Δt an equation 5.8 is obtained and a calculation timestep fulfilling requirements of the CFD analysis and the direct noise formulation is computed and is equal to $8.659 \cdot 10^{-6}$.

$$\Delta t = \frac{Co \cdot \frac{\lambda}{4}}{u_{max}} \quad (5.8)$$

Initial timestep for the DDES analysis is set up to $5.0 \cdot 10^{-6}\text{s}$. Presented time stepping approach fulfills the Shannon-Nyquist-Whitaker theorem presented in section 3.4. First run was conducted for c.a. 30 thousand timesteps, during which following factors were tested: calculation efficiency dependent on the CPU core count used, data output and data format, estimated storage requirements and the output from the embedded FW-H aeroacoustical models. First run concluded, that the assumed timestep does not meet the required convergence criteria and delivered inaccurate results or flowfield with features not resembling the features characteristic for compressor flow.

The timestep was gradually decreased to a value of $1.0 \cdot 10^{-6}\text{s}$, the CPU core count was set to 120 CPU cores distributed over 5 HPC nodes. Once the first run produced a fully developed flowfield with turbulent features characteristic to the LES analysis, the case was saved and set up for a final run with full data acquisition.

It was desired to capture at least 0.05 seconds of the flow but with some relation to geometric and operational features of the rotor. Based on the blade count and rotational speed of the rotor a time of a single periodic passage is calculated to $1.70 \cdot 10^{-4} s$. Next the required computational time is divided by the passage time to obtain the number of blade passages. 294.118 passages will occur during the 0.05s, so the number is rounded up to 295 passages and multiplied again by the passage time. Total calculation time of 0.05015 seconds is obtained. Therefore 50150 timesteps is required for full calculation runtime, with one passage being calculated in 170 timesteps.

5.4 Validation of the results

The experimental study [27] provides a very extensive set of validation data for the passage flowfield. The quoted study presents results of LDA measurements of the NASA R67 compressor for relative Mach number and relative flow angle at constant pitch and constant chord lines intersecting with blade span lines at 10% intervals. Constant pitch line is derived from the blade's suction surface: 0% percent pitch is the suction surface of one blade, 100% pitch is the suction surface of the adjacent blade. Constant chord lines are used to plot blade-to-blade distributions of given parameters at intersection of span and constant z-coordinate surface (fig. 5.2).

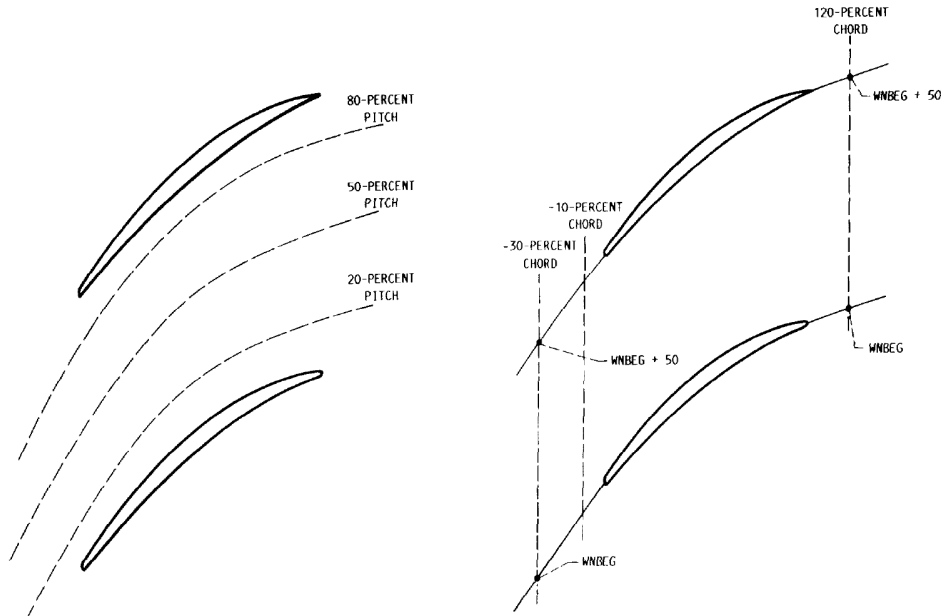


FIGURE 5.2: Constant pitch (left) and constant chord (right) lines [27]

In order to validate the CFD analysis, the constant pitch surfaces for 20%, 50% and 80% constant pitch are combined with 10%, 50% and 90% constant span locations, as measured from the blade tip, thus producing 9 lines to for relative Mach number and

relative flow angle data. Furthermore, Mach contour plots for 10%, 30% and 70% constant span surfaces (measuring from the blade tip) are compared with the experimental study.

For clarity, relative Mach number plots and constant pitch plots are presented in appendix C.

The most simple method for validating the results is comparing the total and static pressure values on inlet and outlet boundary conditions of the domain with experimental data. Plots for static and total pressure at inlets and outlets of the domain are presented in figures 5.3 and 5.4.

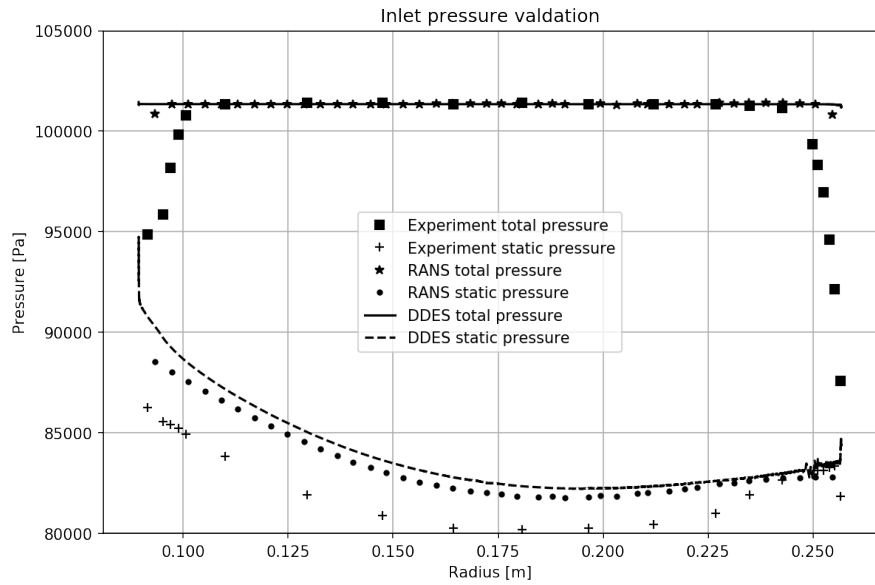


FIGURE 5.3: Inlet pressure validation

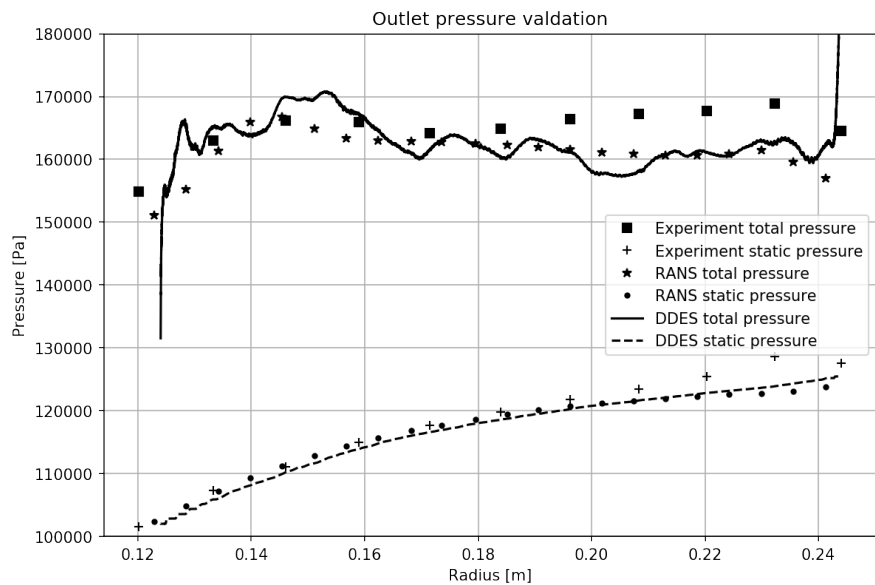


FIGURE 5.4: Outlet pressure validation

Both RANS and DDES analyses produce results that are confirmed by the experimental data. Static inlet pressure plot show the discrepancy between experimental and CFD data resulting from a minor shift between the inlet and outlet CFD boundaries and the location of the pressure rake. The inlet boundary condition is moved closer towards the leading edge of the rotor, than the experimental pressure measurements array, therefore the static pressure is increased. The Mach number contour plots on the corresponding internal surfaces show the same character of the flow. Discrepancies between the experimental study and the obtained CFD results arise from a slight offset between the experimental surfaces as the mesh internal surfaces.

Chapter 6

Results of flow field noise analysis

6.1 Transition from flow-field to sound signal data

The performed DDES analysis delivered a set of files for further postprocessing. Values of static pressure, velocity magnitude, vorticity magnitude, static density and static temperature were gathered from designated boundaries and internal surfaces representing the design streamline cones. The dataset consists of 50150 files for each of the 13 internal surfaces and 5 blade boundaries, resulting in over 5.5 TB of data.

This set was postprocessed to obtain the sound pressure, sound intensity and their respective decibel values for each timestep. The mathematical formulas for obtaining these values are provided in chapter 3 and the Python 3.5x implementation of which is presented in appendix D. The postprocessing of flow field data to sound data was performed on the same HPC infrastructure as the DDES analysis, due to the file accessibility. Postprocessed dataset was saved in a folder structure resembling the source files.

6.2 Sound levels results

6.2.1 Results postprocessing

The time specific sound pressure values were further processed to obtain the Root Mean Square values of sound pressure and sound intensity from internal markers and blade surfaces. Due to large number of figures, the scatter plots of the aforementioned values are provided in the Appendix A in figures A.1 thru A.54. Providing data for both pressure and intensity values and their decibel levels is redundant, yet both plots are shown for clarity and direct comparison of given values.

Internal boundary plots provide information on maximum and minimum values of SPL and SPLdB presented on the plot. As the minimum sound intensity (SIL) is equal 0 and the SILdB values for corresponding points approach negative infinity. Such values were overridden to show 0 SILdB on the plot. For this reason minimum value coordinates are omitted in the plot description.

Sound pressure and intensity plots are scaled with a normalized logarithmic colorbar with common scale across all of the internal surface and blade surface plots. For sound pressure, the maximum obtained value is 13917.395 Pa , therefore the maximum value of the plot scale is liberally rounded up to 15000 Pa . Minimum value for SPL is in range of 10 Pa , so the lower bar limit is set to zero. As for the Decibel values the lowest obtained value is around 116 dB , largest - around 177 dB . The plot scale is therefore set to $100 - 180 \text{ dB}$ range with linear scale. The same approach was used for maximum values of sound intensity. For sound intensity itself, the colorbar was limited from 0 W/m^2 to $1.2 \cdot 10^6 \text{ W/m}^2$ and normalized to logarithmic scale. For SILdB plot, the bar range is limited to 0 dB to 180 dB range with linear scale.

Plots are created by projecting points from 3D surface onto a 2D canvas of the plot, therefore some shape aberrations may occur. Color of the point is normalized as described above. Plot axis labels correspond with the global coordinate system of the geometry.

6.2.2 Qualitative analysis

Averaged sound pressure and sound intensity plots provide some information on the character of the acoustic phenomena modeled in a stationary reference frame for given test compressor.

The sound pressure fluctuations that translate to high SPLdB values occur in regions where flow is turbulent. For internal control surfaces, where flow is globally subsonic (int-01, int-02, int-03 – figures A.5 thru A.14), the sources of the aerodynamically induced noise correspond to the regions on flow separation on the suction surface (upper on the plots). This is especially visible in the wake of the blade. Figures A.1 and A.2 provide the view of the blade's suction surface. A separation of the flow at leading-edge-to-hub transition leading to a very characteristic secondary flow and corner stall separation (separated flow on the suction surface near the trailing-edge-to-hub transition). The largest pressure fluctuations were noted on the trailing edge and trailing-edge-to-tip transition, which is visible on both blade surface plots and internal surfaces plots.

Internal surface contour plots show, that the source of sound pressure is the supersonic-to-subsonic transition occurring on the shockwave. The effect of shock induced flow separation is becoming visible on internal surface plots for surfaces int-04 and int-05 (figures

A.15 thru A.22), with full visibility of described phenomena on surfaces int-06 thru int-12 (figures A.23 thru A.50). Plot for surface adjacent to the blade tip (surface int-tip, figures A.51 thru A.54) show the effect of "tip-leakage" phenomena when high pressure flow at the pressure side of the compressor creeps to the low pressure suction side thru the tip gap (Fig. 6.1).

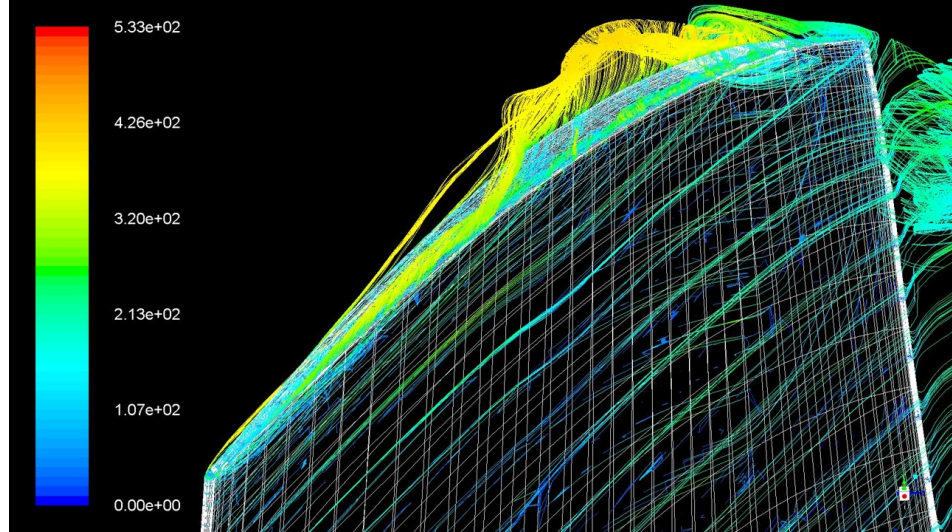


FIGURE 6.1: Tip gap streamlines. Velocity in [m/s]

Presented contour plots show a rather significant noise level in the supersonic (relative to the blade) region along with patterns resembling sound waves. SPLdB noise level in lower range of 120 decibels corresponds to pressure fluctuations in range of 20 Pa in medium where average static pressure is in range of $0.8 \cdot 10^5 \text{ Pa}$, which may result from typical for transient calculations pressure fluctuations.

Sound wave like patterns on blade suction surface in the supersonic region require further investigation. Wave like pattern presented on the RMS plot is likely to show a sort of standing wave pattern evolving towards the leading edge of the blade. Region of flow for containing this phenomena is supersonic relatively to the blade, however both axial and radial components of the flow are subsonic. Moreover, the boundary layer flow for this case is subsonic even in the relative supersonic region, therefore sound propagation is possible near the blade surface.

6.2.3 Quantitative analysis

A brief quantitative analysis is performed on obtained datasets. RMS sound pressure level obtained from direct approach analysis is compared with RANS flowfield data related to turbulence. As described in chapters 2 and 3, the aerodynamically generated sound has its source in turbulence occurring in the flow.

A Pearson correlation coefficient is calculated between flowfield values describing turbulence and RMS sound pressure level. Pearson correlation coefficient is chosen, due to its rather general utilization in establishing the correlation between the two datasets. The data is organized in the same manner as in previous computations, that is on internal surfaces and blade surfaces and compared pointwise for each surface. Value ρ of the correlation coefficient is computed using the formula 6.1:

$$\rho_{X,Y} = \frac{\text{cov}(X, Y)}{\sigma_x \sigma_y} \quad (6.1)$$

As the populations X and Y are discrete, the covariance of X and Y can be expressed as:

$$\text{cov}_{X,Y} = \frac{1}{n} \sum_{i=1}^n (x_i - E(X)) \cdot (y_i - E(Y)) \quad (6.2)$$

where $E(X)$ and $E(Y)$ are the expected values of populations X and Y respectively, defined as:

$$E[X] = \sum_{i=1}^k x_i p_i \quad E[Y] = \sum_{i=1}^k y_i p_i \quad (6.3)$$

where: x_i and y_i is the i-th value of the population X and Y respectively, p_i is the probability of the value occurring. As this probability for given population is equal for all values, the expected value of this population is equal to the arithmetic mean of the population.

Calculated correlation between values of: vorticity magnitude, turbulent kinetic energy, specific dissipation rate, turbulent viscosity, turbulence intensity and RMS SPL values are shown in figures 6.2 for internal surfaces and 6.3 for blade surfaces.

No significant correlation between turbulent values and RMS sound pressure level has been found. Turbulent intensity correlation coefficient for int-01 surface is of value 0.6, however this tendency is not valid for other surfaces. Coefficient for turbulent viscosity is somewhat consistent throughout the surfaces, yet the ρ value oscillating around 0.3 shows little correlation between the populations. Correlation between turbulence properties populations and RMS SPL for blade surface are inconsistent throughout the surface markers and populations.

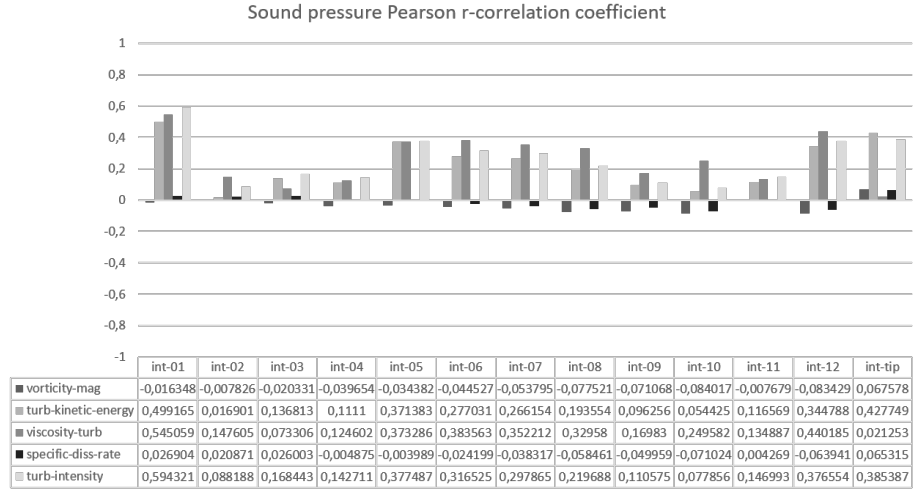


FIGURE 6.2: SPL to flowfield turbulence values correlation. Internal surfaces.

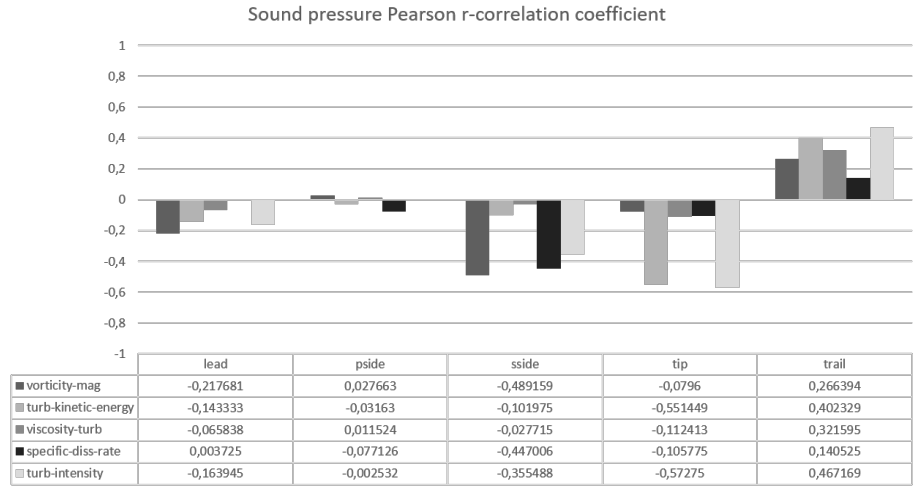


FIGURE 6.3: SPL to flowfield turbulence values correlation. Blade surfaces.

6.3 Frequency analysis results

6.3.1 Results postprocessing

The time specific sound pressure values were further processed by a Python script presented in Appendix G. As described in chapter 5, the timestep set in the CFD analysis was order of magnitude smaller than required by the direct method. The presented algorithm samples every 10th timestep to an intermittent tabular data frame and performs a Discrete Fourier Transform as per formula 3.7. This outputs a complex vector 3.12 of 5015 Fourier coefficients, for every data point on an analyzed surface. Due to large number of figures, the scatter plots of the aforementioned values are provided in the Appendix B in figures B.1, B.2 and B.3.

Obtaining amplitudes and phase shift of ordinary frequencies is rather straightforward. Formulas 3.14 & 3.15 are used element-wise on a complex vector of Fourier coefficients for each node of given control surface. Results are saved to csv files with $\text{Amp}_k(f_{bin})$ and $\theta_k(f_{bin})$ data respectively.

A method for graphical presentation of the FFT analysis results is proposed. At this stage, all nodes on a 3D control surface, having (x, y, z) coordinates are now linked to a 2D spectrum plot, therefore a dataset is now five dimensional, with one dimension being easily reduced. For first assessment of spectrum plots a "spectrum heatmap" is proposed. A heatmap kind plot with x-axis being the frequency bins, y-axis – the node number, and cell color is the magnitude of given frequency bin of given node. Exemplary heatmap is presented in fig. 6.4. Such approach provides some basic qualitative insight to the frequency distribution.

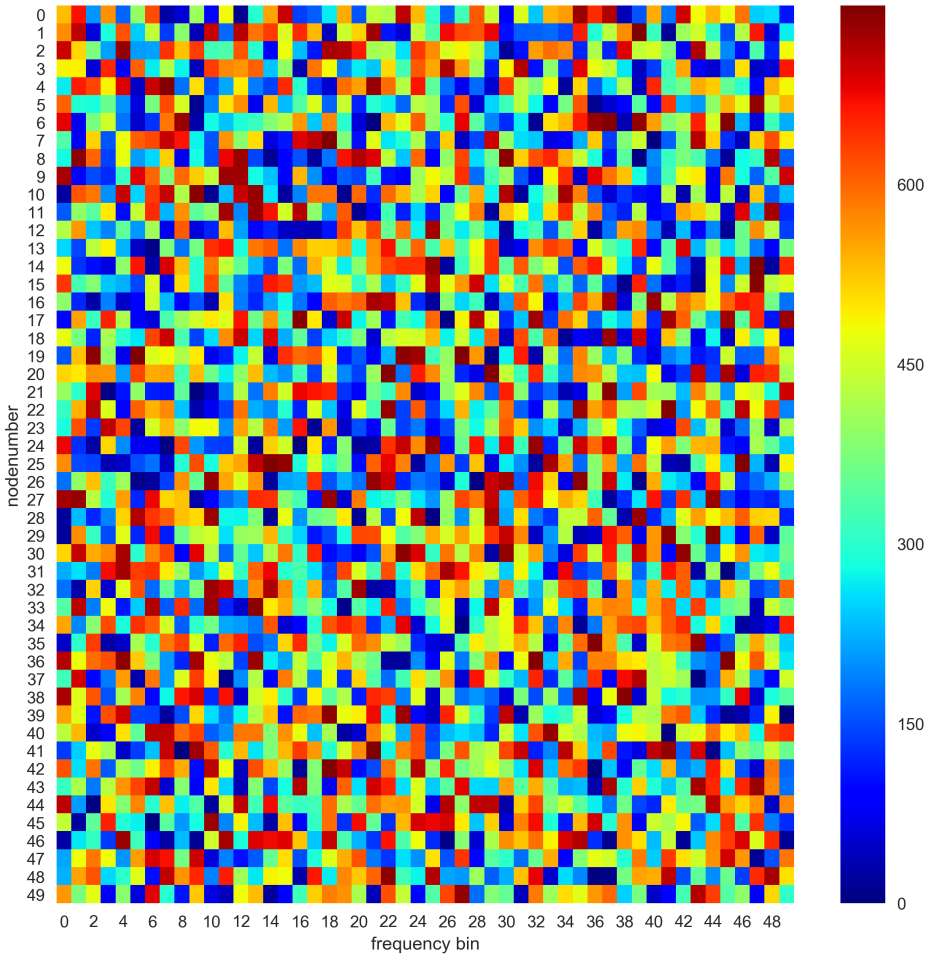


FIGURE 6.4: Exemplary FFT heatmap of magnitude. Random data.

Spectrum plot amplitude range as well as maximum FFT amplitude range are normalized and presented on a logarithmic scale as per formula 6.4.

$$\text{Amp}_{kn} = 20 \cdot \log_{10} \left(\frac{\text{Amp}_k}{\text{Amp}_{max}} \right) \quad (6.4)$$

where Amp_{max} is the global maximum amplitude of all datasets.

This operation has been performed separately on spectrum plots and peak amplitude plots. For spectrum plots the lower [dB] range is calculated by applying the formula 6.4 to global minimum and global maximum amplitudes, resulting in lower end of the scale of -226.41 dB, rounded down to -230dB. For surface plots, where only peak amplitudes are taken into account, the lower end of the plotting range is set as follows: obtain list of maximum amplitudes from all control surfaces, next take the minimum value from the obtained list and apply the aforementioned formula. The lower limit of the surface amplitude plots is calculated to -62.94 dB, rounded down to -65dB. This ensures that color range on is consistent throughout the spectrum plots and surface plots, with maximum value of 0 on every amplitude plot, corresponding to the maximum amplitude value.

Frequency of maximum amplitude for each node is obtained from the dataset. Moreover an amplitude weighted average frequency is calculated (eq. 6.5) to show the dominating frequency range on the given control surface. Frequency range presented on these plots is limited slightly above the maximum frequency possible to resolve by the presented approach and the limits are 0Hz and 25000Hz.

$$\bar{f} = \frac{\sum_{k=1}^N f_{bin_k} \cdot \text{Amp}_k}{\sum_{k=1}^N \text{Amp}_k} \quad (6.5)$$

6.3.2 Qualitative analysis

Analysis of the spectrum plots of the internal surfaces shows the following phenomena. At lower node numbers – towards the inlet of the domain, the lower frequencies are dominant in the spectrum, with little or no high frequency constituents. With increasing node numbers – moving towards the domain outlet, the amplitude of the low frequencies is increasing, whilst the high frequency constituents are also increasing their magnitudes. This pattern is repeated throughout the internal surfaces plots, including the tip internal surface. Moreover, the general observation is, that the magnitudes of given frequency bins, for corresponding node numbers, is increasing along with the distance from the hub. Therefore, the "quietest" region of the flowfield is upstream of the blade and near the hub and the "volume" of the sound increases towards the trailing-edge-to-tip-juncture. One of the most important conclusions appearing from the spectrum plots is, that the flow nearfield sound, although having source in seemingly random flow fluctuations, is not random nor has a characteristic of white noise. The spectrum plots are lacking the

information on the node locations, therefore spatial analysis of the plots poses some difficulties. Further analysis is done on internal surface and blade surface plots.

Amplitude weighted average frequency plots reduces the high dimensional FFT dataset to a plot feasible to show in a printed form. Frequency spectrum is averaged and constituents of high amplitude are highlighted on the plot. The averaged frequency is in higher range of c.a. 10kHz on the int-01 surface (Fig. B.5) and up to 15-16kHz on the int-tip surface (Fig. B.53). These frequencies are represented by a high pitched noise, characteristic to operating jet engines and being one of two main sources of noise of the engine. The plot is consistent with RMS sound pressure and sound intensity plots, suggesting, that the main contributor to the averaged RMS sound pressure is the high frequency noise.

Surface plots of frequencies of maximum FFT amplitude show, that the highest frequency oscillations occur in highly separated regions of the flow: in the wake behind the trailing edge of the blade and in the leading edge-hub juncture induced secondary flow. Surprisingly, the highest frequency fluctuations were captured in tip-to-trailing-edge juncture, which is the region where the largest RMS sound pressure values were noted.

6.3.3 Quantitative analysis

Similar quantitative analysis as in RMS SPL was performed to area weighted average frequency. Pearson correlation coefficient ρ is computed for internal surfaces and blade surfaces. Flow field values of: vorticity magnitude, turbulent kinetic energy, specific dissipation rate, turbulent viscosity, turbulence intensity are correlated with average frequency. Formulas for calculation of the correlation coefficient are the same as for analysis in section 6.2.3 (equations 6.1, 6.2, 6.3).

Correlation coefficients for internal surfaces (fig. 6.5) show no significant correlation between turbulence properties and weighted average frequency. Correlation to turbulent viscosity is somewhat visible, yet values of the correlation coefficient below 0.5 are below significance. Correlation coefficients for blade surfaces (fig. 6.6) are inconsistent throughout the populations of turbulence properties.

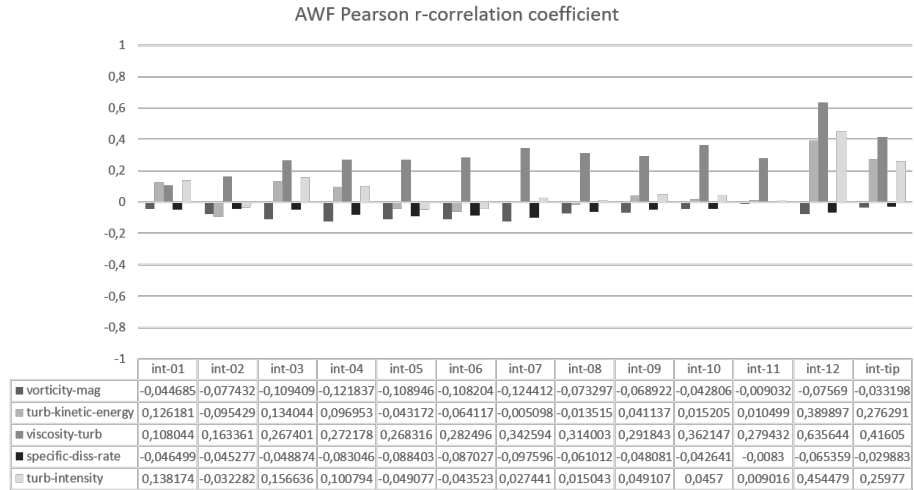


FIGURE 6.5: AWF to flowfield turbulence values correlation. Internal surfaces.

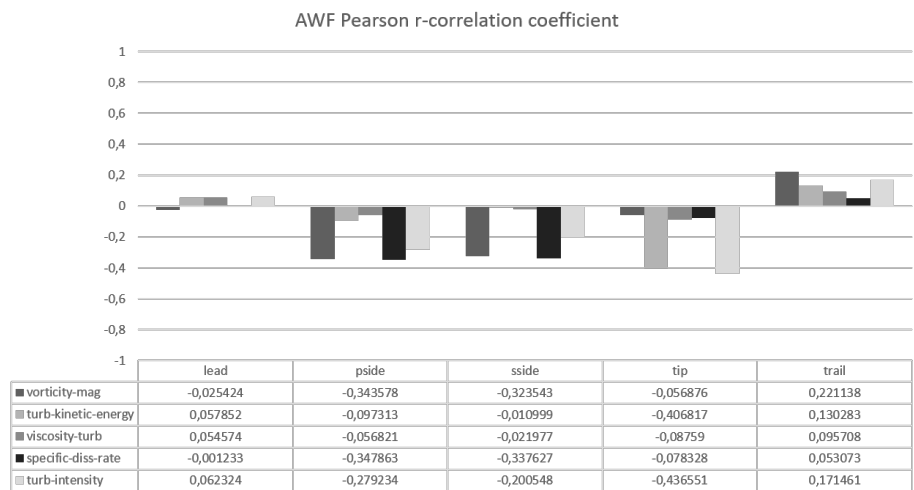


FIGURE 6.6: AWF to flowfield turbulence values correlation. Blade surfaces.

Chapter 7

Conclusions & Further work

7.1 Results discussion

Initially, this thesis intended to investigate the sound generation phenomena on a fan blade of a commercial large by-pass-ratio turbofan engine blade, yet no information on airfoil coordinates and efficiency figures of such devices are available for research purposes. It is assumed, that the phenomena that occur on such blade are similar in character to the ones obtained on the provided test case. Although the practical utilization of presented results is limited at this stage, some conclusion can be drawn out. The approach used on a NASA R67 transonic axial compressor provide some insight to noise generation phenomena in a "frozen-rotor" reference frame. It must be noted, that noise perceived by human or received by a microphone will be different from the ones presented. However, the noise perceived has it's source in the phenomena discussed in this thesis.

The main contributors to the blade's noise generation are the boundary layer separations induced by backflow in the boundary layer or by the shockwave boundary layer interaction. The existence of a shockwave in a device of that kind is also the main contributor of the so-called "buzzsaw noise", which may be recognized by simulating a rotor with a moving mesh and with a stationary receiver or data probe. Largest, in terms of amplitude and frequency, sound pressure fluctuations are found at the trailing edge of the blade and at trailing edge-tip junction. Sound pressure in decibel scale as well as average frequency per node of control surface are in expected range for this kind of device.

Following assumptions can be made. In order to reduce the noise generated by the transonic axial compressor blade one must eradicate the sources of separated flow and, if possible, provide a supersonic to subsonic transition of flow without inducing a shockwave. At time of preparation of this thesis, methods for inverse design of boundary shapes based on pressure and/or other design criteria exist in open source domain. Such software

allows for generating airfoils for fixed wing aircraft and rotating machinery. Furthermore, modification of shape of the blade trailing edge by implementing a shape that reduces the vortex shedding or at least the turbulence intensity in wake. At this stage, there are no suggestions for manipulating the frequency of the fluctuations.

Results of direct noise analysis on hub and casing surfaces are not presented due to a simple mistake – these surfaces were accidentally removed from the CFD solution export of the DDES analysis. Only one low frequency cycle is captured due to another mistake. As described in chapter 5, the timestep of the analysis was decreased by the order of magnitude in order to improve the analysis convergence. However, the solution export was still set up to deliver a dataset per timestep which resulted in a dataset 10 times larger than necessary, with no available walltime to continue the calculation.

The main downside of the presented study is lack of validation data for acoustical nearfield of the given case. It is assumed, that the approach is valid when two following factors coincide: if the CFD analysis that generate flow-field data is validated by experimental data and if FFT and RMS scripts return the expected results while the input is a sum of sine waves of known frequency, amplitudes and phase shifts. The CFD analysis results were validated with the experimental data provided in reference [27] as described in chapter 5, therefore it is assumed that the DDES flowfield data is valid. The RMS script return the expected average amplitude value while processing a set of sine wave signals, whereas the FFT script returned proper frequency spectrum and phase shift of the given signal. By this indirect validation, it is assumed that presented results are valid.

7.2 Improvements to the method

Current approach may be compared to attempts of resolving a turbulent boundary layer with one finite volume element at the boundary wall. Although mathematically possible (and used in wall modeled turbulence models) it is valid under fulfilling some assumptions. For presented direct approach, it is assumed that sinusoidal fluctuation of wavelength enclosed by four finite volumes and resolved by four timesteps.

Resolving a sinusoidal fluctuation with four finite volumes and four timesteps fulfills the continuity and momentum equations, any change in temperature, resulting in changing velocity of sound will disrupt the assumptions presented in chapter 3. FFT amplitude plots for ordinary frequencies, analyzed at random mesh points show, that the amplitudes of frequencies above the assumed by mesh and timestep range are dropped nearly to zero. A solution for this is using a finer mesh, capable of resolving shorter wavelength fluctuations, along with smaller timestepping to compensate for transition of sound wave in the finer mesh, especially in the boundary layer region and in the wake.

Considering that the mesh resolution is increased, a proper method for resolving turbulence flow is required. Although justified from the computational expense standpoint, the hybrid methods with shielding functions may result in filtering the source fluctuations at the boundary due to switching to the RANS part of given model. Using LES methods for further work will be considered.

Utilized method does not include the effects of aeroelasticity. The geometry and mesh is rigid and deformations due to aerodynamic loading are not computed. Deformation caused by the aerodynamic loading is variable and depends on the transient phenomena, such as flow separation, generation of Karmann vortices and pulsation of the shockwaves. These phenomena cause cyclic deformations to the compressor blade, which as a result cause the cyclic displacement of volume that is considered as acoustic source.

Another aspect to be considered for improvement is the walltime management and data management. Presented analyses was performed on a Prometheus HPC and was distributed to 120 nodes. Normalized walltime for the analysis was above 1M CPU hours for both transition DDES and final DDES analyses and around 11TB of data was generated during the process. Using LES methods requires meshes of much greater density and therefore meshes of at least order of magnitude larger than used in this case. Assuming that walltime requirement is scaled linearly with the mesh size, assumed LES analysis of the presented test case, would have had required more than 10M CPU hours and around 1000CPU nodes.

Realtime processing of data to obtain sound information in the flowfield is impractical if even possible for full meshes, due to the amount of data generated. An efficient and high capacity storage storage is therefore required for performing direct approach analyses of sound on full flowfield.

Post-processing of data obtained in this study was performed with use of Matplotlib Pyplot library available for Python scripting language and hence the information about mesh was dropped during the process. This is visible especially in the internal surface scatter plots where lack of interpolation between points is visible. Using a post-processing tool with custom filters such as Paraview, or implementing a mesh file reader into Python (or any other implementation) scripts will solve problem with interpolation of data and allow visualization of full flowfield datasets.

7.3 Further work

As stated above, lack of validation case that directly checks the acoustical nearfield results is somewhat of a challenge. Therefore developing an experimental and numerical case of known acoustic nearfield properties is required.

The implementation of mesh reading or mapping to mesh functionality will be developed in further versions of the post-processing scripts. This will allow for more efficient qualitative and quantitative analysis of the obtained data.

Presented work describes a single passage of the compressor in stationary reference frame ("Frozen rotor") configuration and gives insight to basic aerodynamic phenomena contributing to noise. In order to assess the noise generation in compressor, or fan, flows the analysis ought to be performed with use of rotating mesh with sliding interfaces and include effects of rotor-to-stator interaction, as well as interaction with compressor hub and casing. Furthermore, performing data acquisition and processing on full flow-field of the given case will give a better opportunity to post-process the obtained data. By extending the analysis time to more than 1 cycle of low frequency sound (0.05s), and preferably to more than five of such cycles, it may be possible to obtain information on acoustical wave modes within the flowfield of the case subject to study.

Considering that the geometry of given case is periodic, assuming the periodicity of flow in the DDES and LES analysis is prone to over constraining the resulting flowfield. Hence the analyses should be conducted on full rotor-stator stage, or at least a large portion of a stage, to eradicate or minimize the effect of periodic boundary conditions. This, combined with proposed LES simulation, enforces using a mesh with cell count in 10^8 order of magnitude, which leads to further challenges with data management and required computational resources.

Further improvement may contain including the aeroelastic phenomena in the analysis. As stated above, the phenomena related with cyclic deformation are expected to have a contribution to the noise flowfield. Stress calculations and transient mesh displacements are among the most challenging of numerical calculations. Considering the current requirements for the calculation, implementation of aeroelastic effects may cause a shortage in computational resources.

7.4 Closing remarks

The study presented in this thesis can be interpreted two-wise. One, as a case study on direct formulation of noise analysis and providing the minimum requirements towards the analysis. Second aspect is the study of generating sound by the transonic axial compressor rotor blade. Both aspects of the study are, at least partially, fulfilled.

The provided minimum requirements of the analysis proved to work at relatively high computational expense. Yet, using the acoustical analogies implemented into used CFD code with transonic flows with shockwaves is unjustified by the mathematical formulation

of the FW-H analogy. The resolution of the obtained acoustical nearfield can be improved at a cost of higher computational power requirements.

The presented results of the compressors acoustical nearfield are rather expected and are in correlation to relative Mach number fields and time averaged static pressure fields. Results identify the sources of aerodynamic noise that are consistent with ones described in literature, turbulent regions of the flow are the source of pressure fluctuations of high amplitude and high frequency. Propagation of sound waves was captured for lower end of the frequency spectrum, while the effect of high pitch noise is captured as an increase in RMS sound pressure and decibel figures. These results can be used to design a compressor blade that generates lower aerodynamically induced noise.

The method will be improved in terms of computational efficiency and data storage and attempted to be used in other technical entities where noise generation and acoustical wave mode assessment is required.

Appendix A

RMS values plots

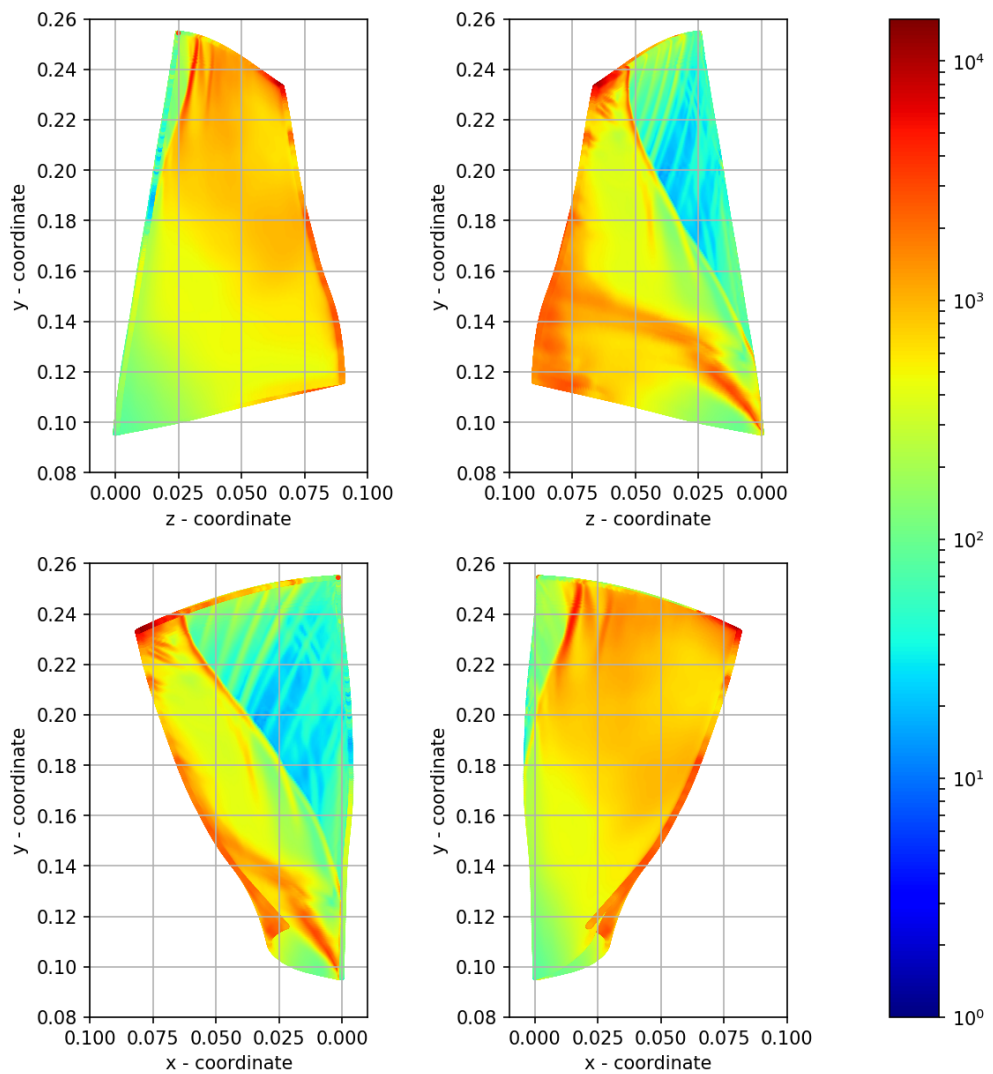


FIGURE A.1: Blade surface RMS Sound pressure [Pa]

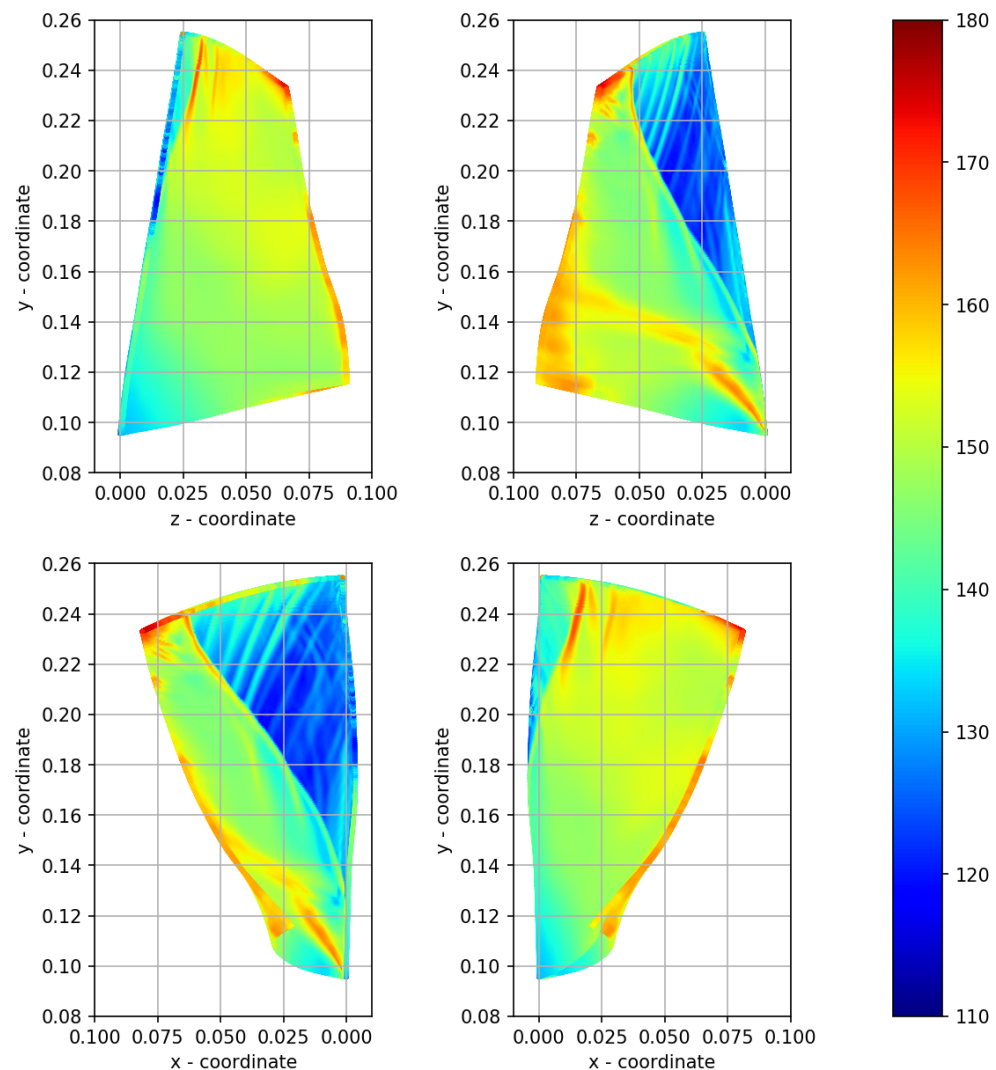


FIGURE A.2: Blade surface RMS SPLdB [dB]

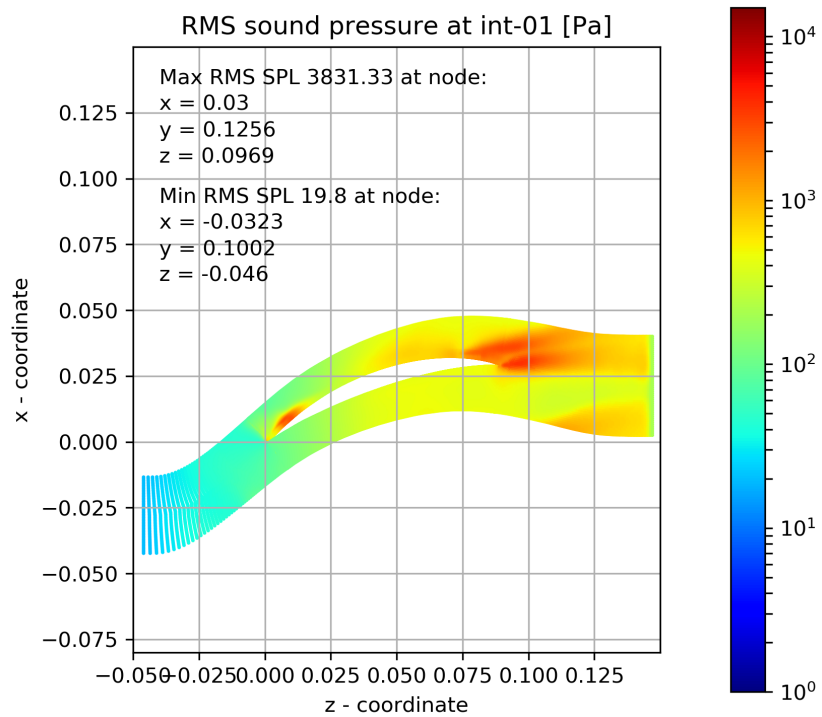


FIGURE A.3: RMS Sound pressure at int-01 mark

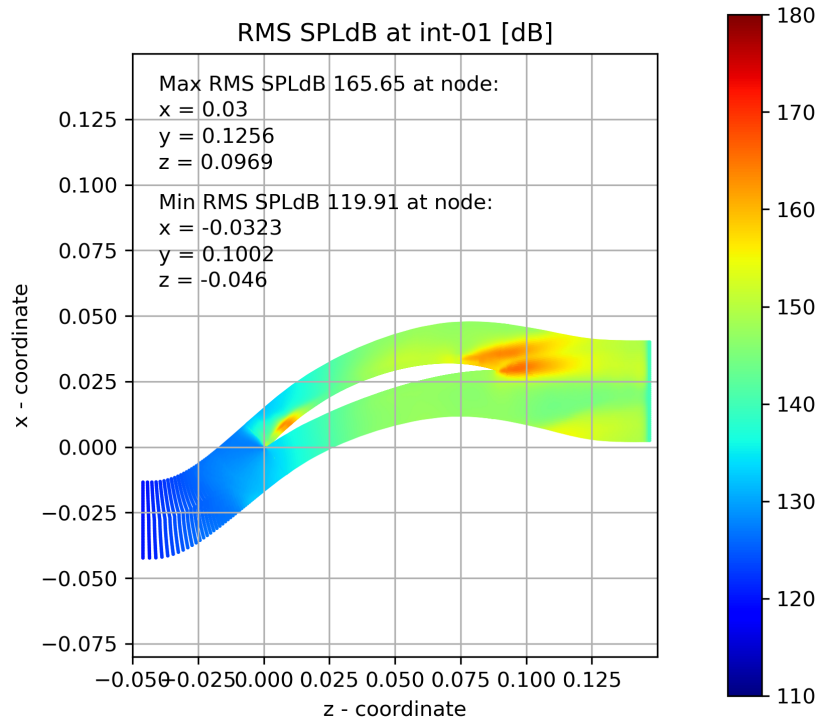


FIGURE A.4: RMS Sound pressure decibel level at int-01 mark

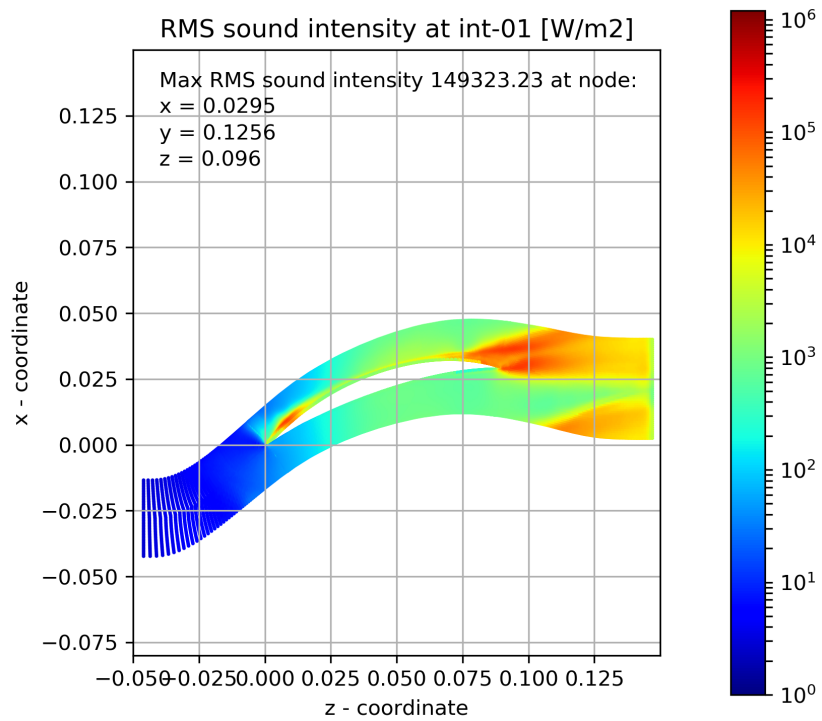


FIGURE A.5: RMS Sound intensity at int-01 mark

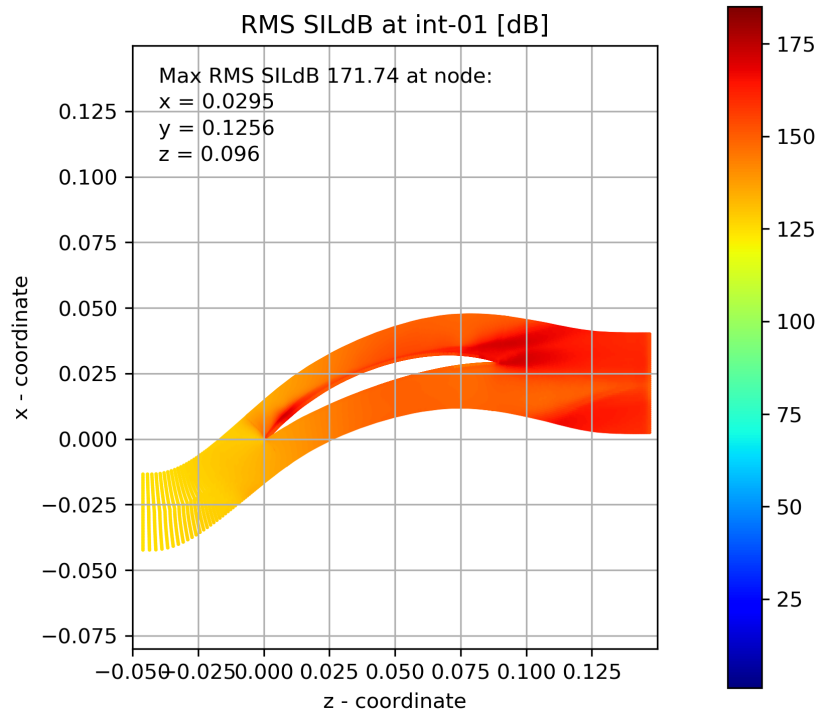


FIGURE A.6: RMS Sound intensity decibel level at int-01 mark

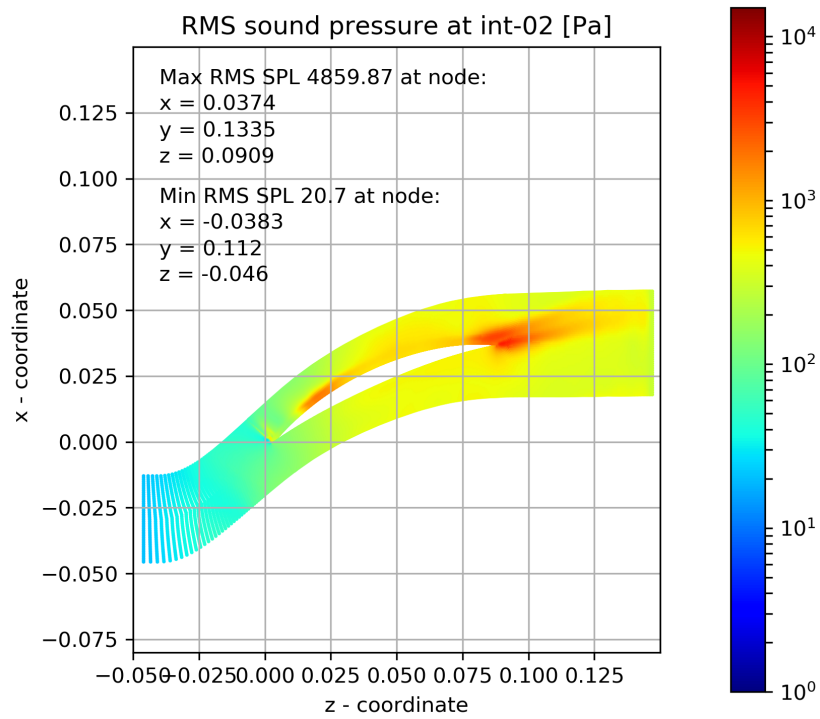


FIGURE A.7: RMS Sound pressure at int-02 mark

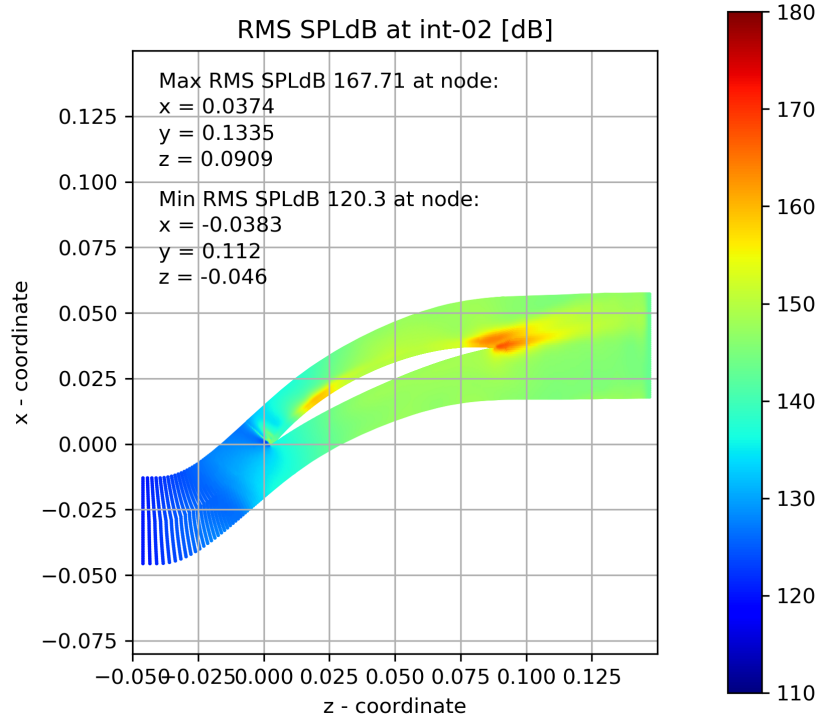


FIGURE A.8: RMS Sound pressure decibel level at int-02 mark

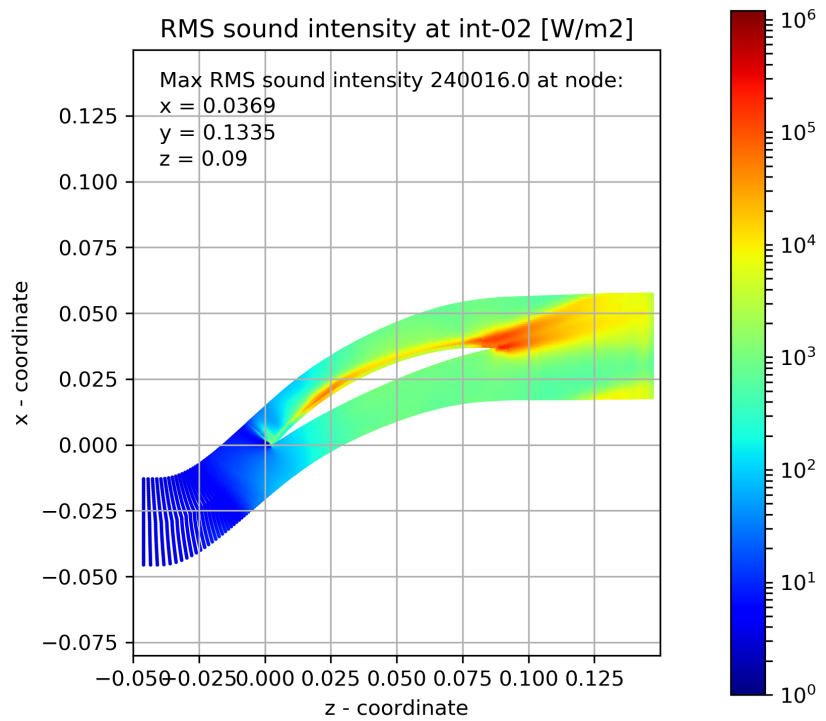


FIGURE A.9: RMS Sound intensity at int-02 mark

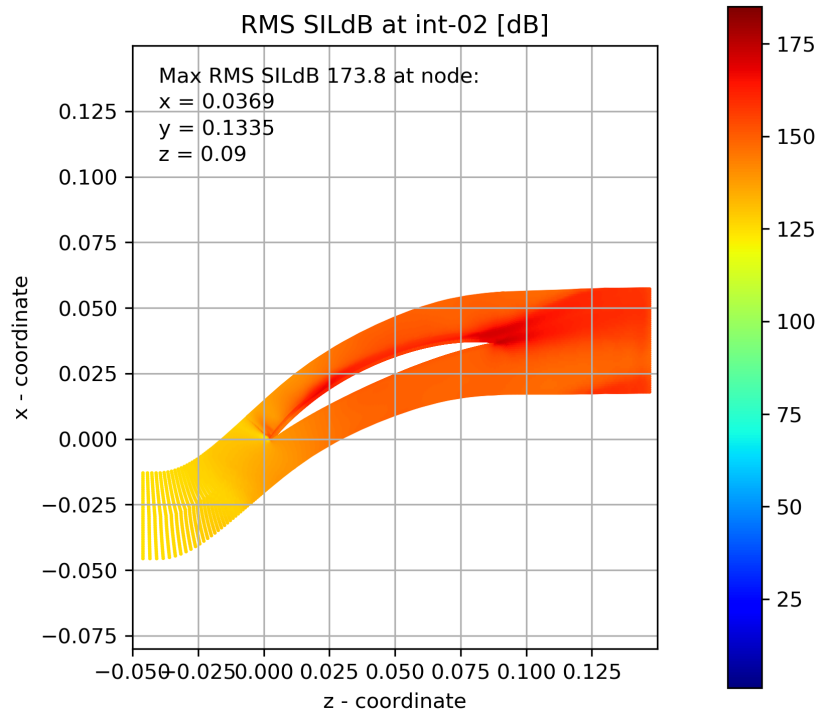


FIGURE A.10: RMS Sound intensity decibel level at int-02 mark

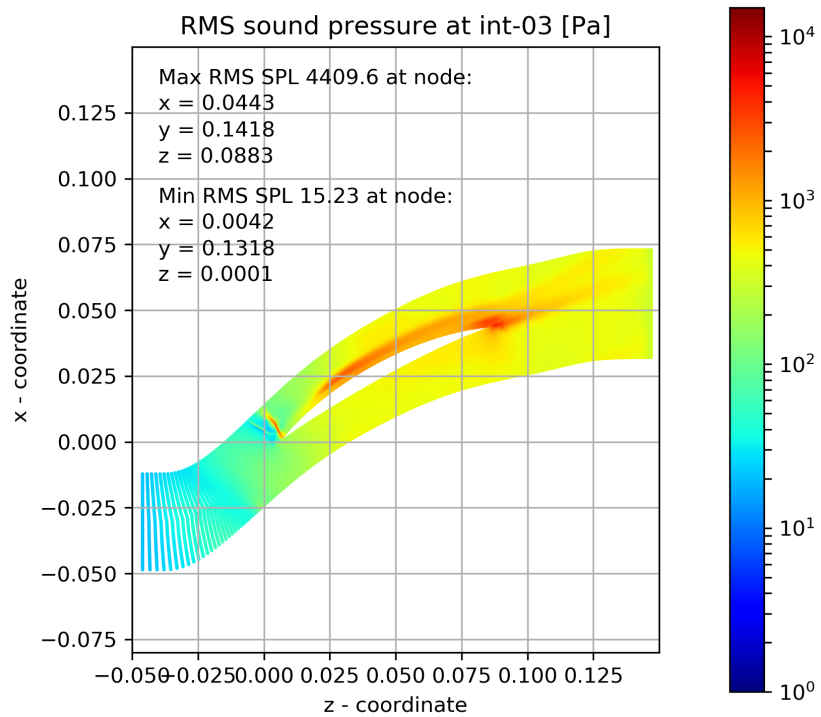


FIGURE A.11: RMS Sound pressure at int-03 mark

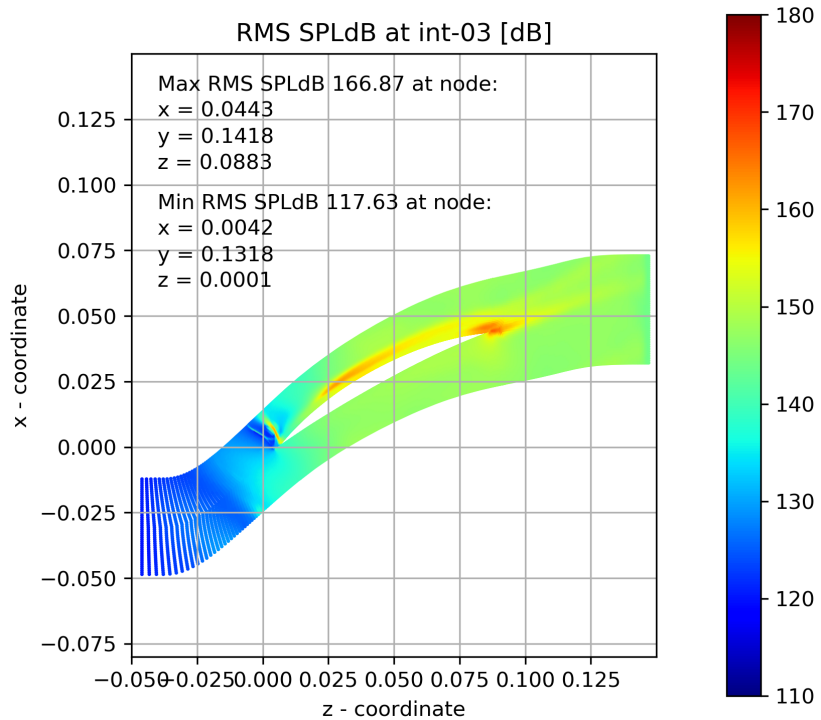


FIGURE A.12: RMS Sound pressure decibel level at int-03 mark

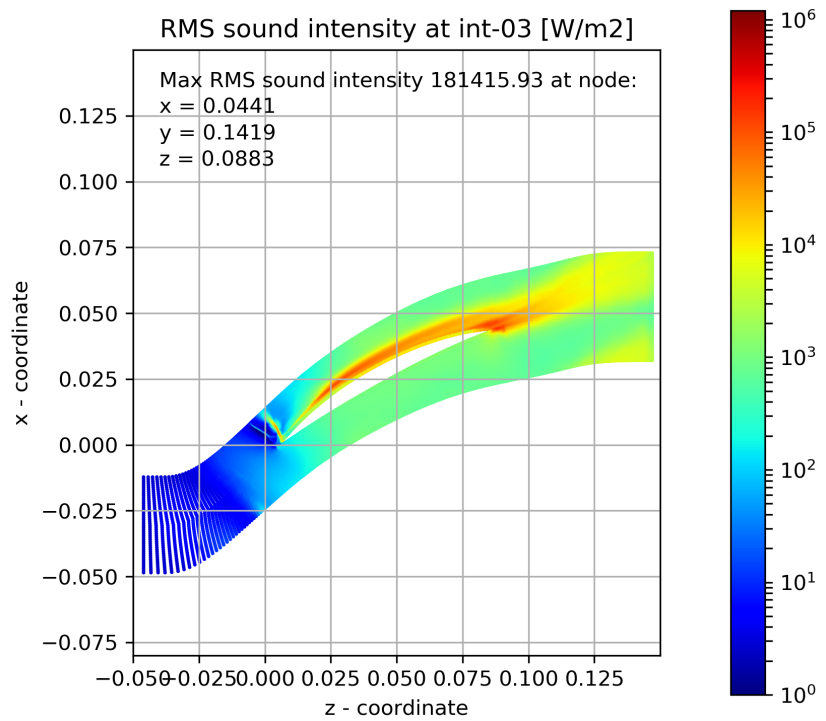


FIGURE A.13: RMS Sound intensity at int-03 mark

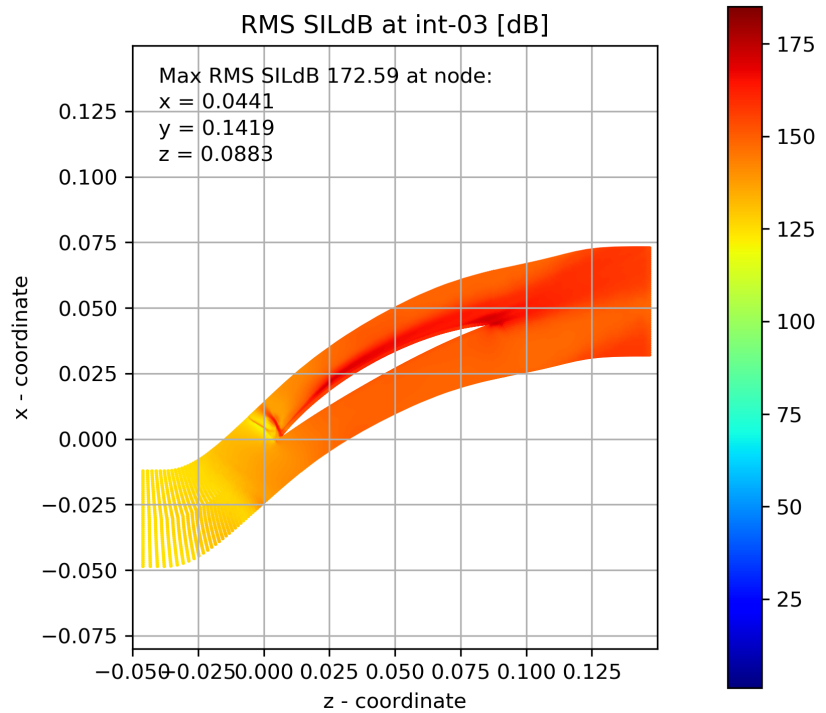


FIGURE A.14: RMS Sound intensity decibel level at int-03 mark

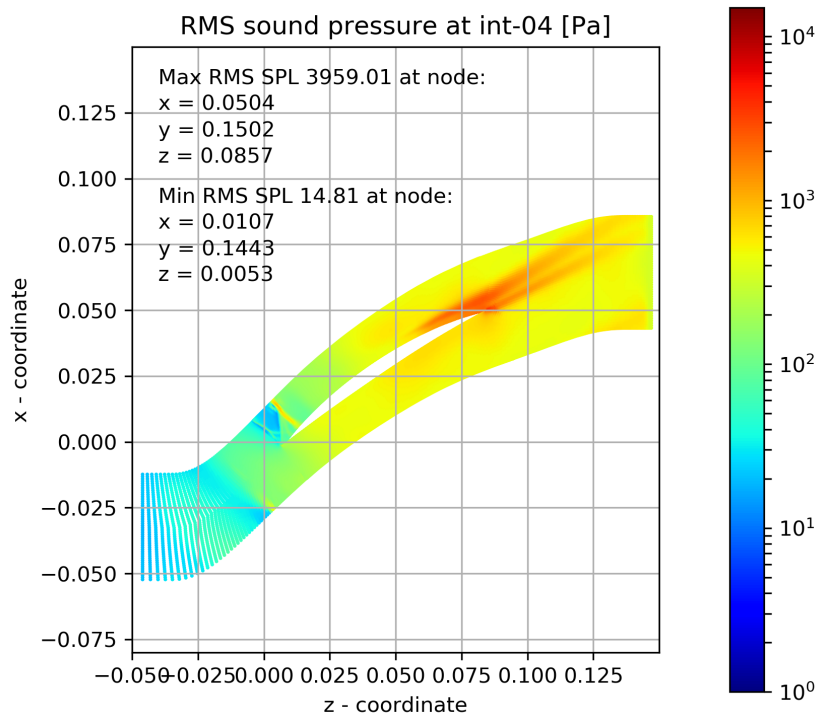


FIGURE A.15: RMS Sound pressure at int-04 mark

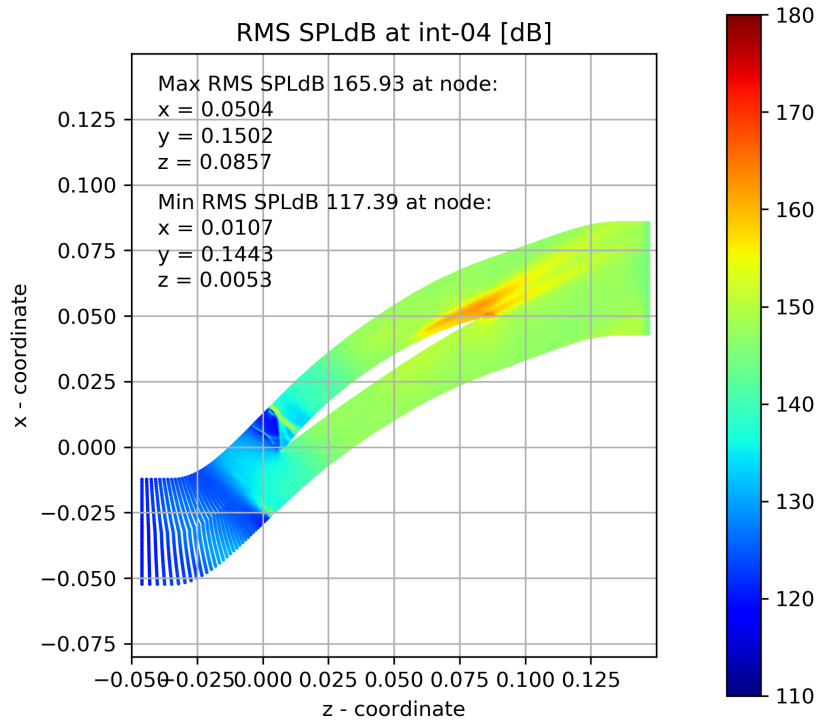


FIGURE A.16: RMS Sound pressure decibel level at int-04 mark

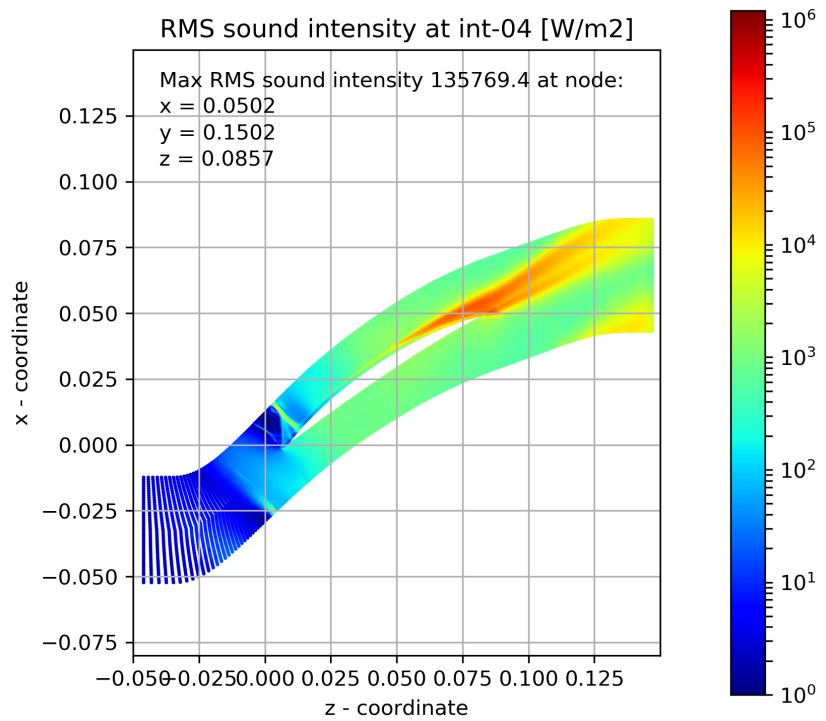


FIGURE A.17: RMS Sound intensity at int-04 mark

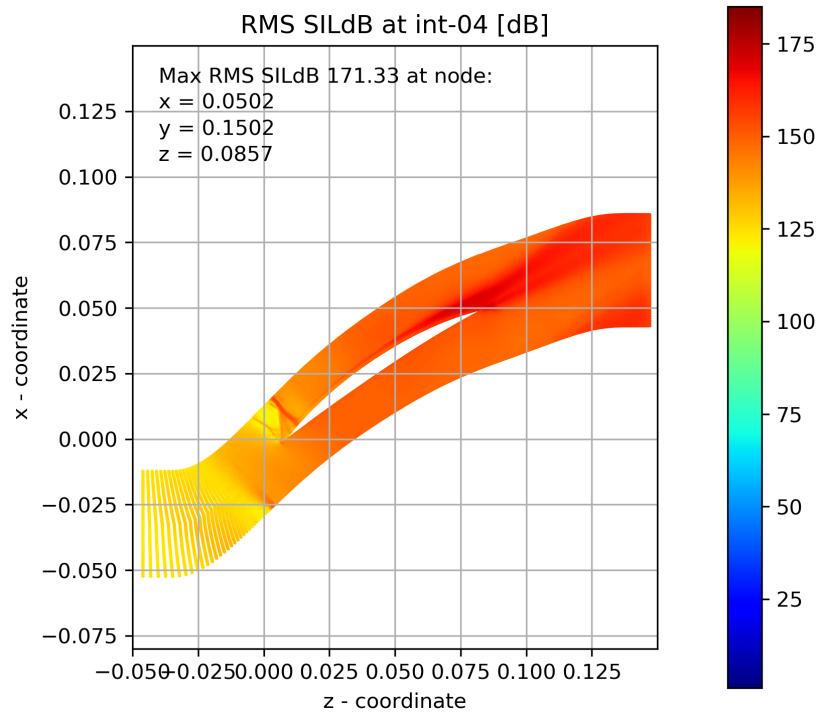


FIGURE A.18: RMS Sound intensity decibel level at int-04 mark

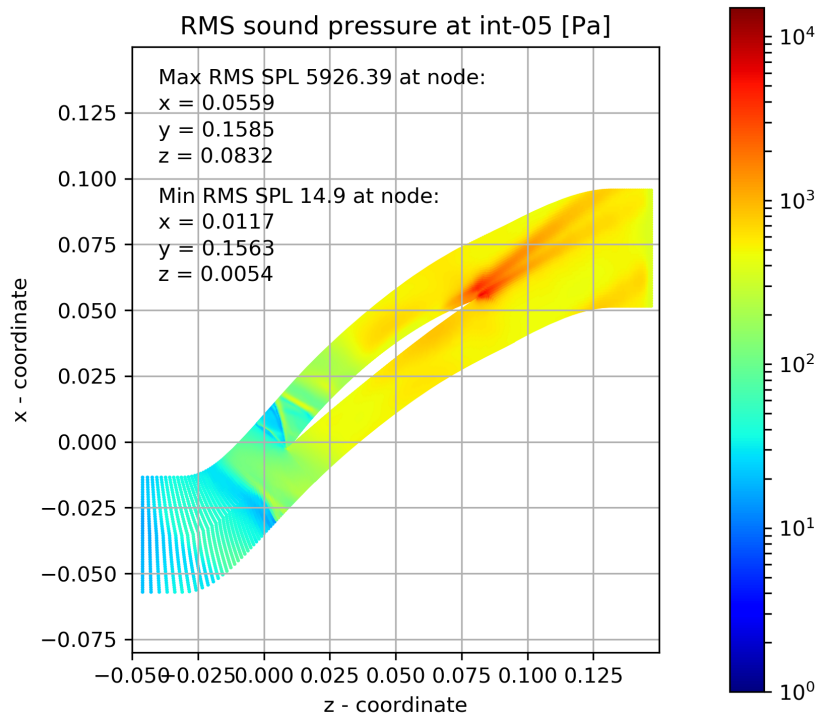


FIGURE A.19: RMS Sound pressure at int-05 mark

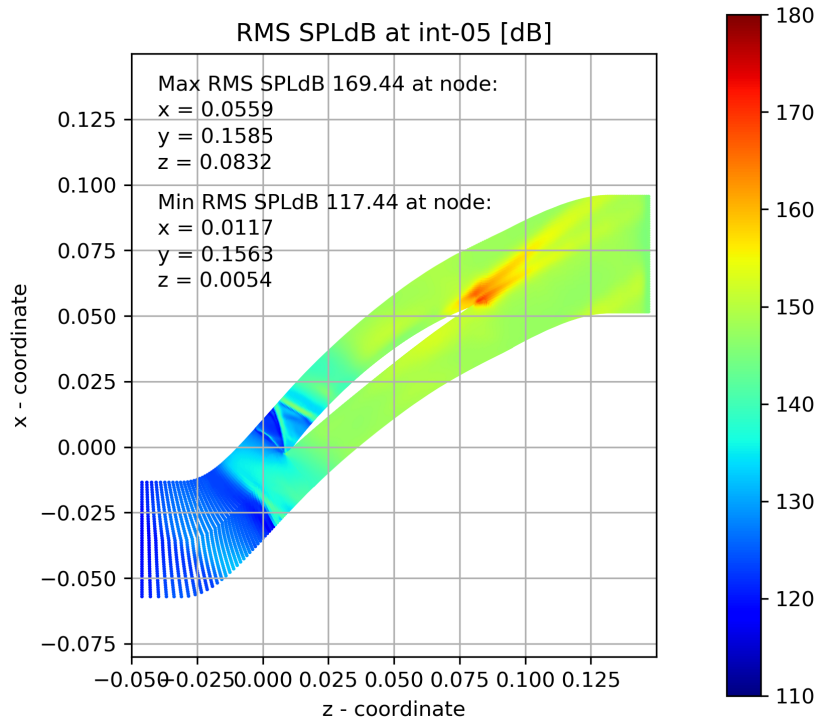


FIGURE A.20: RMS Sound pressure decibel level at int-05 mark

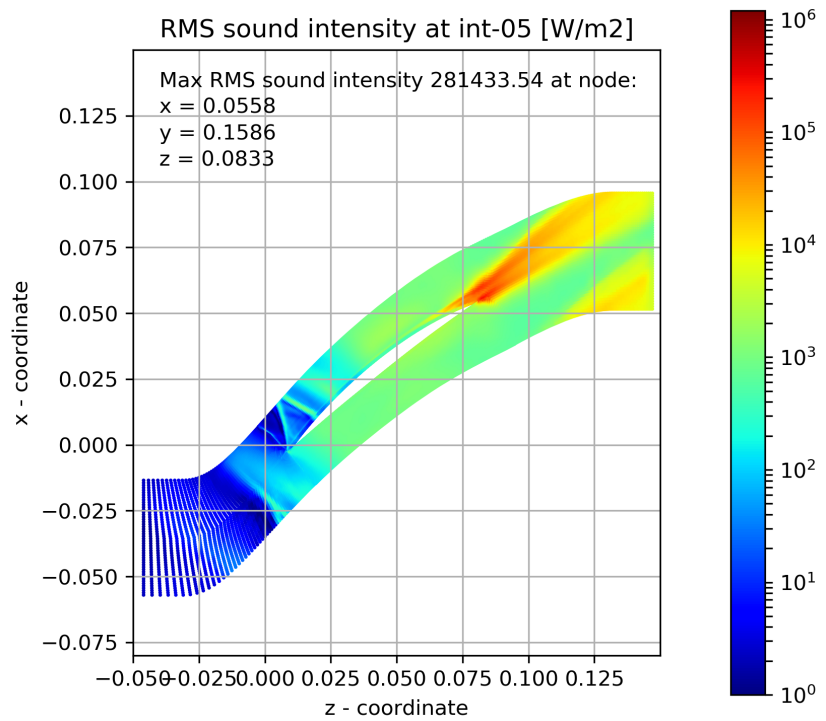


FIGURE A.21: RMS Sound intensity at int-05 mark

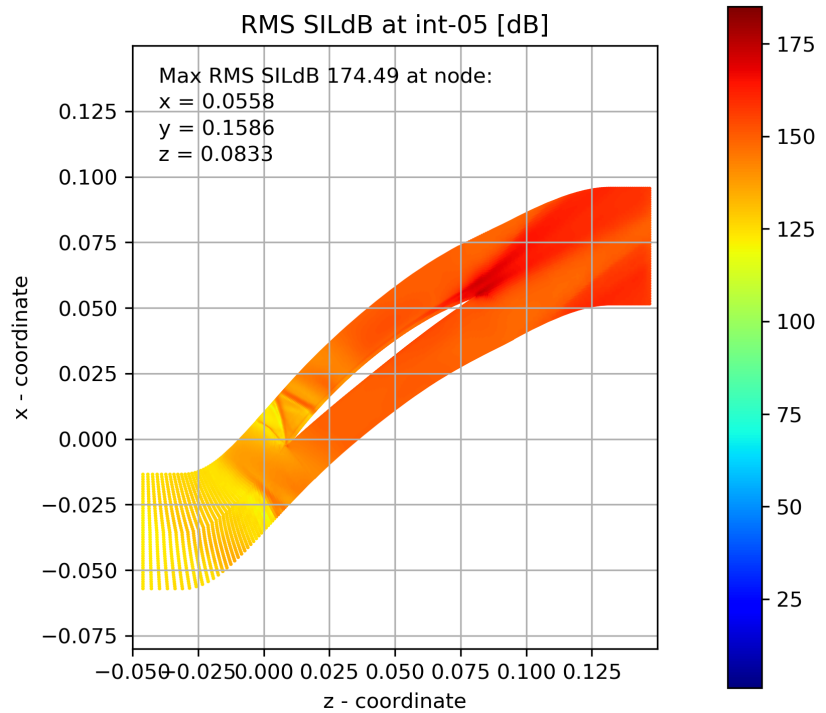


FIGURE A.22: RMS Sound intensity decibel level at int-05 mark

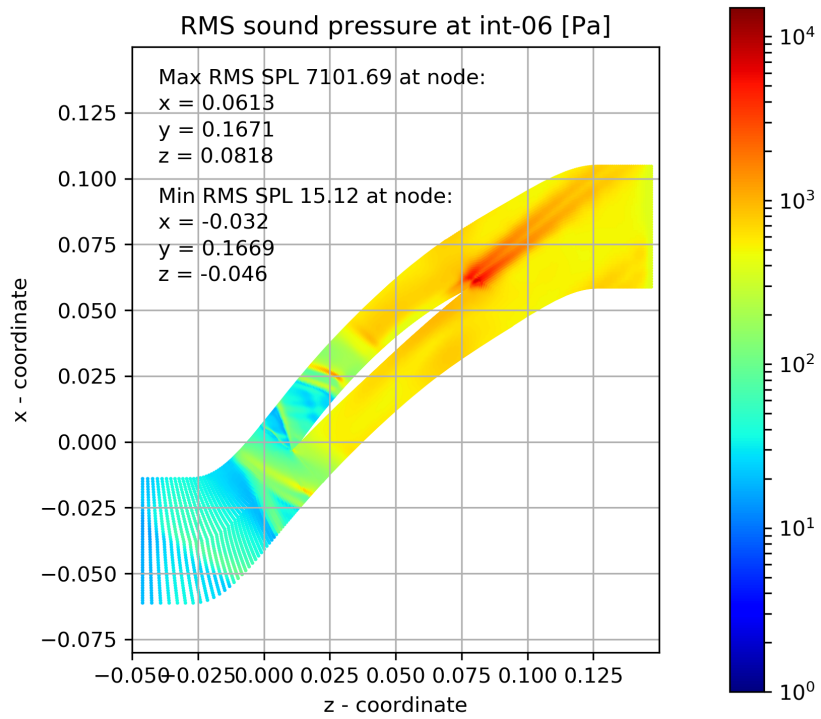


FIGURE A.23: RMS Sound pressure at int-06 mark

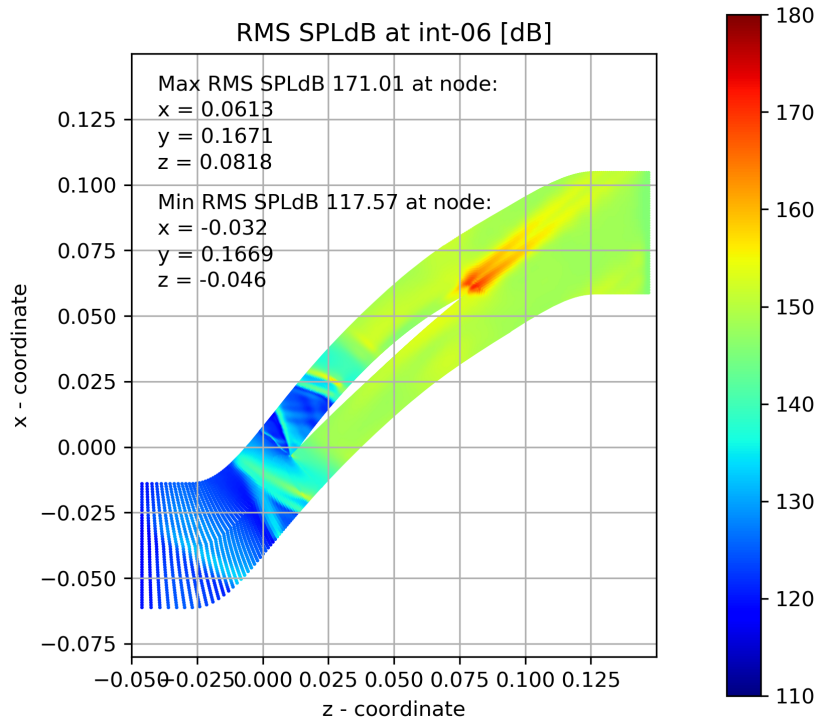


FIGURE A.24: RMS Sound pressure decibel level at int-06 mark

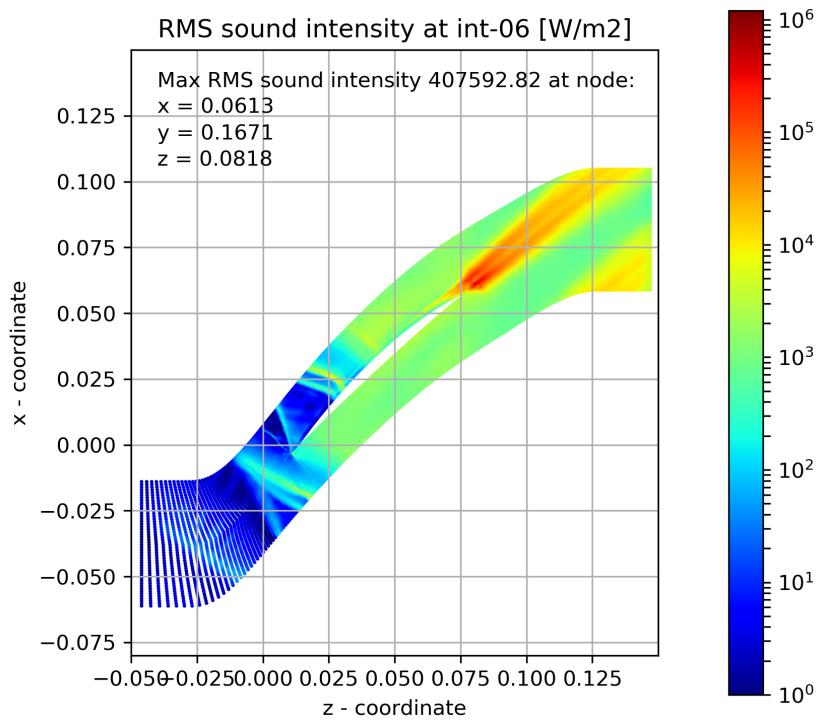


FIGURE A.25: RMS Sound intensity at int-06 mark

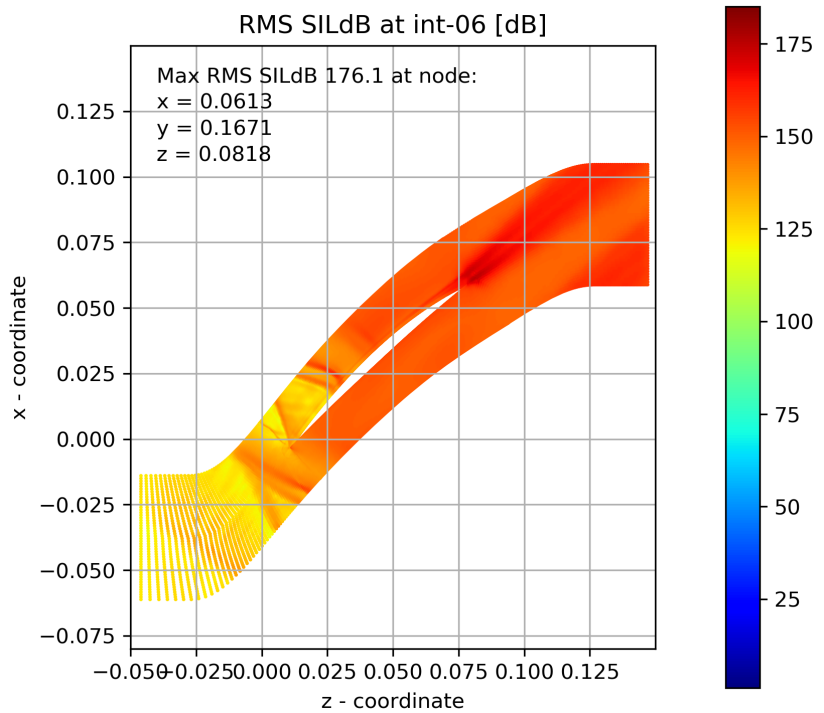


FIGURE A.26: RMS Sound intensity decibel level at int-06 mark

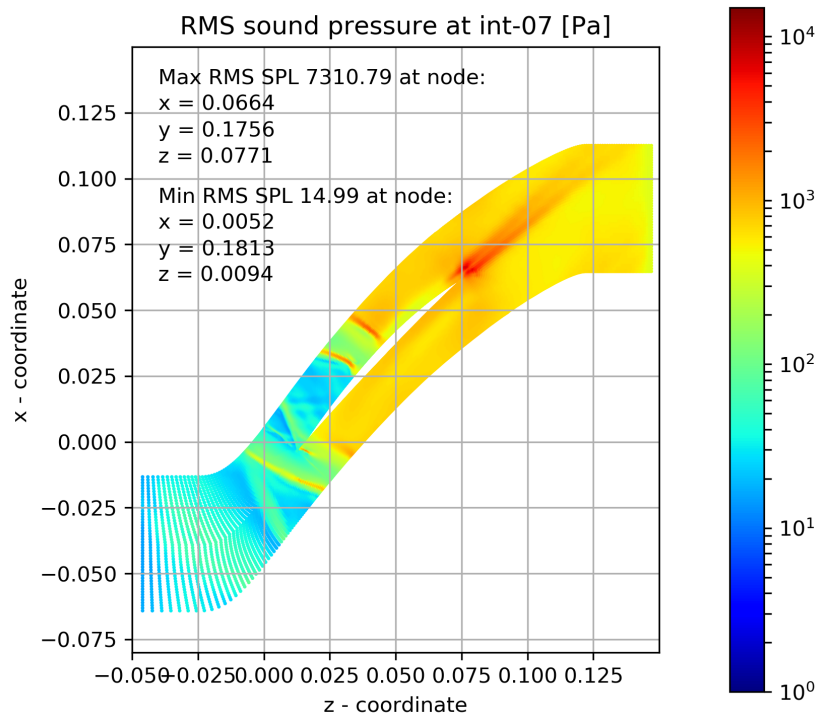


FIGURE A.27: RMS Sound pressure at int-07 mark

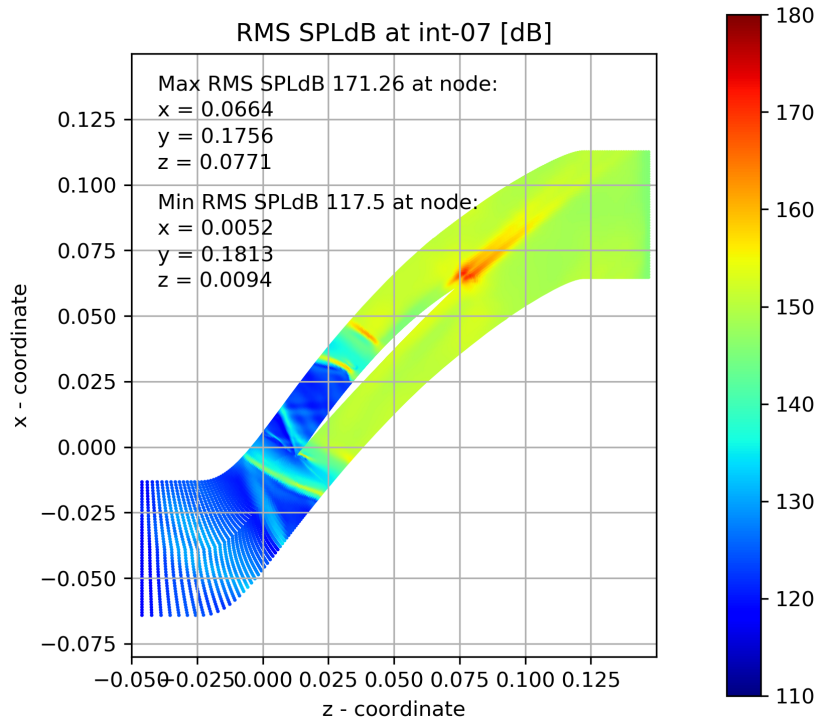


FIGURE A.28: RMS Sound pressure decibel level at int-07 mark

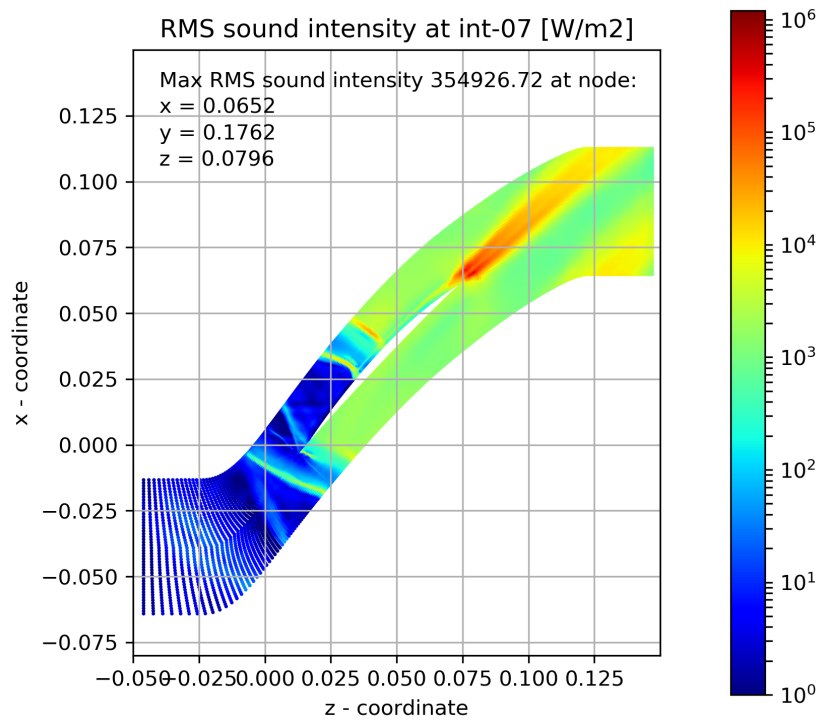


FIGURE A.29: RMS Sound intensity at int-07 mark

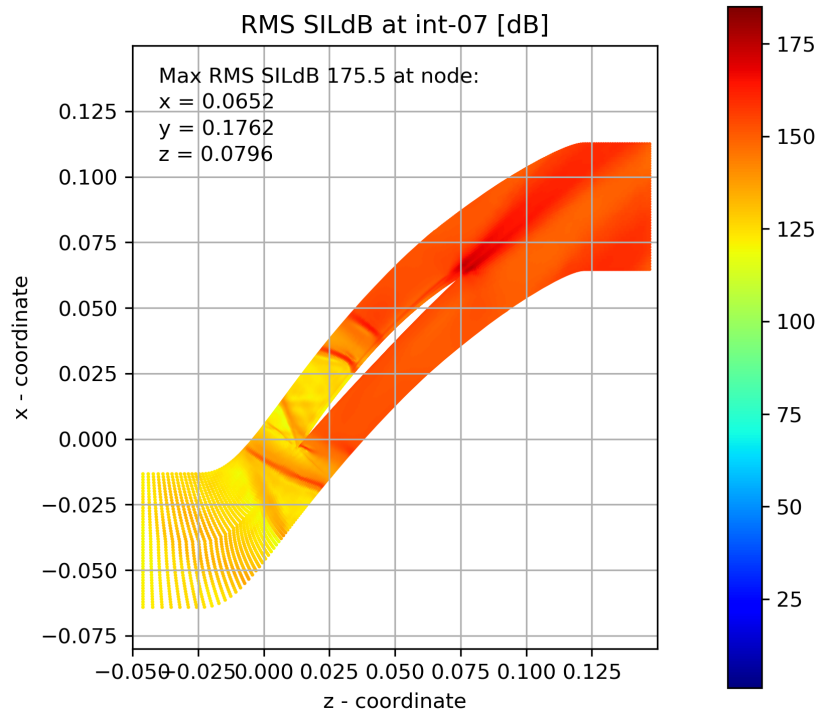


FIGURE A.30: RMS Sound intensity decibel level at int-07 mark

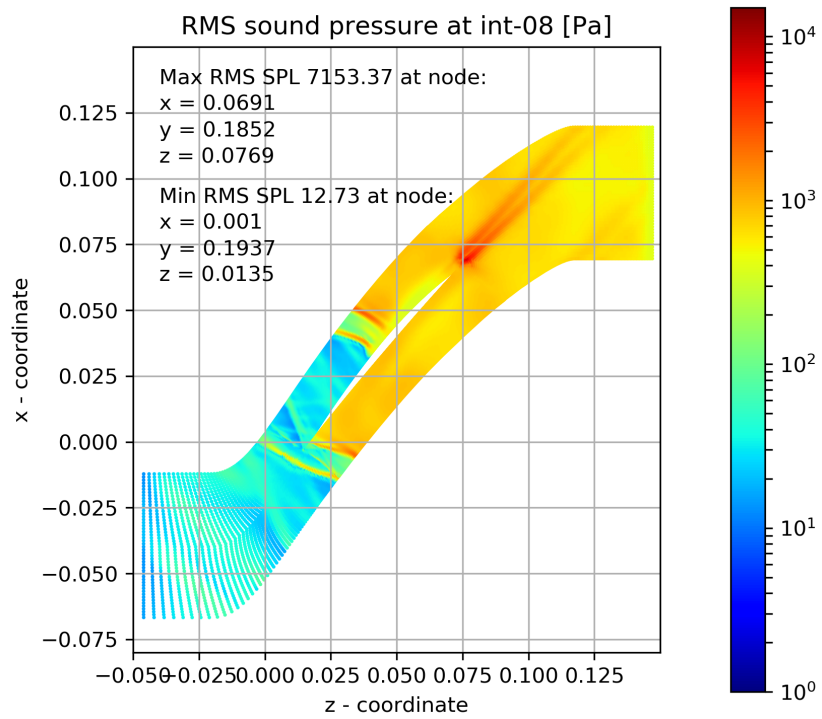


FIGURE A.31: RMS Sound pressure at int-08 mark

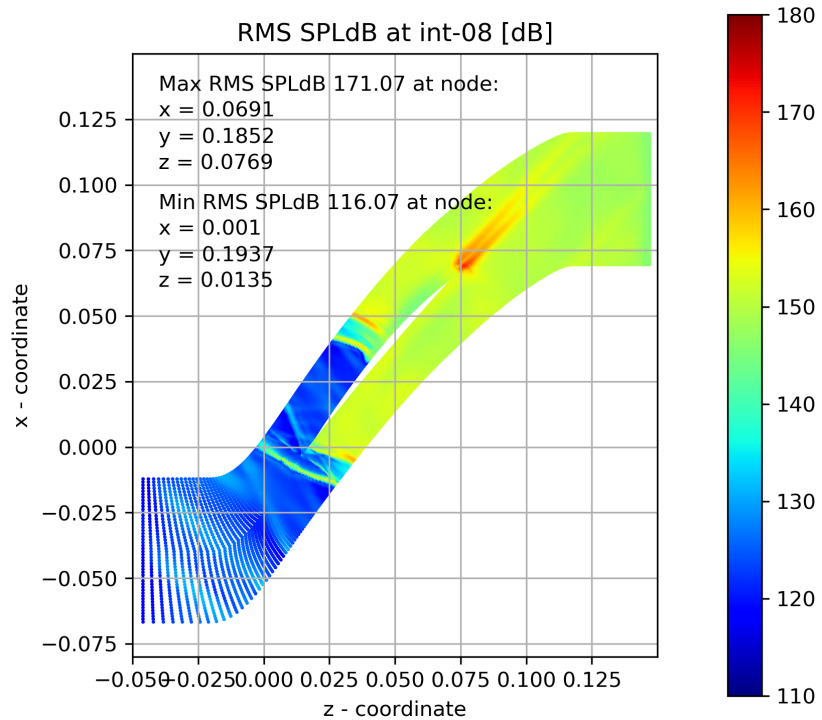


FIGURE A.32: RMS Sound pressure decibel level at int-08 mark

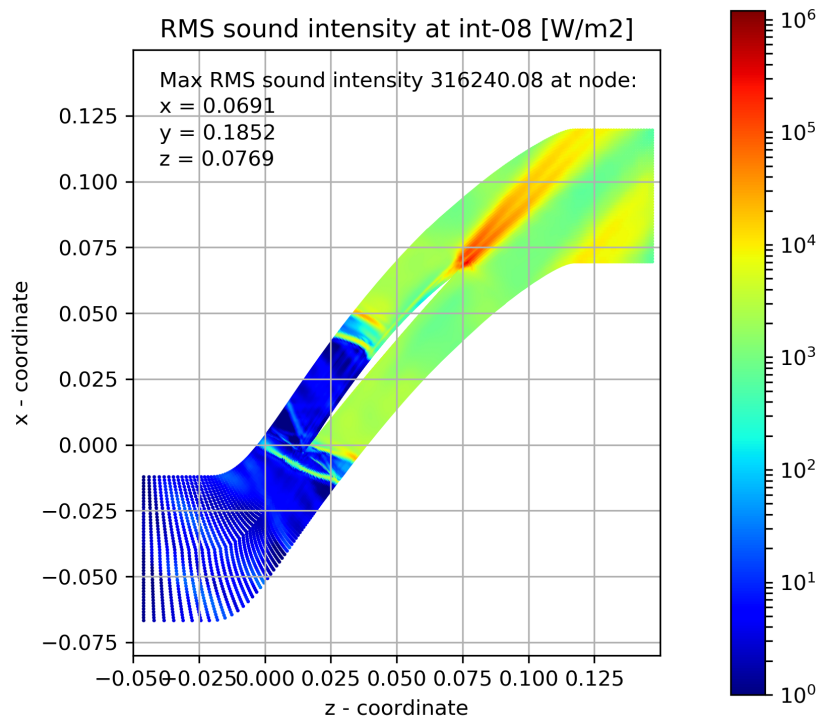


FIGURE A.33: RMS Sound intensity at int-08 mark

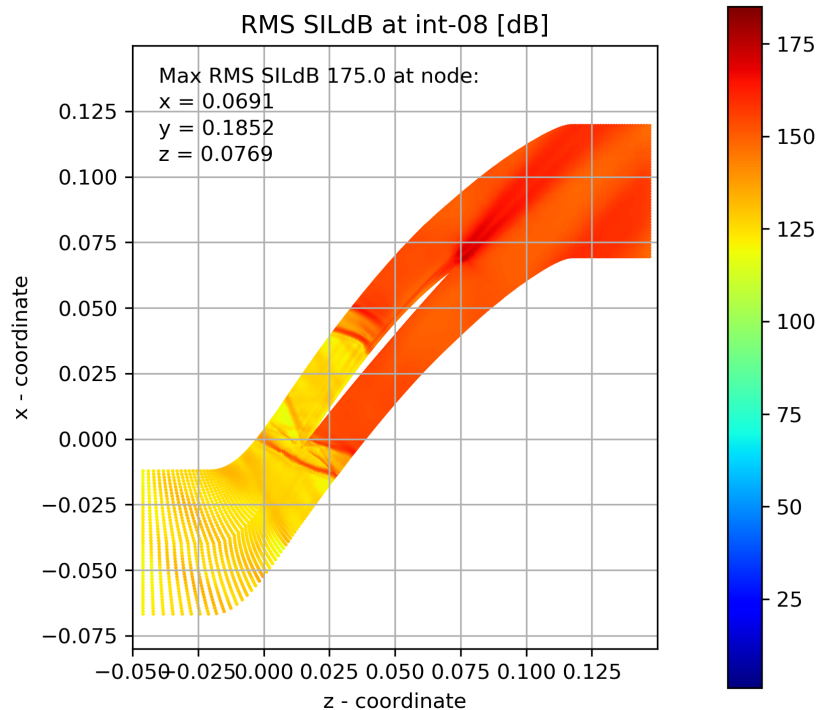


FIGURE A.34: RMS Sound intensity decibel level at int-08 mark

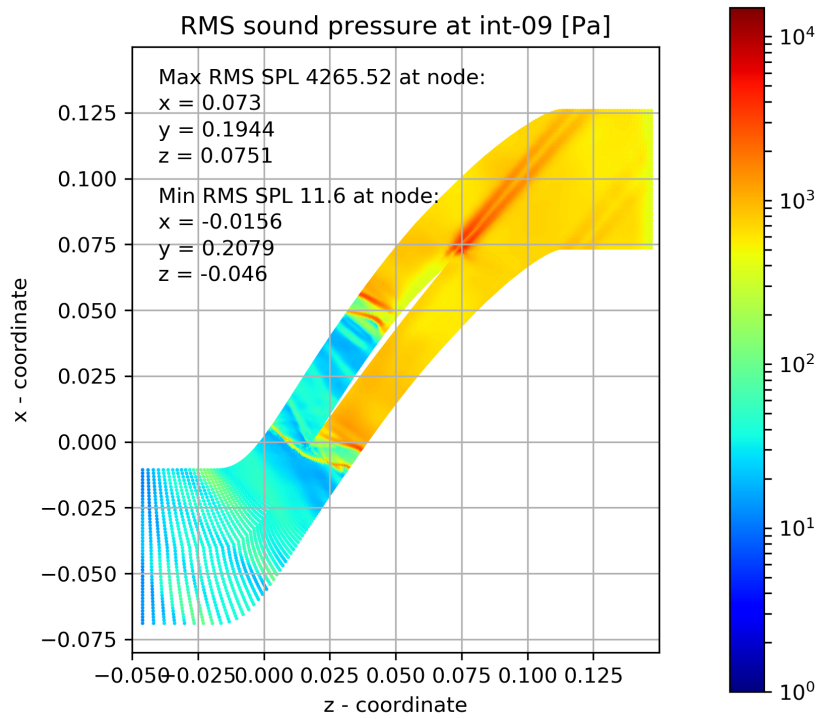


FIGURE A.35: RMS Sound pressure at int-09 mark

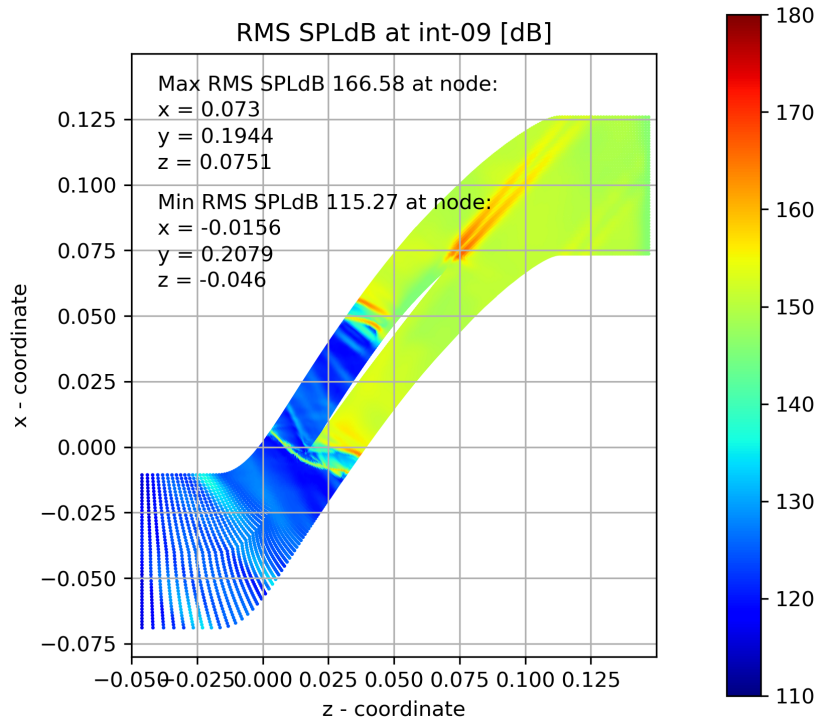


FIGURE A.36: RMS Sound pressure decibel level at int-09 mark

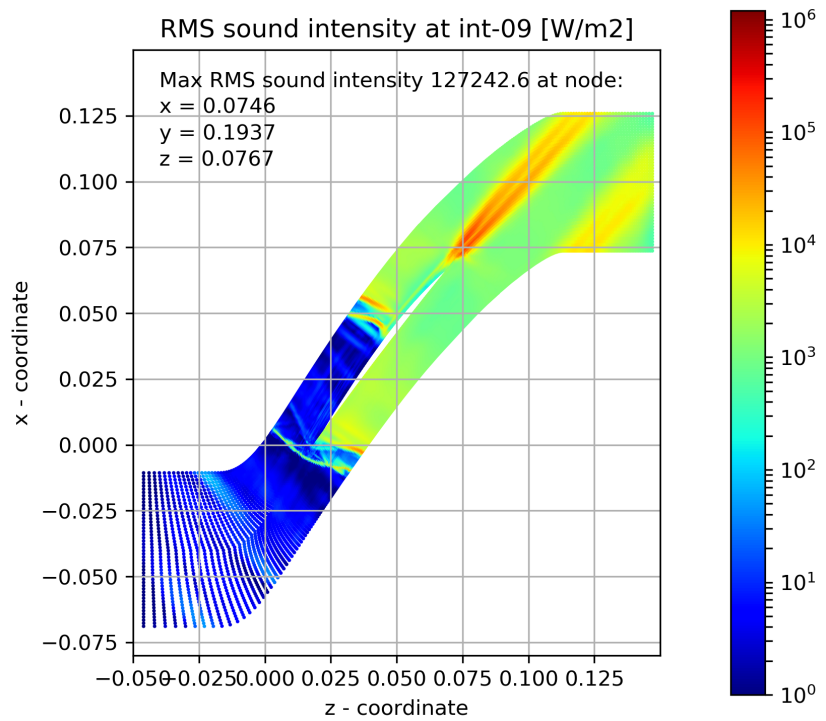


FIGURE A.37: RMS Sound intensity at int-09 mark

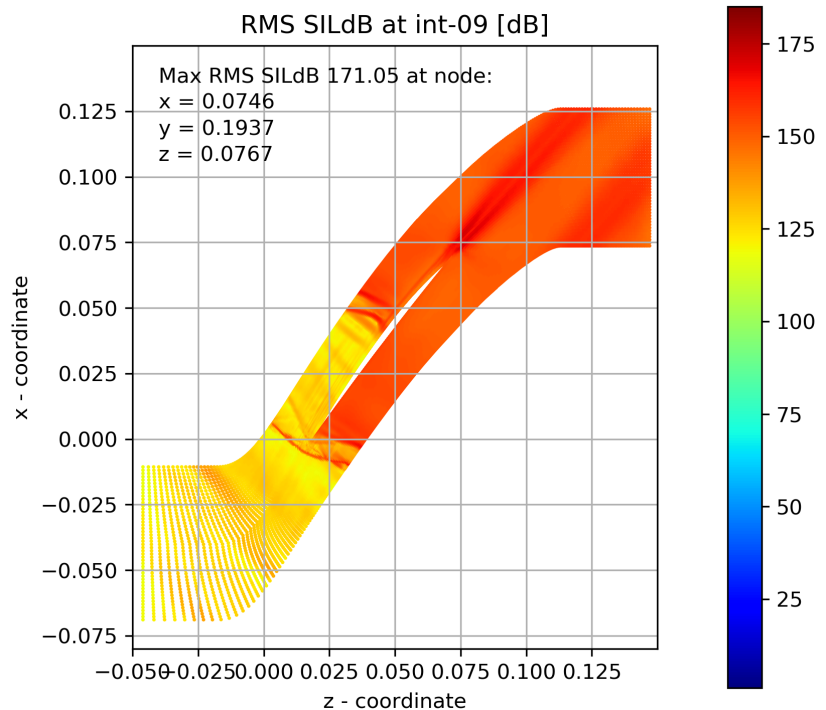


FIGURE A.38: RMS Sound intensity decibel level at int-09 mark

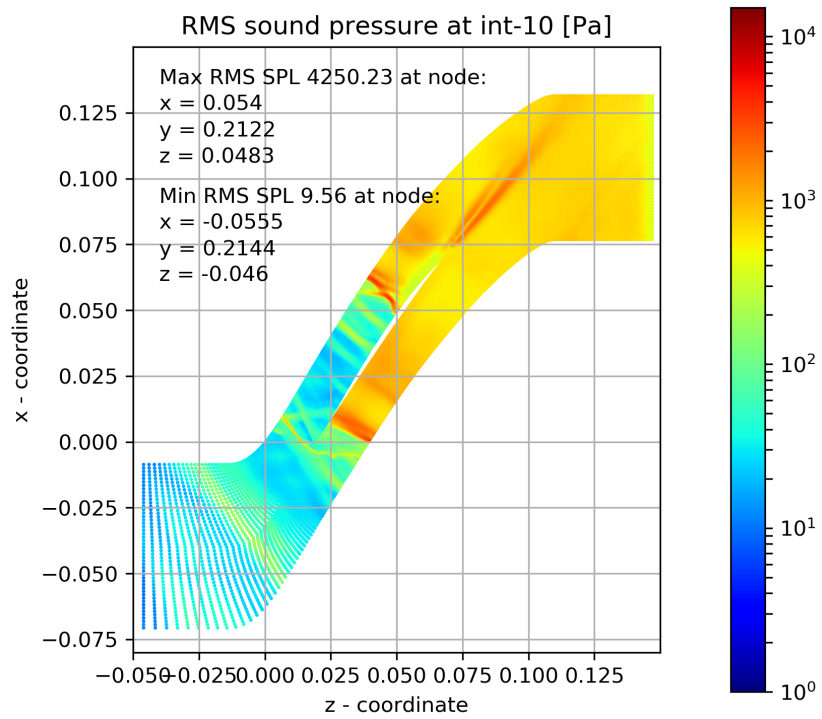


FIGURE A.39: RMS Sound pressure at int-10 mark

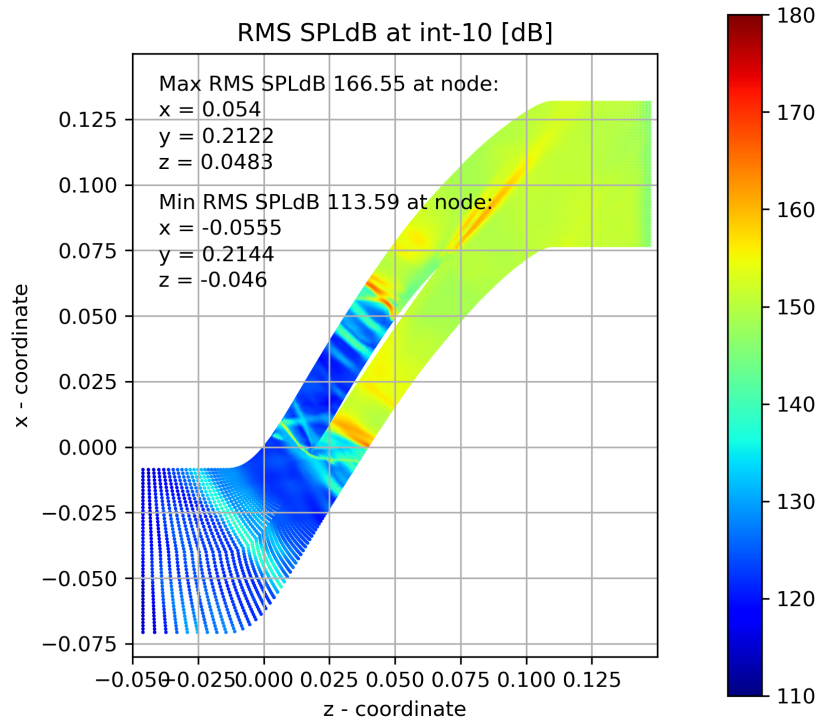


FIGURE A.40: RMS Sound pressure decibel level at int-10 mark

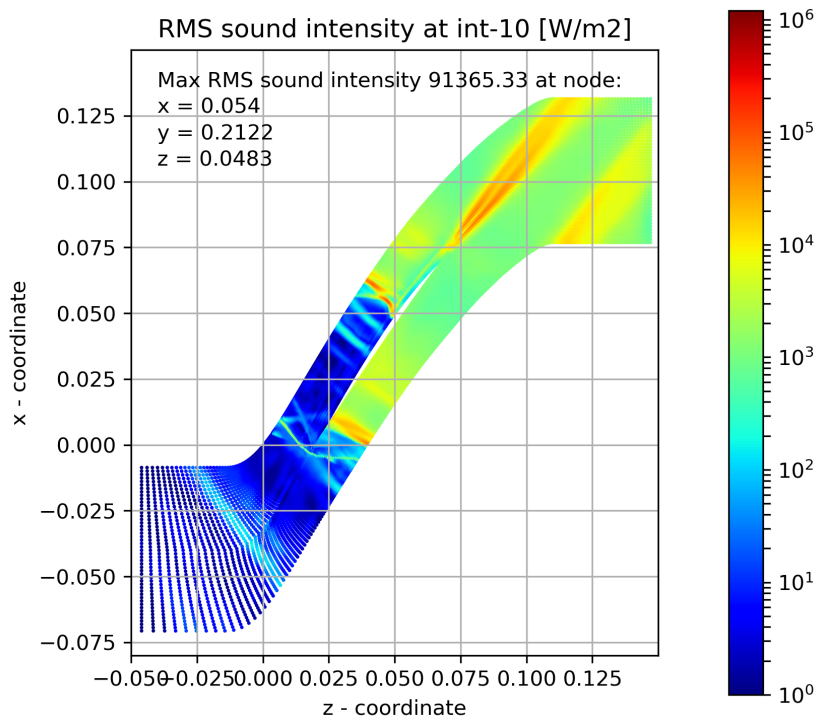


FIGURE A.41: RMS Sound intensity at int-10 mark

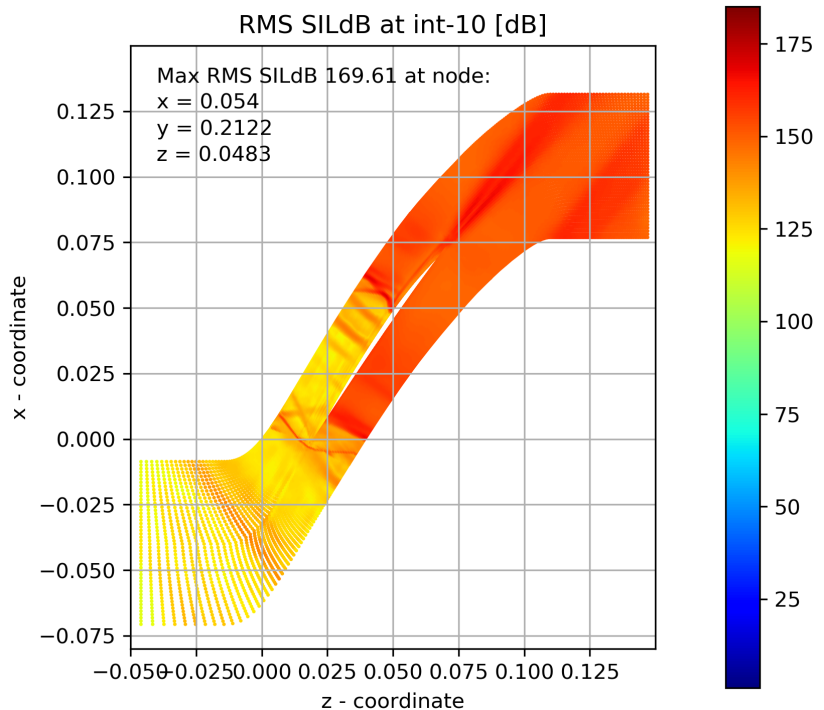


FIGURE A.42: RMS Sound intensity decibel level at int-10 mark

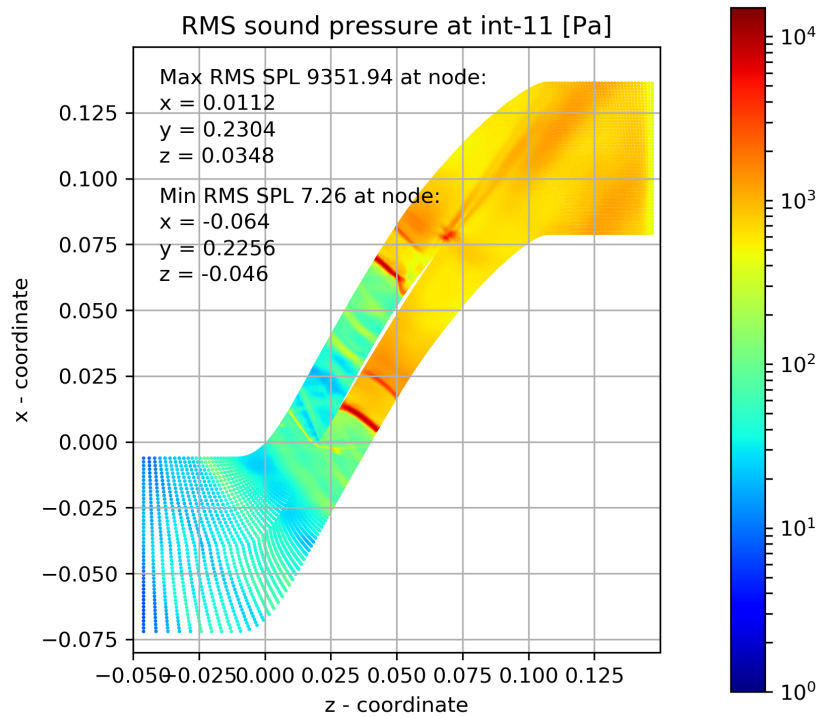


FIGURE A.43: RMS Sound pressure at int-11 mark

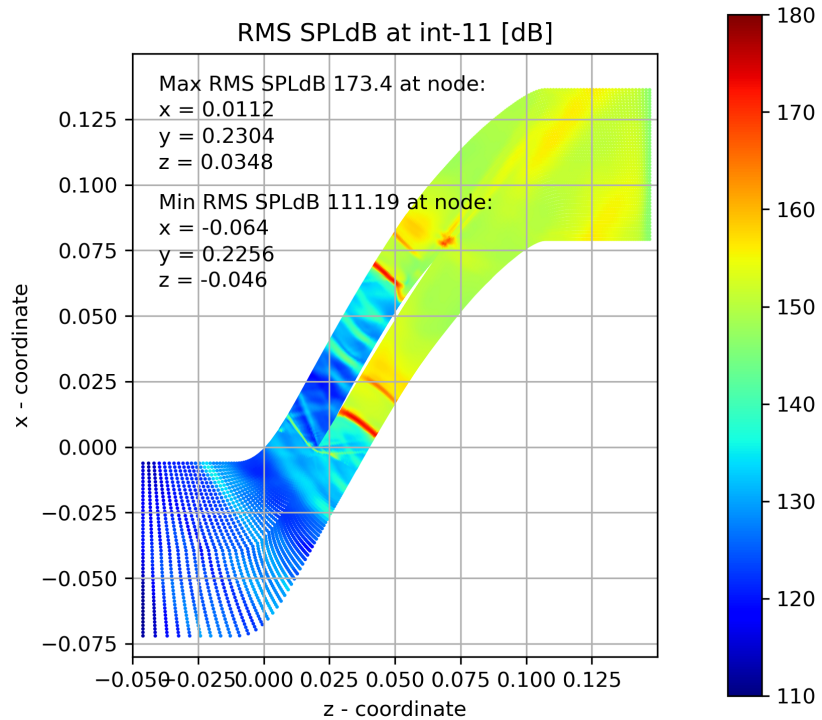


FIGURE A.44: RMS Sound pressure decibel level at int-11 mark

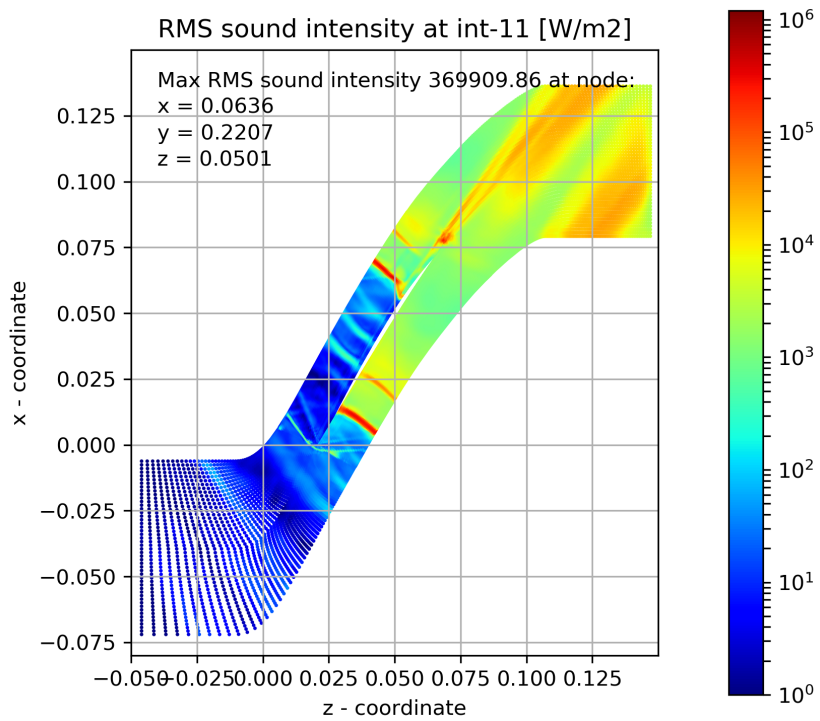


FIGURE A.45: RMS Sound intensity at int-11 mark

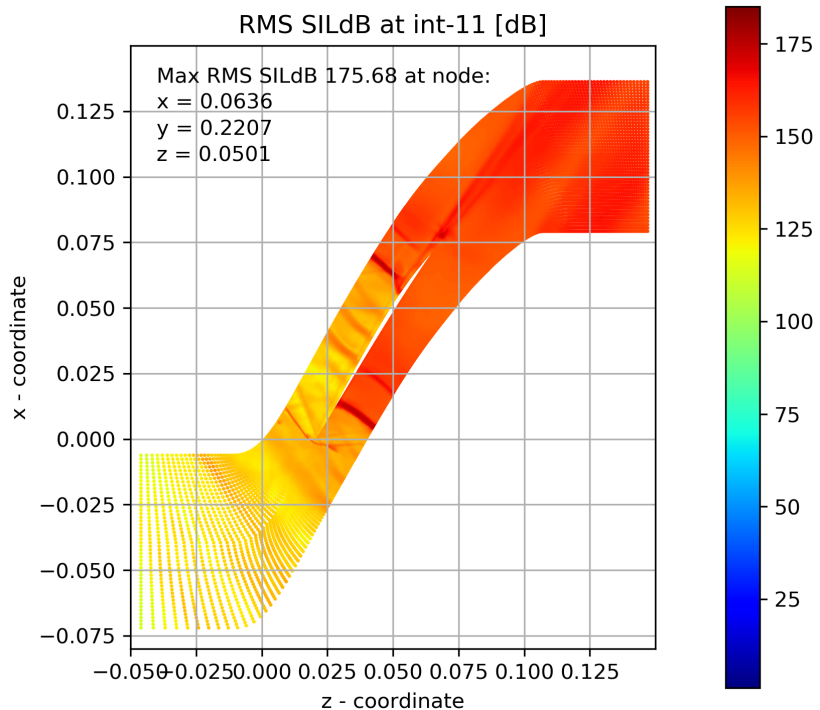


FIGURE A.46: RMS Sound intensity decibel level at int-11 mark

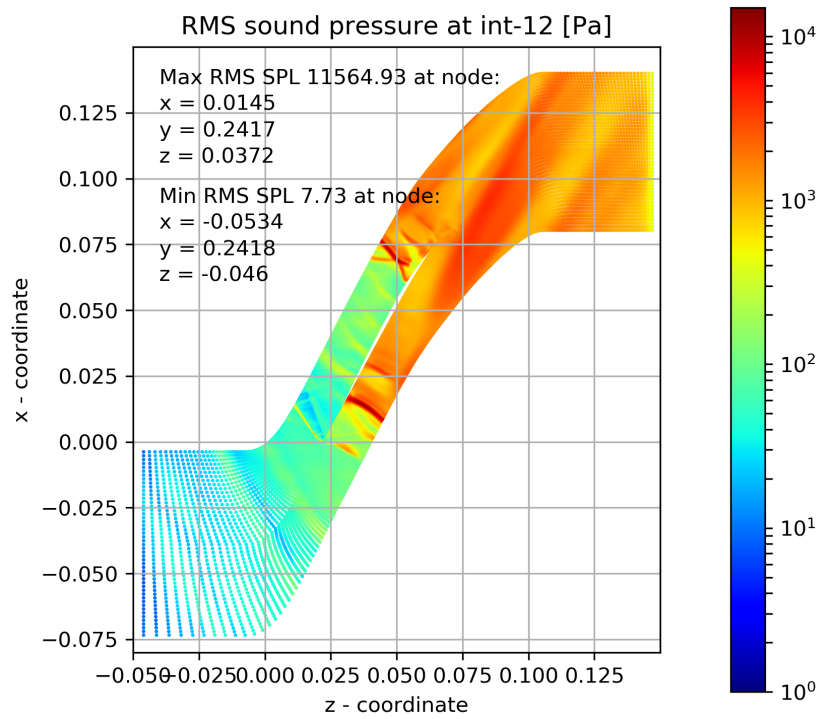


FIGURE A.47: RMS Sound pressure at int-12 mark

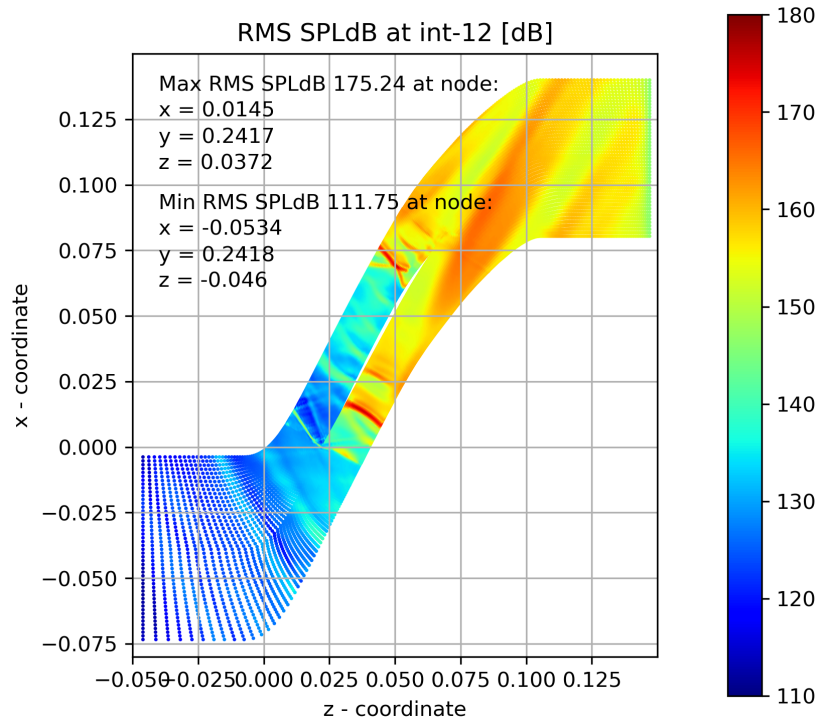


FIGURE A.48: RMS Sound pressure decibel level at int-12 mark

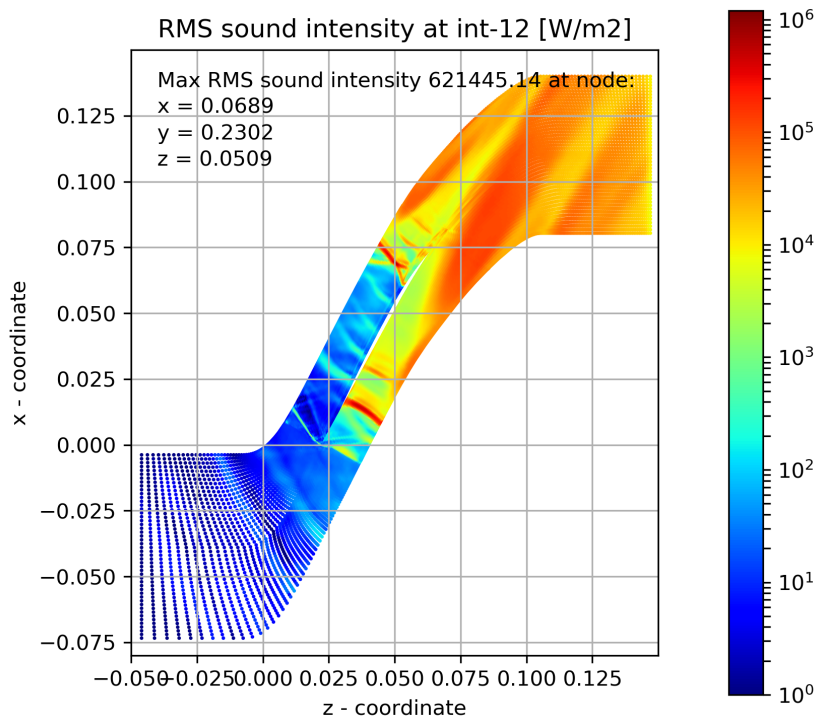


FIGURE A.49: RMS Sound intensity at int-12 mark

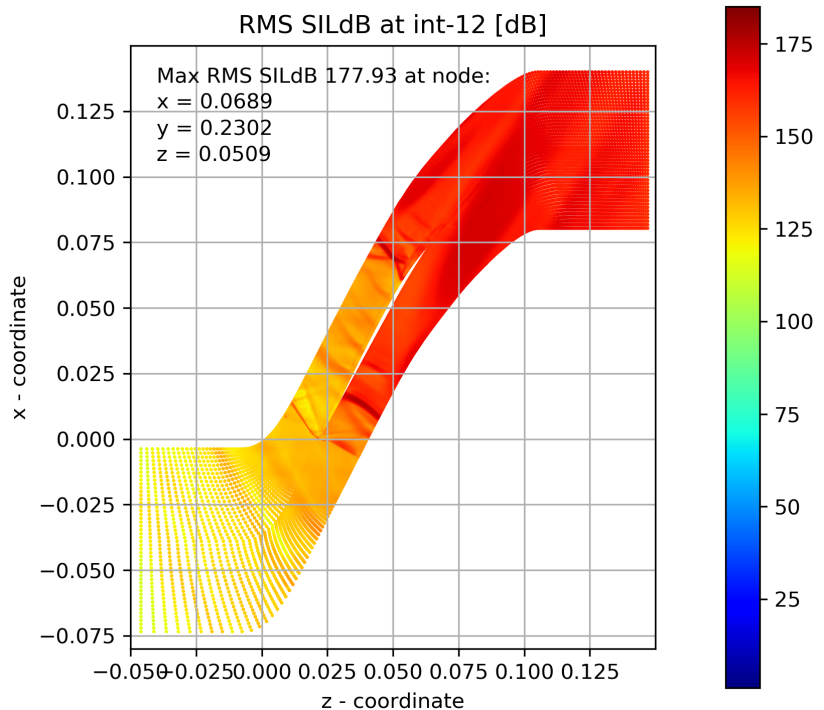


FIGURE A.50: RMS Sound intensity decibel level at int-12 mark

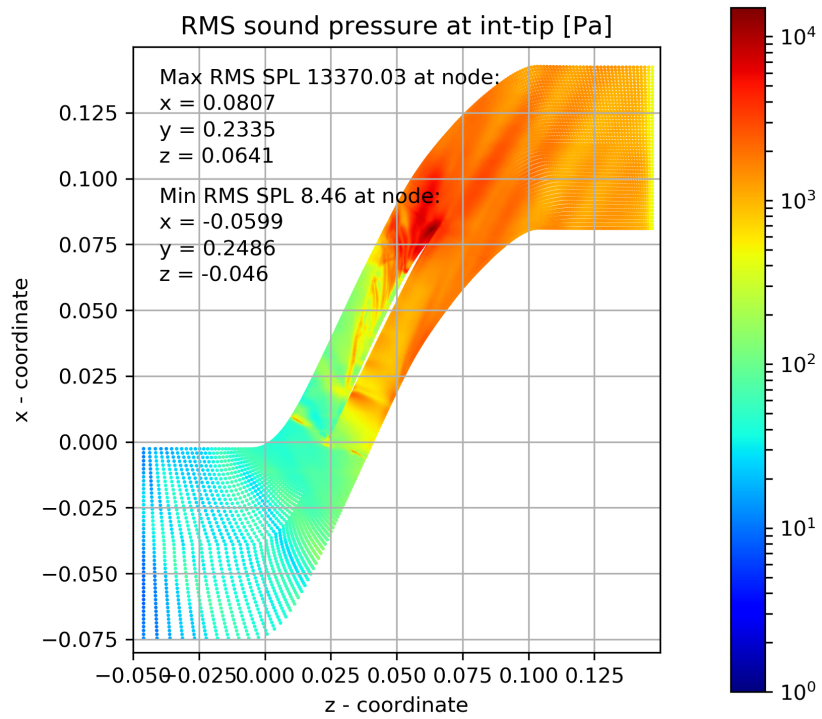


FIGURE A.51: RMS Sound pressure at int-tip mark

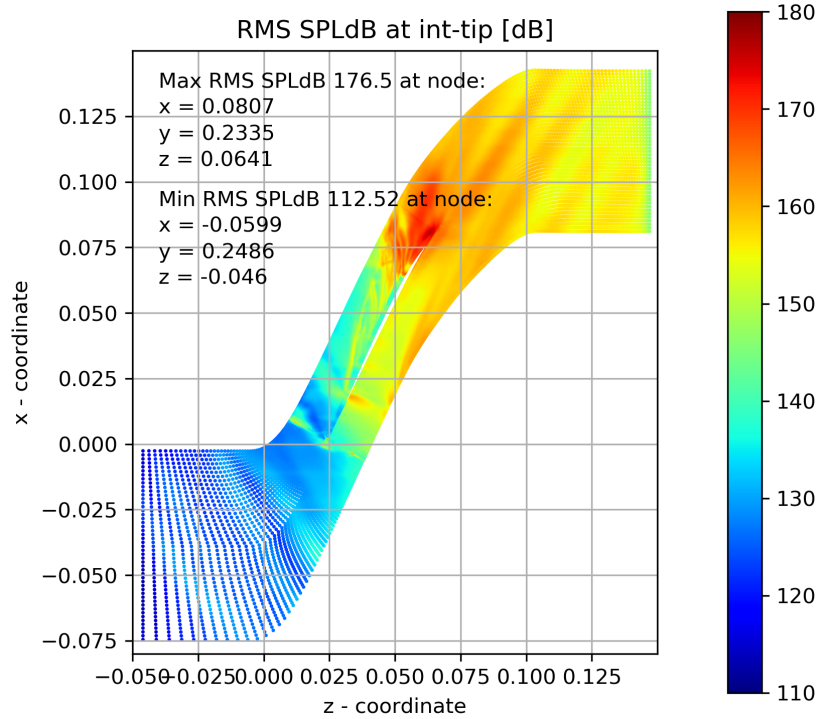


FIGURE A.52: RMS Sound pressure decibel level at int-tip mark

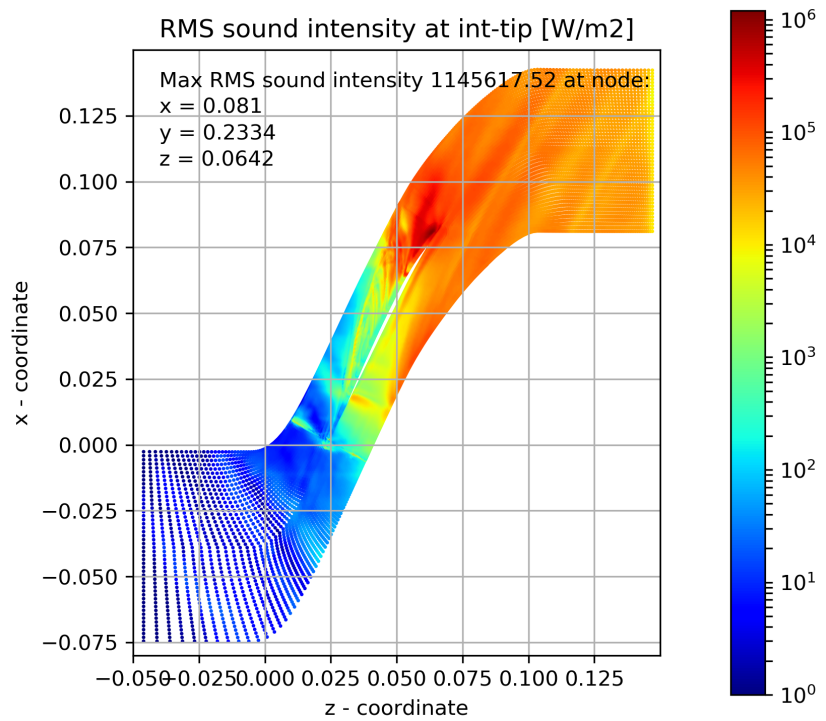


FIGURE A.53: RMS Sound intensity at int-tip mark

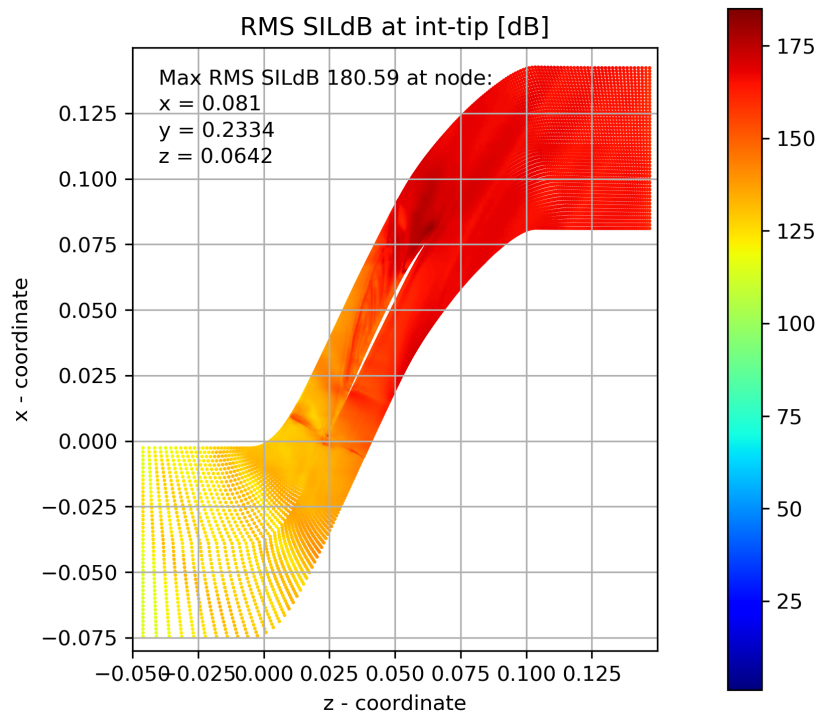


FIGURE A.54: RMS Sound intensity decibel level at int-tip mark

Appendix B

FFT plots

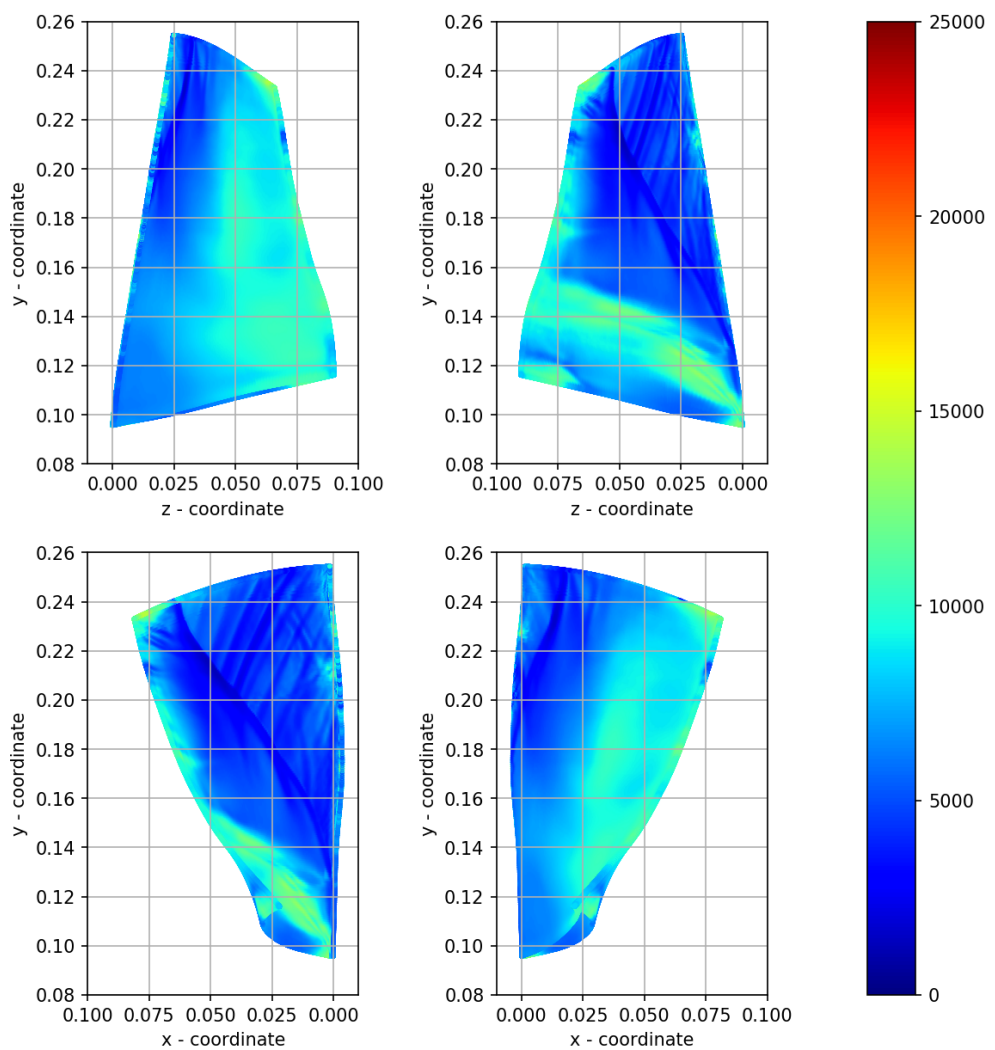


FIGURE B.1: Blade surface amplitude weighted average frequency [dB]

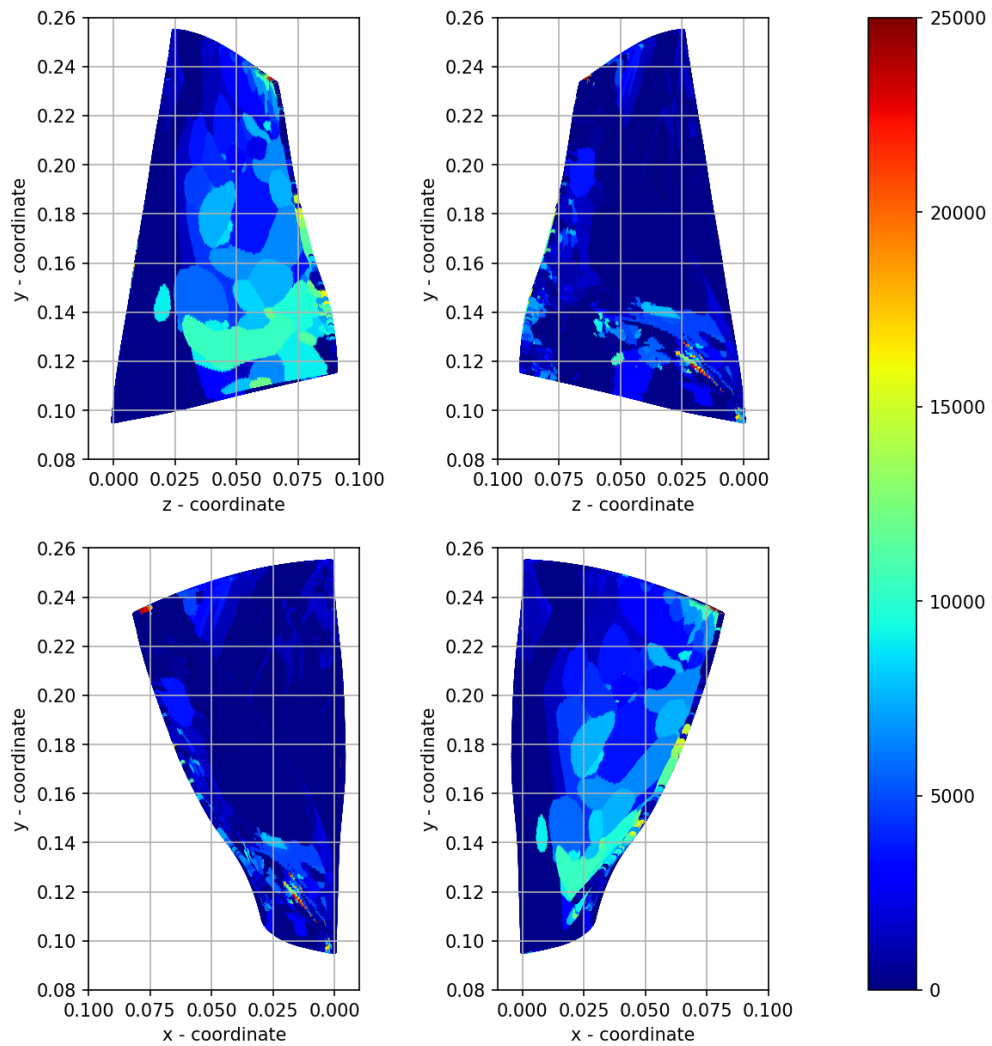


FIGURE B.2: Blade surface frequency of peak amplitude[Hz]

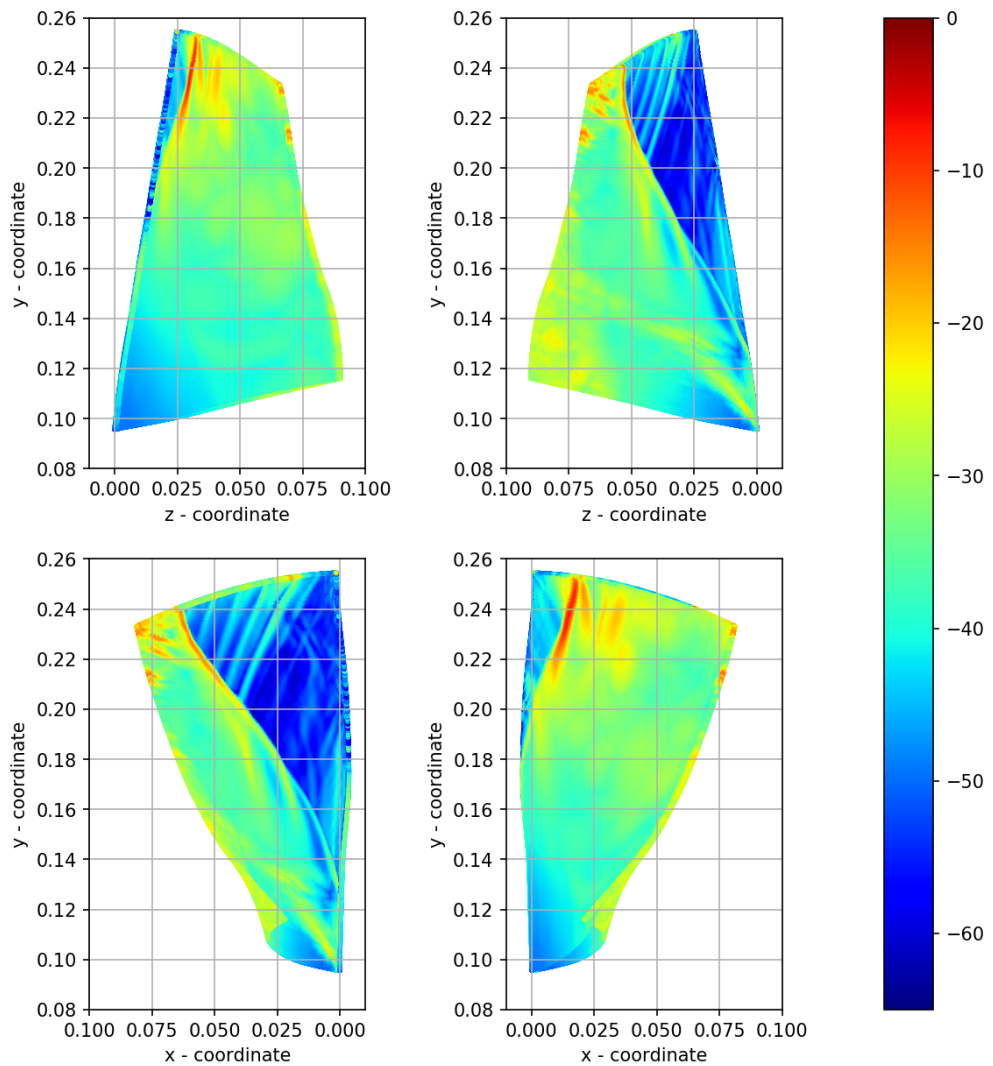


FIGURE B.3: Blade surface peak amplitude [dB]

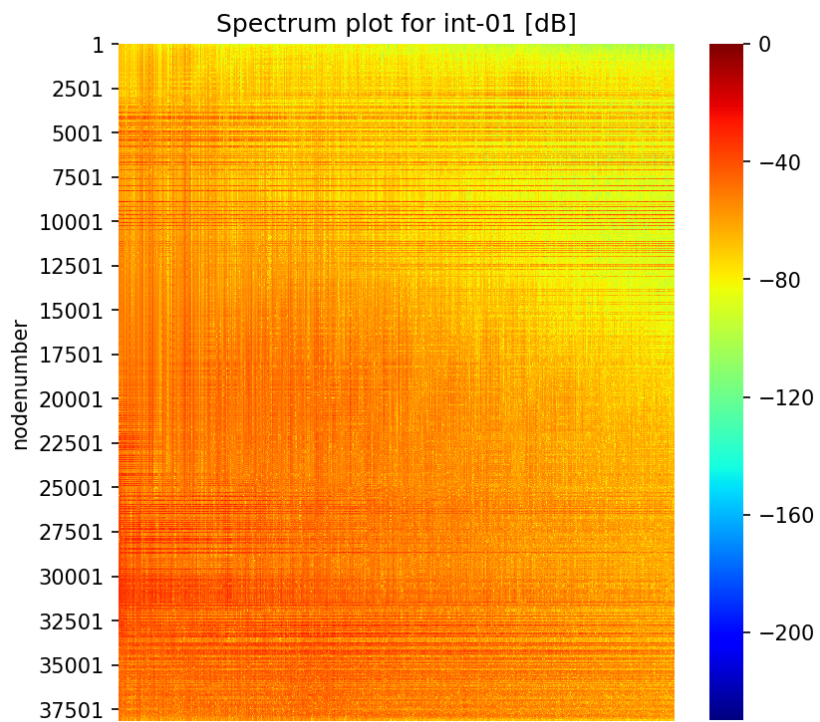


FIGURE B.4: Spectrum plot at int-01 mark

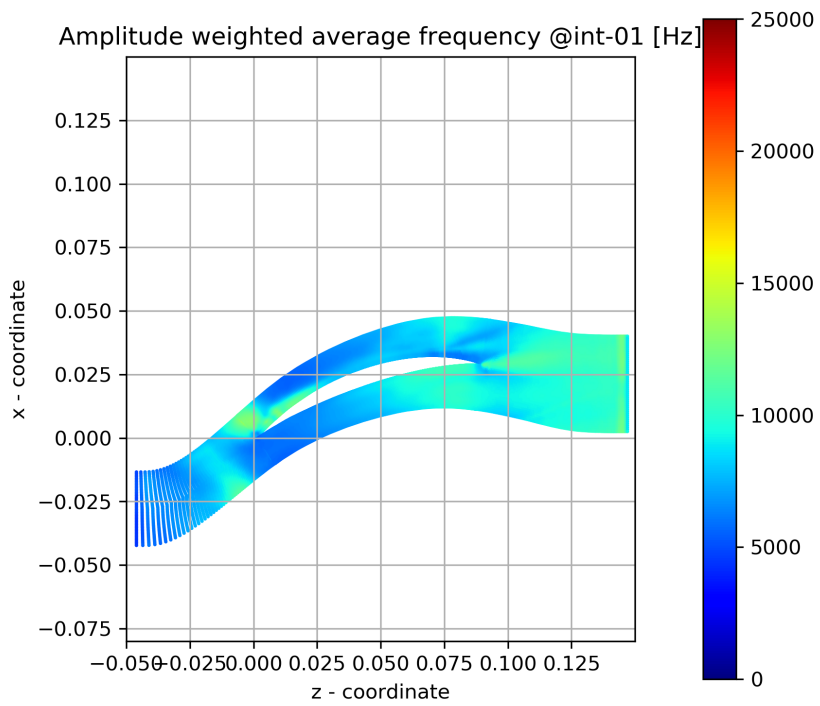


FIGURE B.5: Amplitude weighted average frequency at int-01 mark

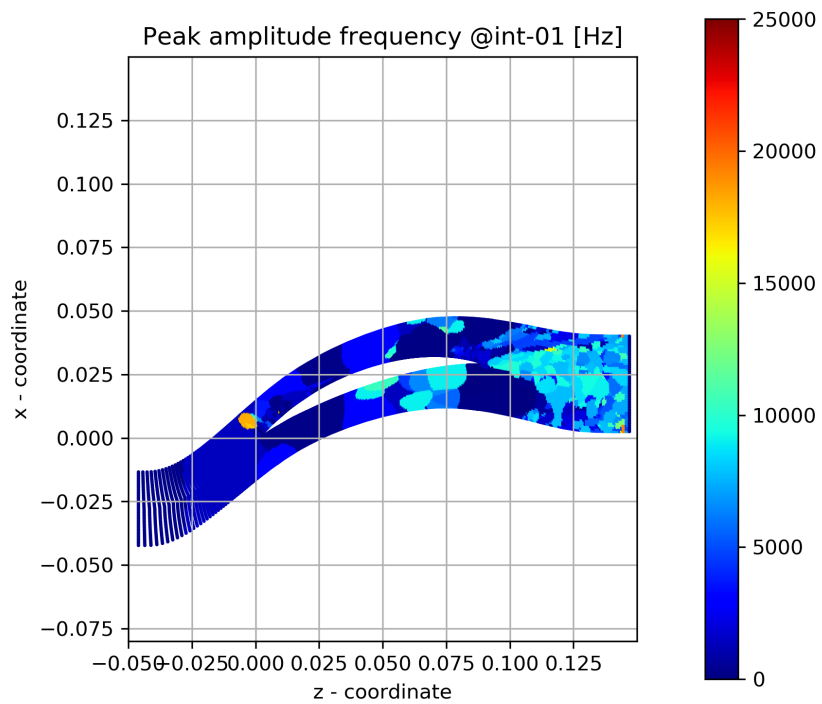


FIGURE B.6: Peak amplitude frequency int-01 mark

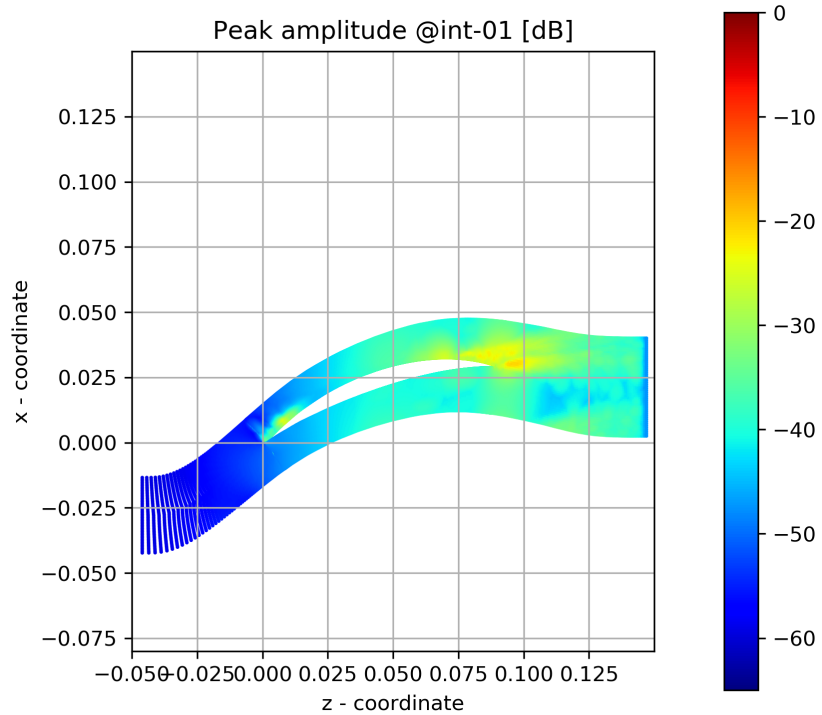


FIGURE B.7: Peak magnitude at int-01 mark

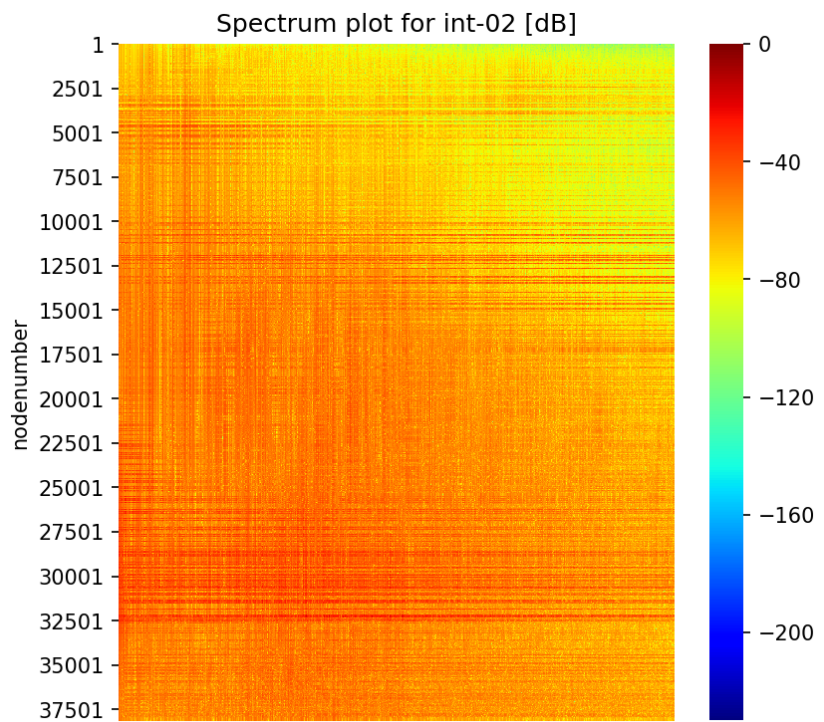


FIGURE B.8: Spectrum plot at int-02 mark

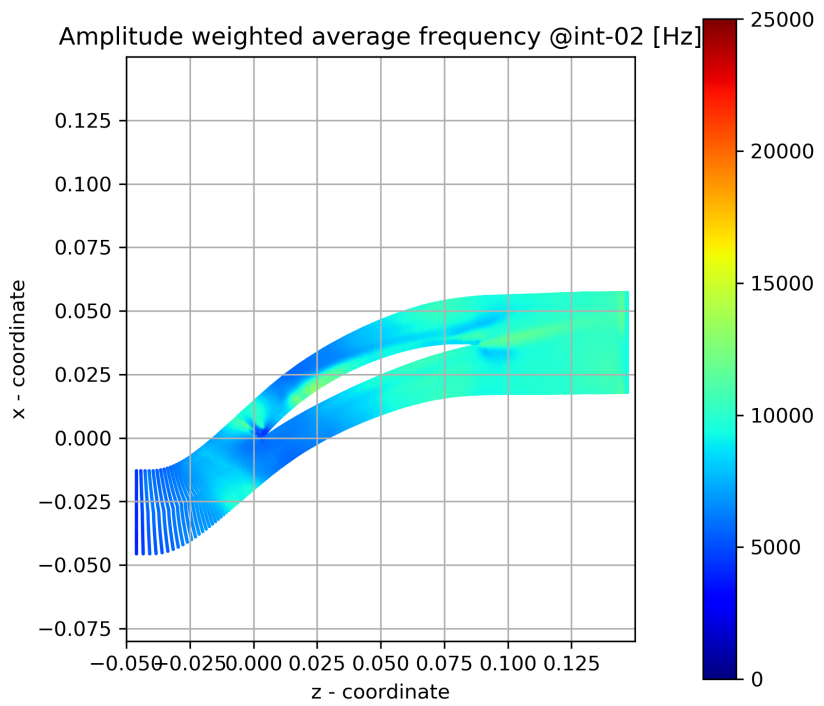


FIGURE B.9: Amplitude weighted average frequency at int-02 mark

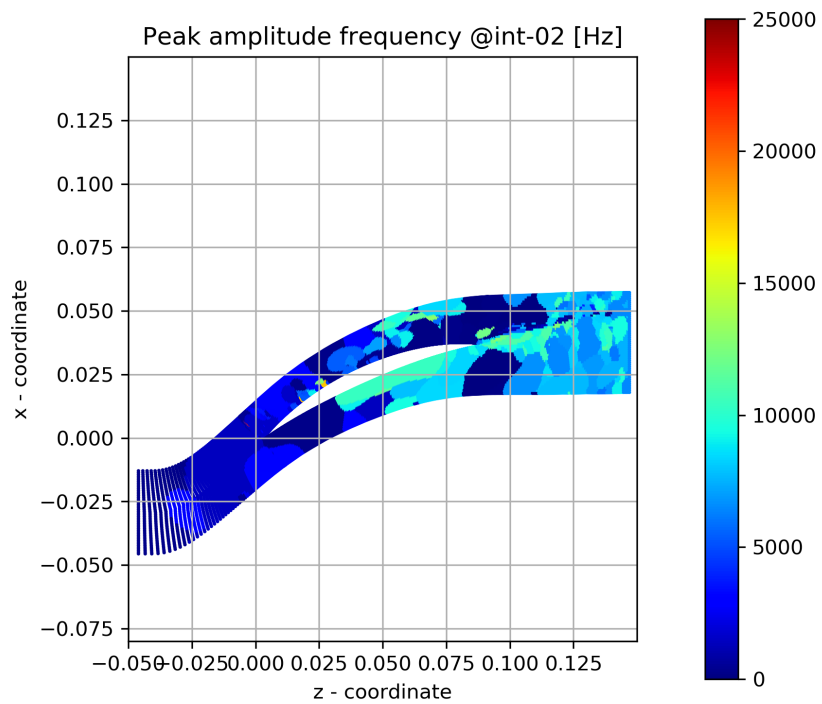


FIGURE B.10: Peak amplitude frequency int-02 mark

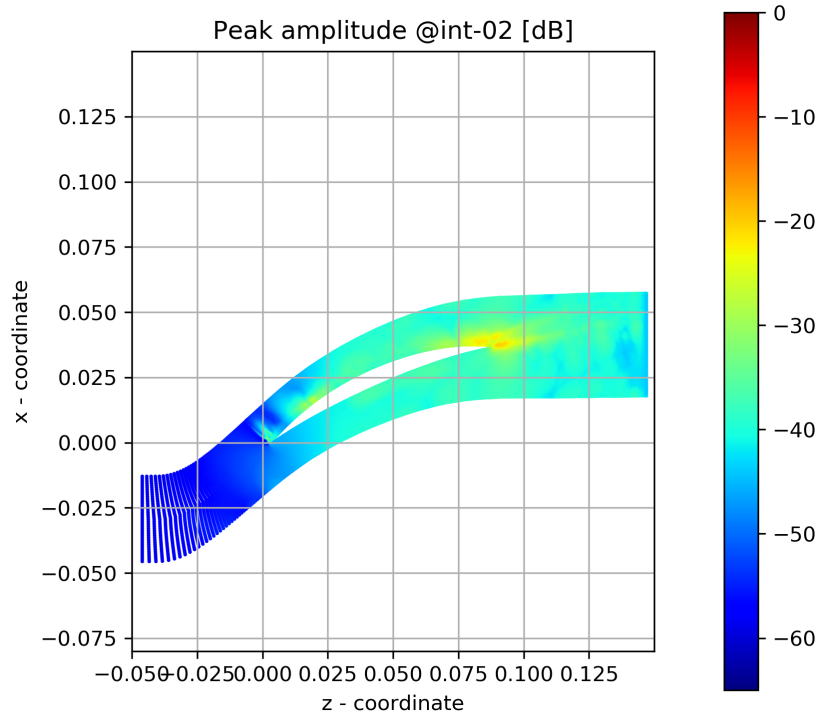


FIGURE B.11: Peak magnitude at int-02 mark

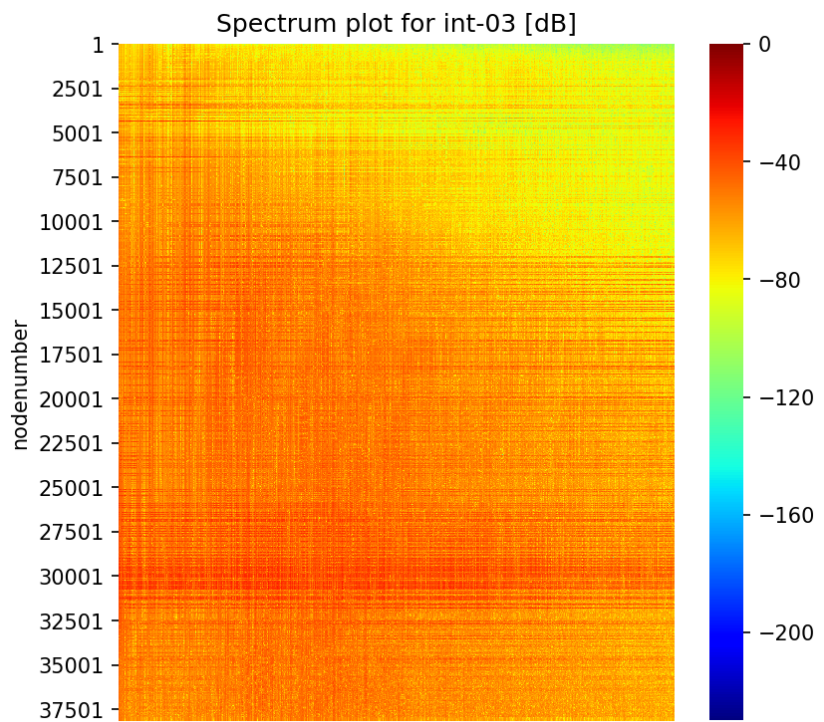


FIGURE B.12: Spectrum plot at int-03 mark

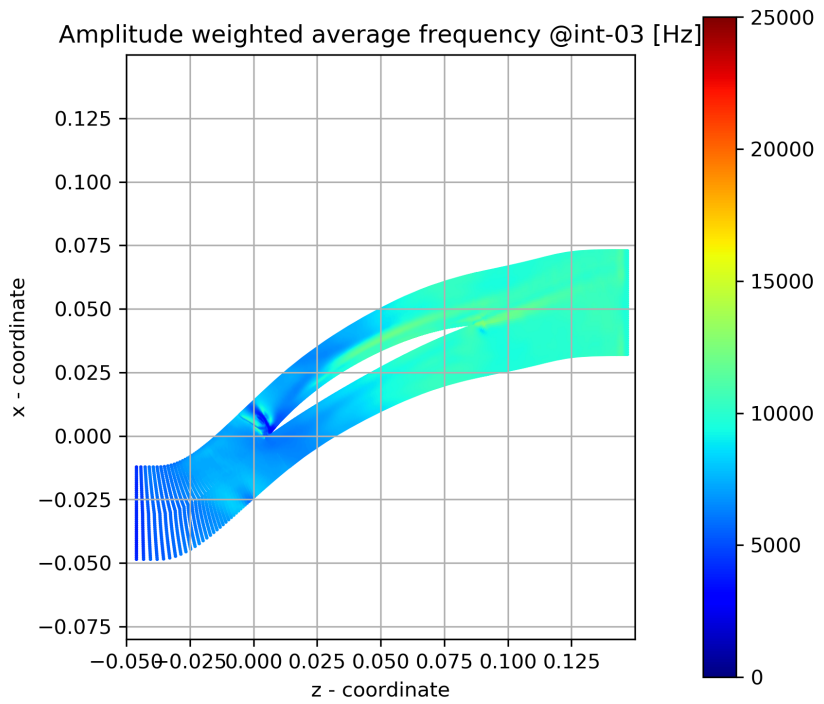


FIGURE B.13: Amplitude weighted average frequency at int-03 mark

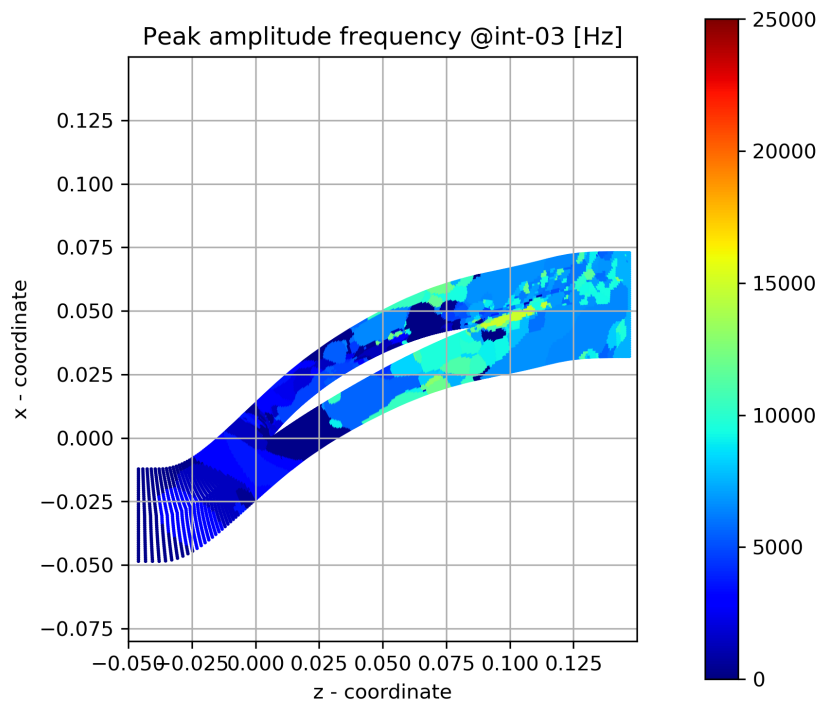


FIGURE B.14: Peak amplitude frequency int-03 mark

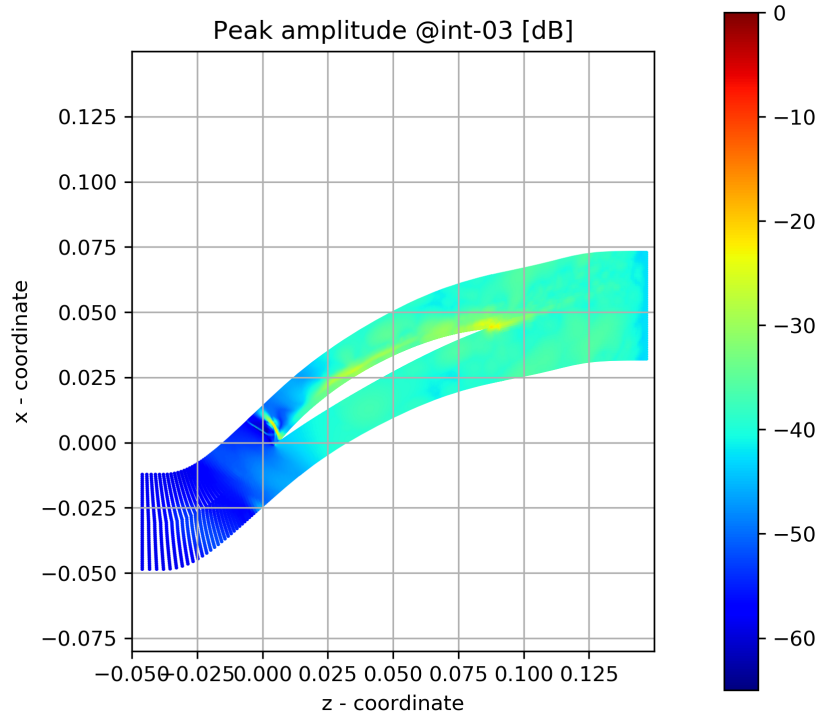


FIGURE B.15: Peak magnitude at int-03 mark

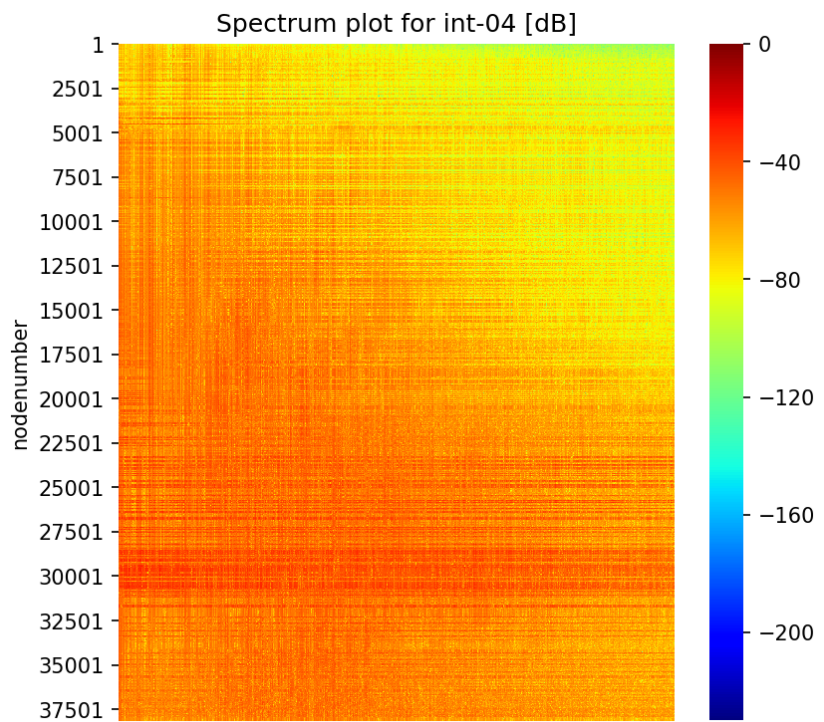


FIGURE B.16: Spectrum plot at int-04 mark

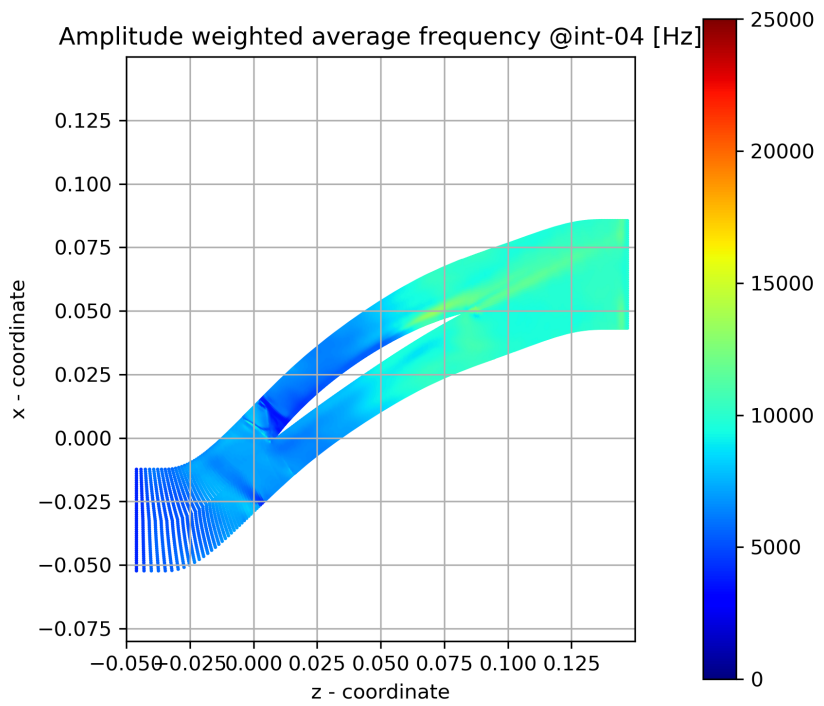


FIGURE B.17: Amplitude weighted average frequency at int-04 mark

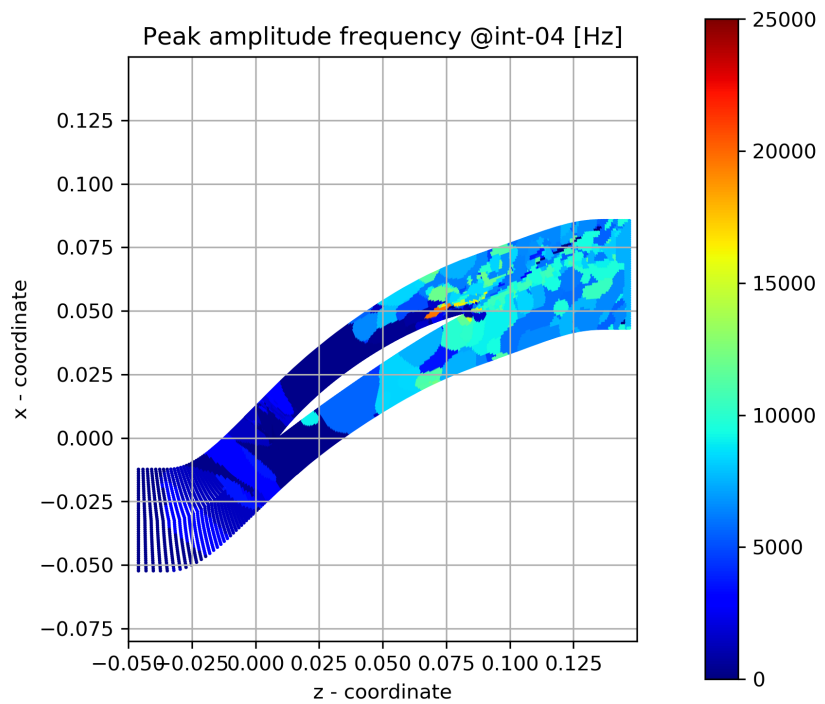


FIGURE B.18: Peak amplitude frequency int-04 mark

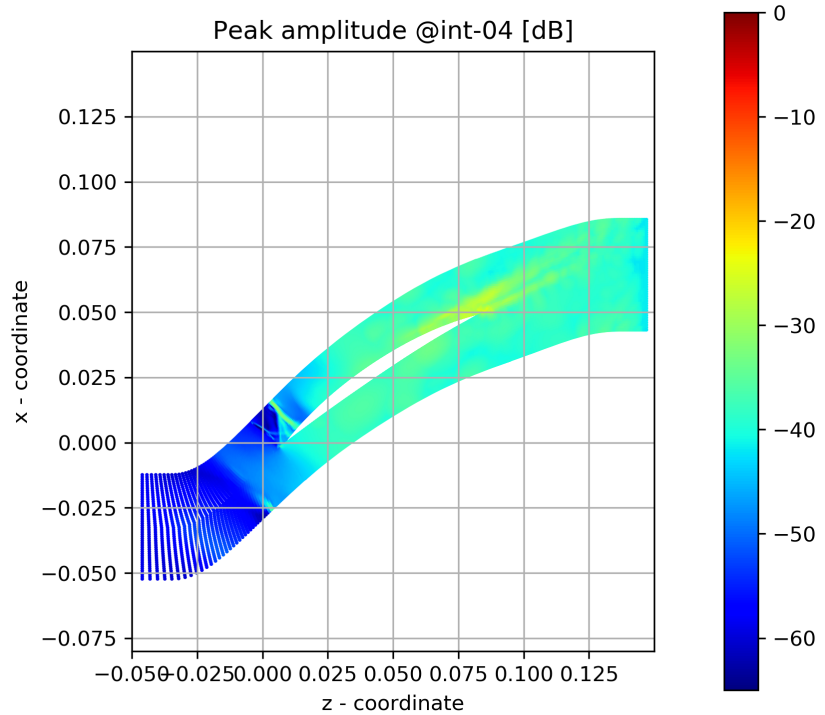


FIGURE B.19: Peak magnitude at int-04 mark

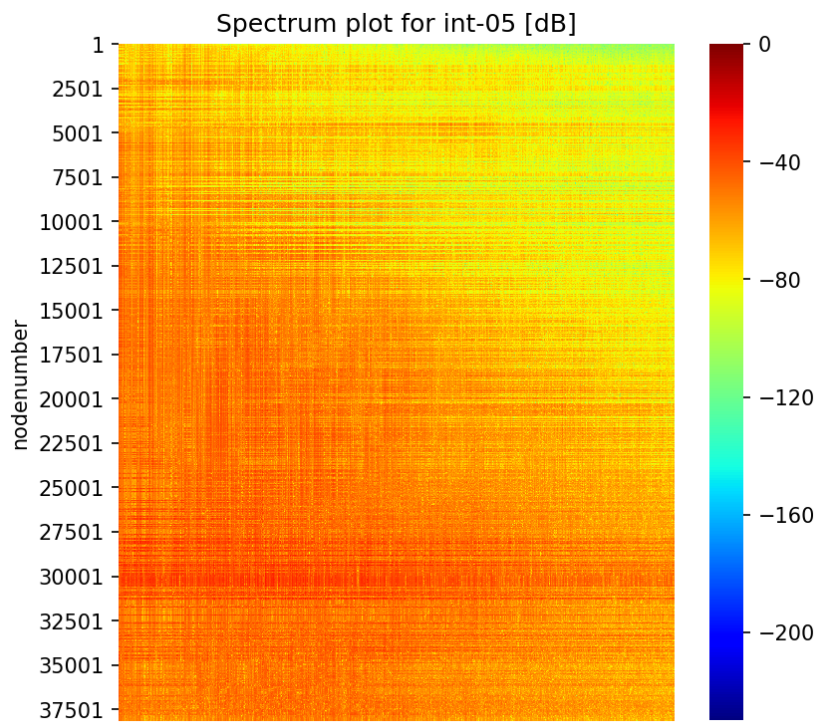


FIGURE B.20: Spectrum plot at int-05 mark

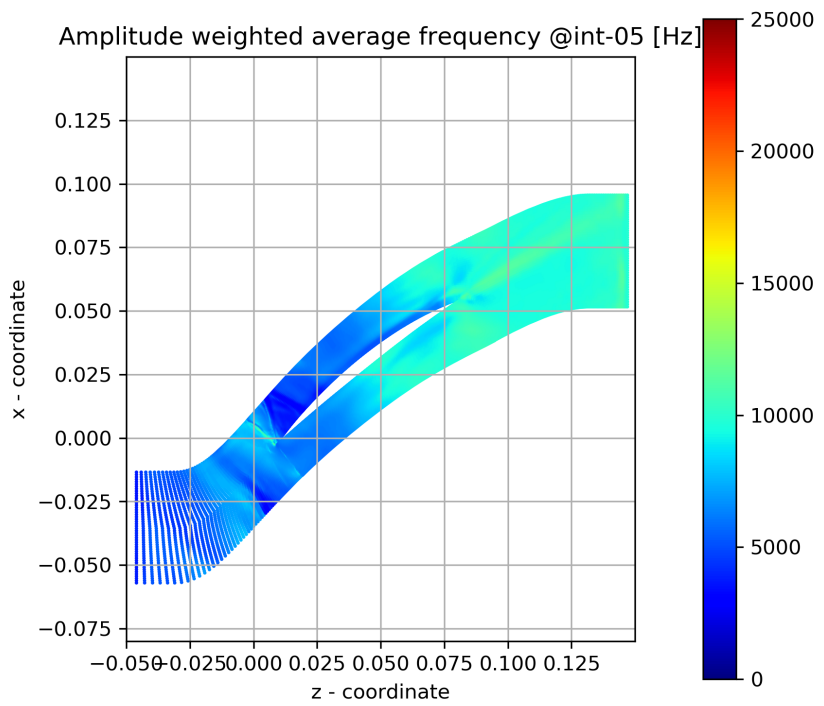


FIGURE B.21: Amplitude weighted average frequency at int-05 mark

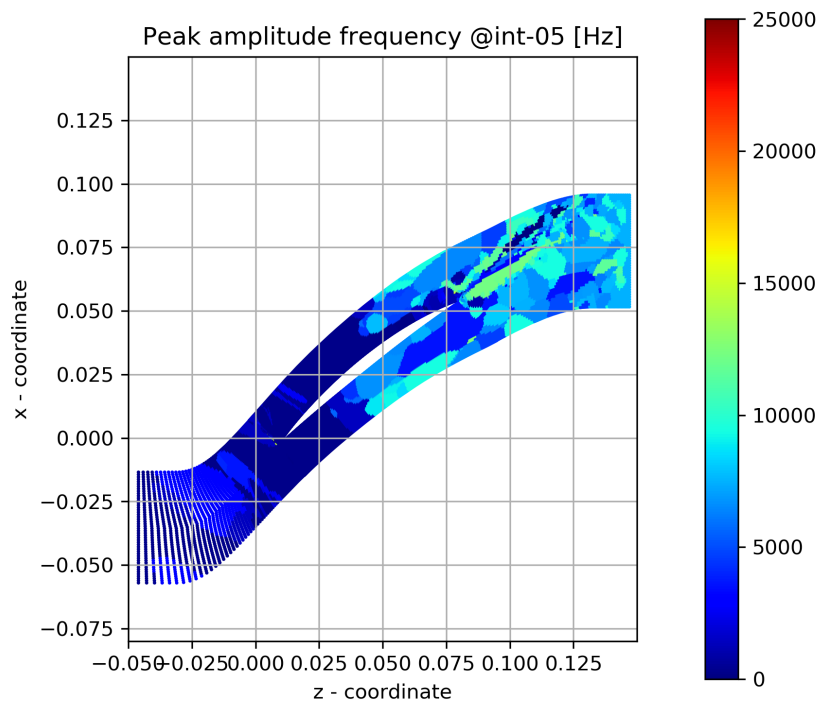


FIGURE B.22: Peak amplitude frequency int-05 mark

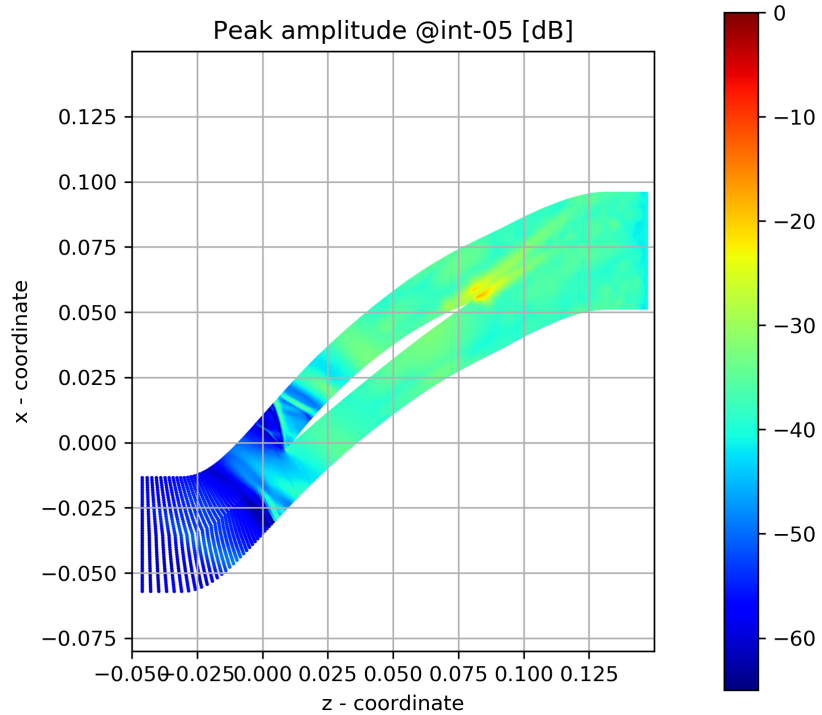


FIGURE B.23: Peak magnitude at int-05 mark

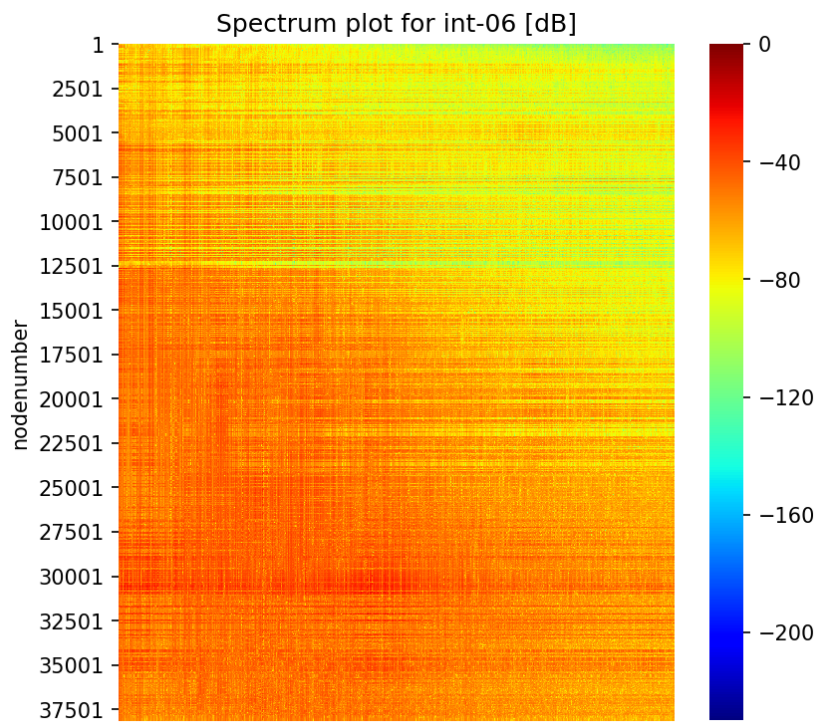


FIGURE B.24: Spectrum plot at int-06 mark

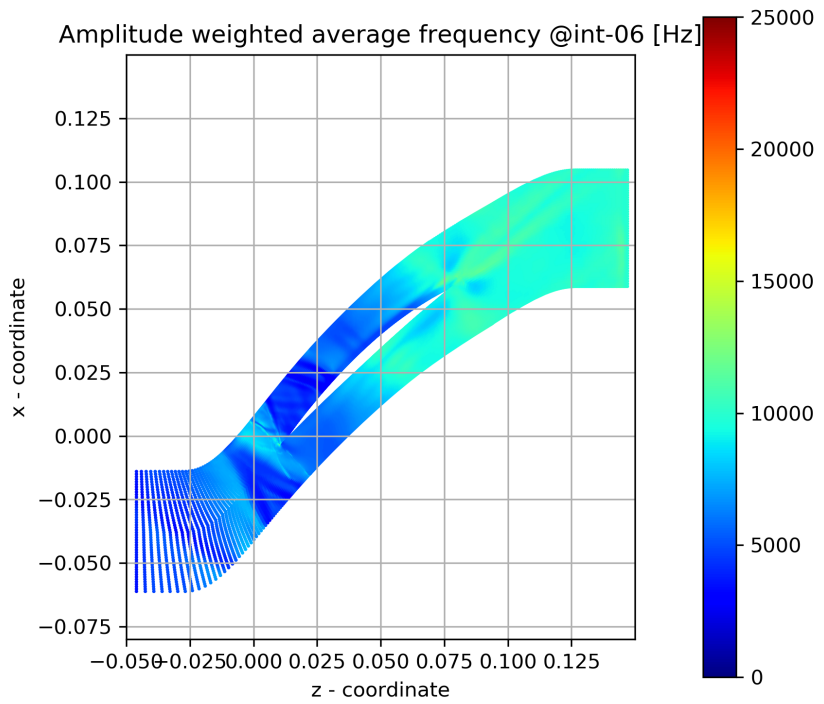


FIGURE B.25: Amplitude weighted average frequency at int-06 mark

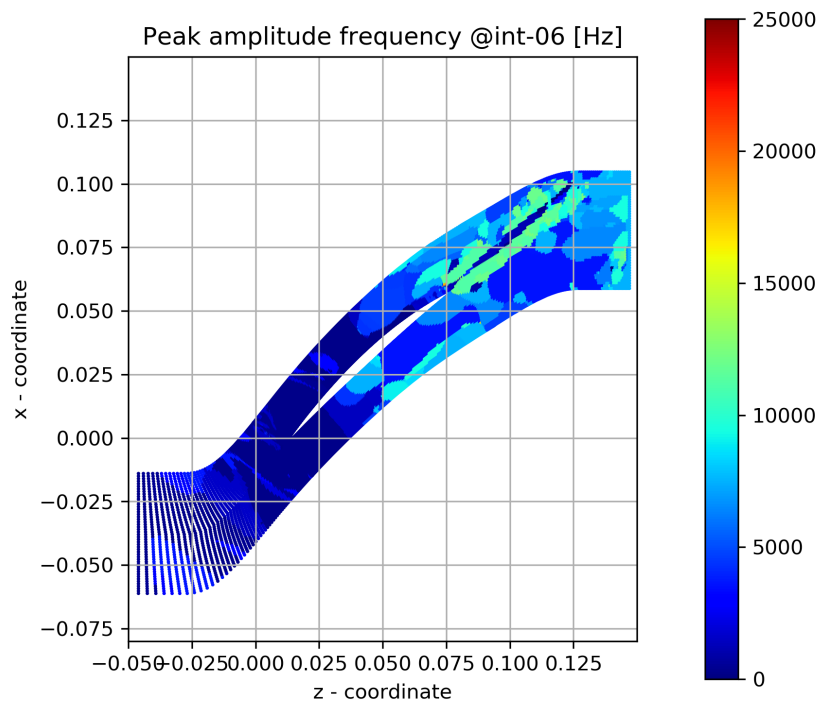


FIGURE B.26: Peak amplitude frequency int-06 mark

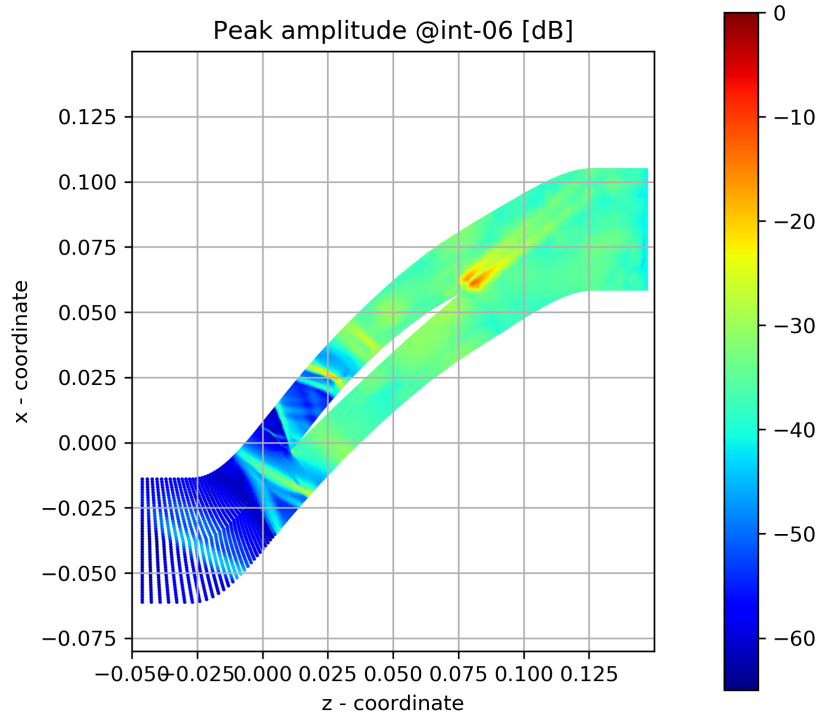


FIGURE B.27: Peak magnitude at int-06 mark

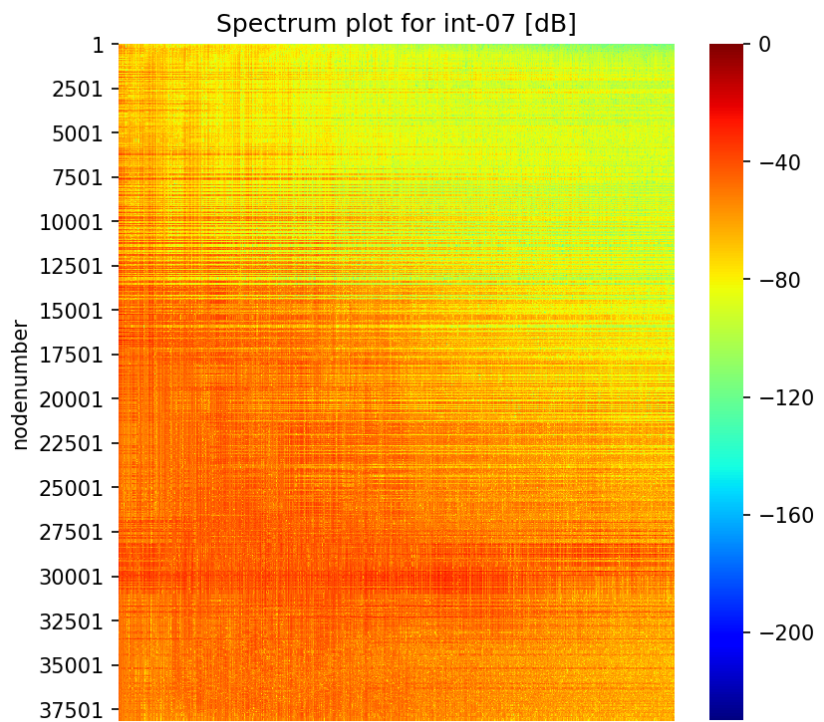


FIGURE B.28: Spectrum plot at int-07 mark

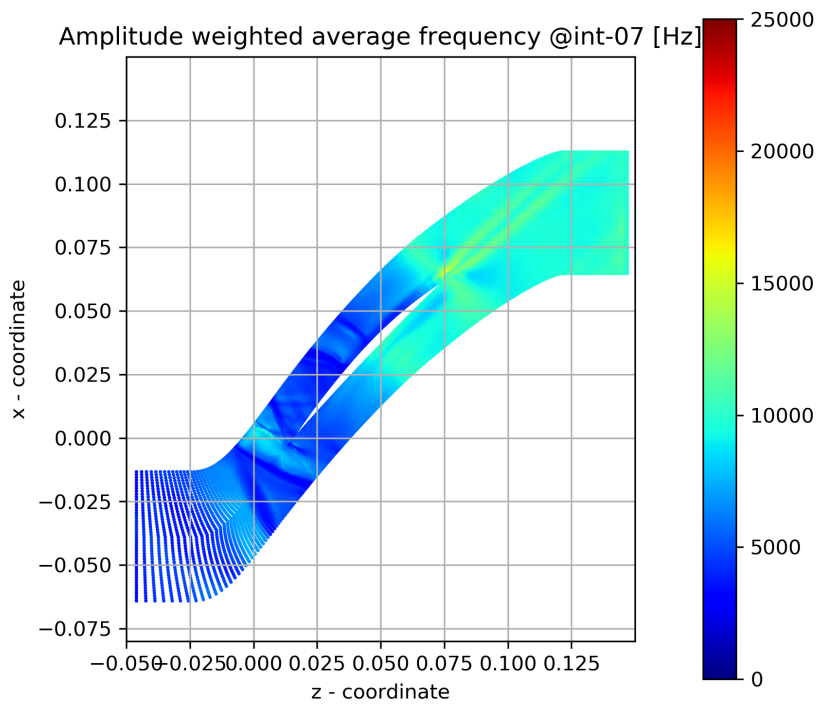


FIGURE B.29: Amplitude weighted average frequency at int-07 mark

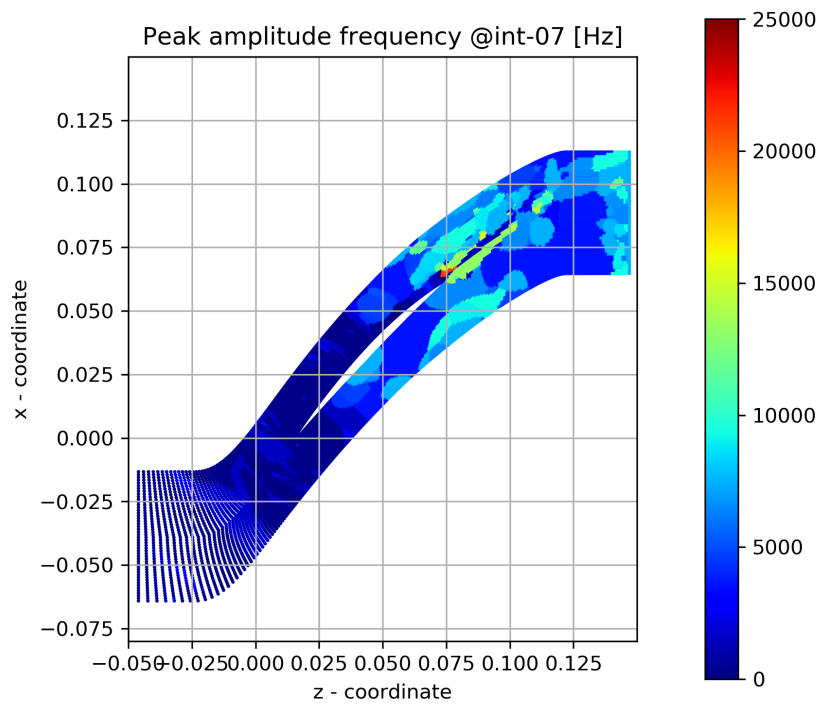


FIGURE B.30: Peak amplitude frequency int-07 mark

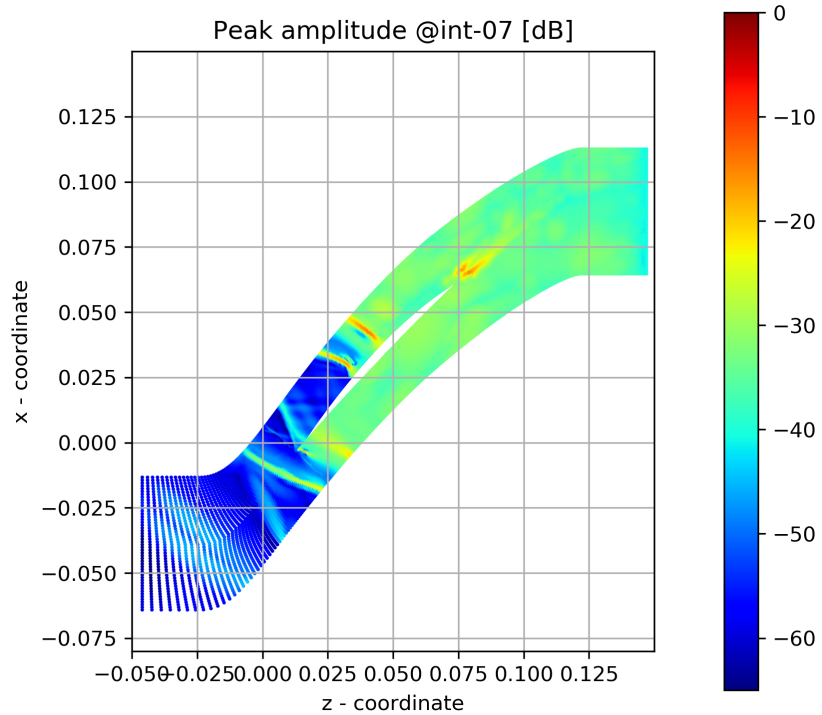


FIGURE B.31: Peak magnitude at int-07 mark

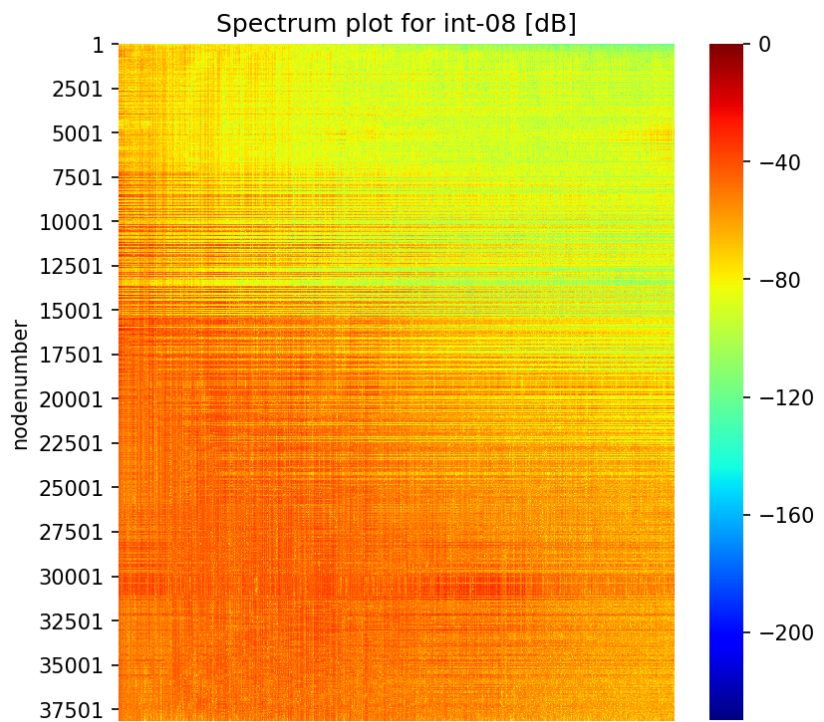


FIGURE B.32: Spectrum plot at int-08 mark

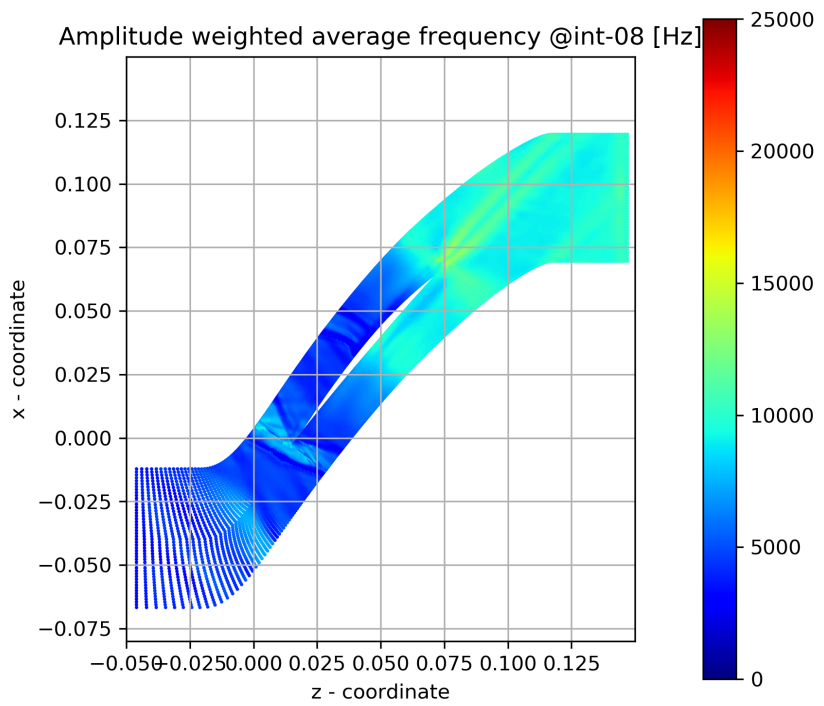


FIGURE B.33: Amplitude weighted average frequency at int-08 mark

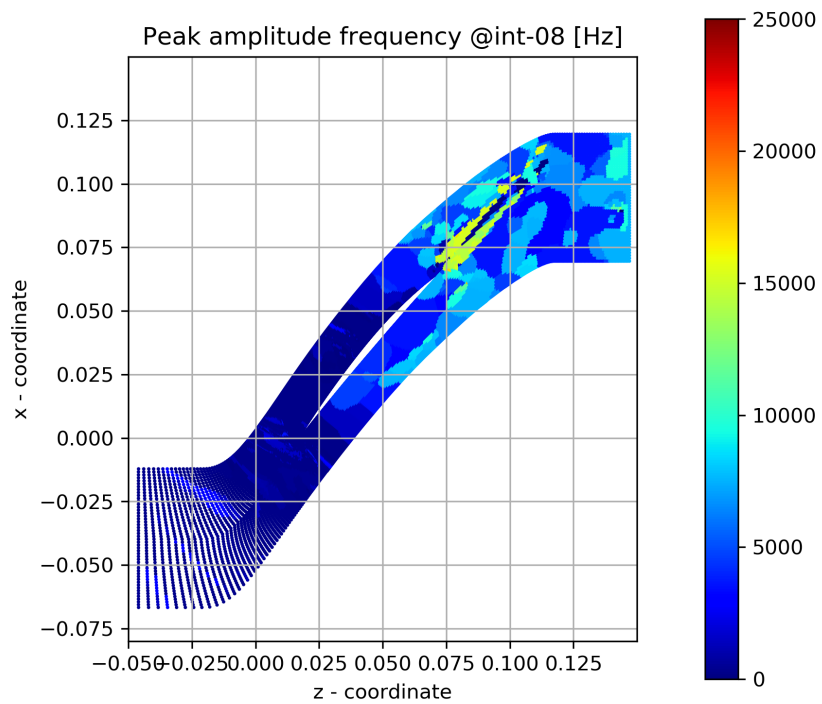


FIGURE B.34: Peak amplitude frequency int-08 mark

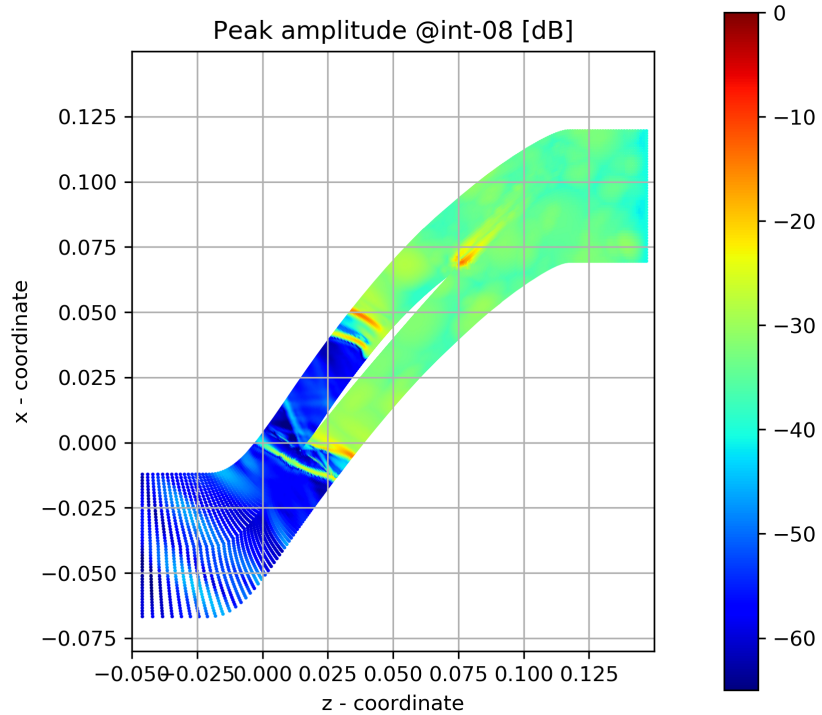


FIGURE B.35: Peak magnitude at int-08 mark

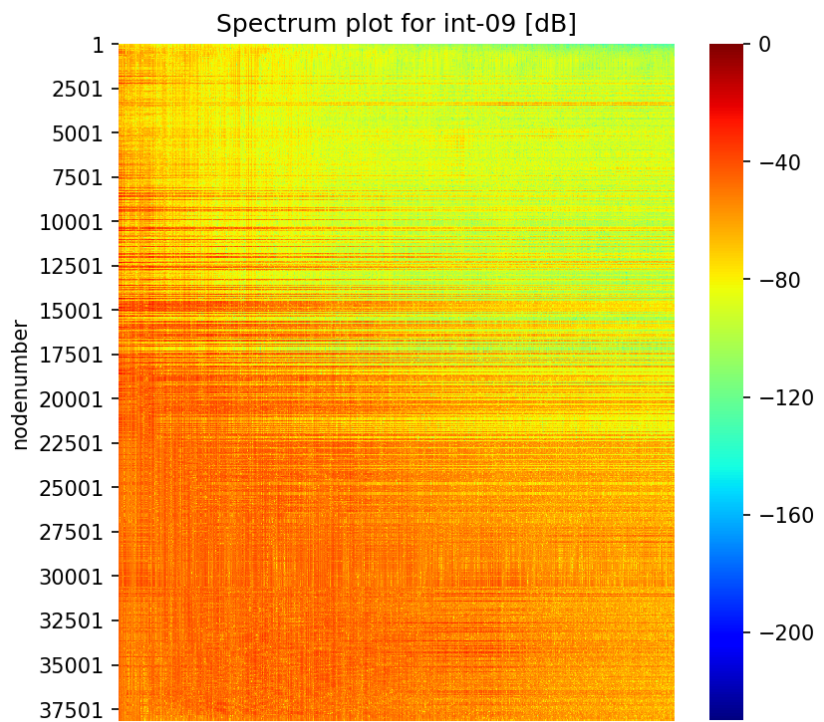


FIGURE B.36: Spectrum plot at int-09 mark

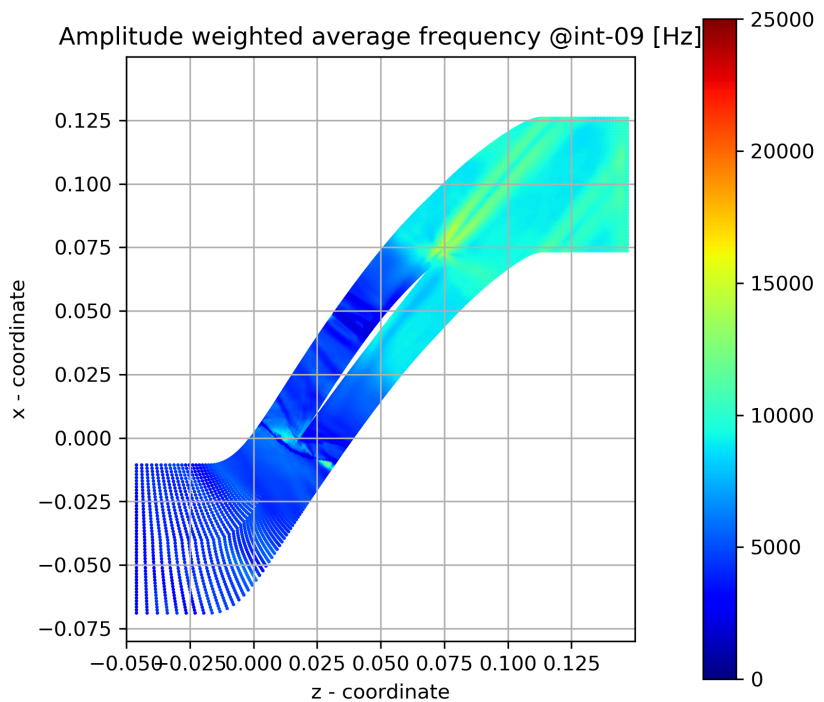


FIGURE B.37: Amplitude weighted average frequency at int-09 mark

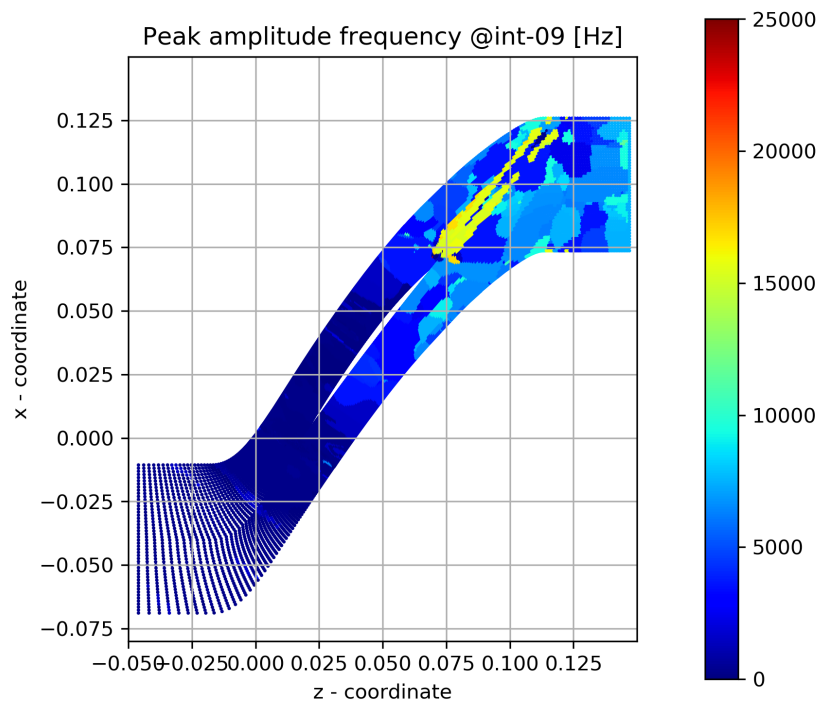


FIGURE B.38: Peak amplitude frequency int-09 mark

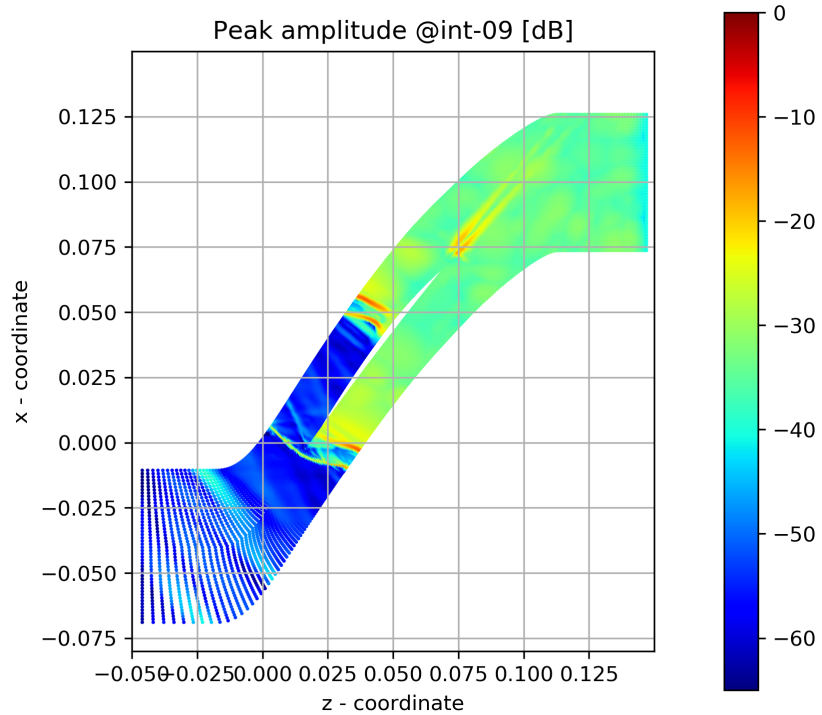


FIGURE B.39: Peak magnitude at int-09 mark

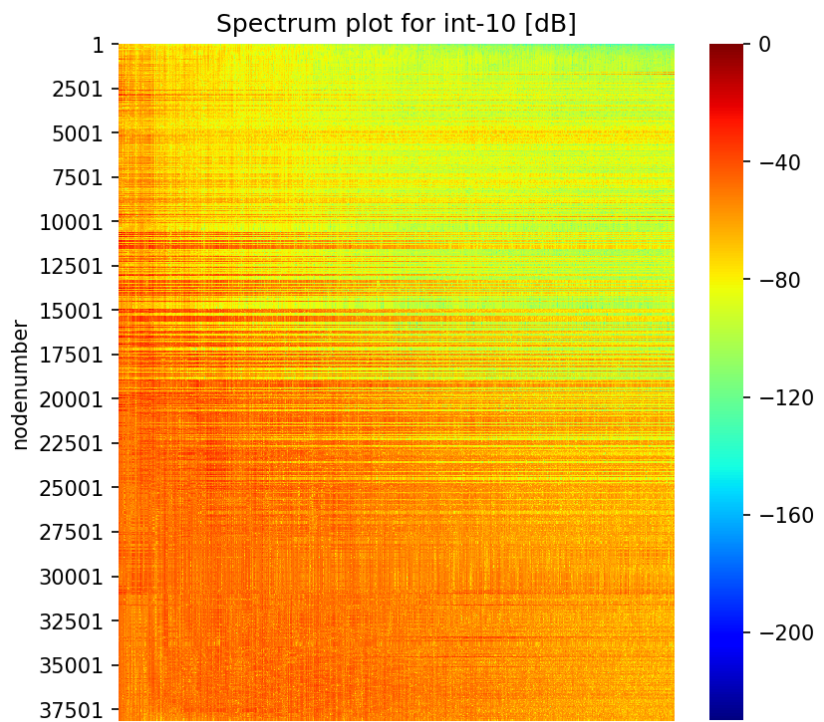


FIGURE B.40: Spectrum plot at int-10 mark

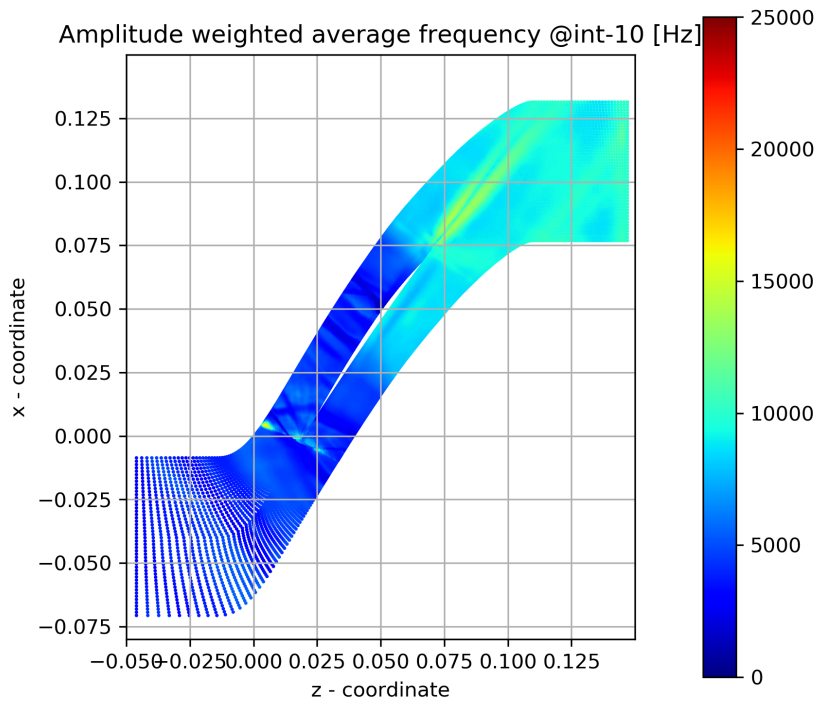


FIGURE B.41: Amplitude weighted average frequency at int-10 mark

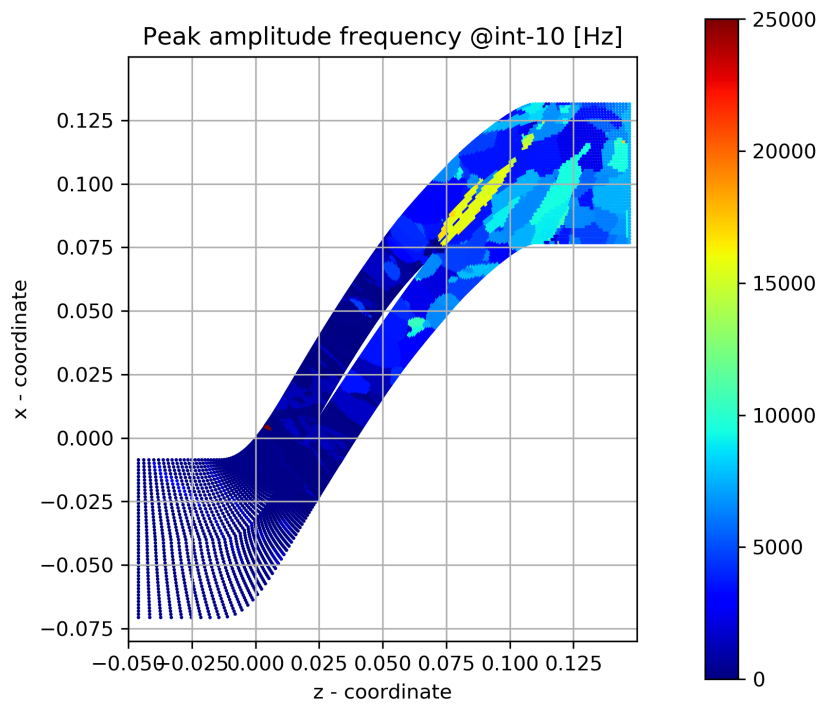


FIGURE B.42: Peak amplitude frequency int-10 mark

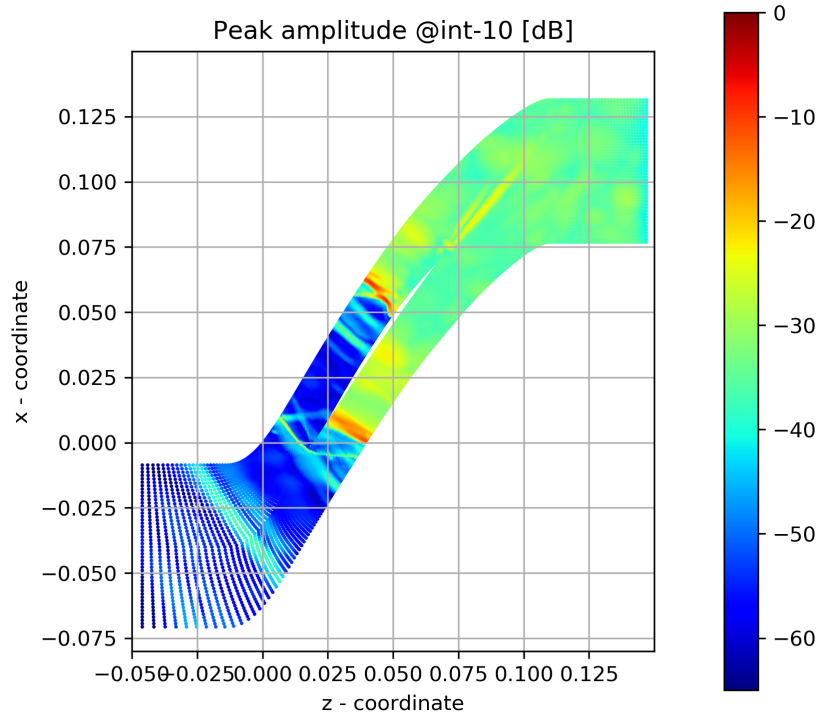


FIGURE B.43: Peak magnitude at int-10 mark

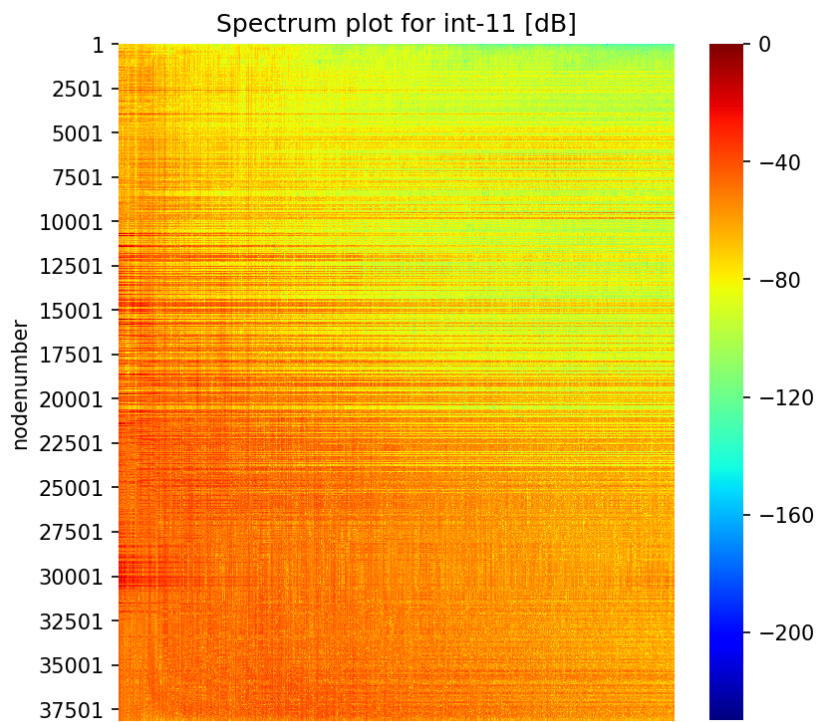


FIGURE B.44: Spectrum plot at int-11 mark

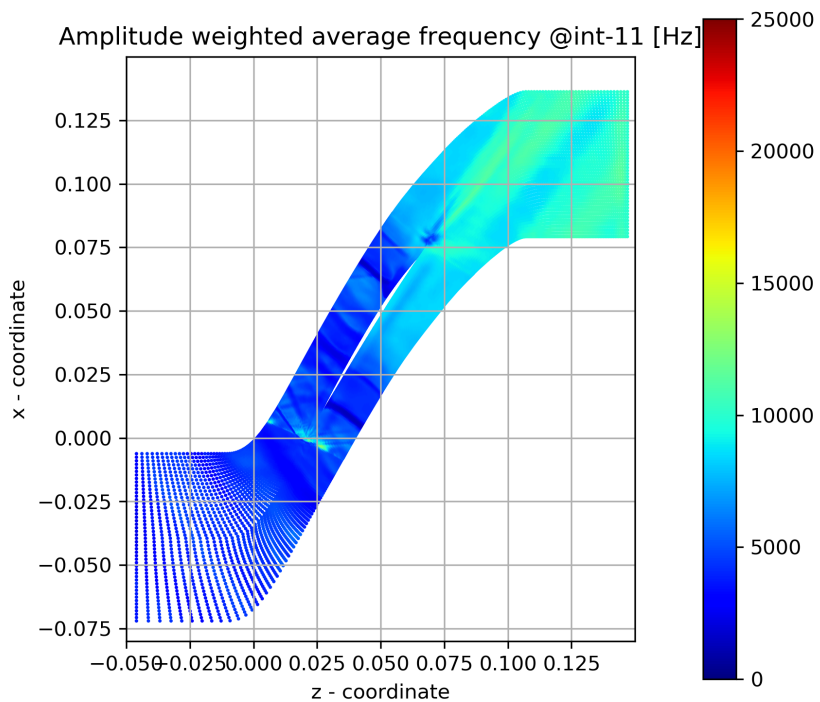


FIGURE B.45: Amplitude weighted average frequency at int-11 mark

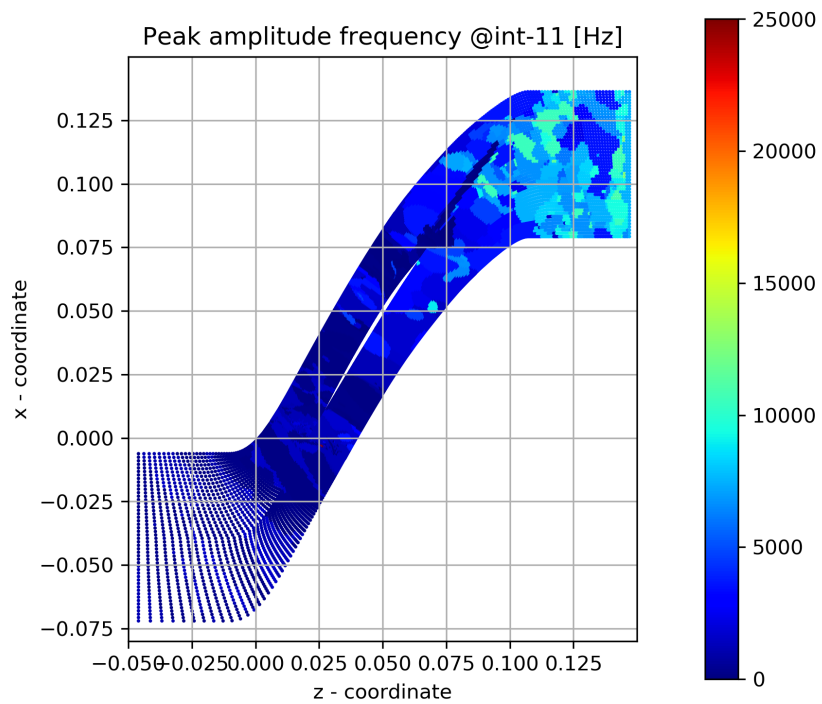


FIGURE B.46: Peak amplitude frequency int-11 mark

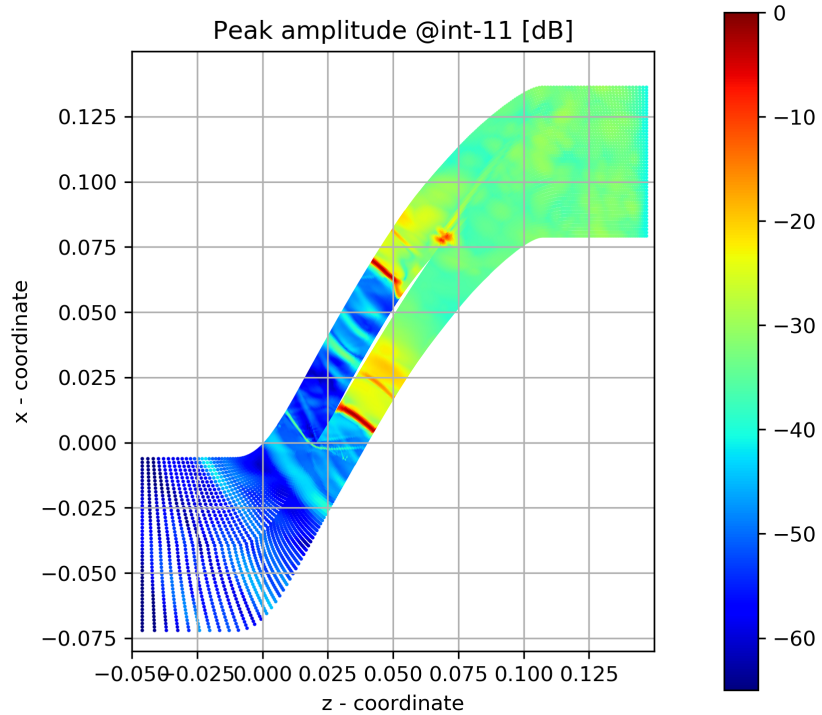


FIGURE B.47: Peak magnitude at int-11 mark

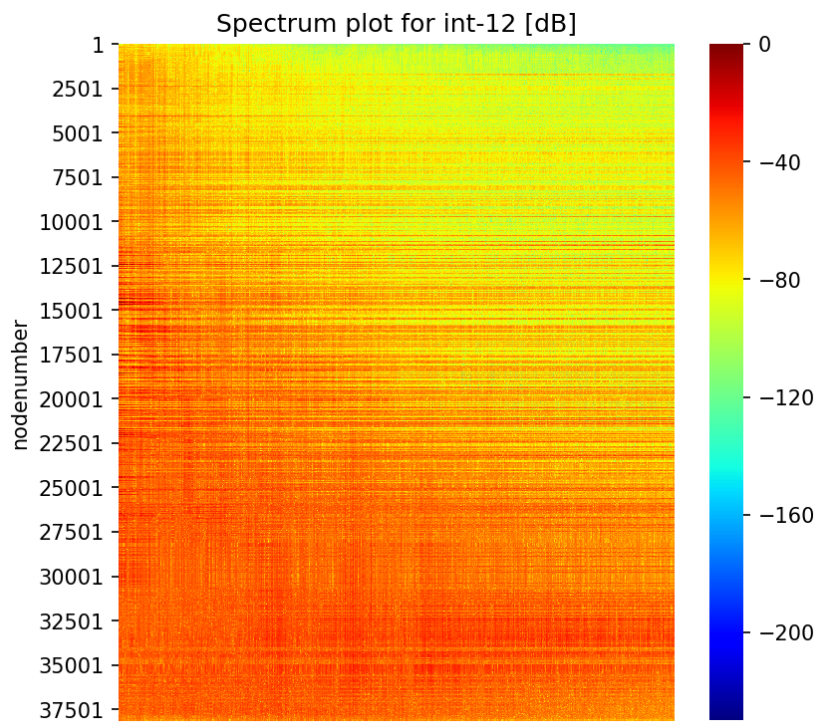


FIGURE B.48: Spectrum plot at int-12 mark

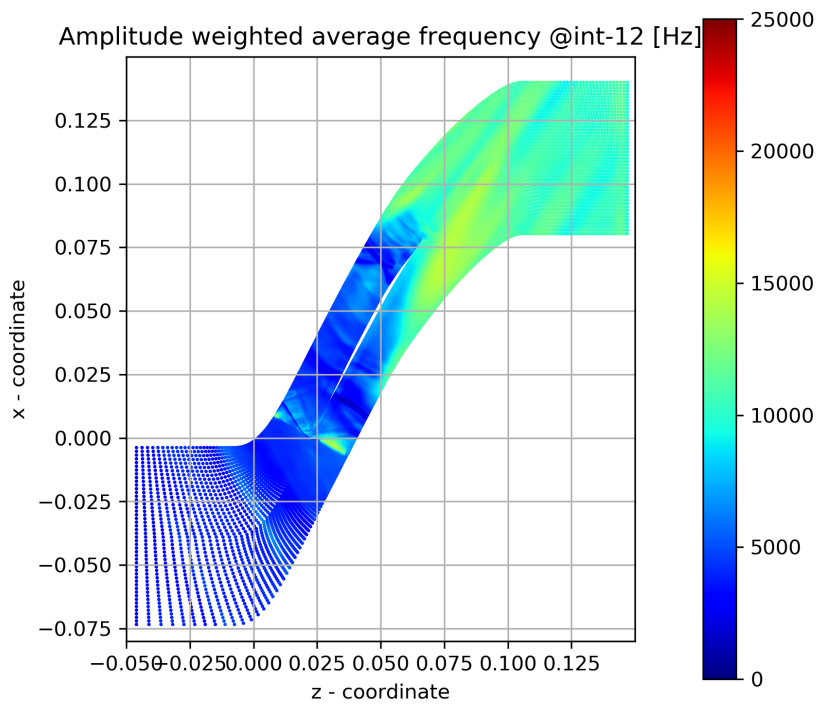


FIGURE B.49: Amplitude weighted average frequency at int-12 mark

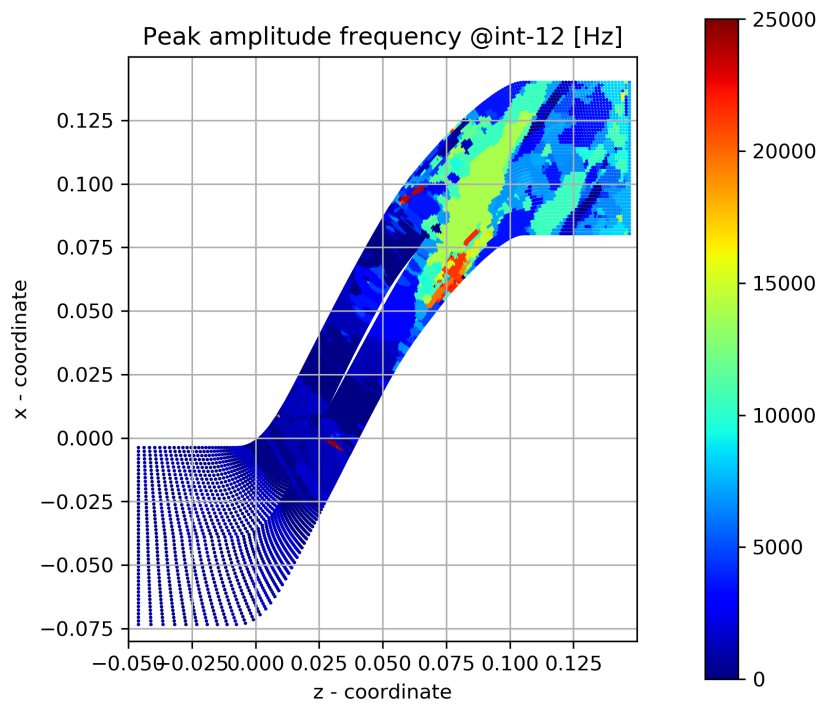


FIGURE B.50: Peak amplitude frequency int-12 mark

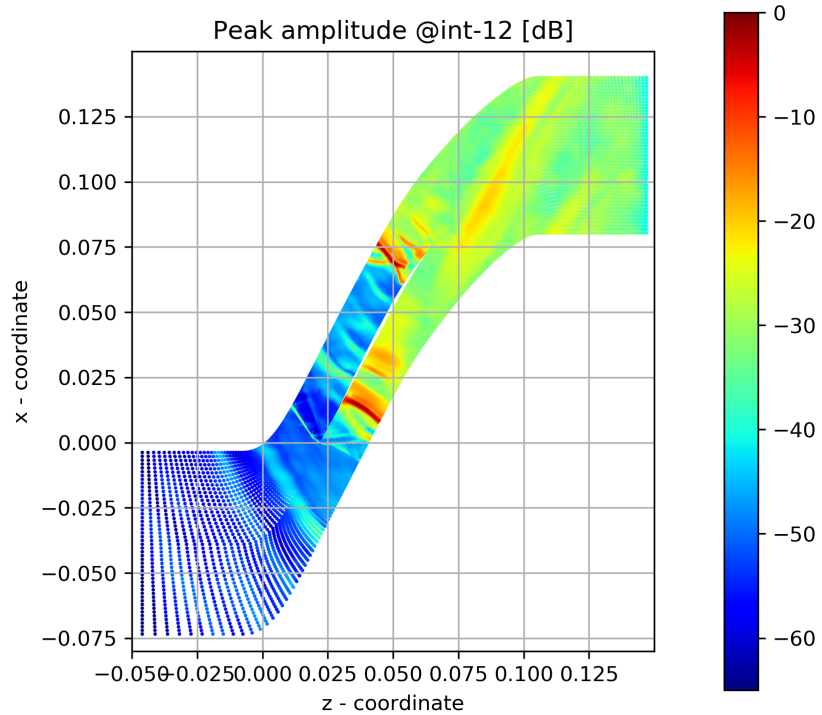


FIGURE B.51: Peak magnitude at int-12 mark

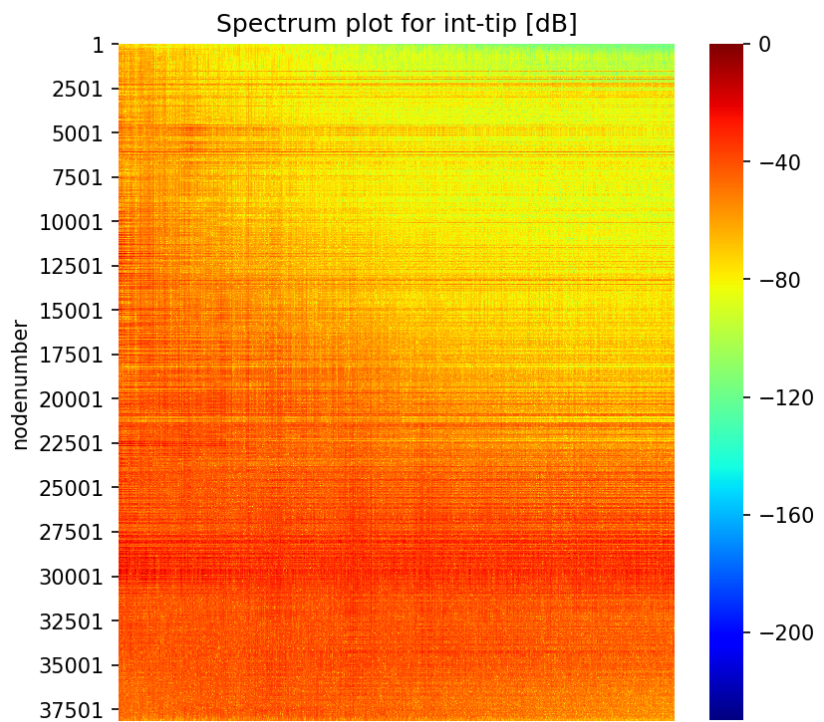


FIGURE B.52: Spectrum plot at int-tip mark

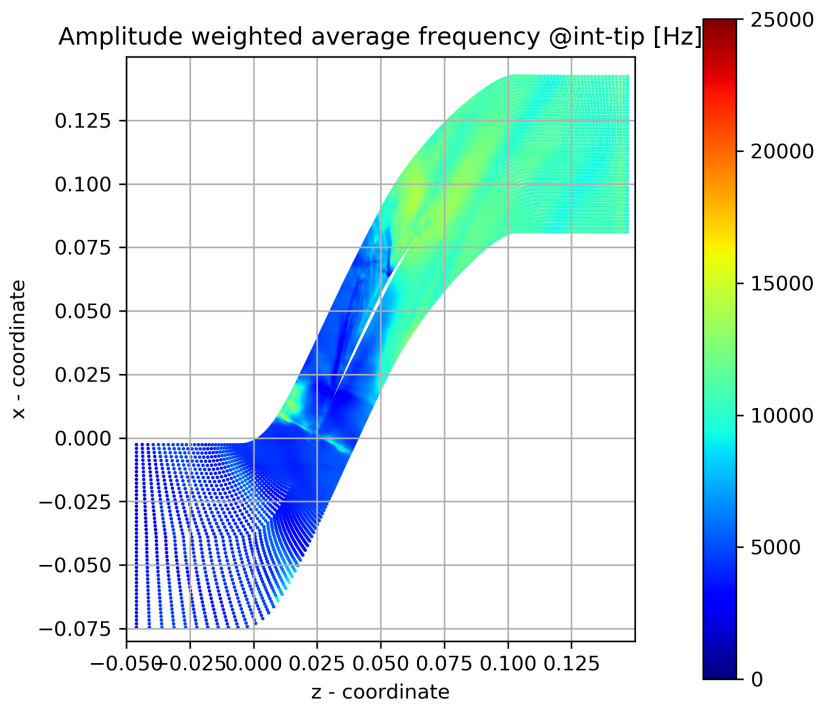


FIGURE B.53: Amplitude weighted average frequency at int-tip mark

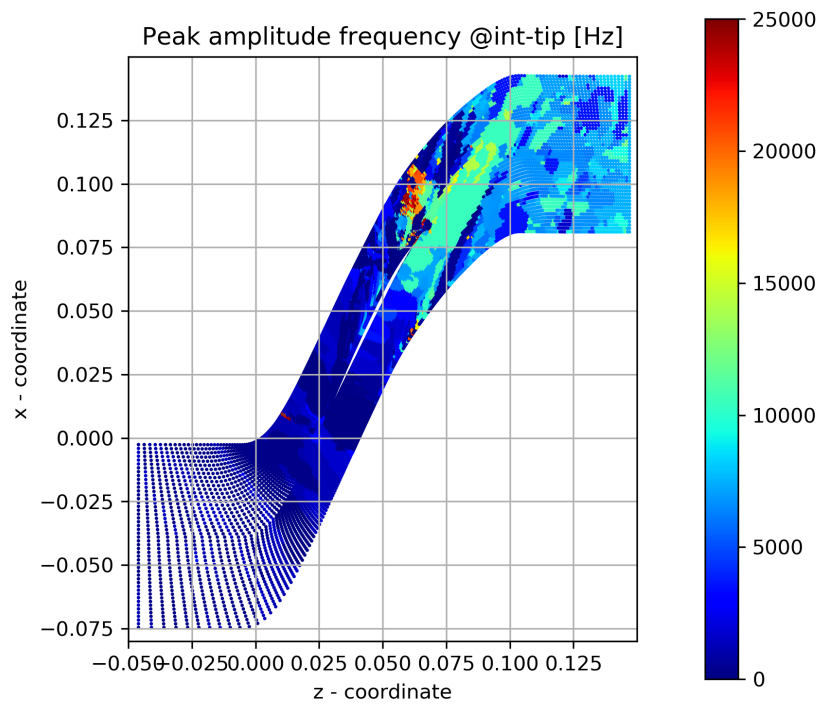


FIGURE B.54: Peak amplitude frequency int-tip mark

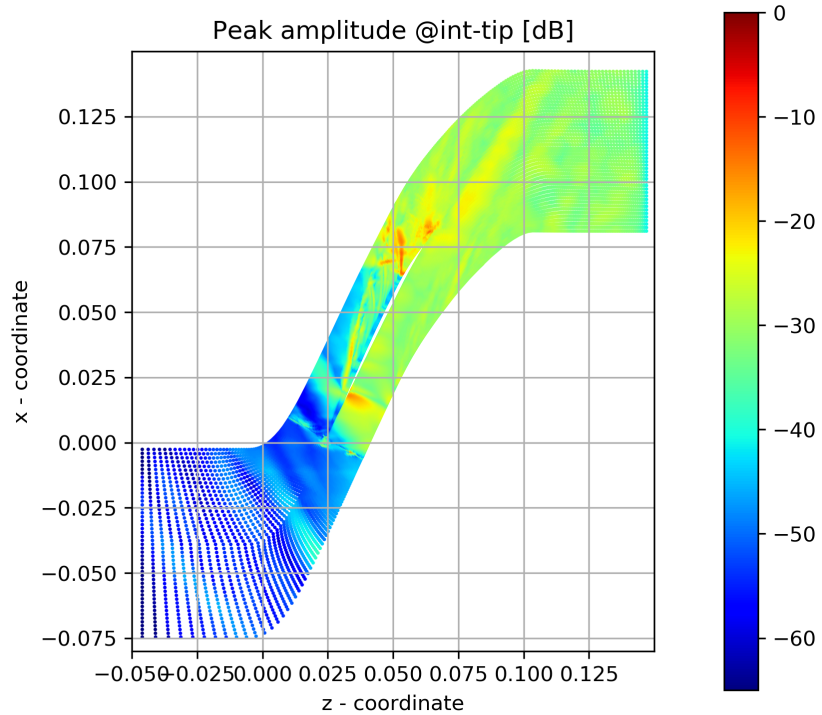


FIGURE B.55: Peak magnitude at int-tip mark

Appendix C

CFD validation

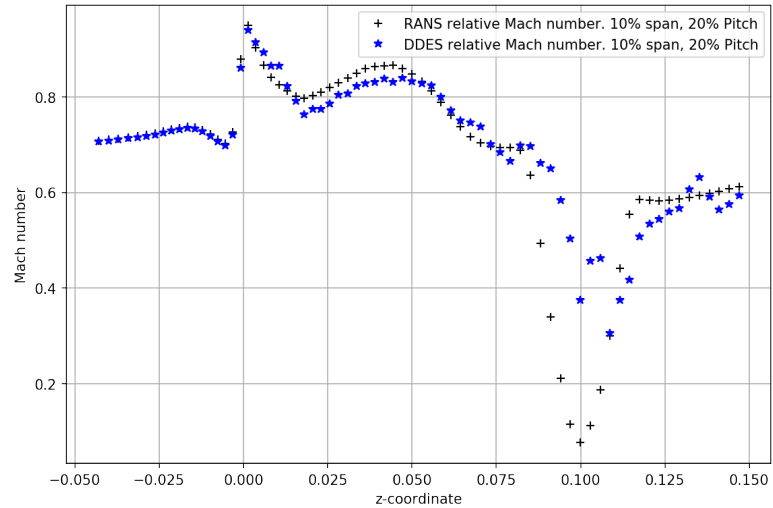


FIGURE C.1: Relative Mach number at S10P20 streamline

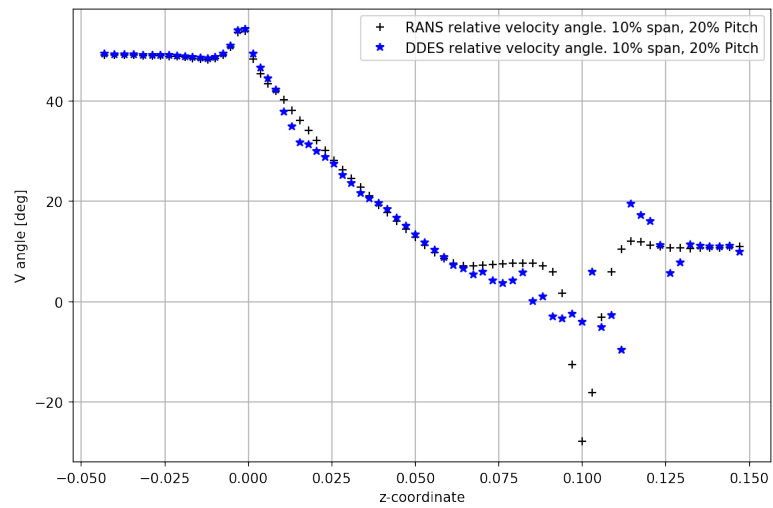


FIGURE C.2: Relative velocity angle at S10P20 streamline

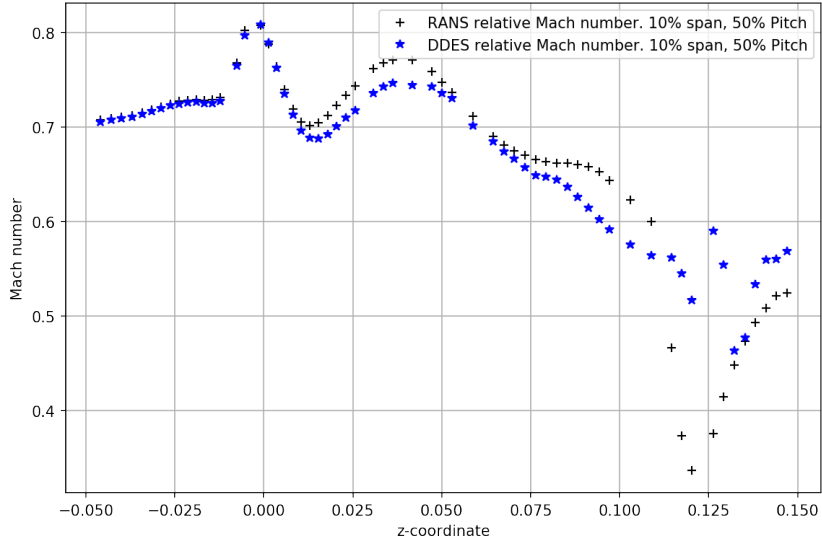


FIGURE C.3: Relative Mach number at S10P50 streamline

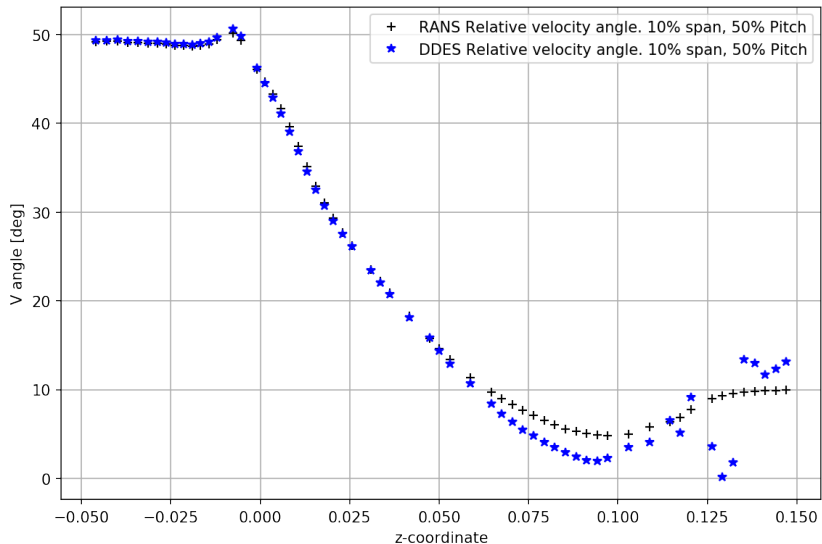


FIGURE C.4: Relative velocity angle at S10P50 streamline

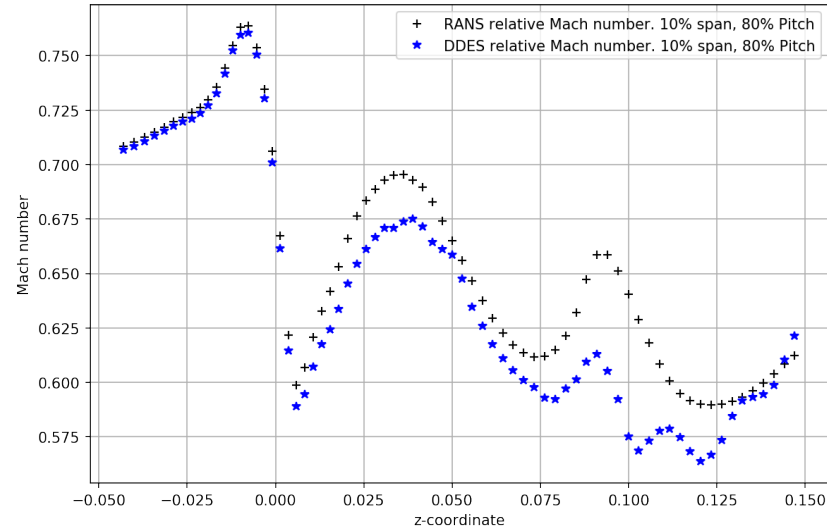


FIGURE C.5: Relative Mach number at S10P80 streamline

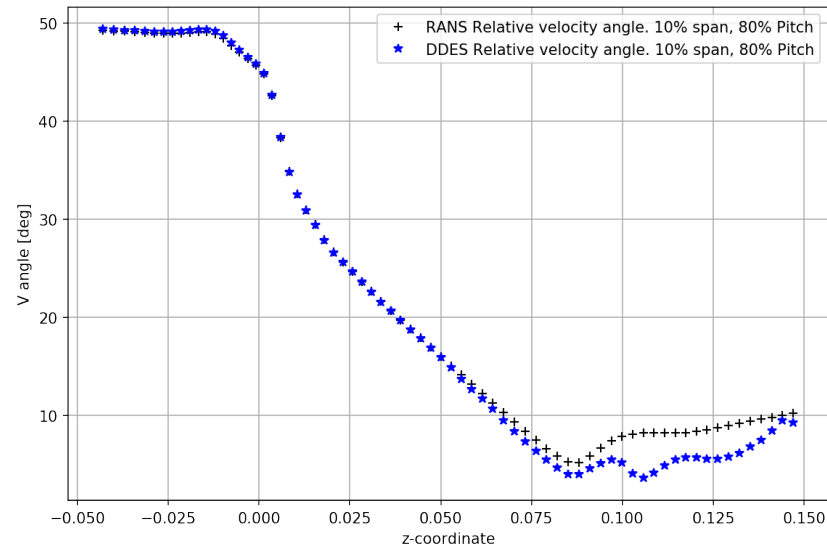


FIGURE C.6: Relative velocity angle at S10P80 streamline

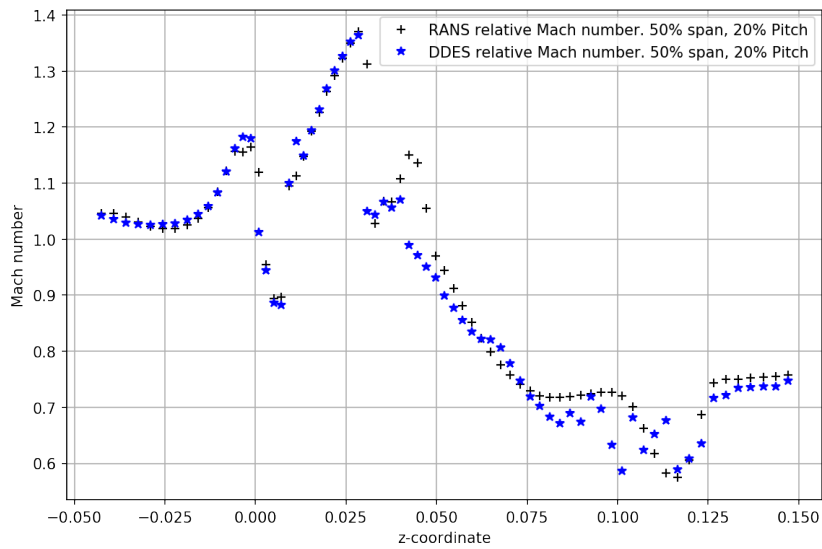


FIGURE C.7: Relative Mach number at S50P20 streamline

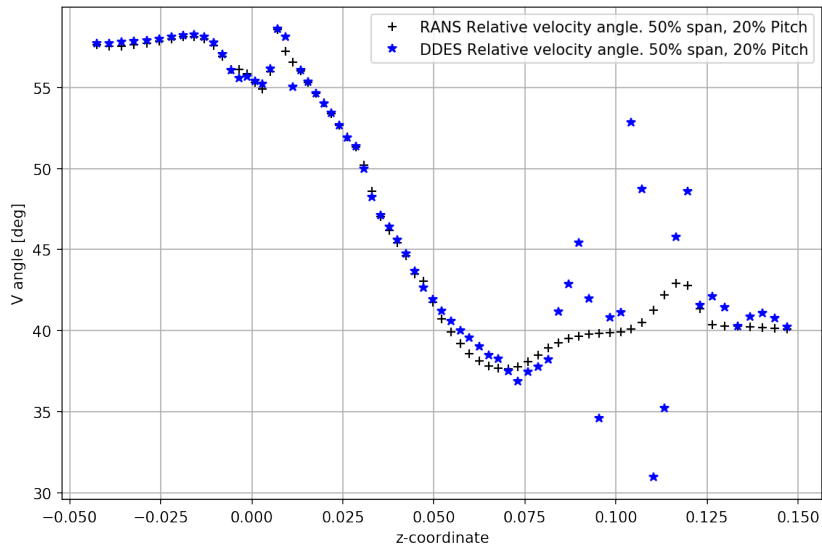


FIGURE C.8: Relative velocity angle at S50P20 streamline

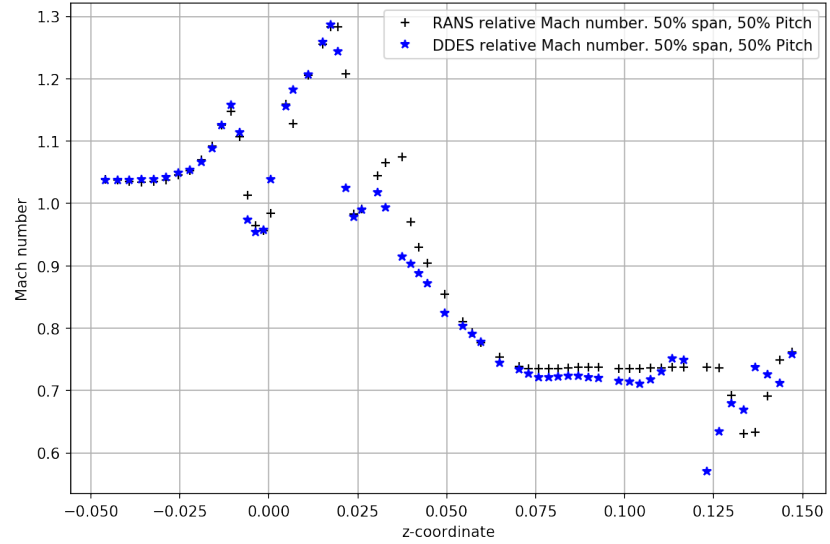


FIGURE C.9: Relative Mach number at S50P50 streamline

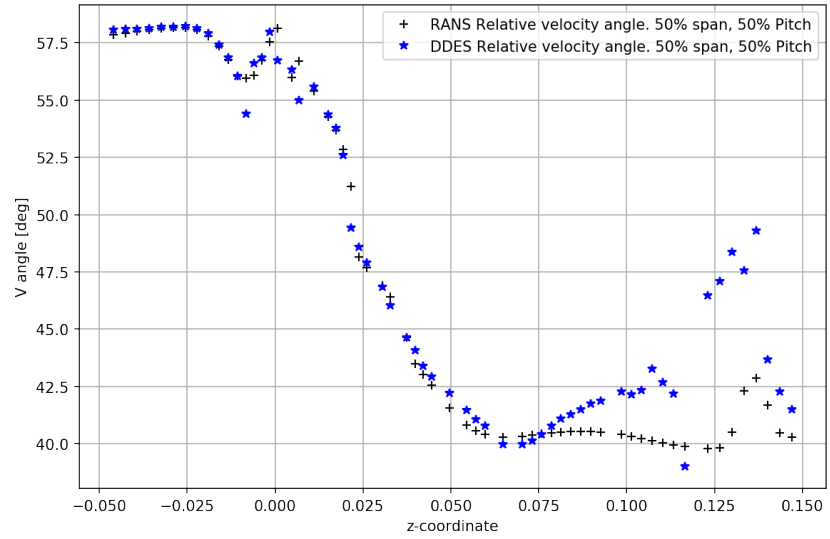


FIGURE C.10: Relative velocity angle at S50P50 streamline

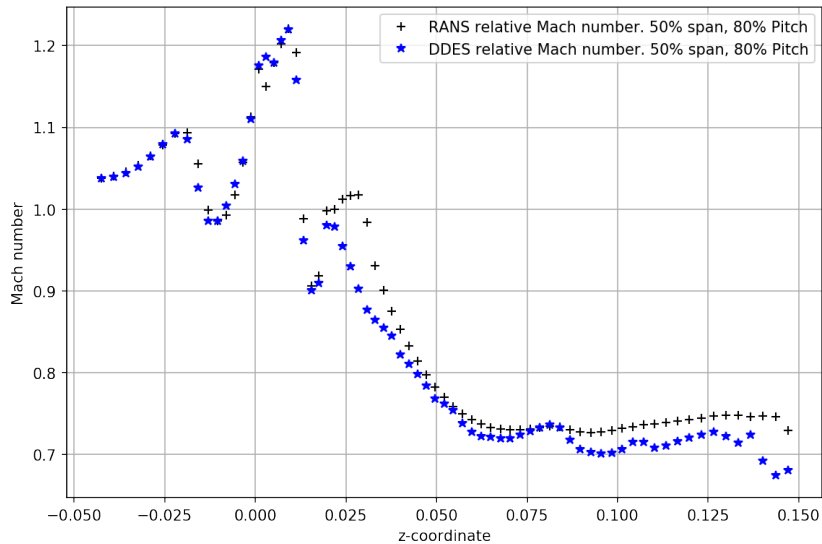


FIGURE C.11: Relative Mach number at S50P80 streamline

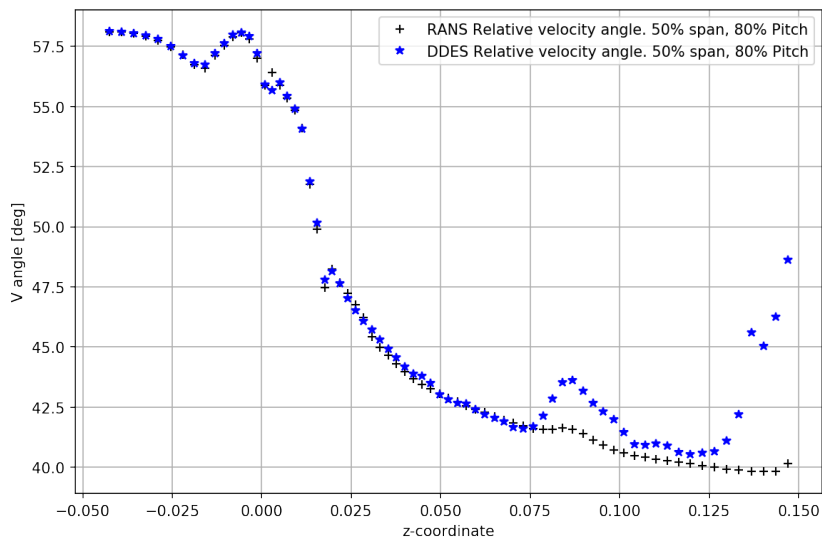


FIGURE C.12: Relative velocity angle at S50P80 streamline

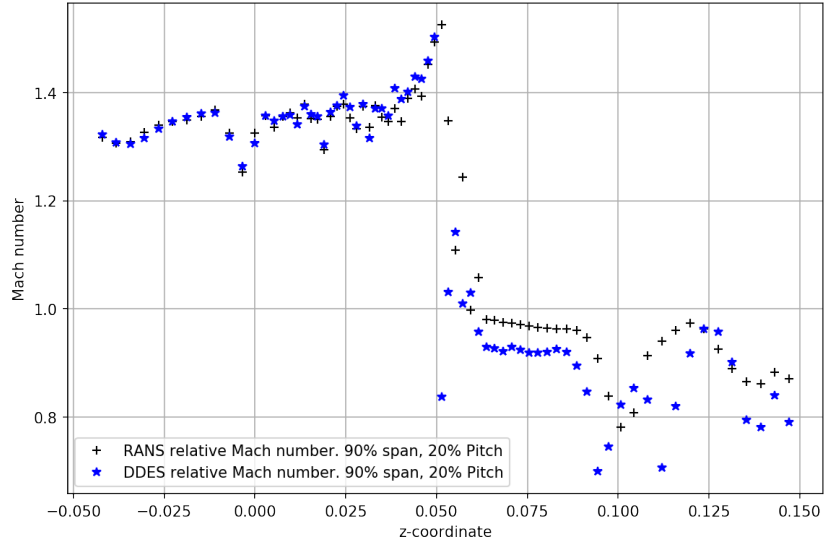


FIGURE C.13: Relative Mach number at S90P20 streamline

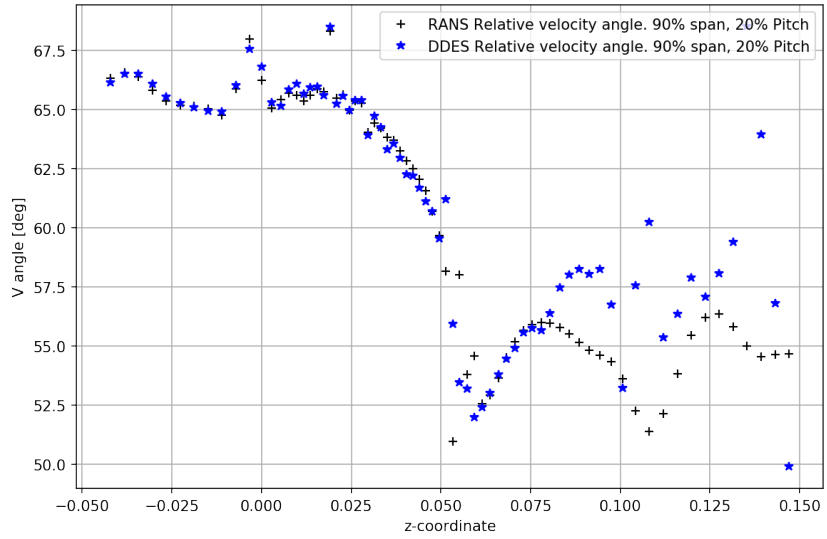


FIGURE C.14: Relative velocity angle at S90P20 streamline

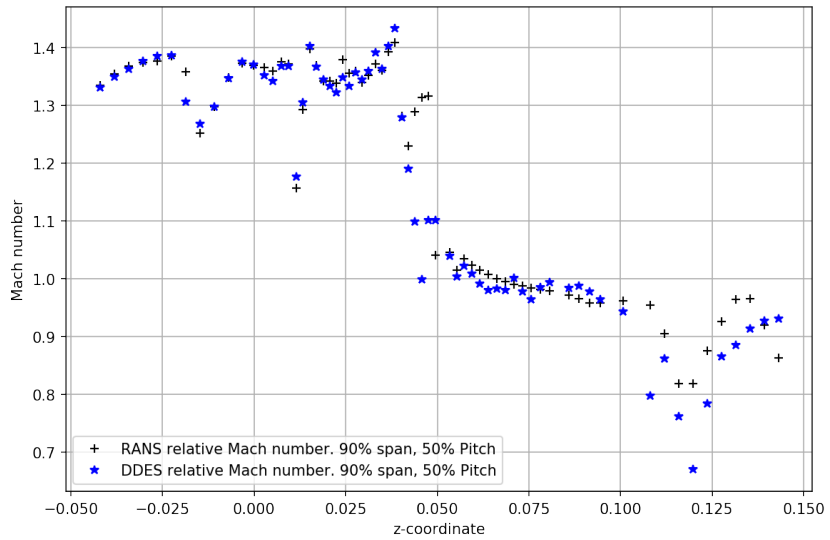


FIGURE C.15: Relative Mach number at S90P50 streamline

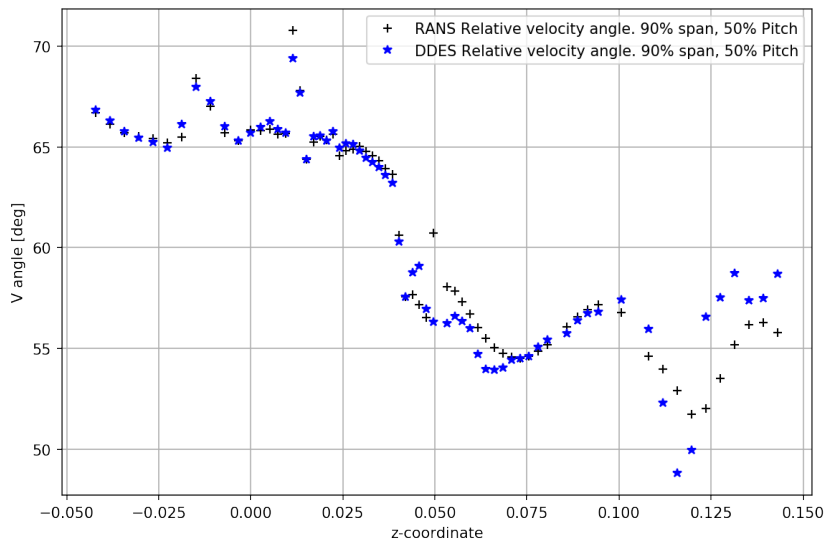


FIGURE C.16: Relative velocity angle at S90P50 streamline

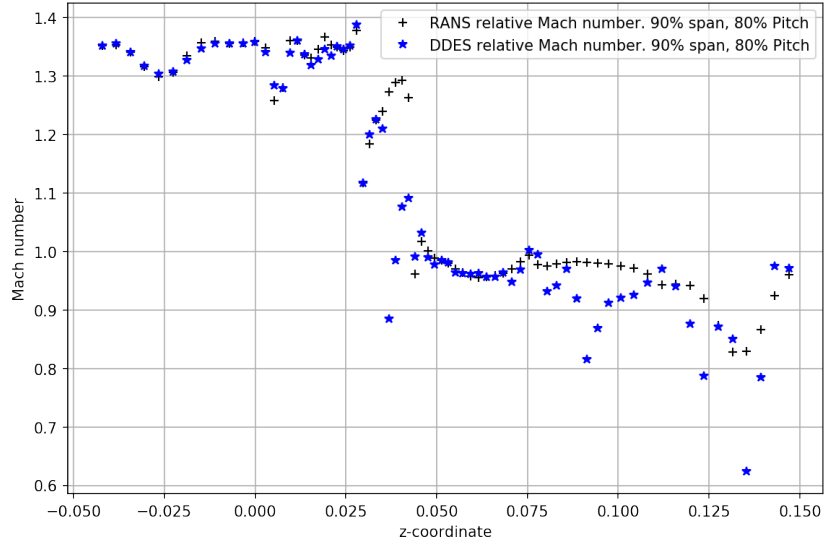


FIGURE C.17: Relative Mach number at S90P80 streamline

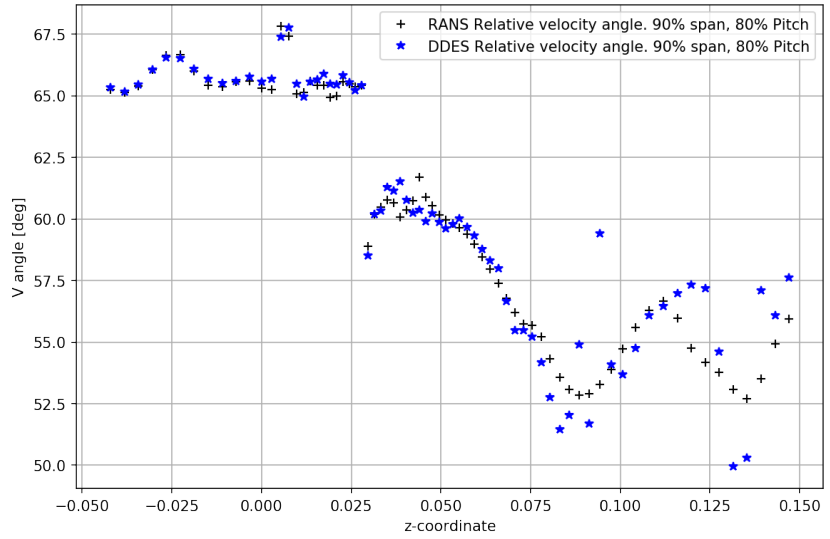


FIGURE C.18: Relative velocity angle at S90P80 streamline

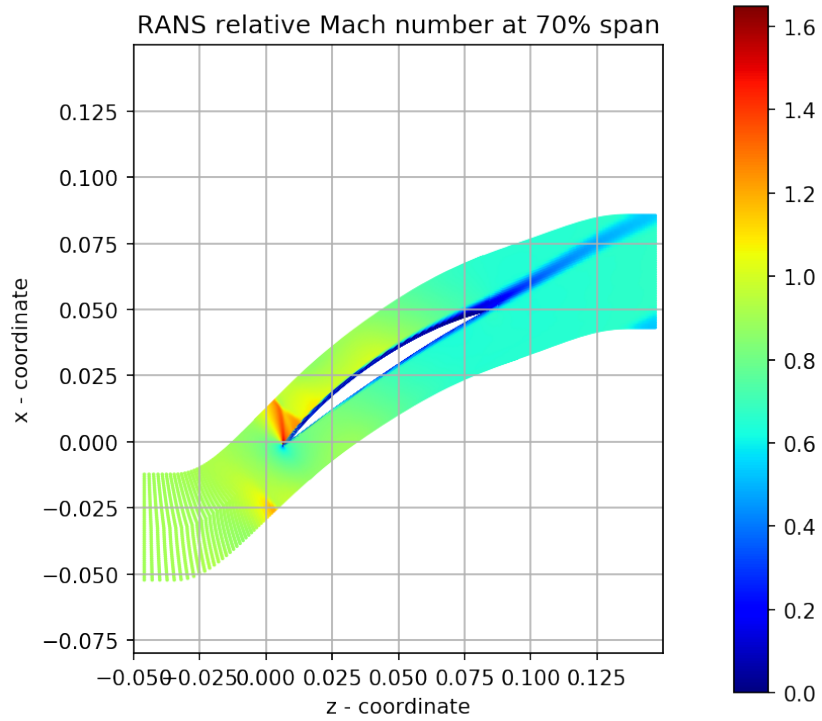


FIGURE C.19: RANS Mach number contour plot at int-04 mark

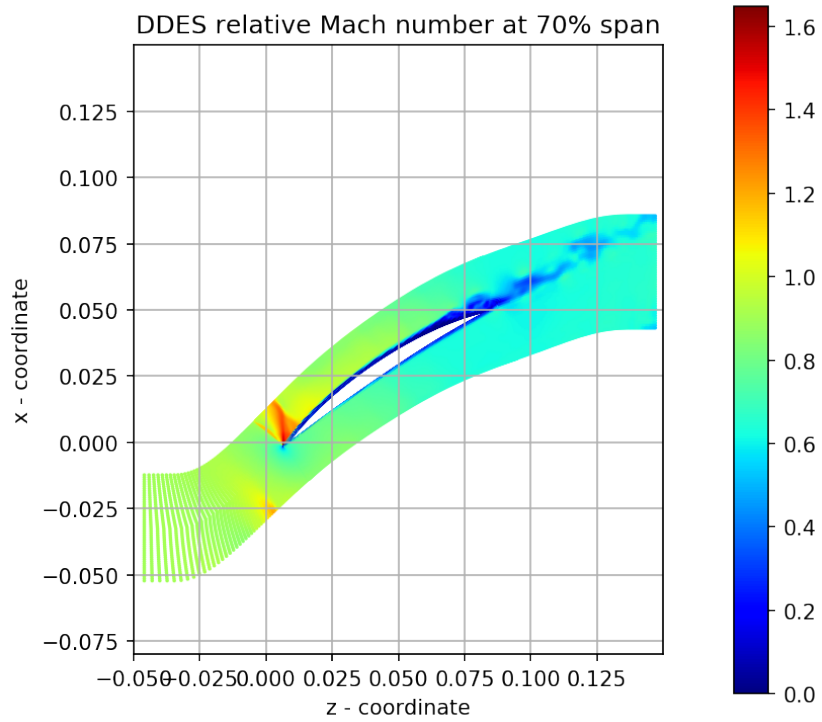


FIGURE C.20: DDES Mach number contour plot at int-04 mark

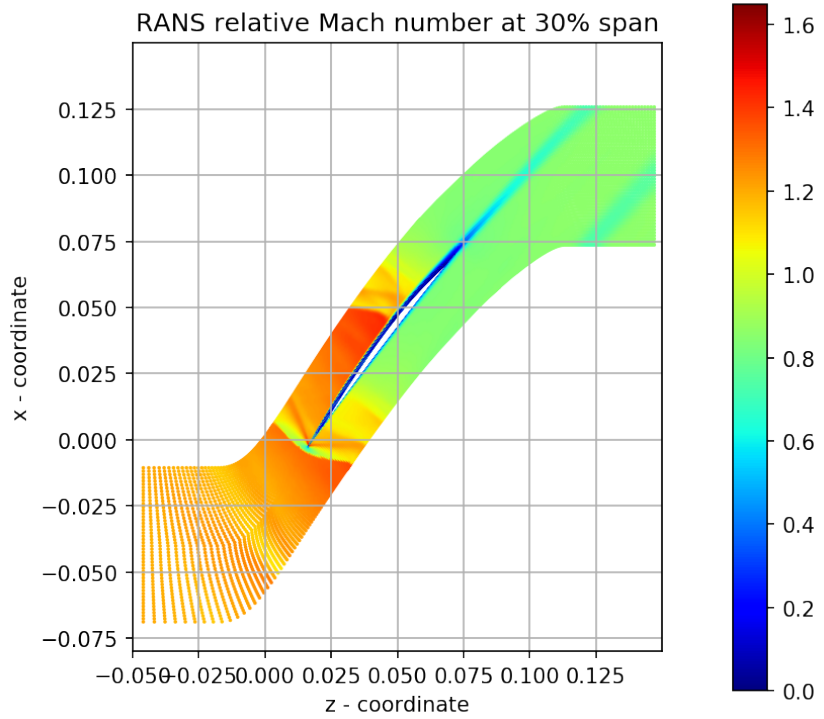


FIGURE C.21: RANS Mach number contour plot at int-09 mark

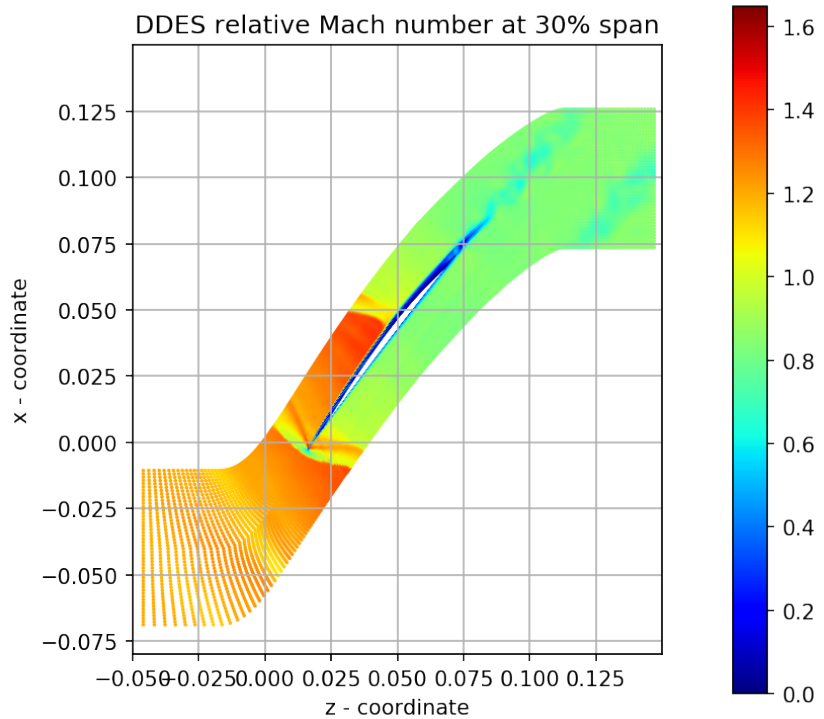


FIGURE C.22: DDES Mach number contour plot at int-09 mark

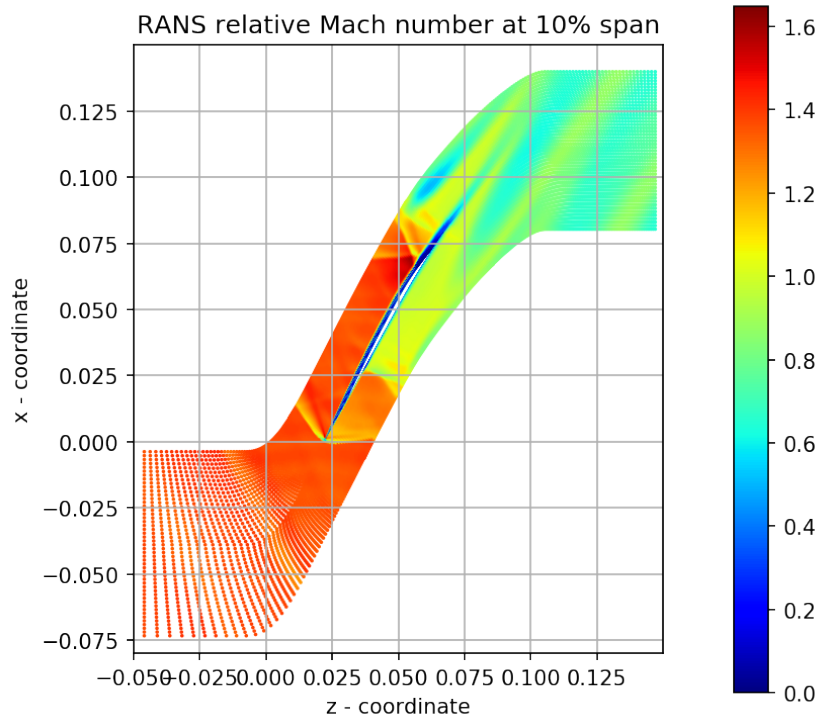


FIGURE C.23: RANS Mach number contour plot at int-12 mark

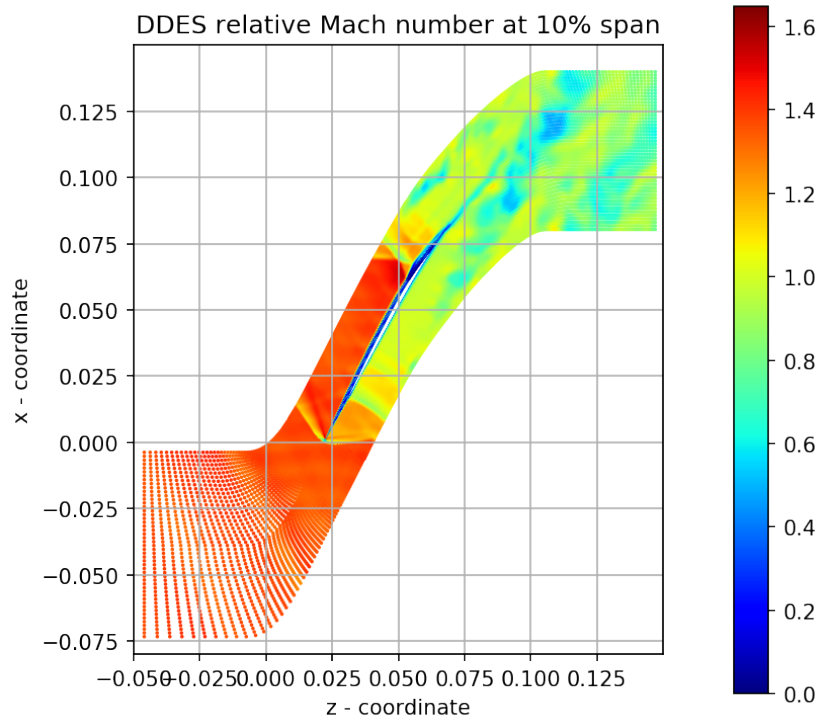


FIGURE C.24: DDES Mach number contour plot at int-12 mark

Appendix D

Code for direct formulation of noise analysis

```
# dask-noise.py
print("Loading Libraries...")
import os, sys
import csv
import platform
import numpy as np
import pandas as pd
import dask.dataframe as dd
import math
print("Loaded Libraries...")
print("Starting code...")
print("Loading directories...")
path_data = './flow-data/<folder_name>'
path_acu = './noise-data/<folder_name>/acu'
print("Loaded directories...")
print("Loading batch data...")
os.chdir(path_data)
batch_data = dd.read_csv('*/dat', delimiter=r"\s+", decimal='.')
print("Batch data done...")
print("Calculating batch averages...")
averages = pd.DataFrame(batch_data.groupby('nodenumber').mean().compute())
print("Batch averages done...")
print("Generating average pressure dataframe")
avg_static_p = pd.DataFrame({'pressure': averages['pressure']})
print("Generating average velocity dataframe")
avg_rel_v = pd.DataFrame(
    {'rel-velocity-magnitude': averages['rel-velocity-magnitude']})
print("Generating node coordinates...")
node_coords = pd.DataFrame({
    'x-coordinate': averages['x-coordinate'],
    'y-coordinate': averages['y-coordinate'],
    'z-coordinate': averages['z-coordinate']
})
del(batch_data)
print("Batch data deleted...")
```

```
print("Listing files...")
filelist = sorted(os.listdir(path_data)) [len(os.listdir(path_acu)):]
print("Starting noise analysis loop...")
for file in filelist:
    os.chdir(path_data)
    timestep = str(os.path.basename(str(file)))[7:-4]
    time_static_p = pd.DataFrame(pd.read_csv(file, delimiter=r"\s+"))
        .set_index('nodenumber')
    acoustic_p = time_static_p.subtract(avg_static_p, fill_value=None)
    spl_db = acoustic_p.apply(lambda x: 20 * np.log10(np.abs(x)/0.00002), axis=1)
    time_rel_vel = pd.DataFrame(pd.read_csv(file, delimiter=r"\s+"))
        .set_index('nodenumber')
    particle_v = time_rel_vel.subtract(avg_rel_v, fill_value=None).abs()
    sound_intensity = pd.DataFrame(
        acoustic_p.values*particle_v.values,
        index=acoustic_p.index)
    sil_db = sound_intensity.apply(
        lambda x: 10 * np.log10(np.abs(x)/1e-12), axis=1)
    acoustic_data = pd.concat(
        [node_coords,
        acoustic_p,
        spl_db,
        particle_v,
        sound_intensity,
        sil_db], axis=1)
    acoustic_data.columns =
        ['x-coordinate',
        'y-coordinate',
        'z-coordinate',
        'sound-pressure',
        'spl-db',
        'particle-velocity',
        'sound-intensity',
        'sil-db']
    os.chdir(path_acu)
    acoustic_data.to_csv(str('<filename>_') + str(timestep) + '.dat'), sep=',')
    print(str('<filename>' + str(timestep) + '.dat done...'))
print("Exiting noise analysis loop...")
print("Script done, exiting.")
```

Appendix E

Folder Structure

```
flow-data
├── int-01 ... int-tip
│   └── ddes analysis output
└── lead pside sside tip trail
    └── ddes analysis output
```

```
noise-data
├── int-01-post ... int-tip-post
│   └── acu
│       └── sound-analysis-results
└── lead pside sside tip trail
    └── acu
        └── sound-analysis-results
```

```
results
├── coords
│   └── surface nodes coordinate files
├── fft
│   └── fft analysis results
├── rms
│   └── rms analysis results
└── plots
    └── output plots
```


Appendix F

Code for RMS computation

```
#rms.py
print("Loading Libraries...")
import os
import csv
import platform
import numpy as np
from scipy.fftpack import fft
import pandas as pd
import dask.dataframe as dd
import math
import matplotlib.pyplot as plt
print("Loaded Libraries...")

#PLGRID
print("Loading directories..")
path_acu = './noise-data/<folder_name>/acu'
path_rms = './results/rms'
print("Loaded directories...")

print("Loading batch data...")
os.chdir(path_acu)
batch_data = dd.read_csv('*1.dat',
                        delimiter=",",
                        decimal=',',
                        usecols=["nodenumber", "sound-pressure", "sound-intensity"])
batch_data = batch_data.set_index("nodenumber")
print("Batch data done...")

print("Calculating rms...")
rms = pd.DataFrame(batch_data.groupby('nodenumber').std().compute())
rms['rms_spldb'] = rms['sound-pressure'].apply(lambda x: 20*np.log10(x/0.00002))
rms['rms_sildb'] = rms['sound-intensity'].apply(lambda x: 10*np.log10(x/1e-12))

print("Saving...")
os.chdir(path_rms)
rms.to_csv(str('<filename>'), sep=",")
```

Appendix G

Code for discrete Fourier analysis

```
#fft.py
print("Loading Libraries...")
import os
import numpy as np
import pandas as pd
print("Loaded Libraries...")
print("Starting code...")

#PLGRID
print("Loading directories...")
path_acu = './noise-data/<folder-name>/acu'
path_fft = './results/fft'
print("Loaded directories...")

print("Getting filelist...")
os.chdir(path_acu)
filelist = sorted(os.listdir(path_acu))[0::10]

print("Starting batch loop...")
batch_data = pd.DataFrame()
for file in filelist:
    batch_data[file] = pd.read_csv(file).set_index('nodenumber')['sound-pressure']
    print(str(file) + " done...")

print("Calculating FFT...")
fft_data = batch_data.apply(lambda x: np.fft.fft(x), axis=1)

print("Saving FFT to dataframe...")
os.chdir(path_fft)
fft_data.to_csv('<filename>', sep=',')
print("Dataframe saved...")
print("Script completed...")
```

Appendix H

Blade design surface coordinates

TABLE H.1: int-00 coordinates

K	Z	THSP1_X	THSP1_Y	THSP2_X	THSP2_Y	THSPM_X	THSPM_Y
1	0.0000	0.74067	85.62460	-0.15242	85.62766	0.29413	85.62729
2	2.7160	3.11951	86.18426	1.39100	86.22948	2.25537	86.21120
3	5.4378	5.37389	86.71885	2.91879	86.83616	4.14676	86.78619
4	8.1570	7.46236	87.24062	4.35340	87.45091	5.90882	87.35960
5	10.8754	9.38840	87.76236	5.60446	88.08499	7.49817	87.94403
6	13.5921	11.25541	88.28179	6.79892	88.73632	9.03003	88.53710
7	16.3072	13.03696	88.80698	7.98425	89.40299	10.51483	89.14079
8	19.0194	14.62103	89.36128	9.09032	90.09205	11.86130	89.76927
9	21.7294	16.06181	89.94555	10.12289	90.80590	13.09942	90.42450
10	24.4372	17.40108	90.55801	11.10789	91.54325	14.26299	91.10498
11	27.1419	18.63870	91.19793	12.05660	92.29898	15.35752	91.80746
12	29.8434	19.77118	91.86337	12.95796	93.06917	16.37567	92.52900
13	32.5408	20.80456	92.54873	13.80767	93.84799	17.31830	93.26400
14	35.2334	21.74766	93.24722	14.60965	94.62855	18.19177	94.00566
15	37.9207	22.60659	93.95188	15.36779	95.40359	19.00106	94.74689
16	40.6023	23.37726	94.65824	16.08421	96.16640	19.74514	95.48198
17	43.2773	24.06404	95.35947	16.75617	96.91097	20.42484	96.20464
18	45.9453	24.66787	96.05004	17.38102	97.63203	21.03932	96.90955
19	48.6060	25.18324	96.72676	17.95914	98.32462	21.58598	97.59256
20	51.2594	25.61310	97.38664	18.48850	98.98668	22.06530	98.25126
21	53.9054	25.95965	98.03052	18.96683	99.62001	22.47729	98.88710
22	56.5443	26.21953	98.66096	19.39503	100.22616	22.82070	99.50208
23	59.1761	26.39038	99.27984	19.77311	100.80656	23.09437	100.09790
24	61.8010	26.47090	99.88845	20.09815	101.36309	23.29619	100.67621
25	64.4192	26.45901	100.48859	20.36736	101.89802	23.42379	101.23913
26	67.0311	26.34948	101.08182	20.57887	102.41259	23.47361	101.78811
27	69.6369	26.13823	101.66972	20.72790	102.90915	23.44126	102.32520
28	72.2368	25.82206	102.25274	20.81474	103.38834	23.32531	102.85102
29	74.8312	25.39490	102.83242	20.83469	103.85241	23.12042	103.36756
30	77.4204	24.85045	103.40908	20.78502	104.30228	22.82210	103.87557
31	80.0045	24.17617	103.98423	20.65989	104.73956	22.42121	104.37670
32	82.5840	23.37613	104.55498	20.45559	105.16537	21.91798	104.87034
33	85.1592	22.43256	105.12306	20.15896	105.58264	21.29700	105.35899
34	87.7309	21.28188	105.69777	19.74814	105.99504	20.51555	105.84918
35	90.2991	19.94258	106.27120	19.24182	106.40032	19.59231	106.33634

TABLE H.2: int-01 coordinates

K	Z	THSP1_X	THSP1_Y	THSP2_X	THSP2_Y	THSPM_X	THSPM_Y
1	0.0000	0.82717	95.62422	-0.17022	95.62765	0.32848	95.62724
2	2.7160	3.48123	96.17772	1.55230	96.22818	2.51689	96.20778
3	5.4378	5.99240	96.69971	3.25473	96.83052	4.62403	96.77479
4	8.1570	8.31463	97.20424	4.85059	97.43854	6.58365	97.33680
5	10.8754	10.45209	97.70563	6.23944	98.06481	8.34769	97.90788
6	13.5921	12.52011	98.20150	7.56288	98.70709	10.04468	98.48549
7	16.3072	14.48941	98.70094	8.87377	99.36335	11.68628	99.07194
8	19.0194	16.23573	99.23005	10.09422	100.04153	13.17123	99.68310
9	21.7294	17.81973	99.78983	11.23082	100.74434	14.53311	100.32119
10	24.4372	19.28810	100.37836	12.31245	101.47043	15.80971	100.98464
11	27.1419	20.64107	100.99540	13.35185	102.21474	17.00739	101.67042
12	29.8434	21.87524	101.63951	14.33695	102.97363	18.11838	102.37598
13	32.5408	22.99778	102.30525	15.26328	103.74148	19.14401	103.09593
14	35.2334	24.01897	102.98586	16.13547	104.51146	20.09170	103.82352
15	37.9207	24.94601	103.67439	16.95811	105.27632	20.96736	104.55167
16	40.6023	25.77487	104.36656	17.73383	106.02940	21.77023	105.27478
17	43.2773	26.51085	105.05551	18.45992	106.76477	22.50162	105.98661
18	45.9453	27.15537	105.73572	19.13372	107.47724	23.16092	106.68190
19	48.6060	27.70279	106.40415	19.75593	108.16188	23.74563	107.35657
20	51.2594	28.15664	107.05775	20.32452	108.81669	24.25653	108.00823
21	53.9054	28.51954	107.69732	20.83715	109.44355	24.69378	108.63836
22	56.5443	28.78792	108.32550	21.29491	110.04402	25.05615	109.24902
23	59.1761	28.95935	108.94423	21.69792	110.61957	25.34248	109.84192
24	61.8010	29.03252	109.55479	22.04307	111.17213	25.55060	110.41878
25	64.4192	29.00526	110.15899	22.32739	111.70406	25.67795	110.98176
26	67.0311	28.87193	110.75845	22.54890	112.21662	25.72075	111.53235
27	69.6369	28.62815	111.35478	22.70244	112.71227	25.67427	112.07270
28	72.2368	28.27051	111.94837	22.78839	113.19164	25.53702	112.60337
29	74.8312	27.79242	112.54076	22.80168	113.65704	25.30321	113.12643
30	77.4204	27.18704	113.13226	22.73936	114.10945	24.96798	113.64261
31	80.0045	26.44075	113.72443	22.59510	114.55052	24.52140	114.15367
32	82.5840	25.55804	114.31404	22.36489	114.98141	23.96379	114.65884
33	85.1592	24.51951	114.90287	22.03439	115.40521	23.27830	115.16074
34	87.7309	23.25574	115.50103	21.57974	115.82587	22.41833	115.66648
35	90.2991	21.78696	116.09965	21.02139	116.24070	21.40429	116.17080

TABLE H.3: int-02 coordinates

K	Z	THSP1_X	THSP1_Y	THSP2_X	THSP2_Y	THSPM_X	THSPM_Y
1	1.2564	0.51949	108.00145	-0.56161	108.0012	-0.02106	108.00270
2	3.9540	3.29388	108.49641	1.228719	108.5394	2.26140	108.52284
3	6.5930	5.91354	108.95874	2.933859	109.0797	4.42411	109.02938
4	9.3607	8.36890	109.39926	4.566279	109.6238	6.46856	109.52805
5	12.0601	10.71429	109.82511	6.176175	110.1735	8.44703	110.02271
6	14.7591	12.85498	110.25412	7.669603	110.7357	10.26511	110.52533
7	17.4533	14.76134	110.70288	8.994109	111.32	11.88173	111.04886
8	20.1436	16.59319	111.15916	10.27277	111.9203	13.43837	111.58451
9	22.8303	18.34107	111.62817	11.54125	112.5346	14.94803	112.13295
10	25.5120	19.94598	112.12431	12.77822	113.1655	16.37038	112.70188
11	28.1881	21.41680	112.64747	13.9579	113.8126	17.69694	113.29144
12	30.8578	22.77094	113.19270	15.08209	114.4711	18.93731	113.89681
13	33.5199	24.02467	113.75389	16.15926	115.1347	20.10382	114.51187
14	36.1736	25.18626	114.32516	17.19899	115.7963	21.20539	115.13002
15	38.8181	26.25827	114.90171	18.2005	116.4502	22.24286	115.74608
16	41.5290	27.23852	115.47915	19.16279	117.0904	23.21464	116.35485
17	44.0775	28.13413	116.05123	20.08366	117.7118	24.12319	116.95080
18	46.6919	28.94778	116.61283	20.9656	118.3088	24.97109	117.52860
19	49.2955	29.67774	117.16053	21.80769	118.8772	25.75702	118.08443
20	51.8890	30.32645	117.69219	22.60706	119.4155	26.48078	118.61667
21	54.4726	30.89370	118.20918	23.36377	119.9248	27.14229	119.12651
22	57.0471	31.37849	118.71413	24.07703	120.4074	27.74068	119.61651
23	59.6128	31.78216	119.20820	24.74601	120.8649	28.27622	120.08811
24	62.1702	32.10511	119.69313	25.37003	121.2994	28.74879	120.54331
25	64.7196	32.34527	120.17056	25.94718	121.7125	29.15642	120.98381
26	67.2618	32.49826	120.64282	26.47687	122.1057	29.49663	121.41160
27	69.7971	32.56336	121.11110	26.95609	122.4812	29.76761	121.82840
28	72.3257	32.54102	121.57575	27.38431	122.8401	29.96933	122.23510
29	74.8483	32.42460	122.03941	27.75866	123.1845	30.09708	122.63416
30	77.3650	32.21087	122.50270	28.07614	123.5159	30.14776	123.02669
31	79.8764	31.89187	122.96801	28.33765	123.8354	30.11788	123.41448
32	82.3827	31.47793	123.43203	28.54154	124.1439	30.01185	123.79667
33	84.8842	30.95622	123.89789	28.67388	124.4459	29.81631	124.17715
34	87.3813	30.26882	124.37856	28.7205	124.7452	29.49523	124.56427
35	89.8742	29.43612	124.86862	28.69638	125.0407	29.06638	124.95521

TABLE H.4: int-03 coordinates

K	Z	THSP1_X	THSP1_Y	THSP2_X	THSP2_Y	THSPM_X	THSPM_Y
1	2.9502	0.10710	120.33905	-0.8917	120.3358	-0.39230	120.33846
2	5.6195	3.10211	120.77207	0.908497	120.8085	2.00539	120.79525
3	8.2913	5.89467	121.16900	2.672294	121.2829	4.28386	121.23664
4	10.9539	8.45856	121.54493	4.385253	121.76	6.42281	121.66949
5	13.6100	10.83582	121.91109	6.014353	122.2438	8.42673	122.10126
6	16.2605	13.07160	122.27368	7.578779	122.7366	10.32779	122.53594
7	18.9031	15.18467	122.63802	9.10043	123.239	12.14627	122.97612
8	21.5377	17.14355	123.01467	10.56687	123.7532	13.86013	123.42774
9	24.1639	18.95960	123.40929	11.97659	124.2815	15.47424	123.89459
10	26.7815	20.66271	123.82251	13.34044	124.8238	17.00894	124.37707
11	29.3896	22.25763	124.25414	14.67027	125.3765	18.47247	124.87298
12	31.9875	23.75235	124.70084	15.96762	125.9345	19.86956	125.37813
13	34.5743	25.15458	125.15811	17.23252	126.4925	21.20405	125.88762
14	37.1492	26.46698	125.62235	18.46358	127.0456	22.47655	126.39731
15	39.7115	27.69448	126.08847	19.66294	127.5878	23.69058	126.90171
16	42.2611	28.84587	126.55088	20.83275	128.114	24.85160	127.39548
17	44.7980	29.92353	127.00447	21.97236	128.6187	25.96050	127.87339
18	47.3222	30.92621	127.44587	23.08123	129.0974	27.01634	128.33159
19	49.8342	31.85648	127.87073	24.15742	129.546	28.01947	128.76594
20	52.3348	32.71772	128.27744	25.19949	129.9636	28.97087	129.17522
21	54.8244	33.51009	128.66731	26.20903	130.3506	29.87142	129.56041
22	57.3041	34.23160	129.04334	27.18538	130.7094	30.71979	129.92413
23	59.7748	34.88794	129.40577	28.12651	131.0417	31.51784	130.26760
24	62.2369	35.47718	129.75684	29.03046	131.3495	32.26365	130.59298
25	64.6912	35.99755	130.09899	29.90332	131.6334	32.95937	130.90169
26	67.1383	36.44844	130.43353	30.73793	131.8961	33.60114	131.19587
27	69.5791	36.83073	130.76176	31.53388	132.1392	34.18924	131.47713
28	72.0138	37.14126	131.08533	32.29327	132.3631	34.72314	131.74650
29	74.4429	37.38102	131.40531	33.01183	132.5704	35.20125	132.00594
30	76.8672	37.54438	131.72427	33.69054	132.7622	35.62124	132.25729
31	79.2869	37.63217	132.04728	34.32755	132.9447	35.98265	132.50627
32	81.7023	37.64559	132.36047	34.92181	133.105	36.28561	132.73974
33	84.1137	37.57883	132.68025	35.46988	133.2595	36.52551	132.97407
34	86.5213	37.39709	133.01208	35.95841	133.4082	36.67829	133.21208
35	88.9254	37.11490	133.35342	36.39559	133.5515	36.75538	133.45296

TABLE H.5: int-04 coordinates

K	Z	THSP1_X	THSP1_Y	THSP2_X	THSP2_Y	THSPM_X	THSPM_Y
1	4.9865	-0.24137	132.62208	-1.24663	132.6164	-0.74401	132.62021
2	7.5827	2.84401	133.00170	0.562724	133.0309	1.70343	133.02119
3	10.1760	5.72934	133.34467	2.352914	133.447	4.04145	133.40650
4	12.7559	8.39580	133.66468	4.118979	133.8647	6.25819	133.78180
5	15.3254	10.89298	133.97098	5.845126	134.2859	8.37053	134.15221
6	17.8851	13.22807	134.27208	7.528788	134.7119	10.38076	134.52217
7	20.4330	15.40169	134.57634	9.164638	135.1444	12.28645	134.89643
8	22.9694	17.45762	134.88546	10.74993	135.585	14.10811	135.27682
9	25.4940	19.41567	135.20182	12.30361	136.0335	15.86509	135.66429
10	28.0063	21.26732	135.53032	13.8489	136.488	17.56464	136.05973
11	30.5057	23.00065	135.87368	15.36513	136.9474	19.19040	136.46397
12	32.9915	24.62758	136.22829	16.84464	137.4079	20.74450	136.87341
13	35.4635	26.17503	136.58758	18.29059	137.865	22.24198	137.28290
14	37.9214	27.64789	136.94689	19.71411	138.312	23.69084	137.68660
15	40.3649	29.05242	137.30157	21.1153	138.744	25.09423	138.07985
16	42.7945	30.38792	137.64821	22.49409	139.1563	26.45176	138.45851
17	45.2108	31.65492	137.98275	23.85021	139.5437	27.76353	138.81808
18	47.6143	32.85684	138.30140	25.18203	139.9025	29.03047	139.15488
19	50.0059	33.99990	138.59956	26.48783	140.2292	30.25484	139.46496
20	52.3868	35.08256	138.87660	27.76622	140.5224	31.43517	139.74737
21	54.7581	36.10273	139.13544	29.02209	140.7828	32.57282	140.00389
22	57.1206	37.06663	139.37623	30.24903	141.013	33.66778	140.23605
23	59.4752	37.97526	139.60113	31.45074	141.2142	34.72237	140.44555
24	61.8229	38.82674	139.81251	32.62526	141.3883	35.73469	140.63459
25	64.1644	39.62072	140.01241	33.77352	141.5367	36.70503	140.80489
26	66.5004	40.35819	140.20198	34.8936	141.6609	37.63297	140.95794
27	68.8319	41.03888	140.38301	35.98511	141.7627	38.51817	141.09546
28	71.1590	41.66098	140.55702	37.04757	141.8428	39.35953	141.21877
29	73.4826	42.22717	140.72490	38.08072	141.9031	40.15826	141.32921
30	75.8034	42.73440	140.88878	39.08282	141.9451	40.91202	141.42873
31	78.1217	43.18109	141.05029	40.05501	141.9697	41.62059	141.51861
32	80.4376	43.56987	141.20960	40.99562	141.9783	42.28450	141.59981
33	82.7518	43.89644	141.36928	41.90451	141.9725	42.90153	141.67438
34	85.0642	44.13653	141.53754	42.77433	141.9552	43.45593	141.74798
35	87.3748	44.30037	141.71382	43.61538	141.9261	43.95800	141.82040

TABLE H.6: int-05 coordinates

K	Z	THSP1_X	THSP1_Y	THSP2_X	THSP2_Y	THSPM_X	THSPM_Y
1	7.0763	-0.97226	144.89514	-1.94303	144.8854	-1.45765	144.89107
2	9.5455	2.17874	145.23876	-0.07117	145.2551	1.05382	145.25128
3	12.0097	5.12820	145.54448	1.794175	145.6237	3.46141	145.59366
4	14.4588	7.86608	145.82410	3.646142	145.9906	5.75671	145.92259
5	16.8954	10.44538	146.08615	5.47483	146.3567	7.96125	146.24256
6	19.3207	12.87564	146.33735	7.278985	146.7223	10.07915	146.55652
7	21.7324	15.16662	146.58437	9.054411	147.0885	12.11314	146.86822
8	24.1305	17.35163	146.82929	10.79386	147.4565	14.07624	147.17941
9	26.5149	19.43920	147.07541	12.50626	147.8264	15.97715	147.49166
10	28.8849	21.42754	147.32631	14.20054	148.1976	17.81937	147.80613
11	31.2401	23.31884	147.58240	15.87057	148.568	19.60090	148.12204
12	33.5798	25.12225	147.84071	17.51425	148.9337	21.32525	148.43596
13	35.9039	26.84822	148.09725	19.13673	149.2897	23.00020	148.74344
14	38.2126	28.50418	148.34837	20.74155	149.6313	24.63122	149.04037
15	40.5057	30.09294	148.59047	22.32754	149.954	26.21910	149.32271
16	42.7842	31.61570	148.82031	23.89039	150.2541	27.76230	149.58707
17	45.0490	33.07803	149.03338	25.43611	150.5261	29.26659	149.82848
18	47.3011	34.48259	149.22626	26.9617	150.7667	30.73180	150.04360
19	49.5420	35.83360	149.39552	28.46559	150.9728	32.15926	150.22932
20	51.7734	37.12670	149.54148	29.94951	151.1426	33.54766	150.38484
21	53.9969	38.36428	149.66591	31.41578	151.2771	34.89933	150.51159
22	56.2138	39.55331	149.76921	32.85768	151.3792	36.21444	150.61140
23	58.4249	40.68894	149.85495	34.2777	151.4501	37.49180	150.68663
24	60.6317	41.77084	149.92544	35.6799	151.4905	38.73328	150.73876
25	62.8351	42.80326	149.98153	37.05777	151.5035	39.93776	150.76987
26	65.0360	43.78741	150.02450	38.41538	151.4891	41.10792	150.78073
27	67.2351	44.72010	150.05698	39.75234	151.4488	42.24195	150.77334
28	69.4332	45.59961	150.08095	41.06523	151.3845	43.33732	150.74977
29	71.6313	46.43192	150.09646	42.35683	151.297	44.39844	150.71049
30	73.8302	47.21241	150.10629	43.62533	151.1878	45.42209	150.65771
31	76.0299	47.94102	150.11192	44.87048	151.0582	46.40816	150.59287
32	78.2309	48.61922	150.11418	46.09207	150.9093	47.35731	150.51704
33	80.4339	49.24558	150.11510	47.29149	150.7421	48.26955	150.43178
34	82.6389	49.80056	150.12219	48.46854	150.5575	49.13503	150.34134
35	84.8456	50.29066	150.13622	49.62506	150.3575	49.95798	150.24725

TABLE H.7: int-06 coordinates

K	Z	THSP1_X	THSP1_Y	THSP2_X	THSP2_Y	THSPM_X	THSPM_Y
1	8.9664	-2.20393	157.18845	-3.18945	157.1715	-2.69670	157.18077
2	11.2823	0.96237	157.50506	-1.1183	157.504	-0.07797	157.50798
3	13.5908	3.95169	157.78212	0.934358	157.8288	2.44314	157.81269
4	15.8806	6.75514	158.02969	2.962426	158.1463	4.85913	158.09935
5	18.1552	9.41776	158.25482	4.95816	158.4572	7.18867	158.37173
6	20.4155	11.95641	158.46237	6.920053	158.7621	9.43942	158.63220
7	22.6598	14.38340	158.65715	8.85136	159.0617	11.61914	158.88351
8	24.8884	16.70792	158.84260	10.75053	159.3567	13.73163	159.12753
9	27.1014	18.93920	159.02146	12.61757	159.6475	15.78149	159.36581
10	29.2991	21.08653	159.19575	14.44925	159.9348	17.77173	159.59979
11	31.4814	23.15883	159.36417	16.25163	160.216	19.70983	159.82738
12	33.6488	25.16157	159.52424	18.02734	160.4871	21.59982	160.04542
13	35.8017	27.09203	159.67425	19.78203	160.7436	23.44313	160.25063
14	37.9410	28.94743	159.81329	21.52453	160.9812	25.24274	160.44017
15	40.0676	30.73274	159.93816	23.25541	161.1952	27.00139	160.61021
16	42.1829	32.45768	160.04479	24.96867	161.3828	28.72097	160.75740
17	44.2880	34.12230	160.13080	26.66786	161.5396	30.40324	160.87836
18	46.3844	35.72670	160.19434	28.35652	161.6618	32.05001	160.97025
19	48.4737	37.27734	160.23203	30.02513	161.7479	33.65977	161.03081
20	50.5573	38.77312	160.24419	31.67904	161.7962	35.23463	161.05924
21	52.6363	40.21509	160.23279	33.31754	161.8077	36.77474	161.05719
22	54.7121	41.60611	160.19982	34.9417	161.7842	38.28210	161.02649
23	56.7854	42.94430	160.14821	36.54778	161.7279	39.75389	160.96984
24	58.8574	44.23113	160.08022	38.13701	161.6405	41.19146	160.88919
25	60.9285	45.46953	159.99684	39.70888	161.523	42.59604	160.78571
26	62.9997	46.65774	159.90045	41.26622	161.376	43.96817	160.66082
27	65.0718	47.79727	159.79255	42.80541	161.2015	45.30682	160.51644
28	67.1457	48.88964	159.67435	44.32452	161.0013	46.61180	160.35409
29	69.2218	49.93318	159.54789	45.82641	160.7756	47.88373	160.17490
30	71.3011	50.92962	159.41476	47.31415	160.525	49.12502	159.98008
31	73.3835	51.87405	159.27749	48.78091	160.2519	50.32984	159.77216
32	75.4697	52.77305	159.13593	50.22983	159.9569	51.50308	159.55147
33	77.5604	53.62513	158.99204	51.66392	159.6401	52.64552	159.31908
34	79.6559	54.41616	158.85222	53.0783	159.3042	53.74771	159.07963
35	81.7558	55.14975	158.71759	54.47471	158.9505	54.81236	158.83443

TABLE H.8: int-07 coordinates

K	Z	THSP1_X	THSP1_Y	THSP2_X	THSP2_Y	THSPM_X	THSPM_Y
1	10.9442	-3.05927	169.47039	-4.06248	169.4493	-3.56089	169.46059
2	13.0927	0.05772	169.75399	-1.82312	169.7442	-0.88272	169.75170
3	15.2340	3.03989	169.99812	0.387657	170.0249	1.71383	170.01666
4	17.3591	5.88138	170.20952	2.566491	170.2918	4.22413	170.25871
5	19.4712	8.61389	170.39321	4.709966	170.5458	6.66236	170.48067
6	21.5715	11.25061	170.55313	6.816342	170.7878	9.03424	170.68488
7	23.6587	13.79289	170.69314	8.88728	171.0187	11.34125	170.87354
8	25.7333	16.25235	170.81567	10.92271	171.2391	13.58918	171.04814
9	27.7957	18.63728	170.92291	12.92598	171.4494	15.78382	171.20999
10	29.8460	20.95087	171.01716	14.90045	171.6502	17.92845	171.36038
11	31.8843	23.19770	171.09757	16.84407	171.8394	20.02432	171.49792
12	33.9108	25.37871	171.16265	18.76145	172.0138	22.07418	171.62011
13	35.9260	27.49299	171.21135	20.65708	172.1699	24.07981	171.72464
14	37.9304	29.54125	171.24228	22.54053	172.3036	26.04629	171.80860
15	39.9245	31.52577	171.25361	24.41433	172.4112	27.97604	171.86918
16	41.9095	33.44533	171.24400	26.27227	172.4902	29.86530	171.90451
17	43.8862	35.29862	171.21223	28.1201	172.5366	31.71627	171.91189
18	45.8558	37.09119	171.15589	29.9566	172.5477	33.53111	171.88880
19	47.8196	38.82350	171.07401	31.78225	172.5209	35.31029	171.83353
20	49.7787	40.49804	170.96653	33.5926	172.4563	37.05281	171.74614
21	51.7344	42.11779	170.83521	35.39041	172.3546	38.76155	171.62786
22	53.6878	43.68760	170.68146	37.17	172.2183	40.43610	171.48087
23	55.6397	45.20559	170.50845	38.93954	172.0476	42.07961	171.30670
24	57.5911	46.67167	170.31872	40.69518	171.8447	43.69009	171.10783
25	59.5427	48.09089	170.11321	42.43311	171.612	45.26820	170.88601
26	61.4955	49.46130	169.89387	44.15625	171.3493	46.81443	170.64219
27	63.4504	50.78301	169.66299	45.86777	171.0573	48.33042	170.37786
28	65.4078	52.06095	169.42044	47.5638	170.7376	49.81673	170.09386
29	67.3685	53.29186	169.16919	49.2424	170.392	51.27078	169.79265
30	69.3331	54.47740	168.91009	50.91004	170.0193	52.69664	169.47410
31	71.3020	55.61441	168.64613	52.56315	169.6219	54.09098	169.14090
32	73.2759	56.70796	168.37686	54.2014	169.2004	55.45621	168.79327
33	75.2553	57.75834	168.10414	55.82474	168.7561	56.79248	168.43290
34	77.2406	58.75566	167.83285	57.43638	168.2889	58.09647	168.06218
35	79.2314	59.70379	167.56406	59.03305	167.8015	59.36854	167.68313

TABLE H.9: int-08 coordinates

K	Z	THSP1_X	THSP1_Y	THSP2_X	THSP2_Y	THSPM_X	THSPM_Y
1	13.0989	-3.06980	181.73527	-4.03658	181.7164	-3.55321	181.72647
2	15.0799	-0.00546	181.97050	-1.74143	181.9622	-0.87346	181.96840
3	17.0553	2.95683	182.16690	0.526531	182.1901	1.74172	182.18257
4	19.0164	5.80914	182.32888	2.767226	182.4004	4.28833	182.37099
5	20.9661	8.57100	182.46070	4.984225	182.5939	6.77794	182.53610
6	22.9064	11.25109	182.56504	7.173774	182.7707	9.21301	182.67923
7	24.8358	13.85271	182.64512	9.335776	182.9316	11.59513	182.80233
8	26.7548	16.37917	182.70328	11.47193	183.0769	13.92680	182.90656
9	28.6641	18.83752	182.74165	13.58214	183.2072	16.21150	182.99331
10	30.5636	21.23480	182.76141	15.66623	183.3227	18.45265	183.06324
11	32.4537	23.57416	182.76198	17.72754	183.4214	20.65348	183.11503
12	34.3347	25.85672	182.74199	19.76555	183.5008	22.81429	183.14670
13	36.2070	28.08353	182.70019	21.78144	183.5582	24.93618	183.15630
14	38.0712	30.25746	182.63557	23.77272	183.5923	27.01933	183.14263
15	39.9279	32.38118	182.54626	25.74222	183.6001	29.06648	183.10329
16	41.7783	34.45362	182.43087	27.70367	183.5772	31.08393	183.03515
17	43.6231	36.46099	182.29128	29.65977	183.5206	33.06609	182.93756
18	45.4633	38.39853	182.12757	31.60938	183.4278	35.00999	182.80919
19	47.3004	40.27986	181.93707	33.54782	183.2979	36.92011	182.64849
20	49.1351	42.10417	181.72045	35.47228	183.1306	38.79463	182.45564
21	50.9686	43.87303	181.48022	37.3859	182.9268	40.63591	182.23237
22	52.8019	45.54590	181.04339	39.25214	182.5114	42.40537	181.80463
23	54.6359	47.26002	180.93551	41.18242	182.4149	44.22740	181.70059
24	56.4712	48.98648	180.60713	43.06277	182.1104	46.03076	181.38296
25	58.3084	50.44952	180.32179	44.93618	181.7741	47.69838	181.06896
26	60.1484	51.97417	179.99308	46.79493	181.4085	49.38962	180.71936
27	61.9921	53.45578	179.65149	48.64241	181.0141	51.05364	180.34884
28	63.8399	54.89065	179.29934	50.48359	180.5897	52.69107	179.95802
29	65.6925	56.28071	178.93791	52.31276	180.1379	54.30005	179.54887
30	67.5502	57.62782	178.56810	54.13142	179.6589	55.88228	179.12203
31	69.4138	58.93227	178.19188	55.93764	179.1545	57.43697	178.67947
32	71.2836	60.19590	177.80984	57.7329	178.6247	58.96581	178.22155
33	73.1600	61.41713	177.42400	59.52056	178.0692	60.46971	177.74913
34	75.0436	62.58921	177.03853	61.30049	177.4889	61.94526	177.26488
35	76.9339	63.72153	176.65253	63.06925	176.8865	63.39550	176.76979

TABLE H.10: int-09 coordinates

K	Z	THSP1_X	THSP1_Y	THSP2_X	THSP2_Y	THSPM_X	THSPM_Y
1	15.0418	-2.74585	194.03987	-3.66362	194.0247	-3.20474	194.03284
2	16.8586	0.25054	194.21864	-1.33427	194.2142	-0.54187	194.21804
3	18.6715	3.16646	194.36361	0.973887	194.387	2.07021	194.37838
4	20.4737	5.99530	194.46481	3.262571	194.5298	4.62905	194.50212
5	22.2680	8.74846	194.53869	5.529739	194.6568	7.13934	194.60439
6	24.0555	11.43125	194.58301	7.771289	194.7635	9.60170	194.68187
7	25.8352	14.04917	194.60022	9.992893	194.8506	12.02168	194.73598
8	27.6076	16.60768	194.59168	12.19045	194.9183	14.39999	194.76750
9	29.3729	19.11038	194.55900	14.36767	194.9666	16.74026	194.77725
10	31.1312	21.55891	194.50375	16.52435	194.996	19.04322	194.76614
11	32.8830	23.95475	194.42555	18.66206	195.0048	21.31037	194.73313
12	34.6285	26.30307	194.32272	20.78224	194.9904	23.54503	194.67615
13	36.3680	28.60907	194.19394	22.87848	194.9521	25.74656	194.59414
14	38.1022	30.87592	194.03812	24.94432	194.8894	27.91336	194.48640
15	39.8315	33.10086	193.85450	27.01604	194.7957	30.06213	194.34892
16	41.5568	35.27526	193.64365	29.0636	194.6728	32.17355	194.18308
17	43.2787	37.40025	193.40510	31.09594	194.5183	34.25262	193.98729
18	44.9981	39.47676	193.13751	33.11203	194.3299	36.29929	193.75984
19	46.7160	41.49827	192.84267	35.12855	194.1041	38.31860	193.49958
20	48.4334	43.46221	192.52202	37.14463	193.8401	40.30881	193.20687
21	50.1509	45.36841	192.17834	39.15588	193.5397	42.26763	192.88404
22	51.8695	47.22450	191.81276	41.15804	193.2053	44.19676	192.53295
23	53.5899	49.03433	191.42696	43.15269	192.838	46.09891	192.15498
24	55.3127	50.79410	191.02436	45.13952	192.439	47.97202	191.75252
25	57.0388	52.50786	190.60678	47.12411	192.0087	49.82091	191.32667
26	58.7685	54.17540	190.17510	49.10201	191.5477	51.64327	190.87827
27	60.5027	55.79884	189.73107	51.0711	191.0579	53.43909	190.40918
28	62.2422	57.38003	189.27539	53.03477	190.5386	55.21102	189.91941
29	63.9873	58.91734	188.81058	54.99471	189.9902	56.95908	189.41053
30	65.7387	60.41267	188.33724	56.9505	189.4129	58.68405	188.88300
31	67.4968	61.87008	187.85593	58.89814	188.8088	60.38599	188.33824
32	69.2625	63.28427	187.37033	60.8413	188.1778	62.06410	187.77802
33	71.0356	64.65518	186.88096	62.78129	187.5188	63.71904	187.20222
34	72.8174	65.98350	186.39043	64.71528	186.8345	65.34977	186.61357
35	74.6073	67.27519	185.89823	66.64089	186.1266	66.95813	186.01267

TABLE H.11: int-10 coordinates

K	Z	THSP1_X	THSP1_Y	THSP2_X	THSP2_Y	THSPM_X	THSPM_Y
1	16.9343	-2.20005	206.37557	-3.06474	206.3645	-2.63240	206.37051
2	18.6159	0.74949	206.47124	-0.7082	206.4714	0.02065	206.47260
3	20.2959	3.63564	206.54901	1.634039	206.5745	2.63487	206.56420
4	21.9675	6.45394	206.59121	3.96411	206.654	5.20912	206.62635
5	23.6335	9.21633	206.59993	6.277647	206.7101	7.74719	206.66024
6	25.2945	11.92651	206.57680	8.576479	206.743	10.25183	206.66668
7	26.9496	14.57993	206.52349	10.86034	206.7525	12.72065	206.64634
8	28.5994	17.18449	206.44150	13.12486	206.7393	15.15541	206.60037
9	30.2438	19.73983	206.33189	15.37596	206.7029	17.55887	206.52893
10	31.8829	22.24976	206.19593	17.61544	206.6434	19.93386	206.43269
11	33.5172	24.71791	206.03298	19.83671	206.5601	22.27887	206.31097
12	35.1466	27.14573	205.84187	22.03922	206.4511	24.59436	206.16228
13	36.7715	29.52852	205.62300	24.22658	206.3149	26.87978	205.98599
14	38.3922	31.88011	205.37457	26.40239	206.1504	29.14383	205.78069
15	40.0093	34.19568	205.09652	28.5639	205.9564	31.38274	205.54574
16	41.6234	36.46224	204.79064	30.71455	205.7312	33.59169	205.28103
17	43.2349	38.68727	204.45547	32.83715	205.4762	35.76585	204.98670
18	44.8445	40.88024	204.08868	34.93504	205.19	37.91164	204.66092
19	46.4530	43.03028	203.69271	37.03422	204.8677	40.03656	204.30223
20	48.0613	45.12871	203.27016	39.13802	204.5081	42.13791	203.91115
21	49.6699	47.16530	202.82607	41.24188	204.1129	44.20827	203.49106
22	51.2794	49.14009	202.36339	43.33319	203.6858	46.24137	203.04538
23	52.8908	51.06347	201.88302	45.41789	203.2276	48.24537	202.57496
24	54.5046	52.93552	201.38712	47.49768	202.7385	50.22115	202.08112
25	56.1212	54.76257	200.87685	49.57039	202.2207	52.17081	201.56551
26	57.7414	56.54253	200.35380	51.63553	201.6742	54.09306	201.02897
27	59.3657	58.27556	199.81984	53.69486	201.0992	55.98886	200.47258
28	60.9945	59.96575	199.27517	55.75001	200.4954	57.86110	199.89642
29	62.6286	61.61133	198.72209	57.80273	199.8631	59.70975	199.30171
30	64.2685	63.21649	198.16094	59.84874	199.2039	61.53483	198.68958
31	65.9145	64.78139	197.59290	61.89172	198.517	63.33824	198.06022
32	67.5672	66.30832	197.01896	63.93146	197.803	65.12107	197.41456
33	69.2273	67.79544	196.44068	65.97154	197.0607	66.88421	196.75280
34	70.8952	69.24518	195.85925	68.01186	196.2909	68.62886	196.07606
35	72.5711	70.65998	195.27566	70.05037	195.4952	70.35526	195.38565

TABLE H.12: int-11 coordinates

K	Z	THSP1_X	THSP1_Y	THSP2_X	THSP2_Y	THSPM_X	THSPM_Y
1	19.0349	-1.19376	218.63584	-2.00927	218.6299	-1.60152	218.63323
2	20.5877	1.74513	218.68364	0.363026	218.6903	1.05408	218.68806
3	22.1409	4.63479	218.69279	2.732015	218.7248	3.68344	218.71088
4	23.6862	7.47032	218.66513	5.093034	218.7334	6.28177	218.70250
5	25.2262	10.25780	218.60266	7.445797	218.7165	8.85198	218.66410
6	26.7632	12.99892	218.50579	9.789966	218.6731	11.39475	218.59531
7	28.2955	15.69325	218.37634	12.12742	218.6034	13.91080	218.49713
8	29.8230	18.34257	218.21545	14.44689	218.5079	16.39538	218.37038
9	31.3472	20.94864	218.02410	16.75679	218.3863	18.85358	218.21525
10	32.8676	23.51325	217.80307	19.06331	218.2376	21.28939	218.03168
11	34.3843	26.04247	217.55191	21.35508	218.0619	23.70015	217.81953
12	35.8981	28.52914	217.27067	23.63157	217.8578	26.08201	217.57799
13	37.4090	30.97495	216.95953	25.89878	217.6238	28.43880	217.30651
14	38.9172	33.38812	216.61819	28.15408	217.3604	30.77334	217.00509
15	40.4237	35.76807	216.24657	30.39688	217.0667	33.08502	216.67329
16	41.9286	38.10778	215.84593	32.63093	216.7415	35.37218	216.31107
17	43.4325	40.41532	215.41511	34.84478	216.386	37.63318	215.91853
18	44.9360	42.69433	214.95290	37.04639	215.998	39.87379	215.49394
19	46.4396	44.93576	214.46192	39.24603	215.5757	42.09458	215.03763
20	47.9441	47.13062	213.94492	41.43659	215.1203	44.28751	214.55149
21	49.4500	49.26609	213.40736	43.61563	214.6335	46.44491	214.03906
22	50.9576	51.35086	212.85011	45.7829	214.1168	48.57101	213.50161
23	52.4679	53.37671	212.27824	47.95112	213.5692	50.66803	212.94102
24	53.9811	55.34817	211.69328	50.12003	212.9917	52.73809	212.35856
25	55.4977	57.26985	211.09676	52.27885	212.3878	54.77815	211.75701
26	57.0181	59.14179	210.48981	54.42508	211.7584	56.78697	211.13728
27	58.5430	60.96427	209.87435	56.56068	211.1037	58.76569	210.50054
28	60.0723	62.73949	209.25082	58.69372	210.4215	60.71942	209.84590
29	61.6069	64.46779	208.62111	60.81772	209.7143	62.64514	209.17564
30	63.1471	66.14945	207.98665	62.93038	208.9832	64.54184	208.49112
31	64.6934	67.78691	207.34839	65.02951	208.2296	66.40967	207.79359
32	66.2456	69.38242	206.70658	67.12109	207.4519	68.25277	207.08232
33	67.8049	70.94053	206.06144	69.2092	206.6494	70.07548	206.35722
34	69.3709	72.46151	205.41403	71.29359	205.8223	71.87784	205.61900
35	70.9442	73.95003	204.76475	73.37435	204.9717	73.66226	204.86844

TABLE H.13: int-12 coordinates

K	Z	THSP1_X	THSP1_Y	THSP2_X	THSP2_Y	THSPM_X	THSPM_Y
1	21.0996	0.11777	230.91807	-0.66504	230.9171	-0.27364	230.91794
2	22.5221	3.03877	230.89660	1.699531	230.9103	2.36916	230.90445
3	23.9458	5.92222	230.83514	4.061517	230.8754	4.99191	230.85714
4	25.3637	8.76294	230.73576	6.427484	230.8126	7.59531	230.77715
5	26.7780	11.56271	230.59939	8.794747	230.7215	10.17891	230.66462
6	28.1908	14.32329	230.42666	11.15598	230.6017	12.73994	230.51962
7	29.6006	17.04192	230.21910	13.51079	230.4533	15.27680	230.34296
8	31.0076	19.72039	229.97744	15.86568	230.2755	17.79366	230.13454
9	32.4129	22.36286	229.70229	18.21792	230.0681	20.29121	229.89455
10	33.8162	24.97008	229.38432	20.56386	229.8212	22.76802	229.61334
11	35.2183	27.54478	229.05365	22.908	229.5637	25.22768	229.32042
12	36.6190	30.08085	228.68055	25.24247	229.2651	27.66320	228.98559
13	38.0190	32.58350	228.27538	27.56999	228.935	30.07855	228.61893
14	39.4185	35.05920	227.83827	29.89468	228.5733	32.47902	228.22037
15	40.8181	37.50066	227.37103	32.21375	228.1801	34.85955	227.79090
16	42.2181	39.90746	226.87425	34.52212	227.7559	37.21740	227.33103
17	43.6190	42.29274	226.34590	36.82151	227.3001	39.56000	226.83948
18	45.0212	44.65385	225.78727	39.11829	226.8119	41.88920	226.31648
19	46.4252	46.97452	225.20179	41.4209	226.2891	44.20105	225.76252
20	47.8316	49.25467	224.59146	43.70408	225.7372	46.48291	225.18145
21	49.2404	51.49647	223.95754	45.96758	225.1574	48.73572	224.57448
22	50.6525	53.69342	223.30432	48.23609	224.5464	50.96854	223.94198
23	52.0680	55.82800	222.63880	50.50269	223.9069	53.16913	223.28870
24	53.4871	57.89395	221.96534	52.76049	223.2412	55.33090	222.61809
25	54.9105	59.88979	221.28796	55.0029	222.553	57.44983	221.93392
26	56.3381	61.82669	220.60457	57.22285	221.8433	59.52799	221.23593
27	57.7708	63.70959	219.91629	59.42486	221.1126	61.57013	220.52484
28	59.2083	65.54088	219.22353	61.6087	220.3609	63.57733	219.80102
29	60.6517	67.31890	218.52902	63.77884	219.5883	65.55101	219.06582
30	62.1006	69.04831	217.83256	65.9351	218.795	67.49342	218.31934
31	63.5557	70.72298	217.13772	68.07088	217.9837	69.39822	217.56474
32	65.0172	72.34992	216.44396	70.19059	217.1538	71.27114	216.80157
33	66.4854	73.93373	215.75069	72.28974	216.3071	73.11226	216.03045
34	67.9606	75.47073	215.06133	74.36863	215.4449	74.91992	215.25383
35	69.4427	76.96984	214.37372	76.42937	214.567	76.69967	214.47053

TABLE H.14: int-tip coordinates

K	Z	THSP1_X	THSP1_Y	THSP2_X	THSP2_Y	THSPM_X	THSPM_Y
1	23.0058	1.21125	243.22008	0.432937	243.2227	0.82209	243.22171
2	24.2980	4.03151	243.13278	2.76474	243.1505	3.39814	243.14246
3	25.5904	6.94936	243.00325	5.104779	243.049	6.02711	243.02788
4	26.8777	9.76726	242.83585	7.447771	242.9181	8.60762	242.87972
5	28.1622	12.55516	242.62998	9.793275	242.7571	11.17440	242.69749
6	29.4454	15.31244	242.38581	12.14324	242.5652	13.72814	242.48070
7	30.7271	18.03860	242.10483	14.49965	242.3425	16.26956	242.23014
8	32.0079	20.73545	241.78660	16.86196	242.0876	18.79931	241.94484
9	33.2881	23.40734	241.43206	19.22969	241.8007	21.31931	241.62539
10	34.5682	26.04401	241.04219	21.59985	241.481	23.82294	241.27183
11	35.8495	28.65939	240.61582	23.96947	241.1282	26.31568	240.88342
12	37.1319	31.25285	240.15296	26.34275	240.741	28.79930	240.45953
13	38.4160	33.81916	239.65556	28.72163	240.3198	31.27215	240.00119
14	39.7031	36.36274	239.12453	31.10562	239.865	33.73621	239.50920
15	40.9933	38.88086	238.56145	33.49187	239.3775	36.18867	238.98466
16	42.2868	41.37550	237.96668	35.88464	238.8564	38.63263	238.42733
17	43.5848	43.84638	237.34150	38.27633	238.3032	41.06417	237.83865
18	44.8873	46.29077	236.68705	40.66168	237.7188	43.47929	237.21962
19	46.1948	48.71796	236.00295	43.04514	237.1032	45.88485	236.57010
20	47.5076	51.14649	235.28595	45.43578	236.4551	48.29467	235.88783
21	48.8261	53.55976	234.54117	47.8428	235.7738	50.70503	235.17484
22	50.1502	55.89695	233.78460	50.27761	235.0572	53.09110	234.43772
23	51.4801	58.17279	233.01661	52.6954	234.316	55.43790	233.68237
24	52.8159	60.37385	232.24341	55.07982	233.5556	57.73056	232.91454
25	54.1575	62.46160	231.47893	57.45213	232.7728	59.96036	232.13940
26	55.5048	64.45989	230.71916	59.77957	231.9759	62.12291	231.35935
27	56.8580	66.38797	229.96163	62.05321	231.169	64.22343	230.57551
28	58.2174	68.24180	229.20946	64.29411	230.348	66.27040	229.78719
29	59.5829	70.02440	228.46408	66.50018	229.5147	68.26431	228.99615
30	60.9545	71.74993	227.72257	68.67151	228.6697	70.21232	228.20134
31	62.3324	73.41005	226.99000	70.80626	227.8157	72.10934	227.40655
32	63.7166	75.01428	226.26443	72.90681	226.9523	73.96134	226.61080
33	65.1070	76.56542	225.54647	74.97569	226.0799	75.77102	225.81459
34	66.5039	78.06185	224.83849	77.00876	225.2014	77.53552	225.02054
35	67.9072	79.51302	224.13831	79.01076	224.3159	79.26194	224.22722

Bibliography

- [1] International standards and recommended practices. annex 16 to the convention on international civil aviation. environmental protection. volume i. aircraft noise. Technical report, ICAO, 2011.
- [2] 7-year ifr flight movements and service units forecast: 2013-2019, 2012.
- [3] Challenges of growth 2013 task 4: European air traffic in 2035, 2013.
- [4] *ANSYS Documentation. Fluent Theory Guide*, 2015.
- [5] *Prometheus HPC maunual*, 2018. <https://kdm.cyfronet.pl/portal/Prometheus>.
- [6] J. D. Anderson. *Computational Fluid Dynamics*. McGraw-Hill, Inc., 1995.
- [7] A. Bjork and G. Dahlquist. *Numerical Methods*. Prentice-Hall, 1974.
- [8] R. Bracewell. *The Fourier Transform and Its Applications*. McGraw-Hill, Inc., 1965.
- [9] K. S. Brentner and F. Farassat. An analytical comparison of the acoustic analogy and kirchhoff formulations for moving surfaces. *AIAA Journal*, 36(8):1379–1386, 1998.
- [10] C. Choi and P. Moin. Grid-point requirements for large eddy simulation: Chapman’s estimates revisited. *Physics of Fluids*, 24(1), January 2012. <https://aip.scitation.org/doi/full/10.1063/1.3676783>.
- [11] J. E. Crouse, J. S. David, C. Janetzke, and R. E. Schwirian. A computer program for composing blading from simulated circular-arc elements on conical surfaces. Technical Report TN D-5437, NASA Langley Research Center, 1969.
- [12] W. S. Cunnan, W. Stevans, and D. C. Urasek. Design and performance of a 427-meter-per-second-tip-speed two stage fan having a 2.40 pressure ratio. Technical Report TP-1314, NASA Langley Research Center, 1978.

- [13] N. Curle. The influence of solid boundaries upon aerodynamic sound. *Proceedings of the Royal Society. Series A, Mathematical, Physical and Engineering Sciences*, 231(1187):505–514, September 1955. <http://rspa.royalsocietypublishing.org/content/231/1187/505>.
- [14] J. D. Durrant and J. H. Lovrinic. *Bases of Hearing Sciences. Second Edition*. Lippincott Williams and Wilkins, 1984.
- [15] J. O. Hinze. *Turbulence*. McGraw-Hill Publishing Co., 1975.
- [16] D. L. Huff. Noise reduction technologies for turbofan engines. Technical Report NASA/TM—2007-214495, NASA Glenn Research Center, 2007.
- [17] R. King. Part ii: Turbomachinery. In *Active Flow Control II*, pages 134–210, 2010.
- [18] J. B. Lee, D. Edmonds, and D. Rhodes. Ercd report 1101. noise exposure contours for heathrow airport 2010. Technical report, CAA, 2011.
- [19] M. J. Lighthill. On sound generated aerodynamically i. general theory. *Proceedings of the Royal Society. Series A, Mathematical, Physical and Engineering Sciences*, 211(1107):564–587, March 1952. <http://rspa.royalsocietypublishing.org/content/211/1107/564>.
- [20] M. J. Lighthill. On sound generated aerodynamically ii. turbulence as a source of sound. *Proceedings of the Royal Society. Series A, Mathematical, Physical and Engineering Sciences*, 222(1148):1–32, March 1954. <http://rspa.royalsocietypublishing.org/content/222/1148/1>.
- [21] J. Mosiezny. Github repository for nasa r67 input data and noise analysis, 2018. <https://github.com/JedrzejMosiezny/R67-data-analysis>.
- [22] T. Oetkier, H. Partl, I. Hyba, and E. Schleg. *The Not So Short Introduction to LATEX 2e*, 2018. <https://tobi.oetiker.ch/lshort/lshort.pdf>.
- [23] A. Schwarz and J. Janicka. *Combustion Noise*. Springer Science and Business Media, 2009.
- [24] J. Smagorinsky. General circulation experiments with the primitive equations. *Monthly Weather Review*, 91(3):99–164, 1963.
- [25] P. R. Spalart et al. A new version of detached-eddy simulation, resistant to ambiguous grid densities. *Theoretical and Computational Fluid Dynamics*, 20:181–195, 2006.

- [26] P. R. Spalart, W. H. Jou, M. Strelets, and S. R. Allmaras. Comments of feasibility of les for wings, and on a hybrid rans/les approach. In *First International conference: Advances in DNS LES: Direct numerical simulation and large eddy simulation*, pages 137–148, 1997.
- [27] A. J. Strazisar, J. R. Wood, M. D. Hathaway, and K. L. Suder. Laser anemometer measurements in a transonic axial-flow fan rotor. Technical Report TP-2897, NASA Langley Research Center, 1989.
- [28] P. Traub. Noise aspects of future jet engines. Technical report, LTH Triebwerke, 2012.
- [29] D. C. Urasek, W. T. Gorrel, and W. S. Cunnan. Performance of a two-stage fan having a low-aspect-ratio, first-stage rotor blading. Technical Report TP-1493, NASA Langley Research Center, 1979.
- [30] H. K. Versteeg and W. Malalasekera. *An introduction to Computational Fluid Dynamics: The Finite Volume Method*. Longman Scientific & Technical, 1995.
- [31] C. Wagner, T. Hüttl, and P. Sagaut. *Large-Eddy Simulation for Acoustics*. Cambridge University Press, 2007.
- [32] I. Wieczorek and J. Mosieżny. Development of air transport in statistical terms. *Journal of Mechanical and Transport Engineering*, 66(1):51–68, 2013.
- [33] J. E. F. Williams and D. L. Hawkings. Sound generation by turbulence and surfaces in arbitrary motion. *Philosophical Transactions of the Royal Society of London. Series A, Mathematical and Physical Sciences*, 264(1151):321–342, May 1969. <http://www.jstor.org/stable/73790>.